FERMILAB-LOI-2009-01

SiD Letter of Intent

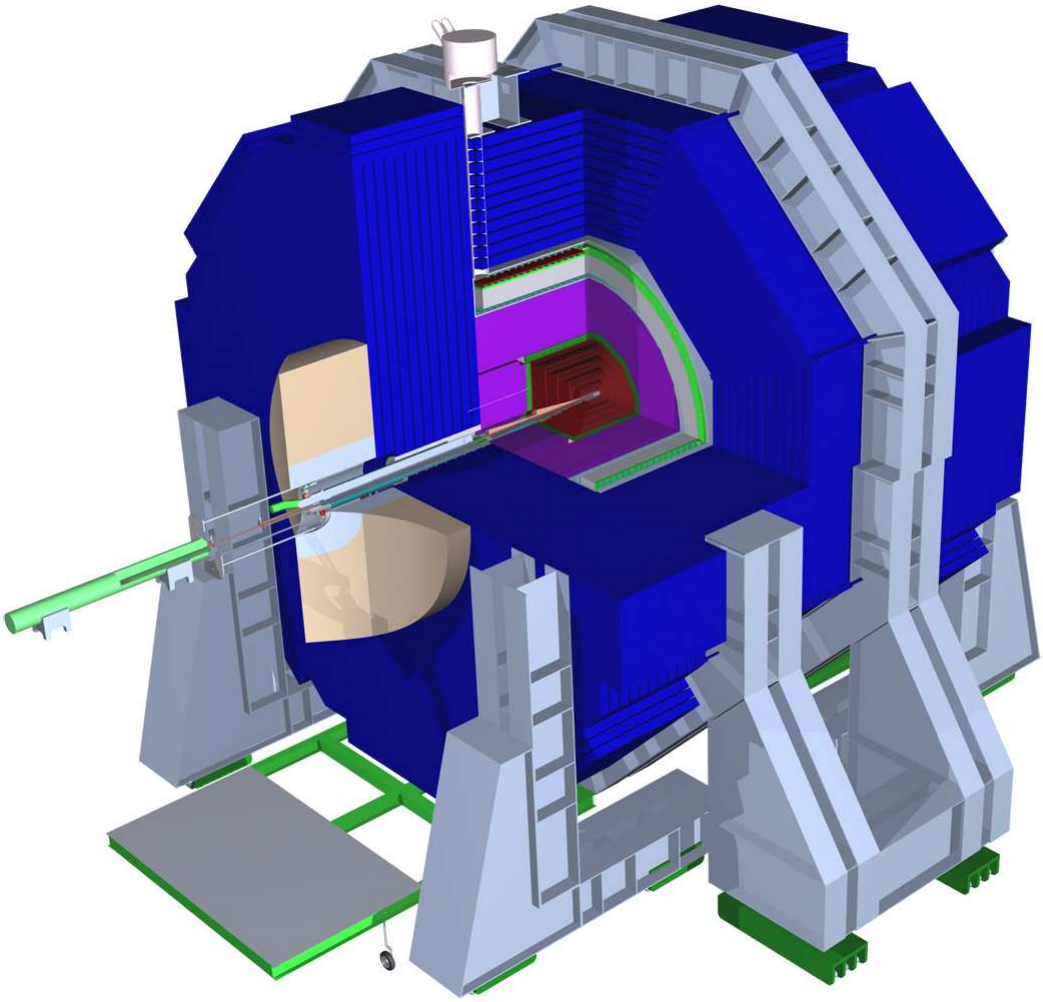

This manuscript has been authored by Fermi Research Alliance, LLC under Contract No. DE-AC02-07CH11359 with the U.S. Department of Energy, Office of Science, Office of High Energy Physics.


MUON
Solenoid
HCAL
ECAL
Tracker
HCAL
MUON
QD0
7000
6000
5000
4000
3000
2000
1000
0
0
1000
2000
3000
4000
5000
6000
7000
8000
9000

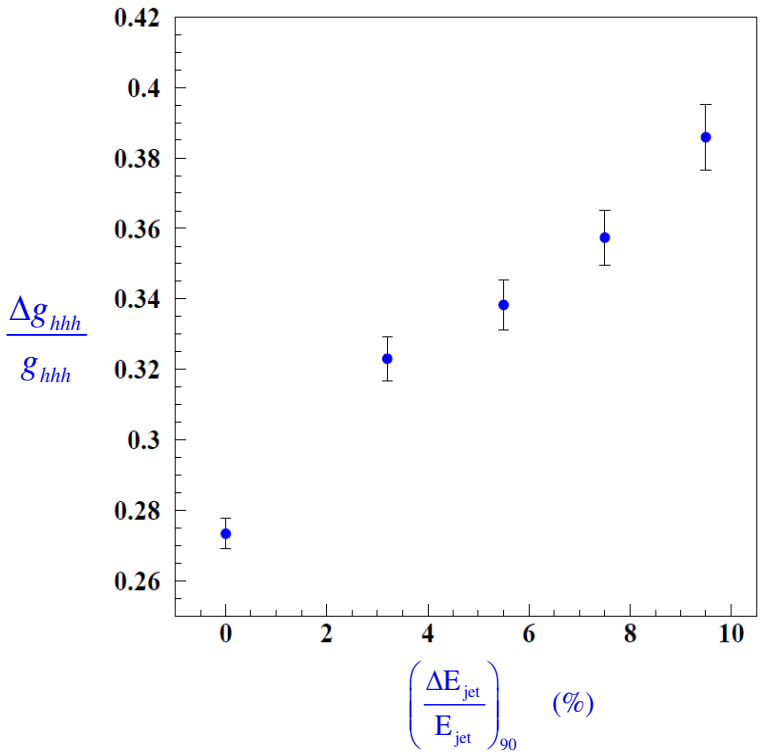
0.42
0.4
0.38
0.36
0.34
0.32
0.3
0.28
0.26
0
2
4
6
8
10
$\frac{\Delta g_{hhh}}{g_{hhh}}$
$\left(\frac{\Delta E_{jet}}{E_{jet}}\right)_{90}$ (%)

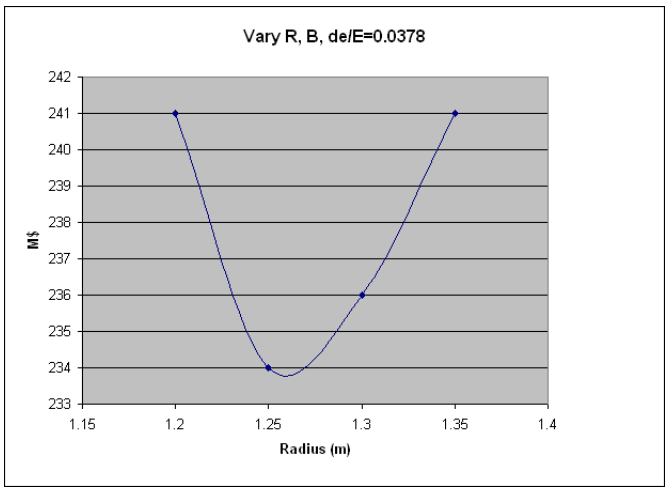
Vary R, B, de/E=0.0378
M$
242
241
240
239
238
237
236
235
234
233
1.15
1.2
1.25
1.3
1.35
1.4
Radius (m)

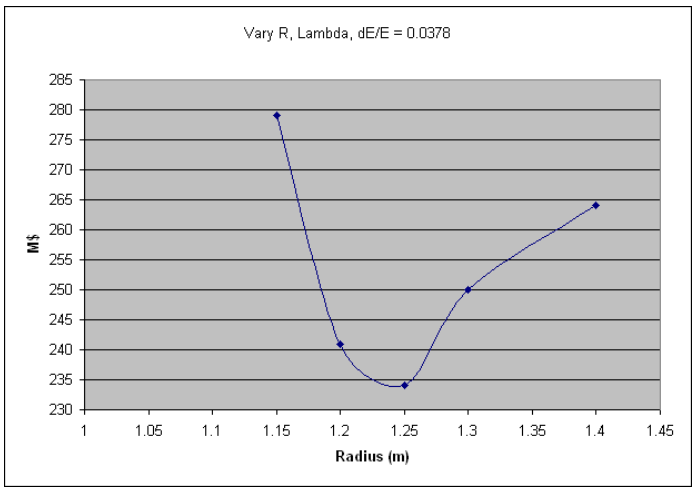
Vary R, Lambda, dE/E = 0.0378
M$
285
280
275
270
265
260
255
250
245
240
235
230
1
1.05
1.1
1.15
1.2
1.25
1.3
1.35
1.4
1.45
Radius (m)

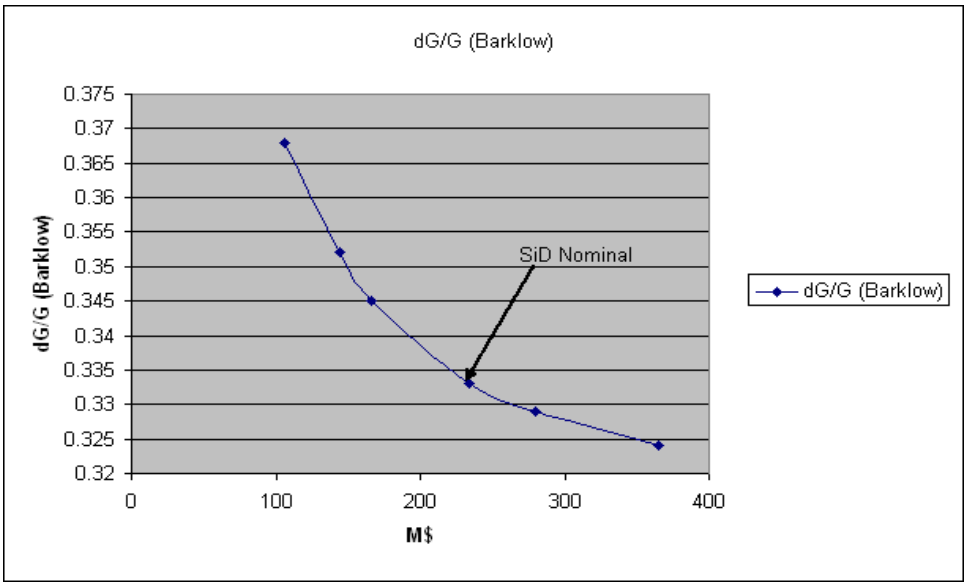
dG/G (Barklow)
0.375
0.37
0.365
0.36
0.355
0.35
0.345
0.34
0.335
0.33
0.325
0.32
dG/G (Barklow)
SiD Nominal
0
100
200
300
400
M$
dG/G (Barklow)

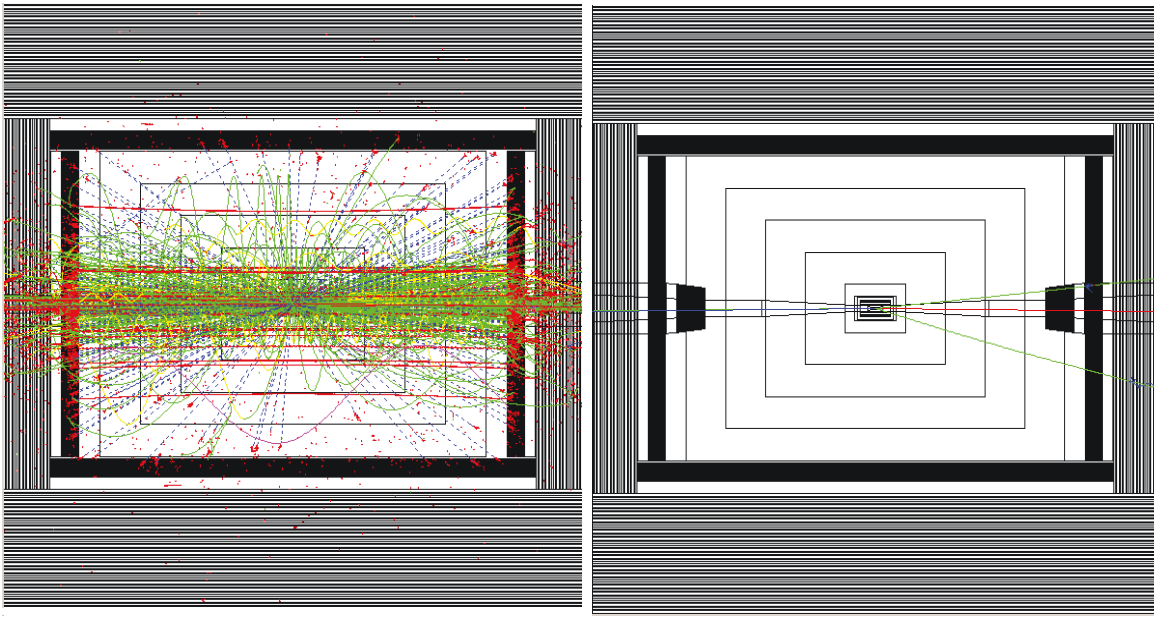

SiD Organization Chart

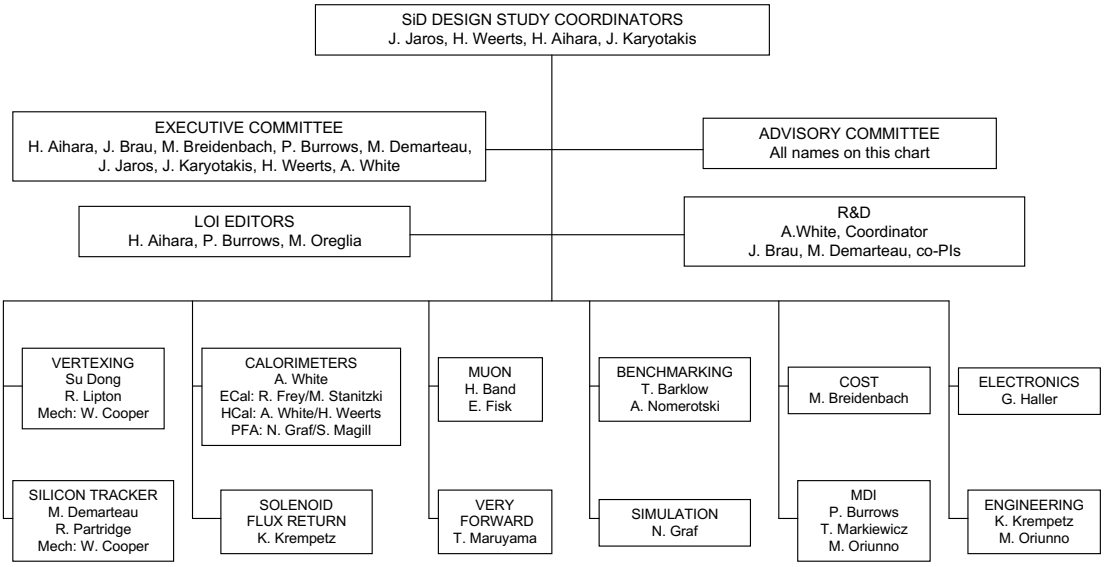

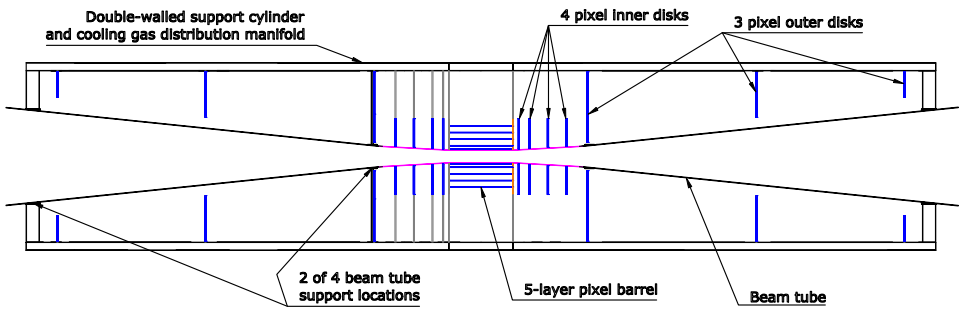
Double-walled support cylinder
and cooling gas distribution manifold
4 pixel inner disks
3 pixel outer disks
2 of 4 beam tube
support locations
5-layer pixel barrel
Beam tube

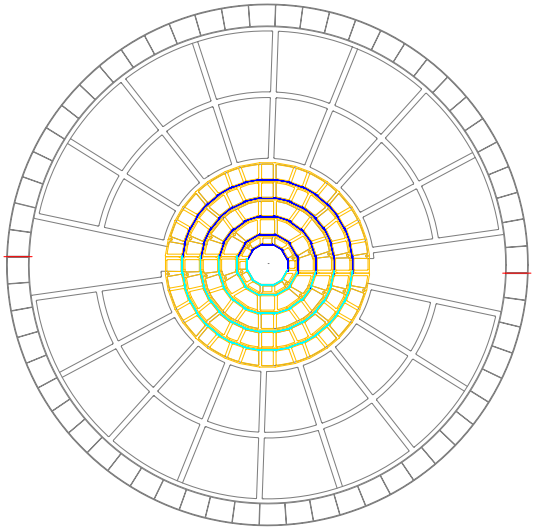

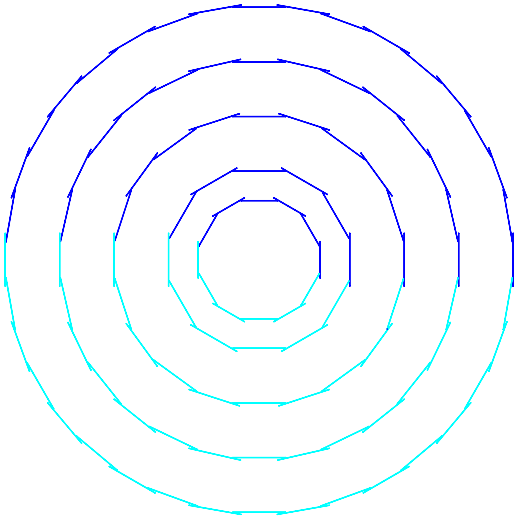

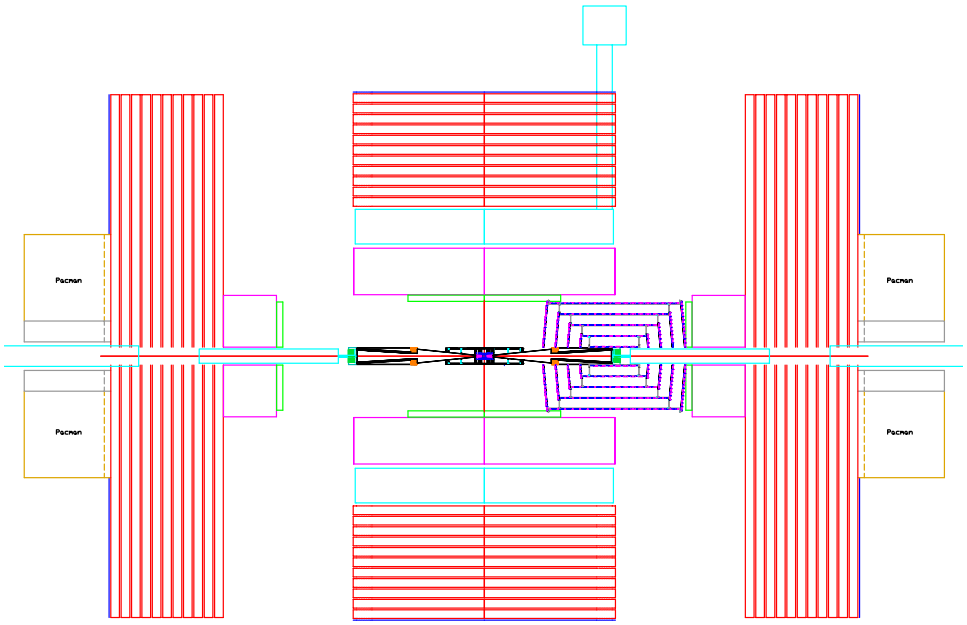
Pacman
Pacman
Pacman
Pacman

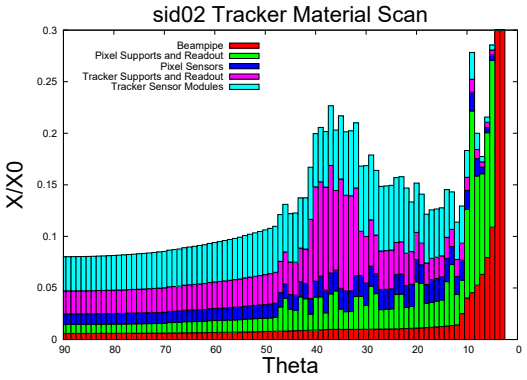
sid02 Tracker Material Scan
Beampipe
Pixel Supports and Readout
Pixel Sensors
Tracker Supports and Readout
Tracker Sensor Modules
X/X0
Theta
0.3
0.25
0.2
0.15
0.1
0.05
0
90
80
70
60
50
40
30
20
10
0

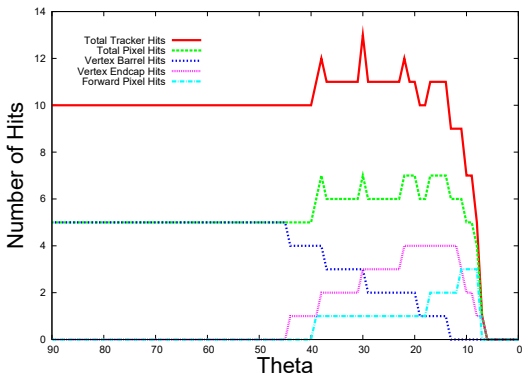
Total Tracker Hits
Total Pixel Hits
Vertex Barrel Hits
Vertex Endcap Hits
Forward Pixel Hits
Number of Hits
Theta
14
12
10
8
6
4
2
0
90
80
70
60
50
40
30
20
10
0

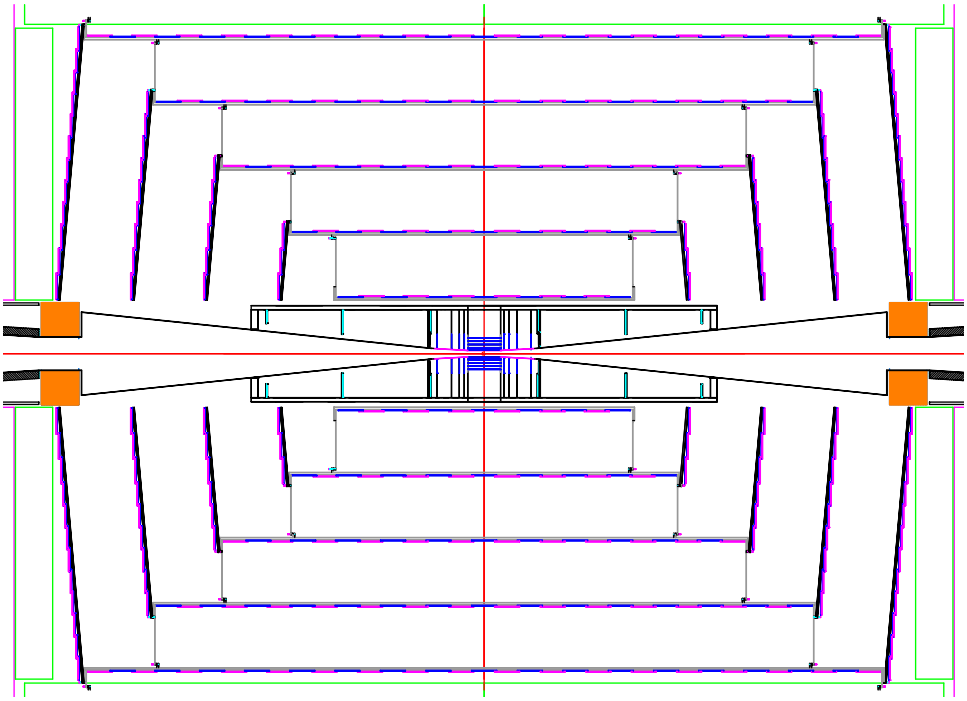

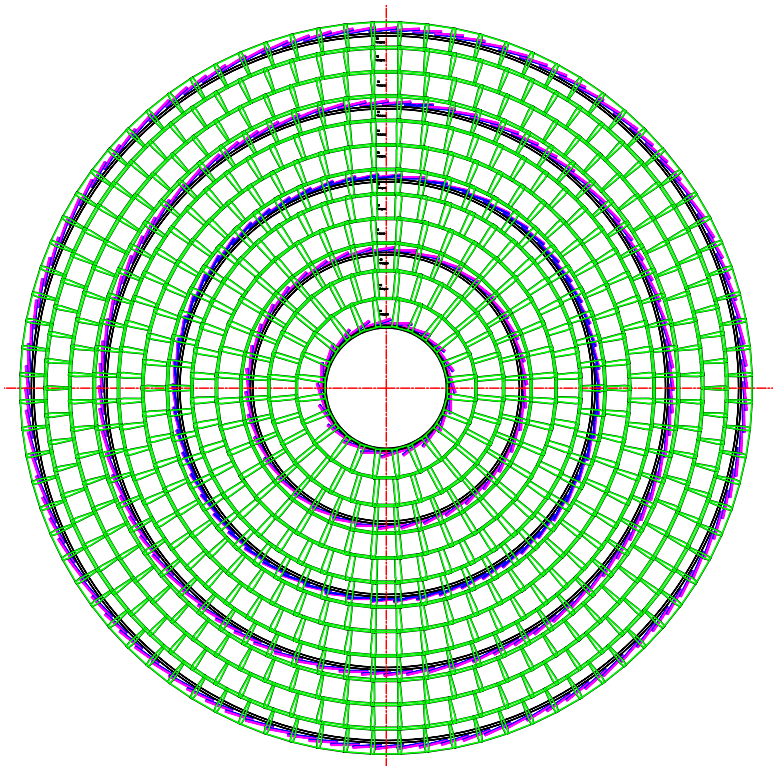

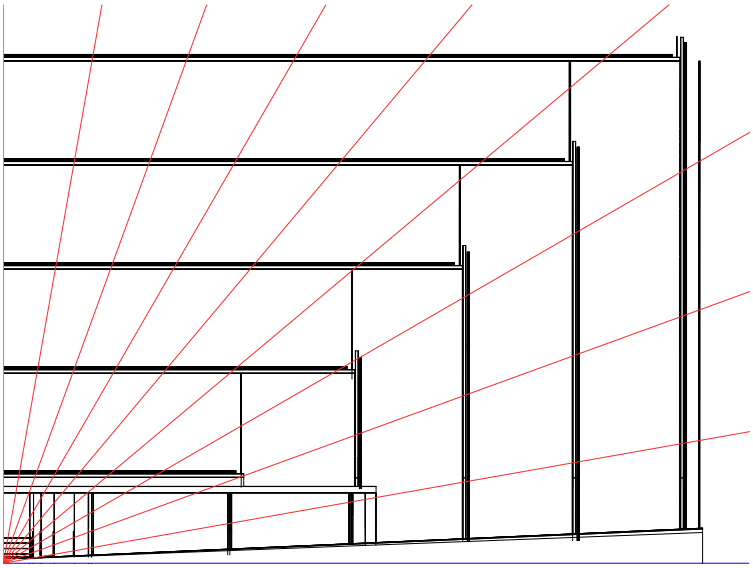

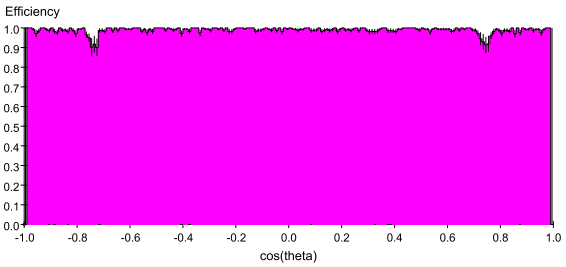
Efficiency
1.0
0.9
0.8
0.7
0.6
0.5
0.4
0.3
0.2
0.1
0.0
-1.0
-0.8
-0.6
-0.4
-0.2
0.0
0.2
0.4
0.6
0.8
1.0
cos(theta)

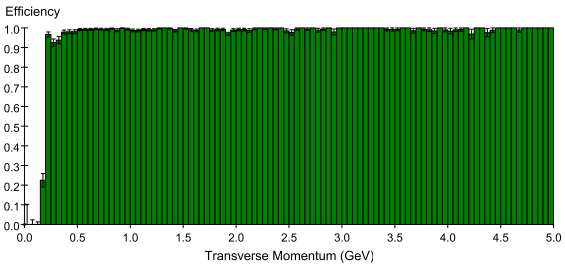
Efficiency
1.0
0.9
0.8
0.7
0.6
0.5
0.4
0.3
0.2
0.1
0.0
0.0
0.5
1.0
1.5
2.0
2.5
3.0
3.5
4.0
4.5
5.0
Transverse Momentum (GeV)

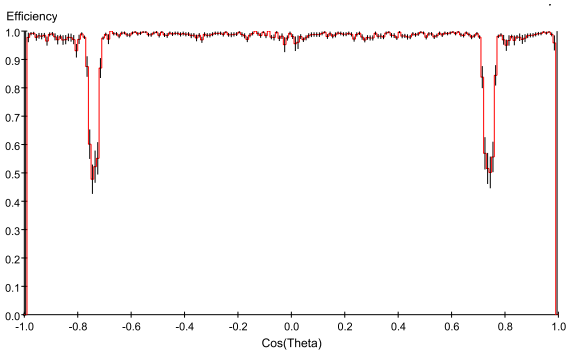
Efficiency
1.0
0.9
0.8
0.7
0.6
0.5
0.4
0.3
0.2
0.1
0.0
-1.0
-0.8
-0.6
-0.4
-0.2
0.0
0.2
0.4
0.6
0.8
1.0
Cos(Theta)

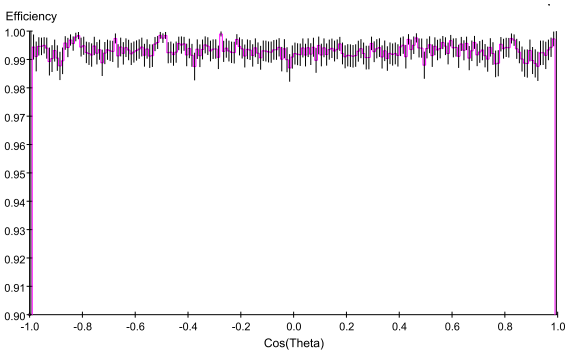
Efficiency
1.00
0.99
0.98
0.97
0.96
0.95
0.94
0.93
0.92
0.91
0.90
-1.0
-0.8
-0.6
-0.4
-0.2
0.0
0.2
0.4
0.6
0.8
1.0
Cos(Theta)

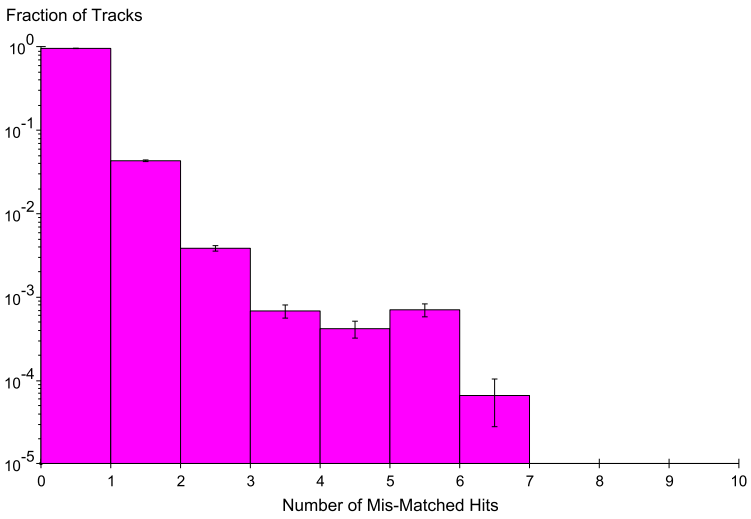
Fraction of Tracks
10^{0}
10^{-1}
10^{-2}
10^{-3}
10^{-4}
10^{-5}
0
1
2
3
4
5
6
7
8
9
10
Number of Mis-Matched Hits

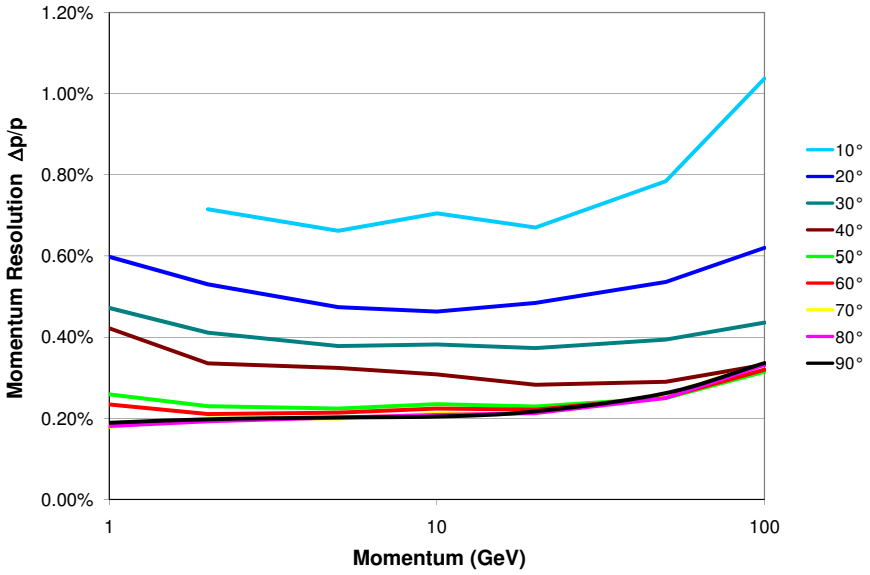
1.20%
1.00%
0.80%
0.60%
0.40%
0.20%
0.00%
Momentum Resolution Δp/p
1
10
100
Momentum (GeV)
10°
20°
30°
40°
50°
60°
70°
80°
90°

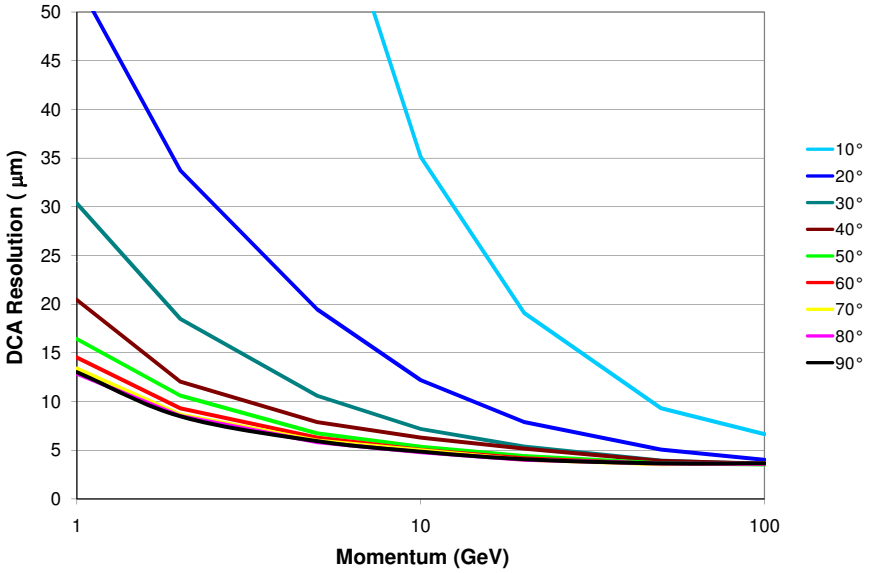
50
45
40
35
30
25
20
15
10
5
0
DCA Resolution (μm)
1
10
100
Momentum (GeV)
10°
20°
30°
40°
50°
60°
70°
80°
90°

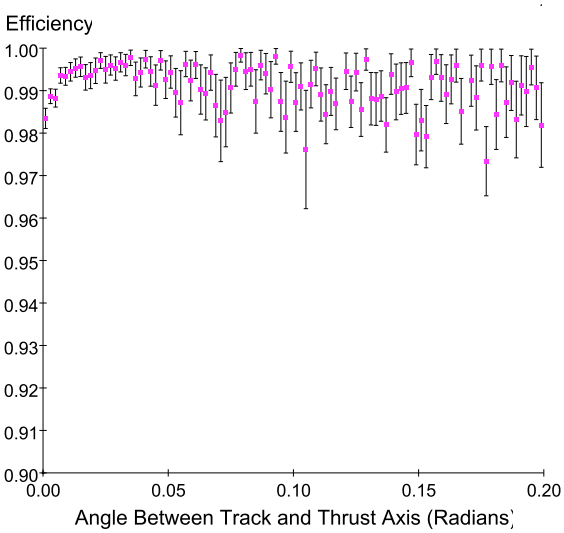
Efficiency
1.00
0.99
0.98
0.97
0.96
0.95
0.94
0.93
0.92
0.91
0.90
0.00
0.05
0.10
0.15
0.20
Angle Between Track and Thrust Axis (Radians)

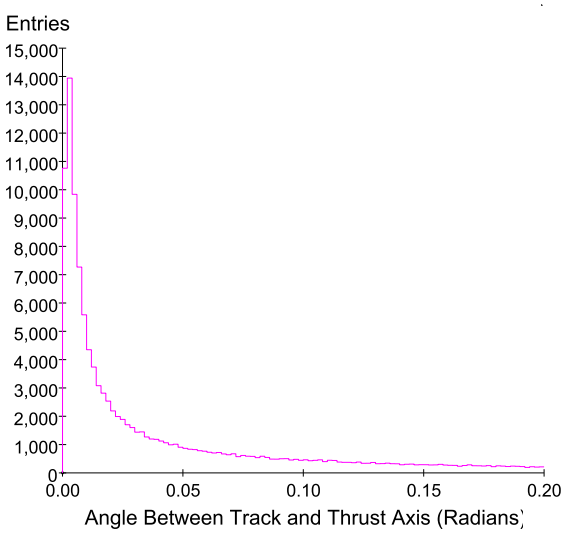
Entries
15,000
14,000
13,000
12,000
11,000
10,000
9,000
8,000
7,000
6,000
5,000
4,000
3,000
2,000
1,000
0
0.00
0.05
0.10
0.15
0.20
Angle Between Track and Thrust Axis (Radians)

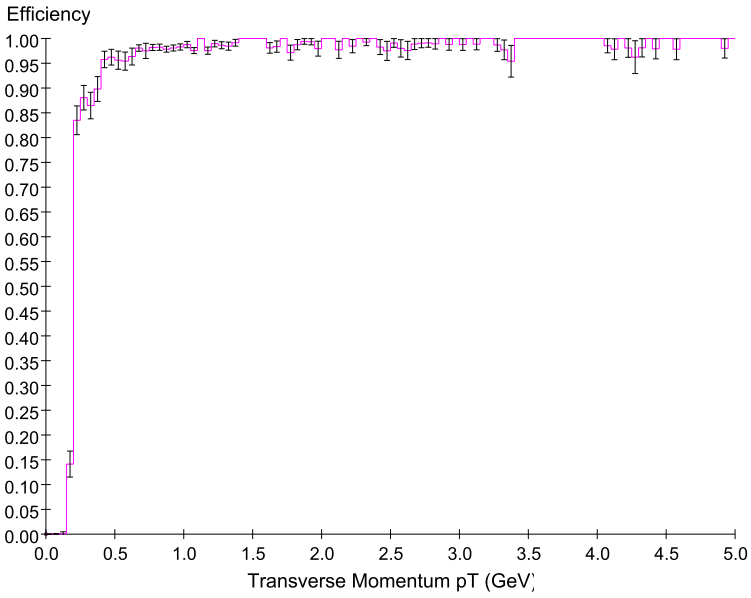
Efficiency
1.00
0.95
0.90
0.85
0.80
0.75
0.70
0.65
0.60
0.55
0.50
0.45
0.40
0.35
0.30
0.25
0.20
0.15
0.10
0.05
0.00
0.0
0.5
1.0
1.5
2.0
2.5
3.0
3.5
4.0
4.5
5.0
Transverse Momentum pT (GeV)

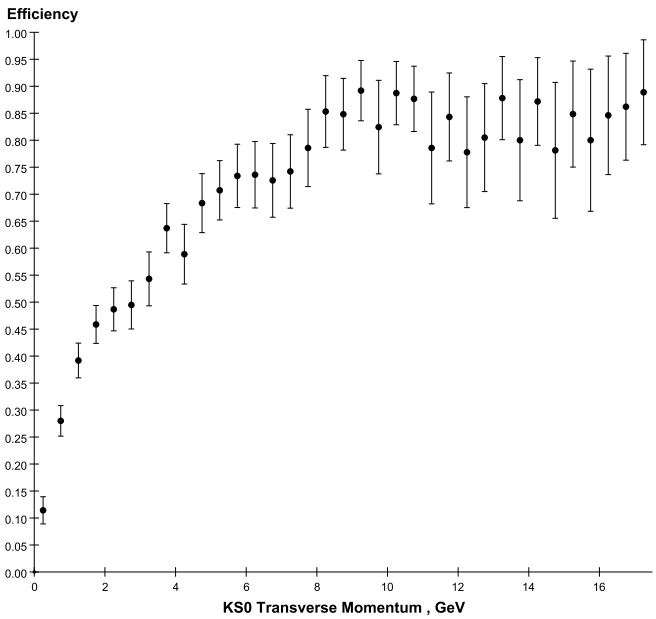
Efficiency
1.00
0.95
0.90
0.85
0.80
0.75
0.70
0.65
0.60
0.55
0.50
0.45
0.40
0.35
0.30
0.25
0.20
0.15
0.10
0.05
0.00
0
2
4
6
8
10
12
14
16
KS0 Transverse Momentum , GeV

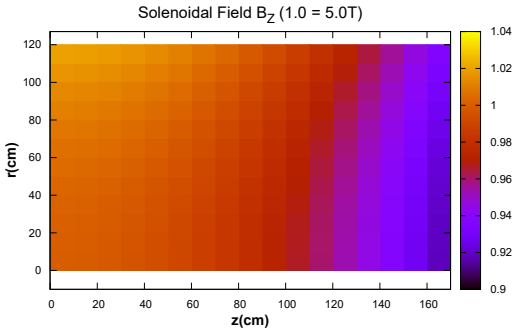
Solenoidal Field B_Z (1.0 = 5.0T)
r(cm)
z(cm)
0
20
40
60
80
100
120
140
160
0.9
0.92
0.94
0.96
0.98
1
1.02
1.04

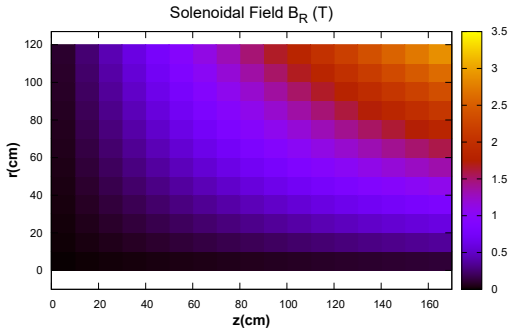
Solenoidal Field B_R (T)
r(cm)
z(cm)
0
20
40
60
80
100
120
140
160
0
0.5
1
1.5
2
2.5
3
3.5

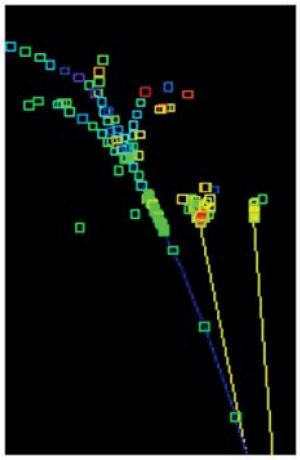

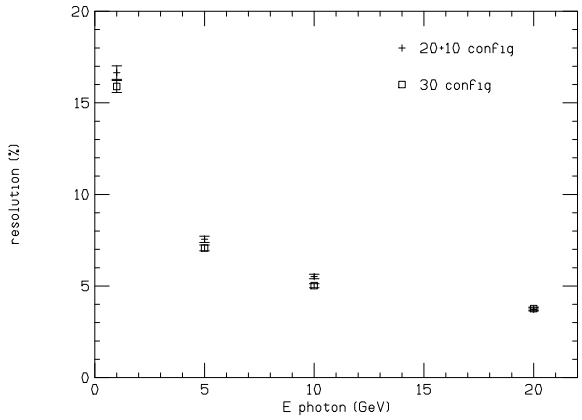
20
15
10
5
0
0
5
10
15
20
resolution (%)
E photon (GeV)
20*10 config
30 config

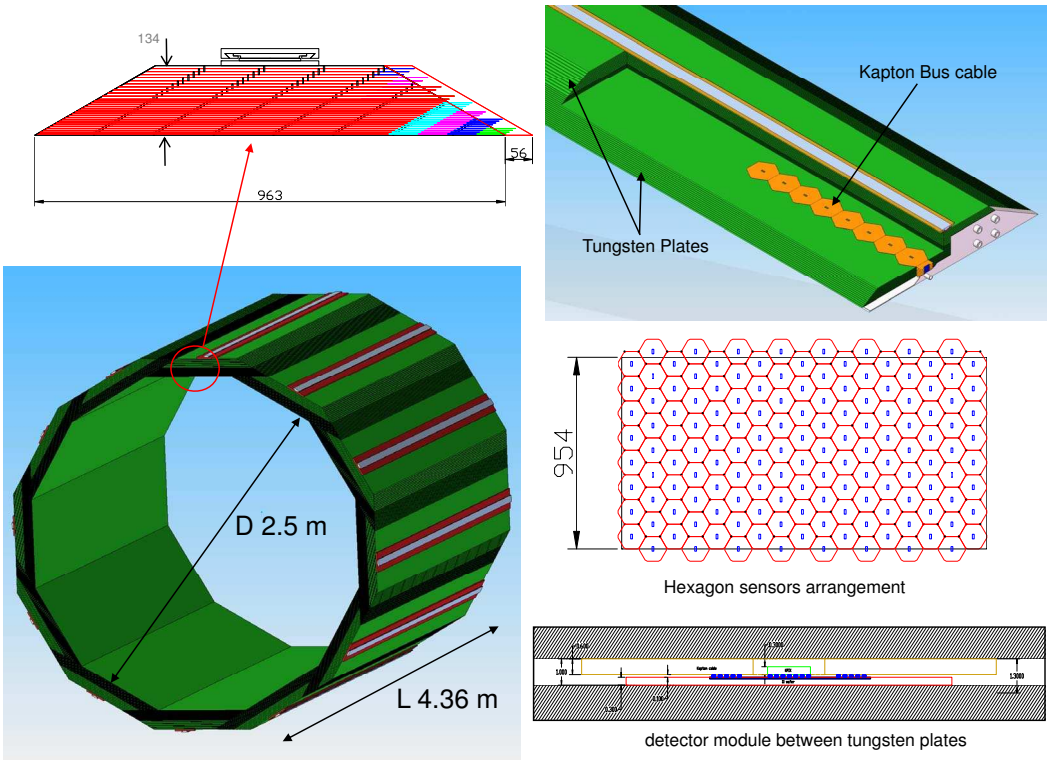

Hexagon sensors arrangement

detector module between tungsten plates

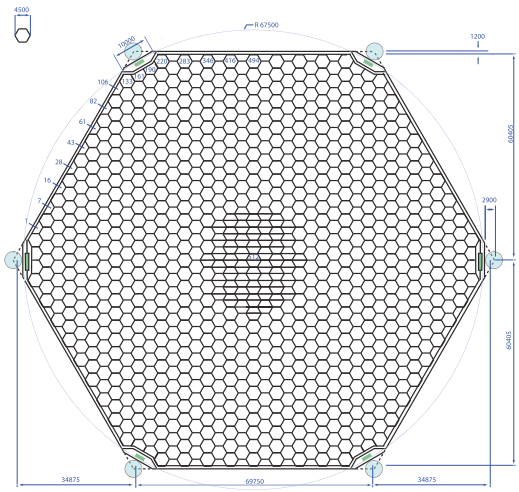
4500
R 67500
10900
1200
106
82
61
43
28
14
7
2900
60950
60405
34875
69750
34875

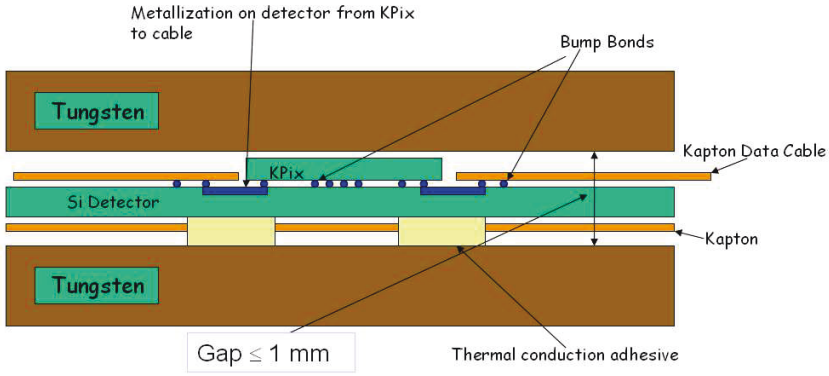

Figure 2.19: View into a readout gap in the vicinity of the KPiX readout chip. Representative bump bond connections are indicated by the small blue circles. Traces (dark blue lines) connect the KPiX serial readout stream, control signals, and power to the polyimide.

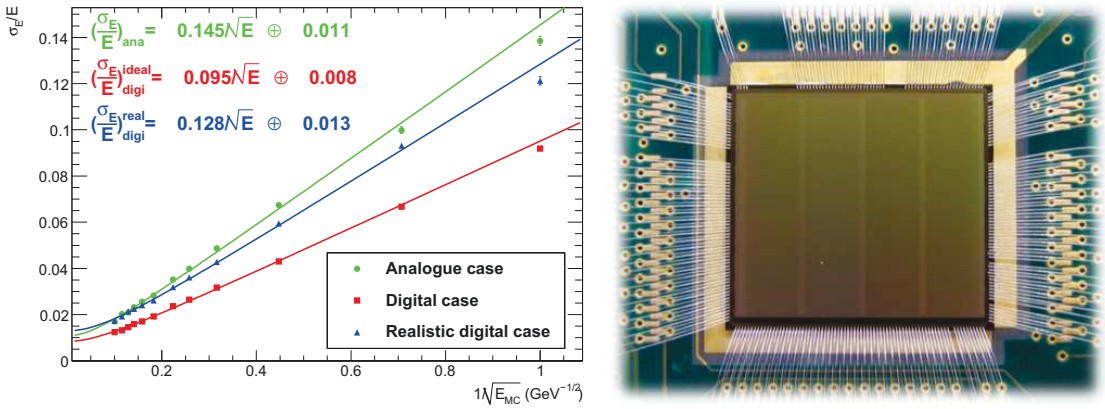

Figure 2.20: Left: The energy resolution as a function of the incident energy for single electrons for both analog and digital readout using a GEANT4 simulation. The realistic digital cases includes effects of saturation and charge sharing, leading to a degradation of 35% [9]. Right: a picture of a bonded TPAC sensor.

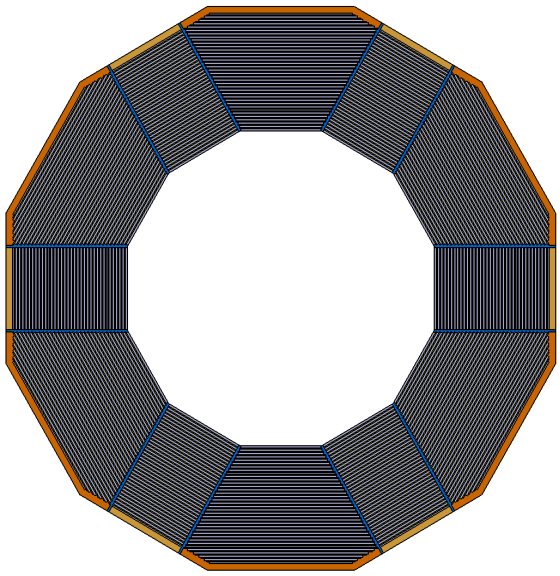

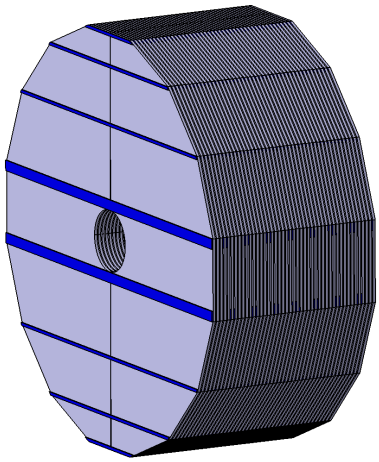

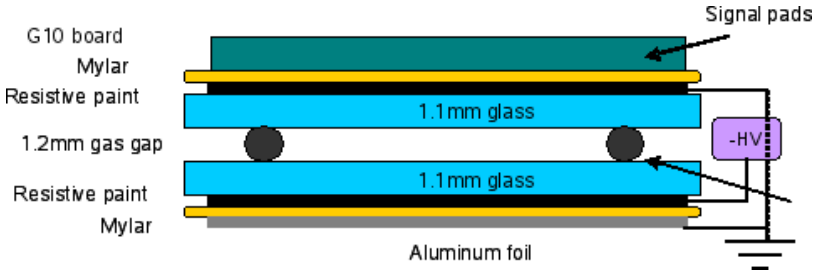
Signal pads
G10 board
Mylar
Resistive paint
1.1mm glass
1.2mm gas gap
-HV
1.1mm glass
Resistive paint
Mylar
Aluminum foil

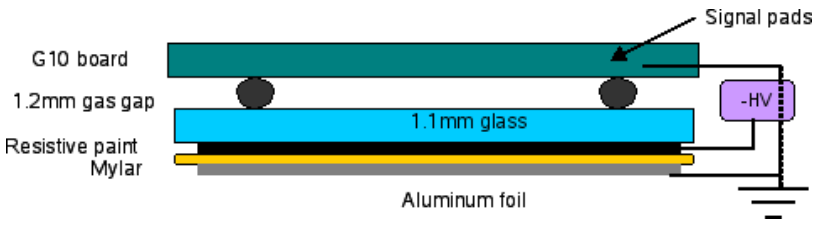
Signal pads
G10 board
1.2mm gas gap
-HV
1.1mm glass
Resistive paint
Mylar
Aluminum foil

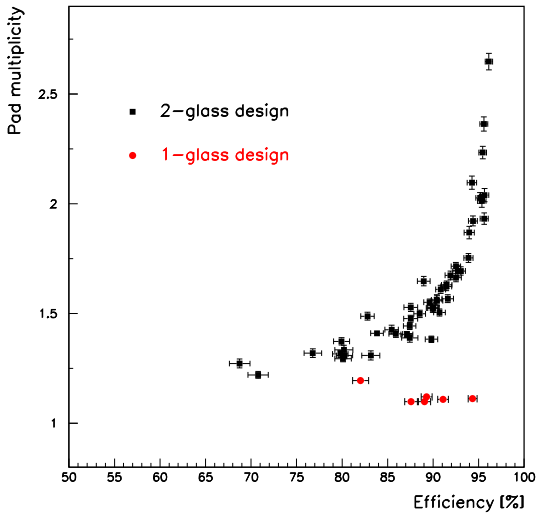
Pad multiplicity
2.5
2
1.5
1
2−glass design
1−glass design
50
55
60
65
70
75
80
85
90
95
100
Efficiency [%]

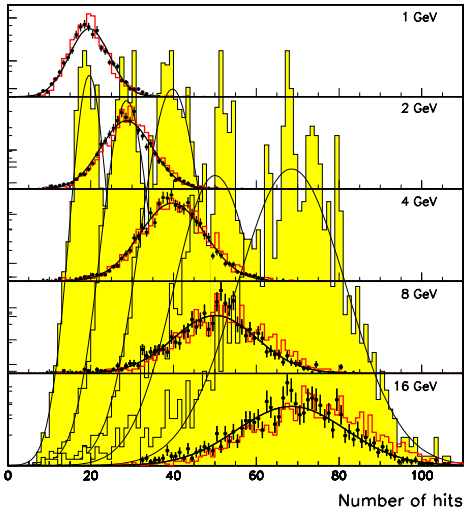
1 GeV
2 GeV
4 GeV
8 GeV
16 GeV
0
20
40
60
80
100
Number of hits

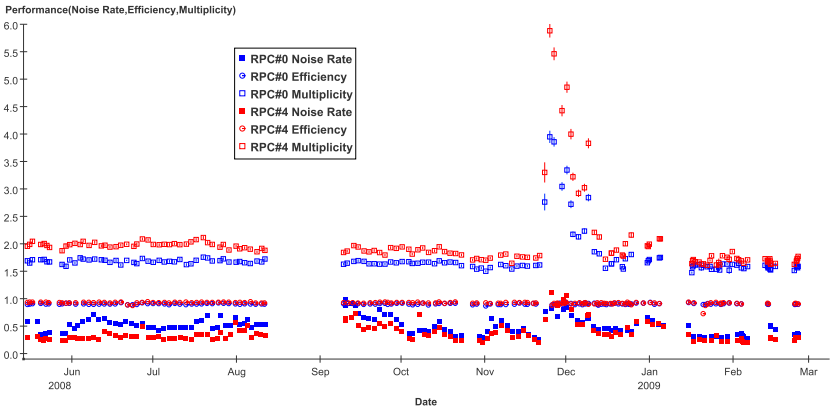
Performance(Noise Rate,Efficiency,Multiplicity)
RPC#0 Noise Rate
RPC#0 Efficiency
RPC#0 Multiplicity
RPC#4 Noise Rate
RPC#4 Efficiency
RPC#4 Multiplicity
6.0
5.5
5.0
4.5
4.0
3.5
3.0
2.5
2.0
1.5
1.0
0.5
0.0
Jun
2008
Jul
Aug
Sep
Oct
Nov
Dec
Jan
2009
Feb
Mar
Date

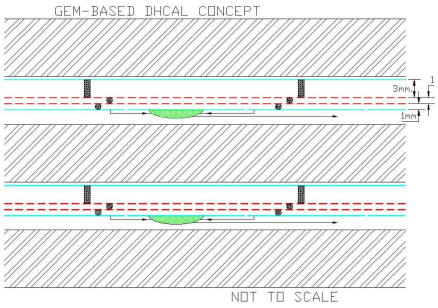
GEM-BASED DHCAL CONCEPT
3mm
1
1mm
NOT TO SCALE

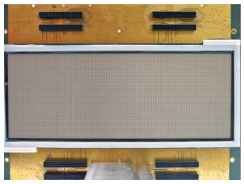

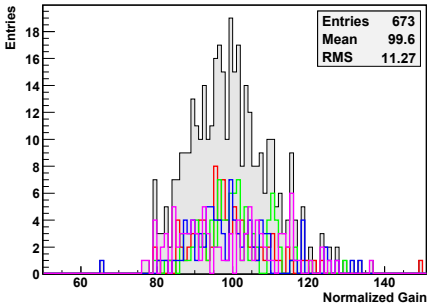
Entries
Entries 673
Mean 99.6
RMS 11.27
0
2
4
6
8
10
12
14
16
18
60
80
100
120
140
Normalized Gain

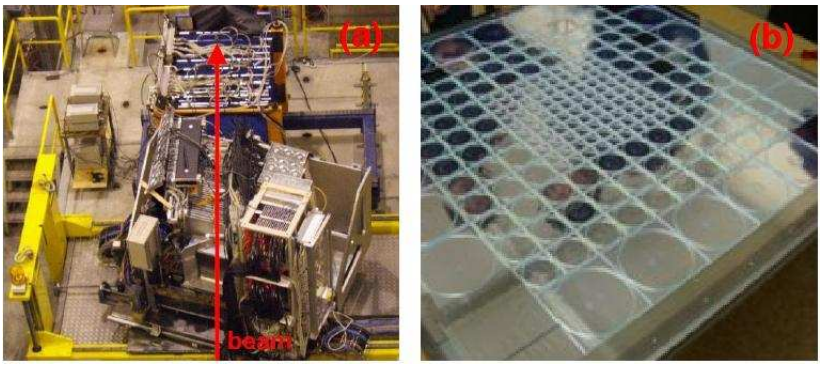
(a)
beam
(b)

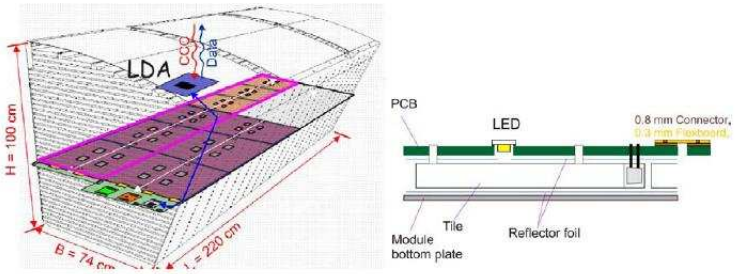
LDA
CCC
Data
H = 100 cm
L = 220 cm
PCB
LED
0.8 mm Connector,
0.3 mm Flexboard
Tile
Module
bottom plate
Reflector foil

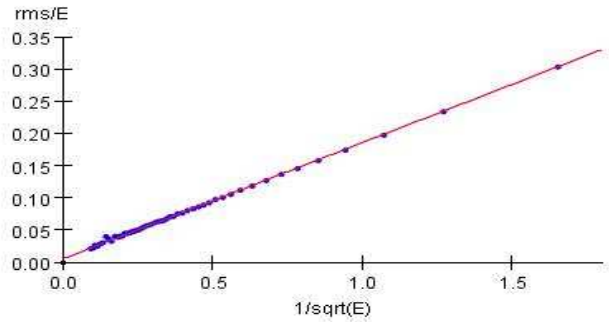
rms/E
0.35
0.30
0.25
0.20
0.15
0.10
0.05
0.00
0.0
0.5
1.0
1.5
1/sqrt(E)

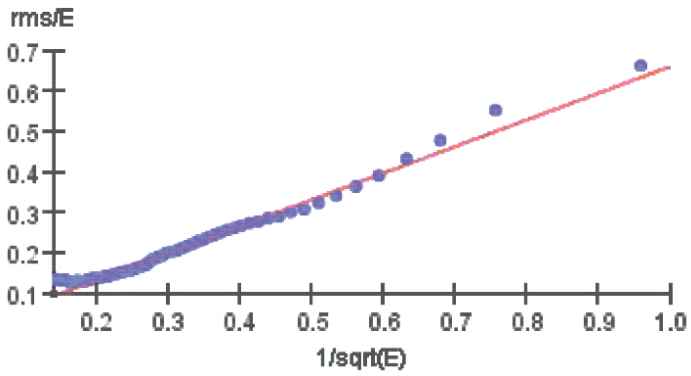
rms/E
0.7
0.6
0.5
0.4
0.3
0.2
0.1
0.2
0.3
0.4
0.5
0.6
0.7
0.8
0.9
1.0
1/sqrt(E)

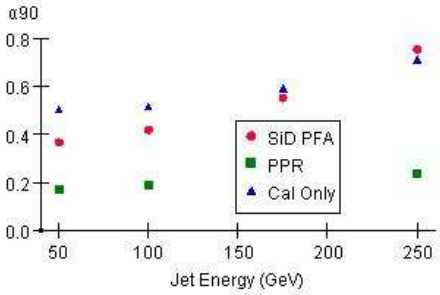
α90
0.8
0.6
0.4
0.2
0.0
50
100
150
200
250
Jet Energy (GeV)
SiD PFA
PPR
Cal Only

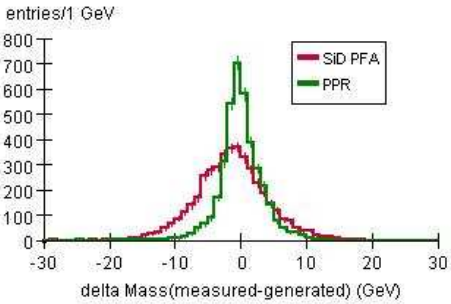
entries/1 GeV
800
700
600
500
400
300
200
100
0
-30
-20
-10
0
10
20
30
delta Mass(measured-generated) (GeV)
SiD PFA
PPR

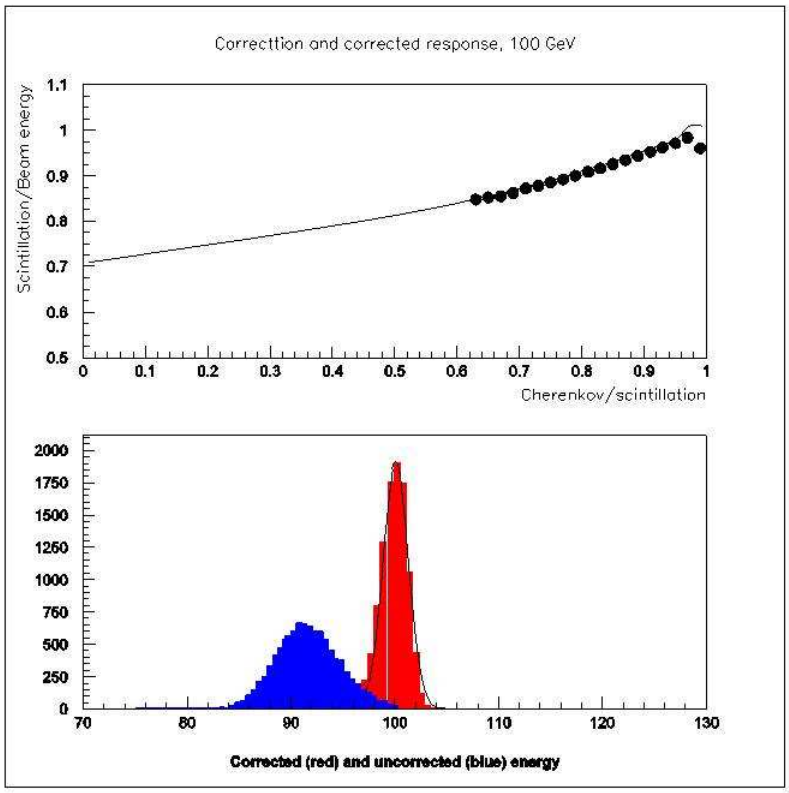
Correcttion and corrected response, 100 GeV
Scintillation/Beam energy
1.1
1
0.9
0.8
0.7
0.6
0.5
0
0.1
0.2
0.3
0.4
0.5
0.6
0.7
0.8
0.9
1
Cherenkov/scintillation
2000
1750
1500
1250
1000
750
500
250
0
70
80
90
100
110
120
130
Corrected (red) and uncorrected (blue) energy

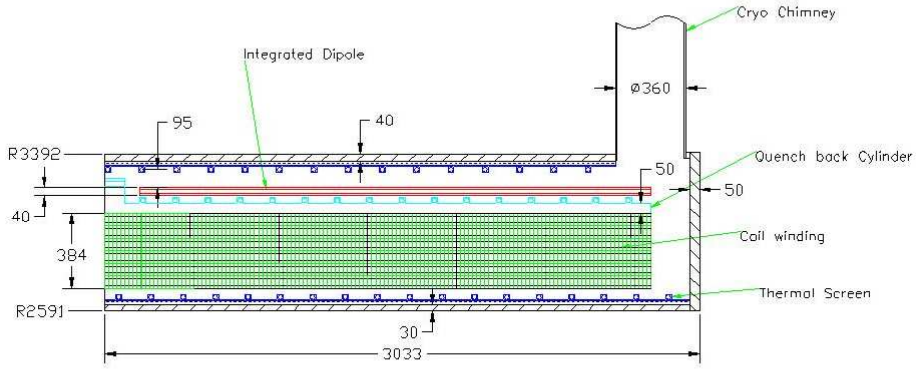
Cryo Chimney
Integrated Dipole
Ø360
95
40
R3392
50
Quench back Cylinder
50
40
Coil winding
384
Thermal Screen
R2591
30
3033

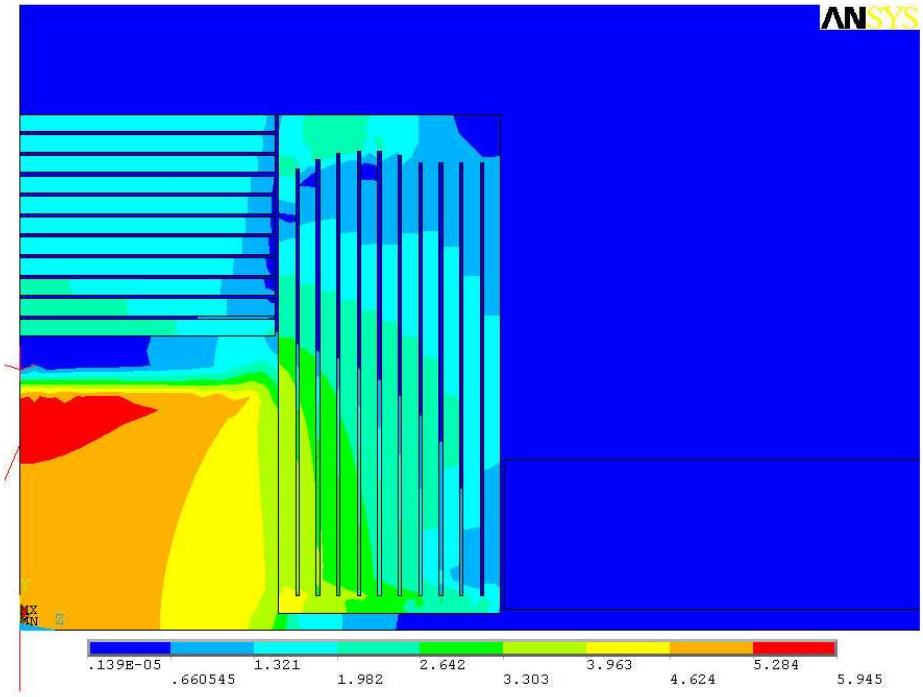
ANSYS
.139E-05
.660545
1.321
1.982
2.642
3.303
3.963
4.624
5.284
5.945

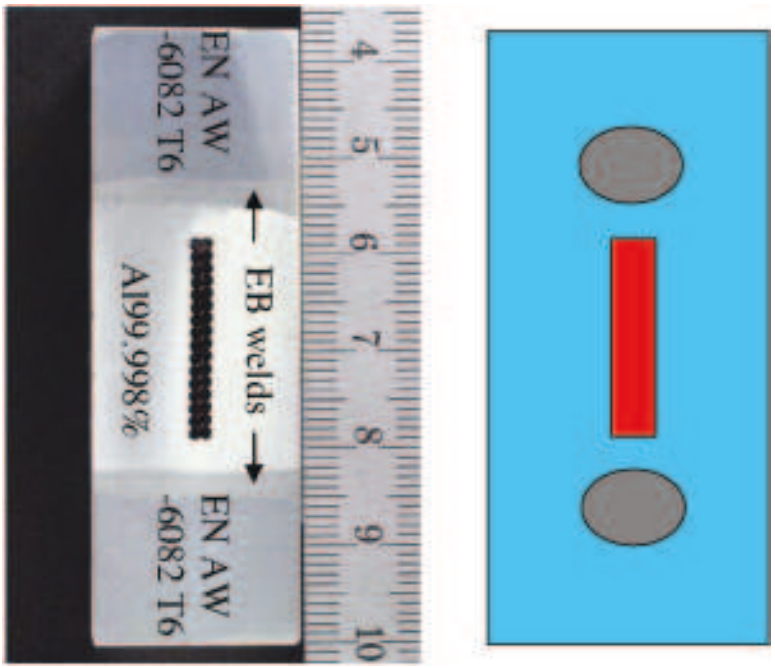
EN AW
-6082 T6
EB welds
Al99.998%
EN AW
-6082 T6
4
5
6
7
8
9
10

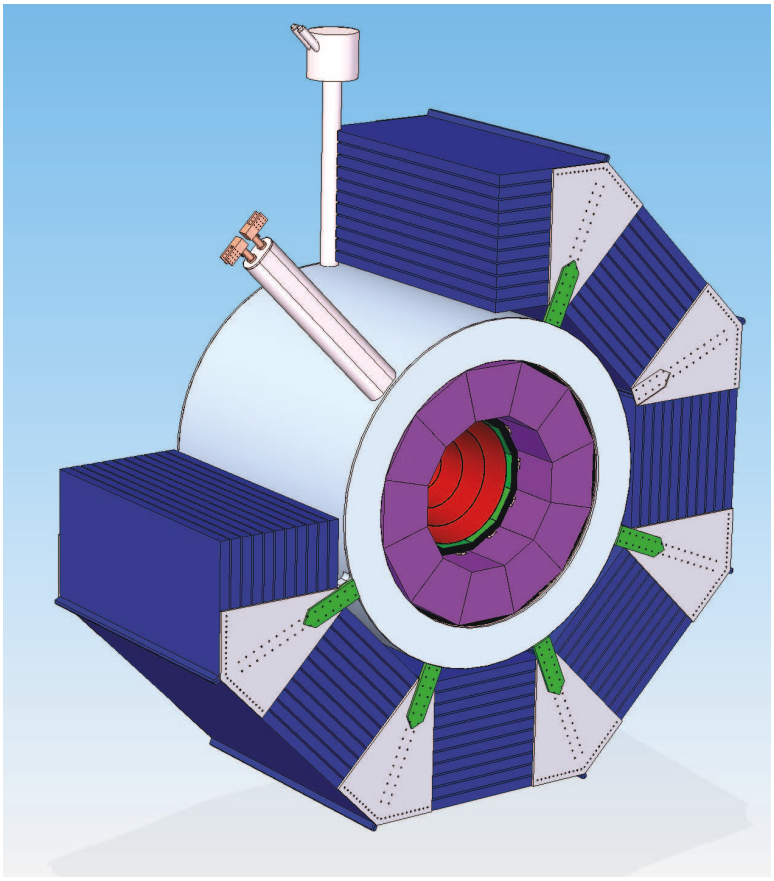

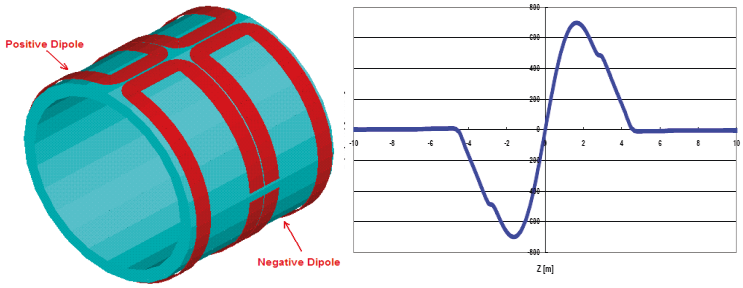
Positive Dipole
Negative Dipole
800
600
400
200
0
-200
-400
-600
-800
-10
-8
-6
-4
-2
0
2
4
6
8
10
Z [m]

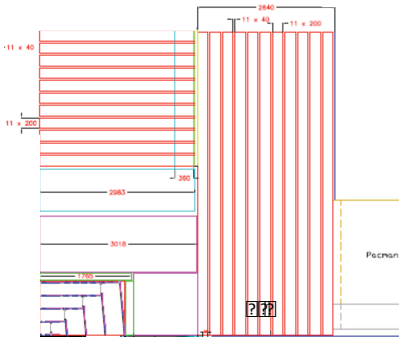
2640
11 x 40
11 x 200
11 x 40
11 x 200
360
2983
3018
1765
Pecman
??

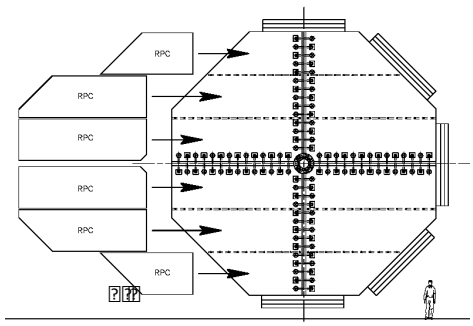
RPC
RPC
RPC
RPC
RPC
RPC
??

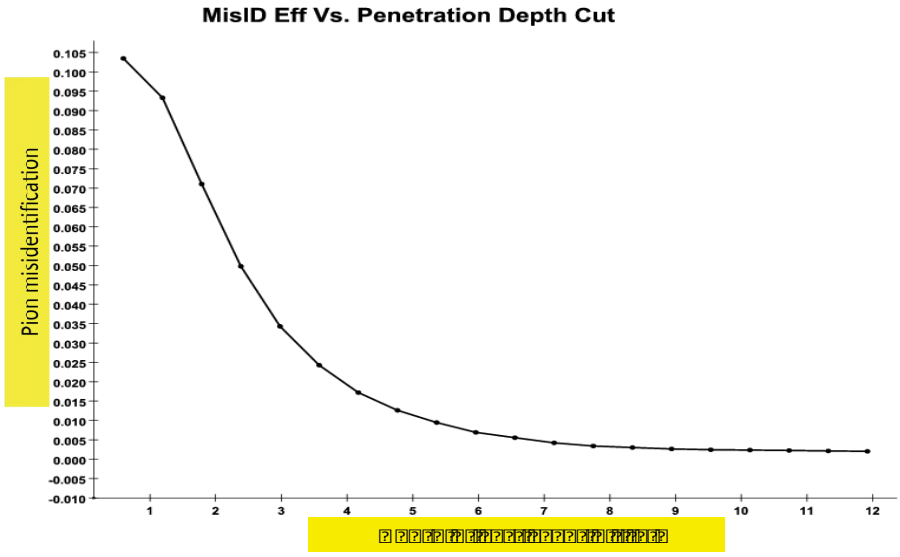
MisID Eff Vs. Penetration Depth Cut
Pion misidentification
0.105
0.100
0.095
0.090
0.085
0.080
0.075
0.070
0.065
0.060
0.055
0.050
0.045
0.040
0.035
0.030
0.025
0.020
0.015
0.010
0.005
0.000
-0.005
-0.010
1
2
3
4
5
6
7
8
9
10
11
12

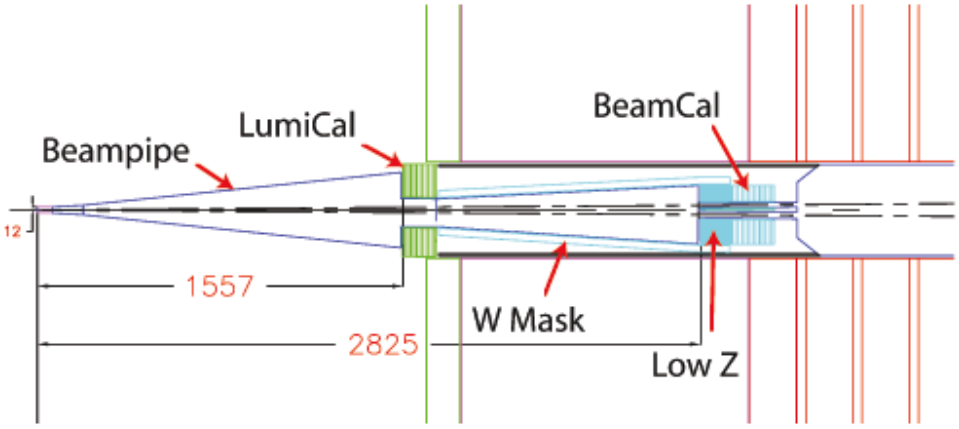
Beampipe
LumiCal
BeamCal
12
1557
2825
W Mask
Low Z

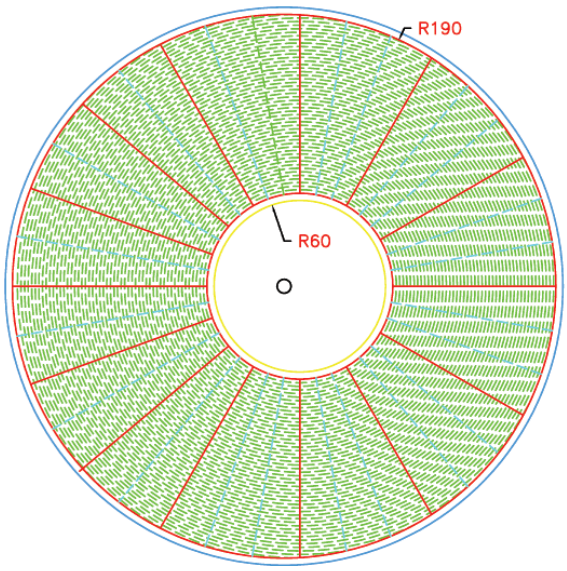
R190
R60

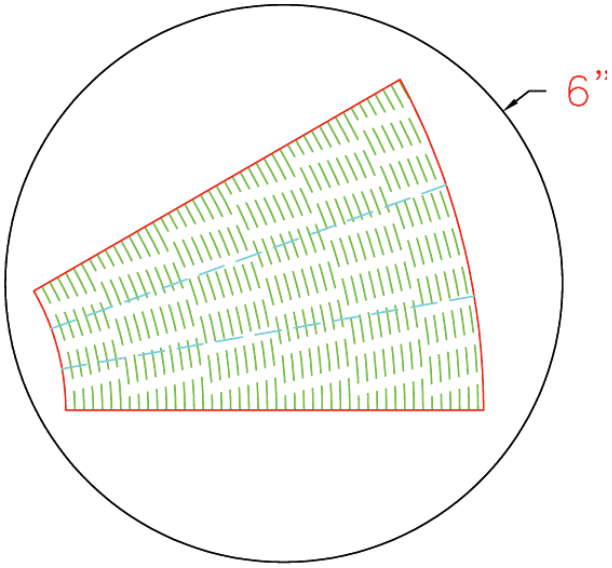
6"

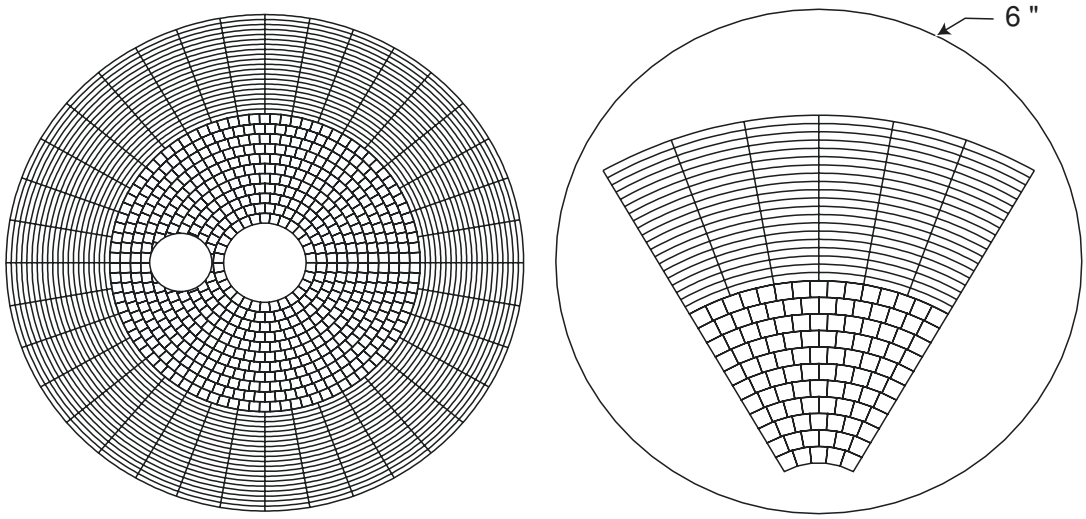
6 "

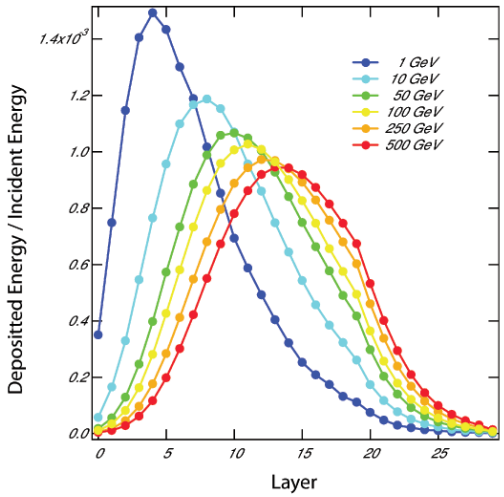
Deposited Energy / Incident Energy
1.4x10^-3
1.2
1.0
0.8
0.6
0.4
0.2
0.0
0
5
10
15
20
25
Layer
1 GeV
10 GeV
50 GeV
100 GeV
250 GeV
500 GeV

(a)

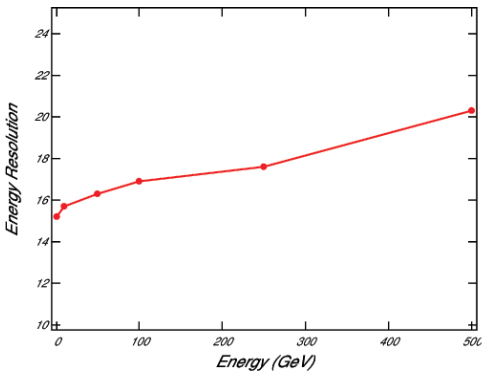
Energy Resolution
24
22
20
18
16
14
12
10
0
100
200
300
400
Energy (GeV)

(b)

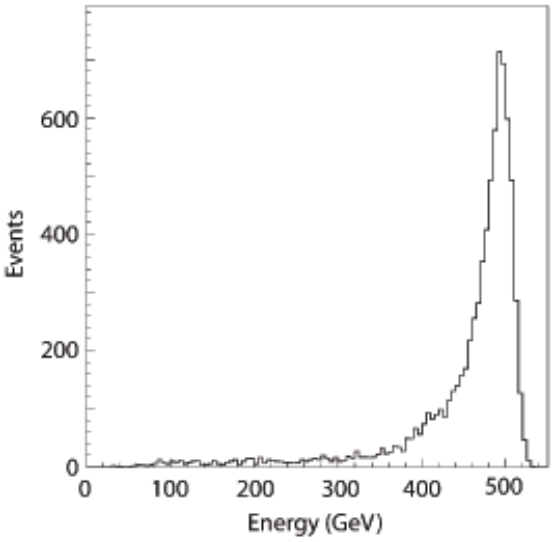
Events
600
400
200
0
0
100
200
300
400
500
Energy (GeV)

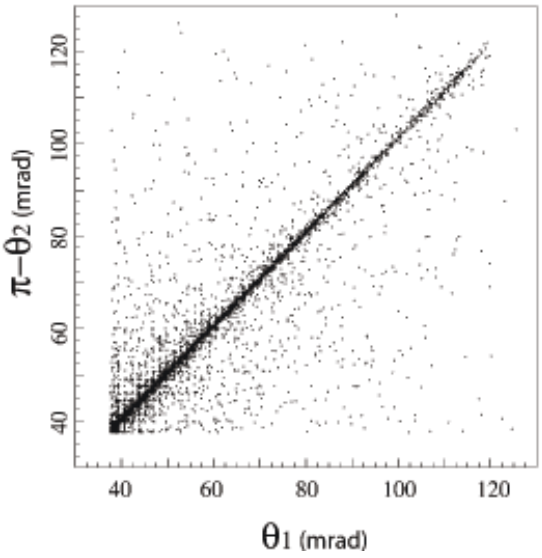
π−θ2 (mrad)
120
100
80
60
40
40
60
80
100
120
θ1 (mrad)

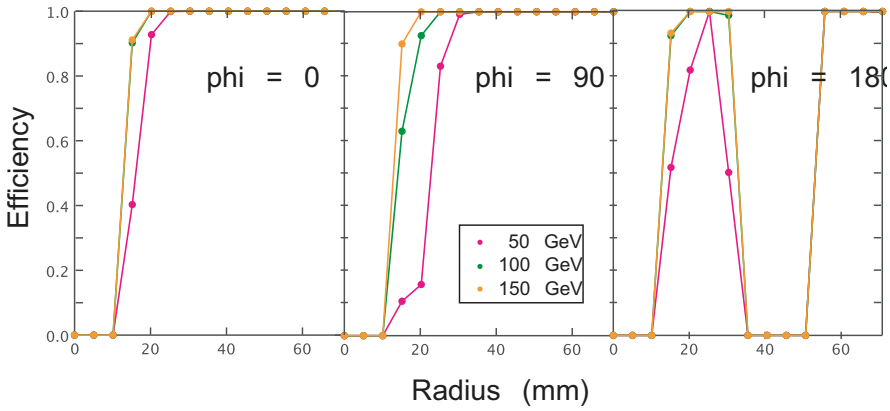
Efficiency
1.0
0.8
0.6
0.4
0.2
0.0
0
20
40
60
phi = 0
phi = 90
phi = 180
50 GeV
100 GeV
150 GeV
Radius (mm)

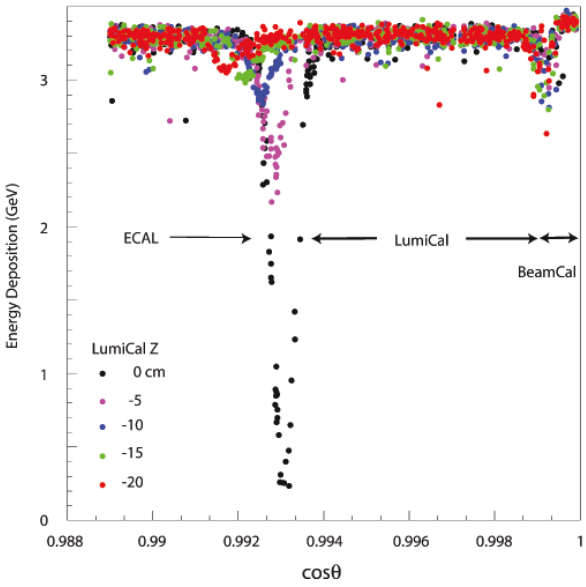
Energy Deposition (GeV)
3
2
1
0
ECAL
LumiCal
BeamCal
LumiCal Z
0 cm
-5
-10
-15
-20
0.988
0.99
0.992
0.994
0.996
0.998
1
cosθ

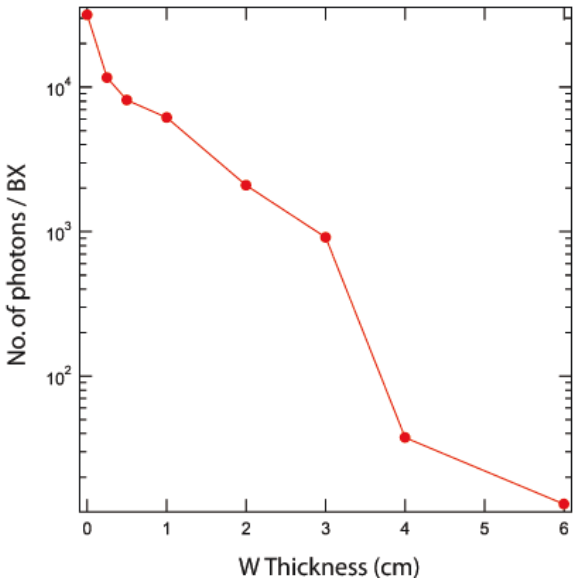
No. of photons / BX
10^4
10^3
10^2
0
1
2
3
4
5
6
W Thickness (cm)

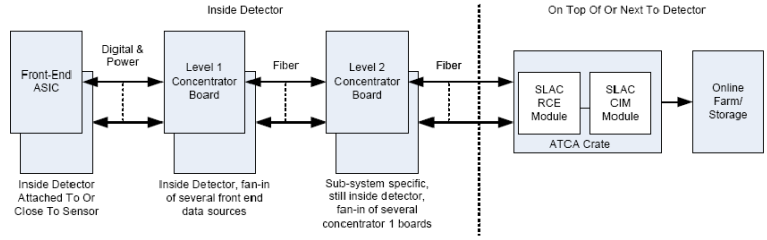
Inside Detector
On Top Of Or Next To Detector
Front-End ASIC
Digital & Power
Level 1 Concentrator Board
Fiber
Level 2 Concentrator Board
Fiber
SLAC RCE Module
SLAC CIM Module
ATCA Crate
Online Farm/ Storage
Inside Detector Attached To Or Close To Sensor
Inside Detector, fan-in of several front end data sources
Sub-system specific, still inside detector, fan-in of several concentrator 1 boards

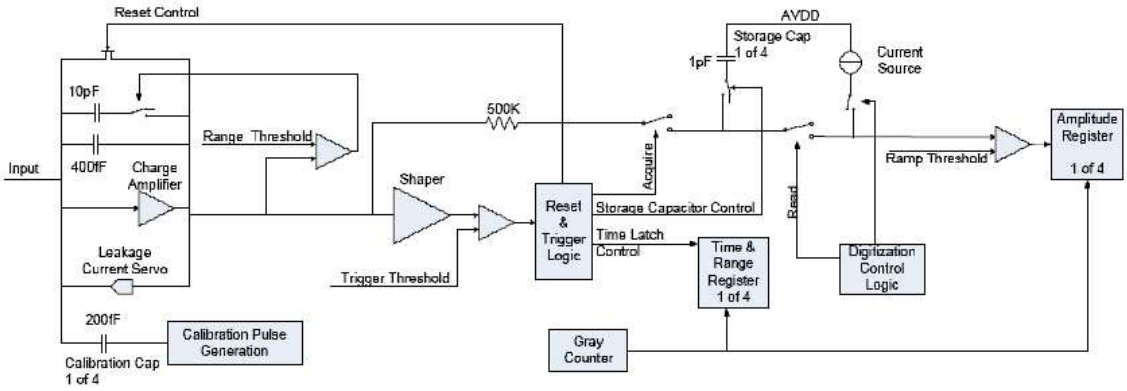
Reset Control
AVDD
Storage Cap 1 of 4
1pF
Current Source
10pF
500K
Range Threshold
Input
400fF
Charge Amplifier
Shaper
Acquire
Reset & Trigger Logic
Storage Capacitor Control
Time Latch Control
Read
Ramp Threshold
Amplitude Register 1 of 4
Leakage Current Servo
Trigger Threshold
Time & Range Register 1 of 4
Digitization Control Logic
200fF
Calibration Pulse Generation
Calibration Cap 1 of 4
Gray Counter

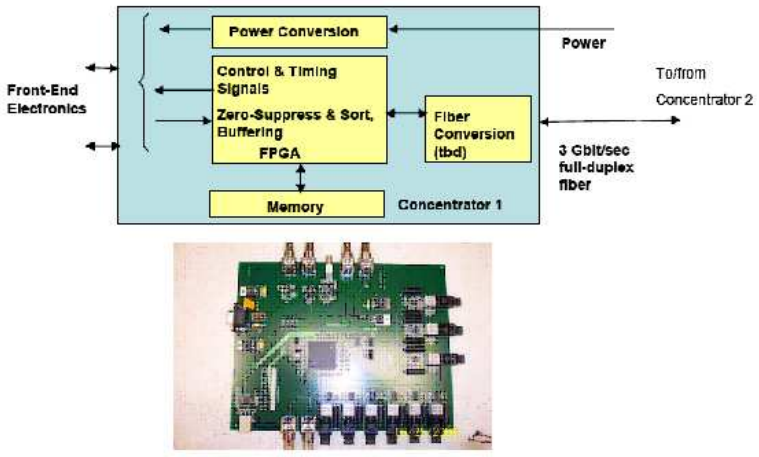
Power Conversion
Power
Control & Timing Signals
Zero-Suppress & Sort, Buffering
FPGA
Front-End Electronics
Fiber Conversion (tbd)
To/from Concentrator 2
3 Gbit/sec full-duplex fiber
Memory
Concentrator 1


Rear Transition Module
Reconfigurable Cluster Element Module

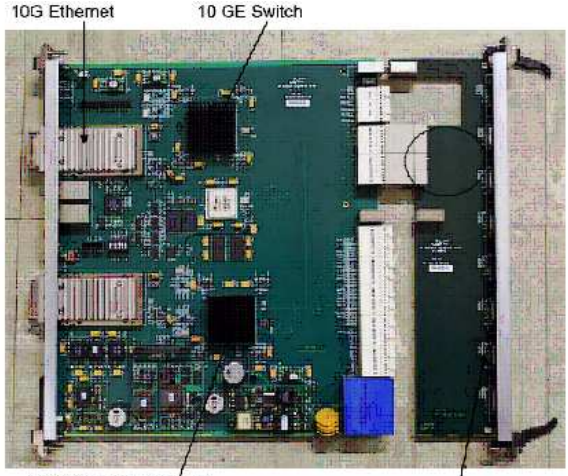
10G Ethernet
10 GE Switch
Management Processor
Ethernet on Rear-Transition Board


CIM
RCE
ATCA
Crate

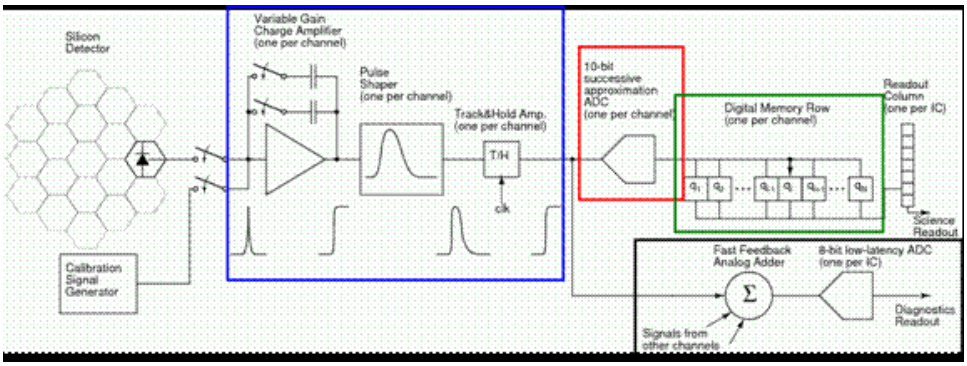
Silicon Detector
Variable Gain Charge Amplifier (one per channel)
Pulse Shaper (one per channel)
Track&Hold Amp. (one per channel)
T/H
clk
10-bit successive approximation ADC (one per channel)
Digital Memory Row (one per channel)
Readout Column (one per IC)
Science Readout
Calibration Signal Generator
Fast Feedback Analog Adder
8-bit low-latency ADC (one per IC)
Σ
Diagnostics Readout
Signals from other channels

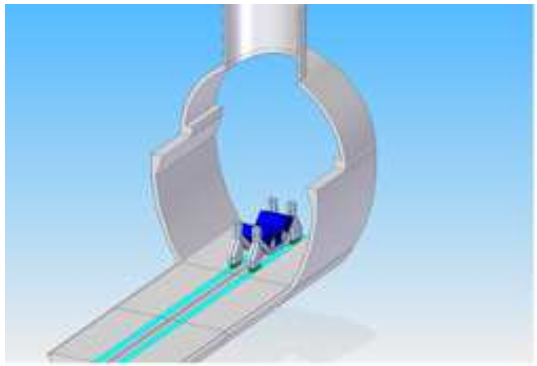

1

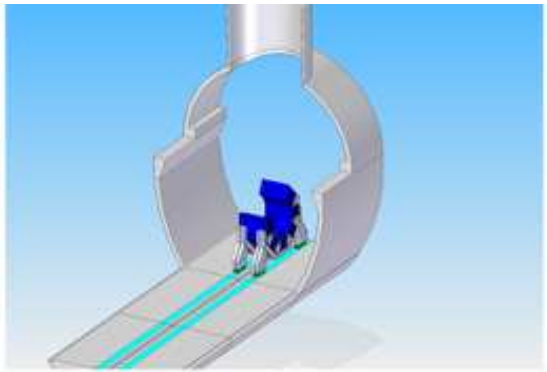

2

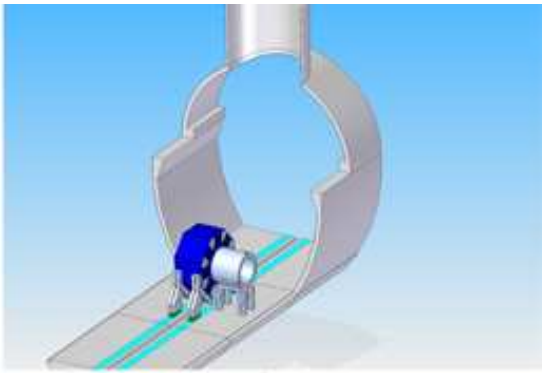

3

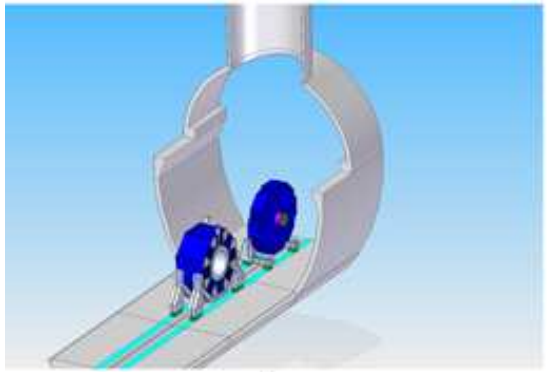

4

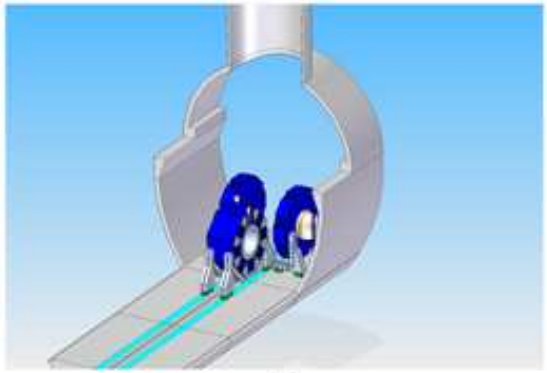

5

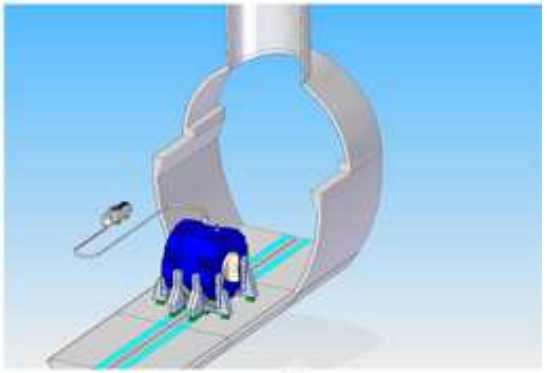

6

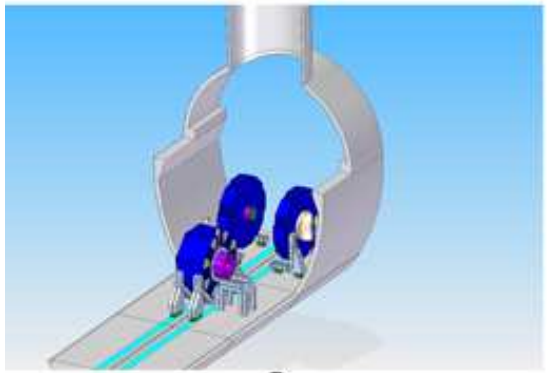

7

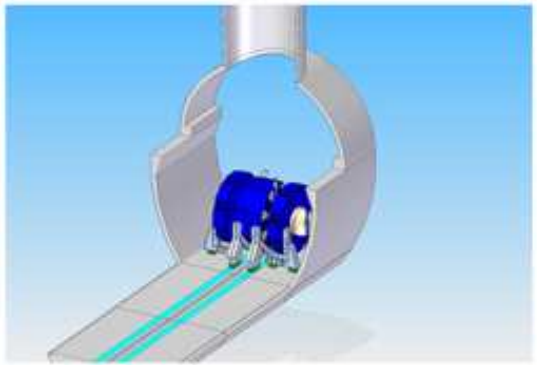

8

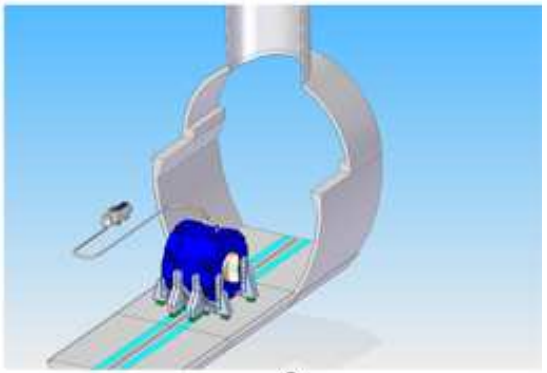

9

ID	Task Name	Duration
1	Secure ILC Beams	1 hr
2	De-energize magnets	3 hrs
3	Open Beamline Shielding	1 hr
4	Disconnect Beamlines	2 hrs
5	Checkout Detetctor Transport system	2 hrs
6	Transport Detector 20 m	2 hrs
7	Transport other detector on beamline	2 hrs
8	Connect beamline	2 hrs
9	Close Beamline shielding	1 hr
10	Check gross detector alignment & adjust if	2 hrs
11	Energize magnets	3 hrs
12	Safety Checks before beams	1 hr
13	Begin Beam Based alignment	10 hrs

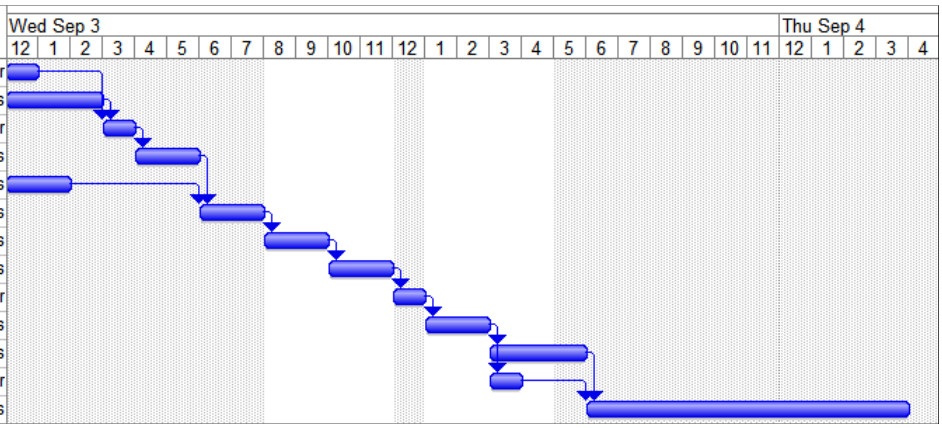

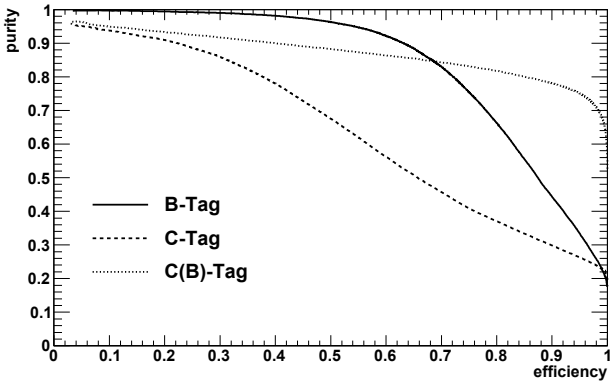
purity
efficiency
B-Tag
C-Tag
C(B)-Tag

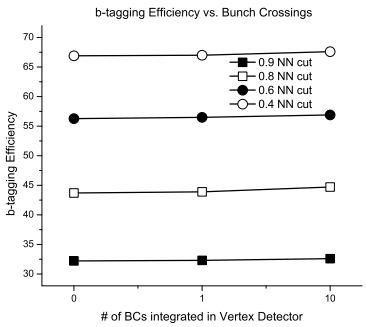
b-tagging Efficiency vs. Bunch Crossings
b-tagging Efficiency
# of BCs integrated in Vertex Detector
0.9 NN cut
0.8 NN cut
0.6 NN cut
0.4 NN cut

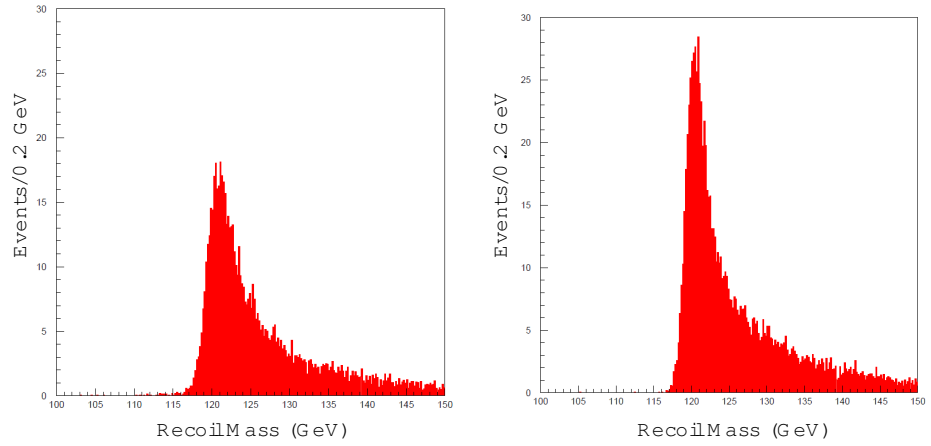
Events/0.2 GeV
RecoilMass (GeV)
Events/0.2 GeV
RecoilMass (GeV)

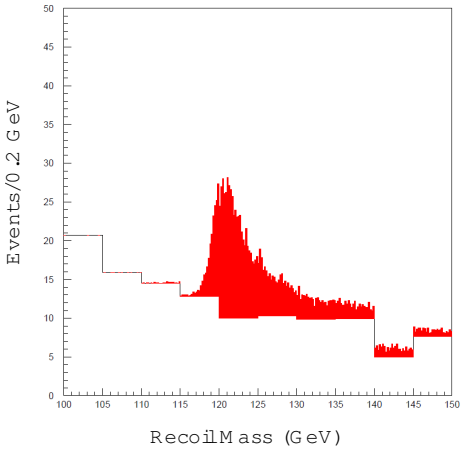
Events/0.2 GeV
RecoilMass (GeV)

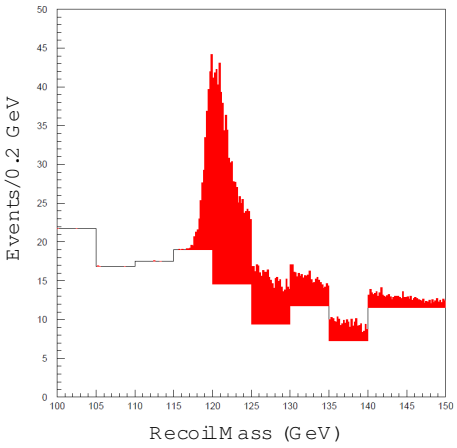
Events/0.2 GeV
RecoilMass (GeV)

Visible energy before classification

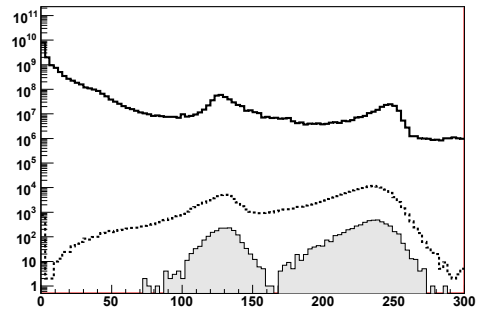

Number of Leptons before classification

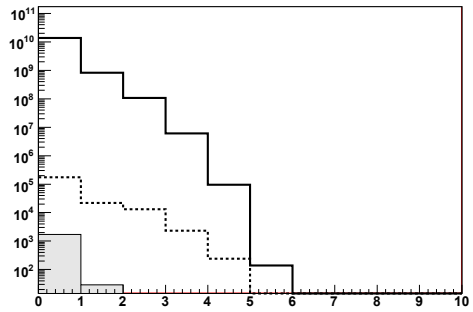

di−jet Invariant Mass after classification

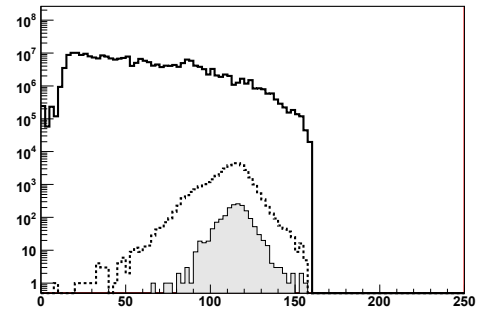

Minimum y value

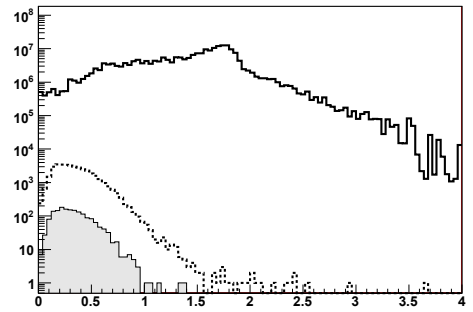

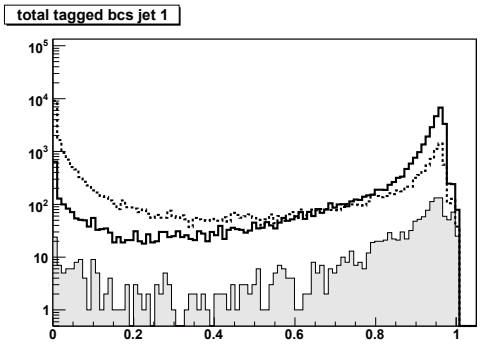
total tagged bcs jet 1
10^5
10^4
10^3
10^2
10
1
0
0.2
0.4
0.6
0.8
1

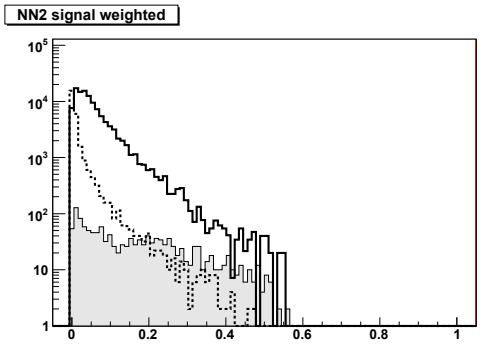
NN2 signal weighted
10^5
10^4
10^3
10^2
10
1
0
0.2
0.4
0.6
0.8
1

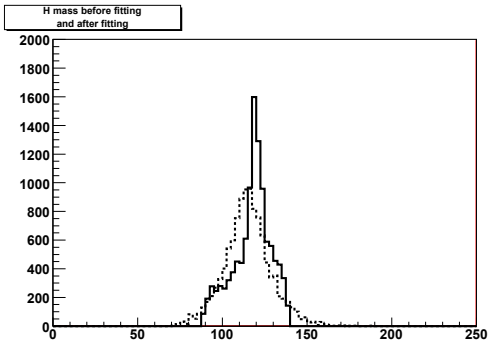
H mass before fitting
and after fitting
2000
1800
1600
1400
1200
1000
800
600
400
200
0
0
50
100
150
200
250

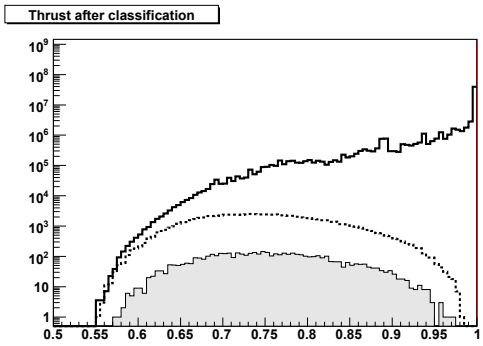
Thrust after classification
10^9
10^8
10^7
10^6
10^5
10^4
10^3
10^2
10
1
0.5
0.55
0.6
0.65
0.7
0.75
0.8
0.85
0.9
0.95
1

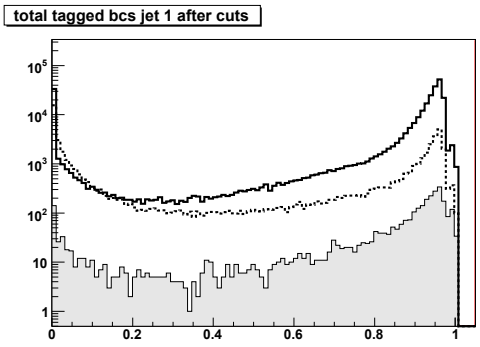
total tagged bcs jet 1 after cuts
10^5
10^4
10^3
10^2
10
1
0
0.2
0.4
0.6
0.8
1

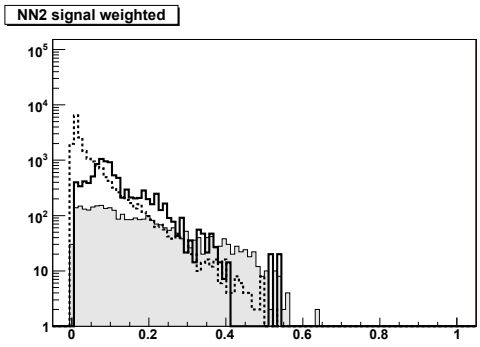
NN2 signal weighted
10^5
10^4
10^3
10^2
10
1
0
0.2
0.4
0.6
0.8
1

final states are 67.0 % for the hadronic final states and 22.9 % for the neutrino final state. Contribution due to the WW fusion process to the neutrino channel, 16.1 %, complicates this analysis as this channel does not exhibit a peak in the missing mass. The integrated luminosity of the sample is 250 fb^{-1}.

The primary aim of this analysis are the hadronic channel and the neutrino channel. For both we require in each event a presence of two muons which are identified by associating a reconstructed track to a MIP segment in the calorimeter and a stub in the muon system. For the leading muon we require its energy to be larger than 50 GeV and for the second muon we require it to be larger than 30 GeV. The number of identified muons is shown in Figure 4.9 for the signal and background samples. The energy distribution of the most energetic muon

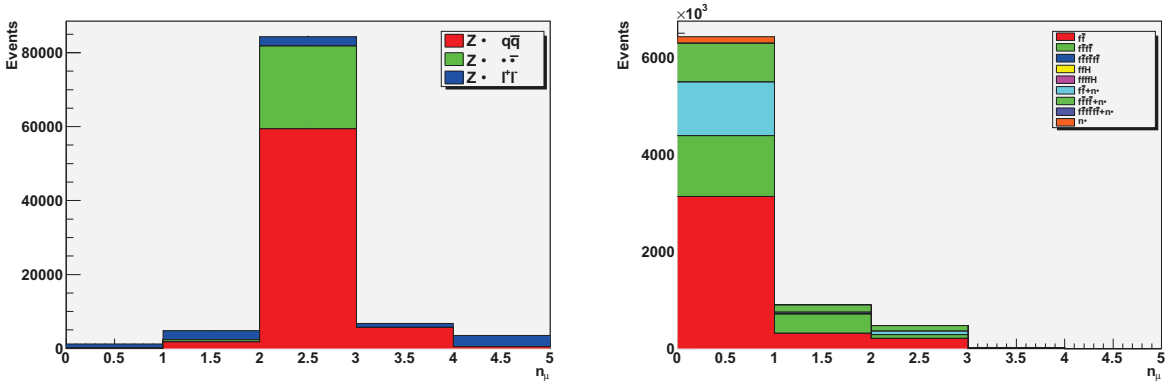

Figure 4.9: The Number of identified muons in the signal sample (left) and the background sample (right).

is shown in Figure 4.10. The signature of the hadronic channel consists of two high-energetic

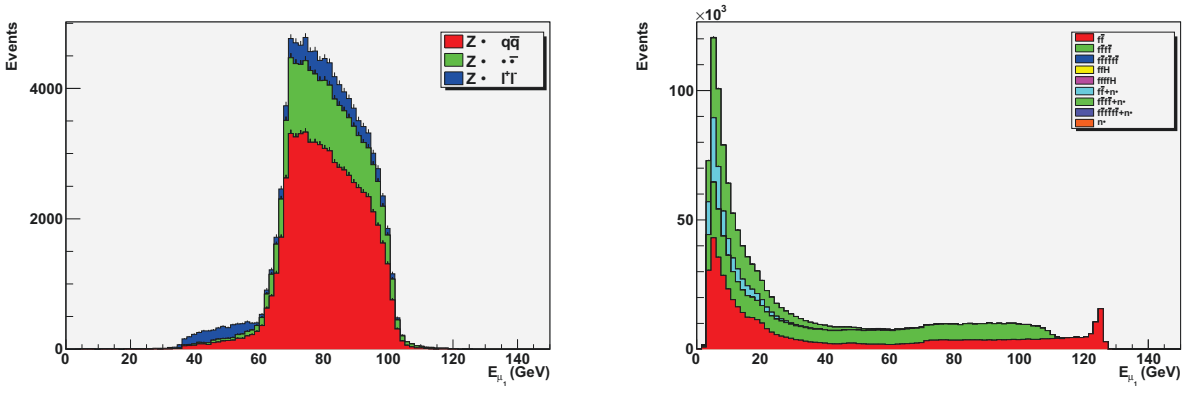

(a) (b)

Figure 4.10: The energy spectrum of the most energetic muon for the signal (a) and the SM background (b).

muons from the Higgs decay and two jets from the hadronically decaying Z boson. For this channel we force the event into two jets using the Durham algorithm, after excluding the

previously identified muons. We require the y_{min} parameter of the jet clustering to be larger than 0.05.

Preselecting hadronic events compatible with the di-jet di-muon signature we require the number of charged tracks to be greater than 5 and the visible energy to be larger than 190 GeV. We then select events where the leading jet has an energy between 30 and 105 GeV and second jet has an energy between 10 and 70 GeV. We also require the jet P_T to be smaller than 90 and 60 GeV respectively. Finally we require the mass of the di-muon system to be compatible with the m_H=120 GeV $\pm$ 0.9 GeV.

We check the mass resolution for the signal both for the di-muon and the di-jet system before any kinematic fitting and corrections for energy losses have been applied. We obtain 120.07 GeV with a width of 304 MeV for the di-muon system and 90.84 GeV with a width of 7.58 GeV for the di-jet system. The results are shown in Figure 4.11.

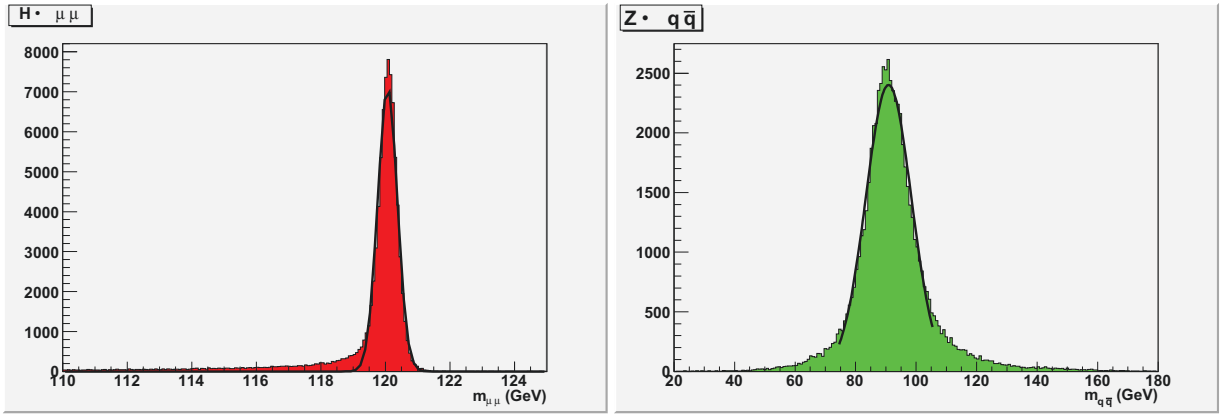

Figure 4.11: The mass resolution for the di-muon system (left) and the di-jet system(right) for the signal sample $Z \to q\bar{q}$; $H \to \mu^+\mu^-$.

After the preselection, the dominant background originates from four-fermion processes, mainly ZZ production with $e^+e^- \to ZZ \to q\bar{q}\mu^+\mu^-$. To select "good" muons, we cut on the muon opening angle, $\cos(\theta_{\mu\mu}) < -0.5$. The signal tends to be very back-to-back, and we exploit this fact by cutting on the angle between the two reconstructed bosons (from the di-jet and di-muon pairs) $\cos(\theta_{BB}) < -0.8$. Furthermore, we require the distance of any muon with respect to any jet to be at least 0.1 radians. Finally we select events with an acoplanarity in the reconstructed boson-boson system larger than 2.8 radians.

In order to test the compatibility of each event with either the HZ or ZZ hypothesis, we construct a χ^2 as follows

$$\chi^2_{ZZ} = \left(\frac{m_{JetJet} - m_Z}{\sigma_{m_{JetJet}}}\right)^2 + \left(\frac{m_{\mu\mu} - m_Z}{\sigma_{m_{\mu\mu}}}\right)^2 \tag{4.1}$$

$$\chi^2_{HZ} = \left(\frac{m_{JetJet} - m_Z}{\sigma_{m_{JetJet}}}\right)^2 + \left(\frac{m_{\mu\mu} - m_H}{\sigma_{m_{\mu\mu}}}\right)^2 \tag{4.2}$$

For the uncertainties we assume the resolutions derived above, but for the resolution the di-muon pair in the ZZ case we assume the natural width of the Z which is considerably larger

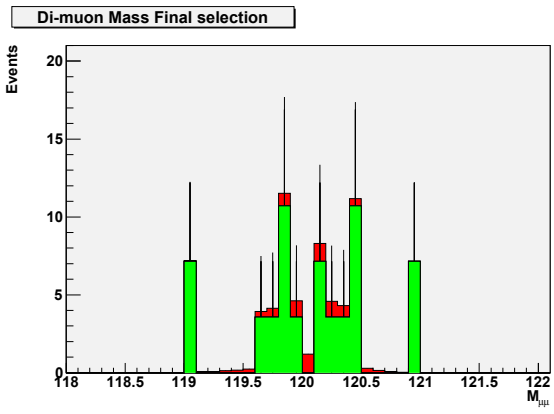
Di-muon Mass Final selection
Events
20
15
10
5
0
118
118.5
119
119.5
120
120.5
121
121.5
122
$M_{\mu\mu}$

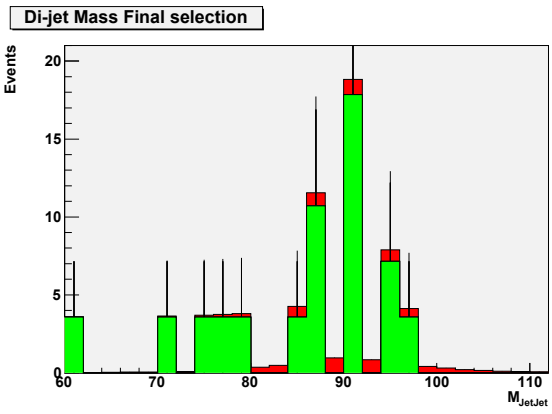
Di-jet Mass Final selection
Events
20
15
10
5
0
60
70
80
90
100
110
M_{JetJet}

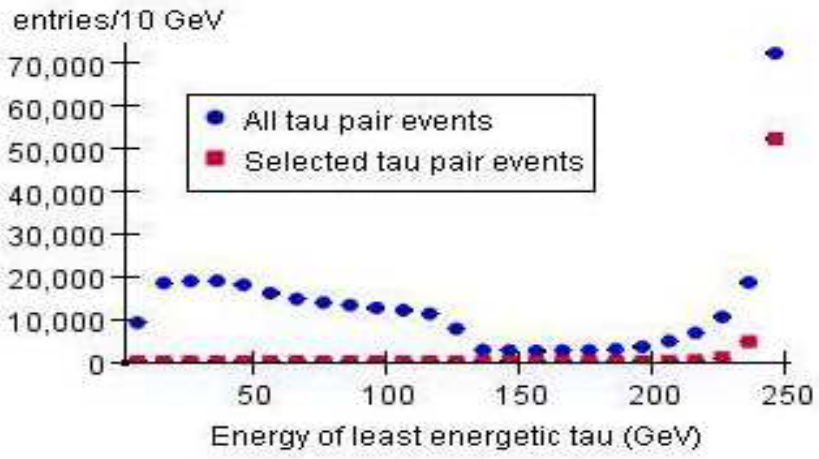
entries/10 GeV
70,000
60,000
50,000
40,000
30,000
20,000
10,000
0
All tau pair events
Selected tau pair events
50
100
150
200
250
Energy of least energetic tau (GeV)

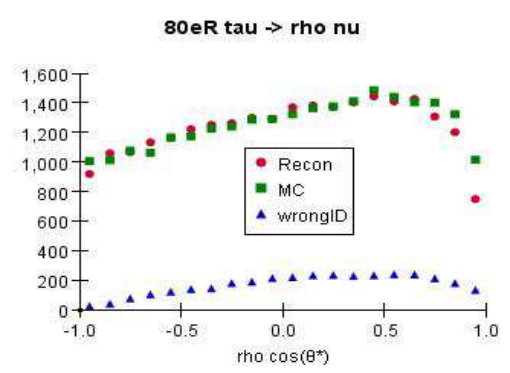
80eR tau -> rho nu
Recon
MC
wrongID
rho cos(θ*)

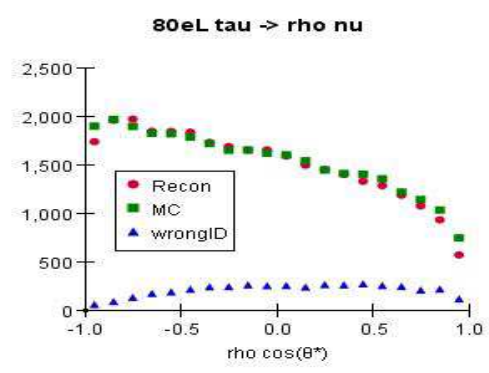
80eL tau -> rho nu
Recon
MC
wrongID
rho cos(θ*)

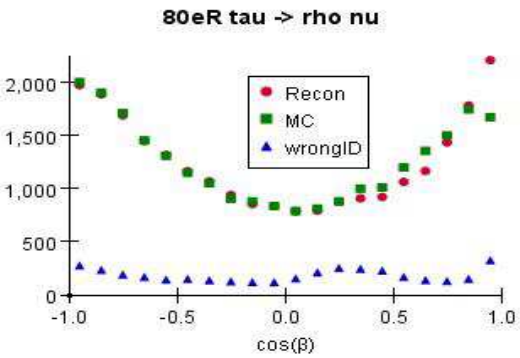
80eR tau -> rho nu
Recon
MC
wrongID
cos(β)

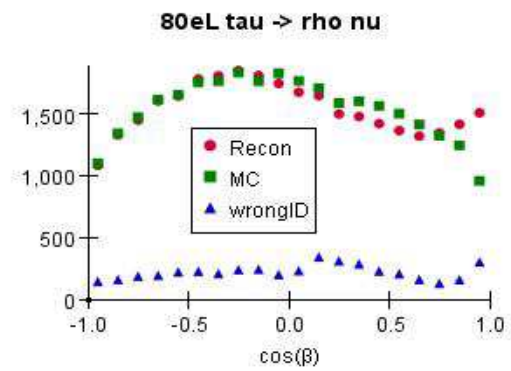
80eL tau -> rho nu
Recon
MC
wrongID
cos(β)

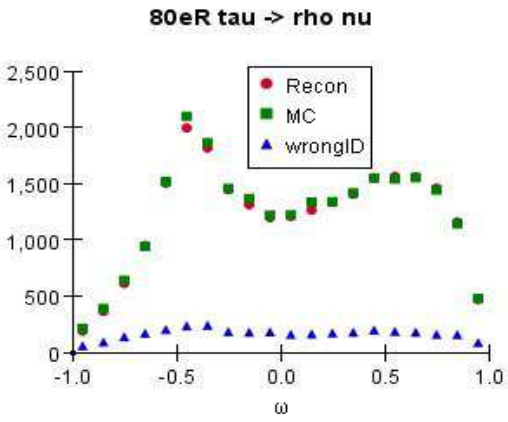
80eR tau -> rho nu
Recon
MC
wrongID
ω

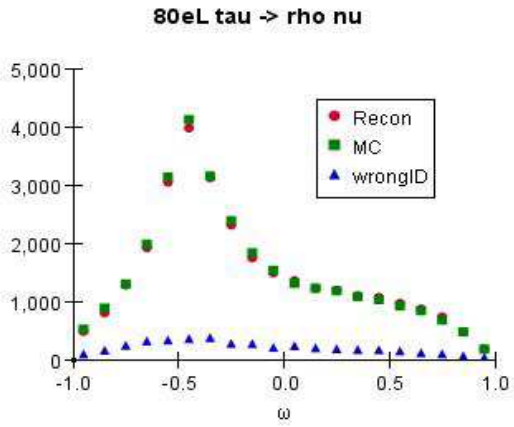
80eL tau -> rho nu
Recon
MC
wrongID
ω

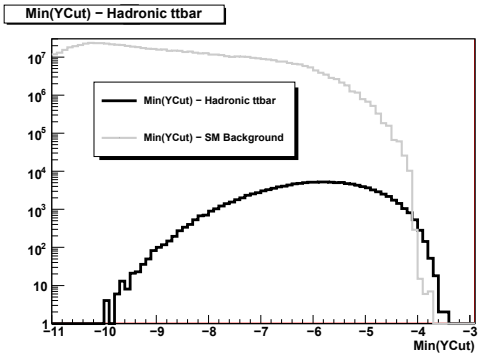
Min(YCut) − Hadronic ttbar
Min(YCut) − Hadronic ttbar
Min(YCut) − SM Background
Min(YCut)

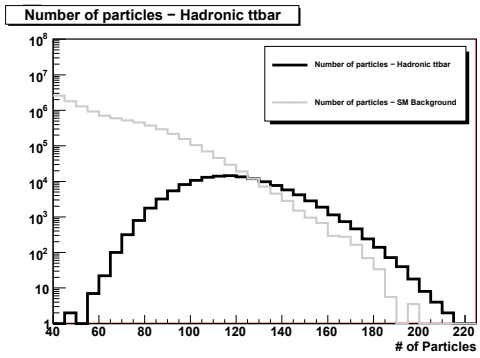
Number of particles − Hadronic ttbar
Number of particles − Hadronic ttbar
Number of particles − SM Background
# of Particles

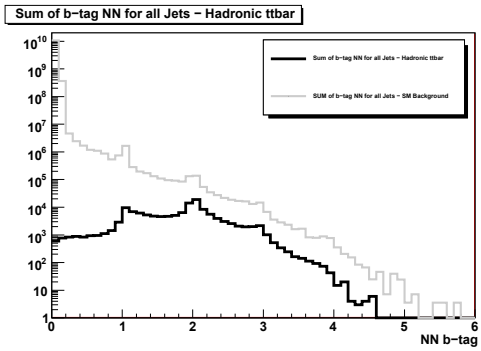
Sum of b−tag NN for all Jets − Hadronic ttbar
Sum of b−tag NN for all Jets − Hadronic ttbar
SUM of b−tag NN for all Jets − SM Background
NN b−tag

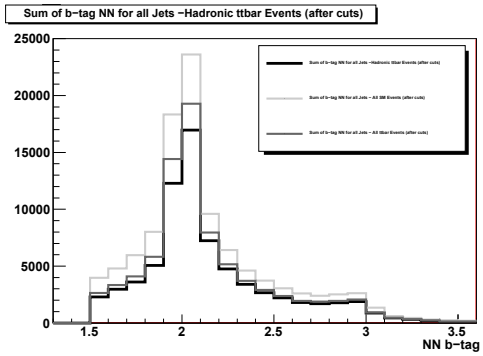
Sum of b−tag NN for all Jets −Hadronic ttbar Events (after cuts)
NN b−tag

mass(top1)	= mass(top2)
mass(W1)	= 80.4 GeV
mass(W2)	= 80.4 GeV
E_{total}	= 500 GeV
p_x; p_y; p_z	= 0

Table 4.10: Kinematic fitting constraints.

meet the fitting constrains with probability less than 10% were rejected. This requirement selects only well reconstructed top events and is quite sensitive to the jet energy and angular resolutions which are the input parameters for the fitter. Although this selection reduces the efficiency to 31.3%, but it also increases the purity to 85.1% and overall improves the precision of mass resolution.

It is now possible to perform a mass fit using an asymmetric double Gaussian convoluted with a Breit-Wigner as a signal fit function. The function is fitted on a separate signal sample in the mass range of 166 GeV - 200 GeV where the parameters of the Gaussians are determined keeping all other parameters fixed. The Standard Model background is then described by a second order polynomial function. The combined function is fitted on the data sample with all the parameters fixed for the exception of the top mass and the Breit-Wigner width. This method results in the top mass of 173.918 ± 0.053 GeV thus predicting the accuracy of about 50 MeV of the top mass determination with 500 fb^{-1}. The distribution of the top mass and the corresponding fit is shown in Figure 4.18. It is also possible to estimate the $t\bar{t}$ cross-section in the hadronic channel as 284.1 ± 1.4 fb.

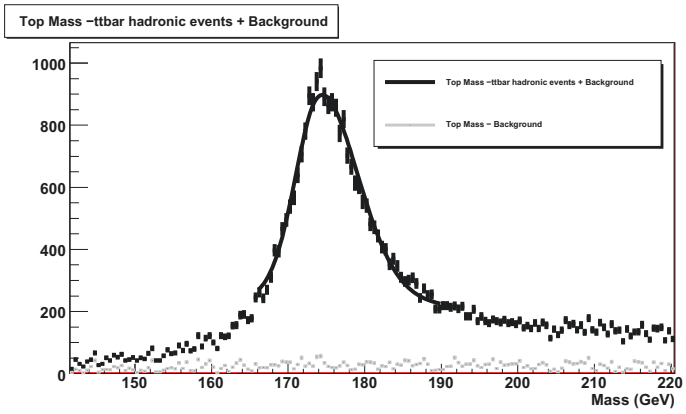

Figure 4.18: Distribution of the top invariant mass after the kinematic fitting and probability cut.

The determination of top quark mass uncertainty can be calculated also using a template method. The data sample, without the SM background, is compared with a template produced at the same mass and with a template with the top mass shifted by 0.5 GeV. From

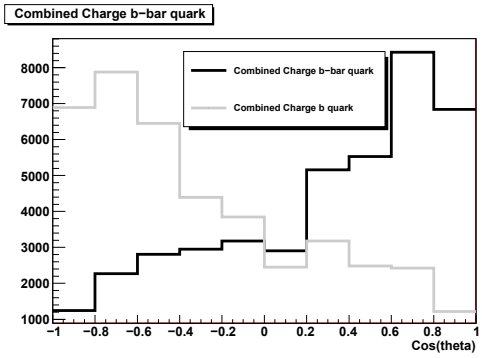
Combined Charge b−bar quark
Combined Charge b−bar quark
Combined Charge b quark
8000
7000
6000
5000
4000
3000
2000
1000
−1
−0.8
−0.6
−0.4
−0.2
0
0.2
0.4
0.6
0.8
1
Cos(theta)

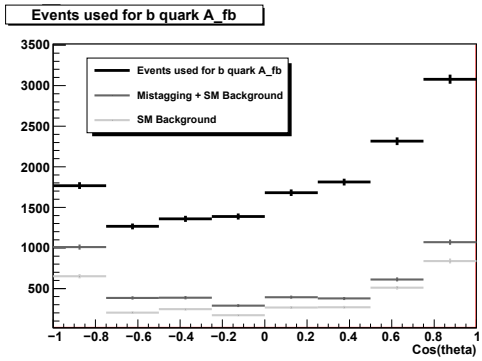
Events used for b quark A_fb
Events used for b quark A_fb
Mistagging + SM Background
SM Background
3500
3000
2500
2000
1500
1000
500
−1
−0.8
−0.6
−0.4
−0.2
0
0.2
0.4
0.6
0.8
1
Cos(theta)

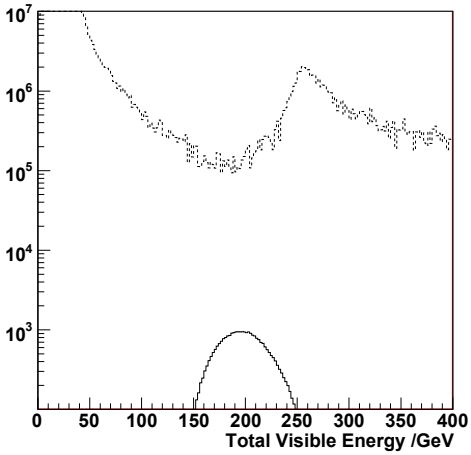
10^7
10^6
10^5
10^4
10^3
0 50 100 150 200 250 300 350 400
Total Visible Energy /GeV

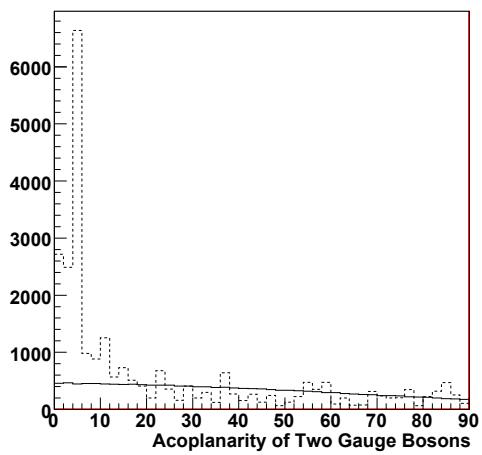
6000
5000
4000
3000
2000
1000
0
0 10 20 30 40 50 60 70 80 90
Acoplanarity of Two Gauge Bosons

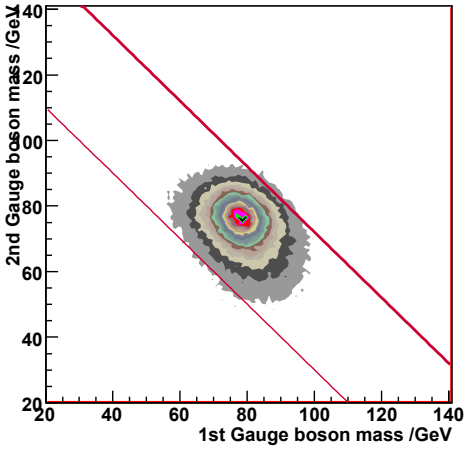
2nd Gauge boson mass /GeV
1st Gauge boson mass /GeV

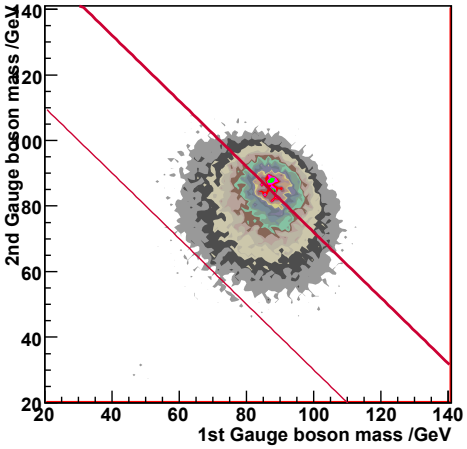
2nd Gauge boson mass /GeV
1st Gauge boson mass /GeV

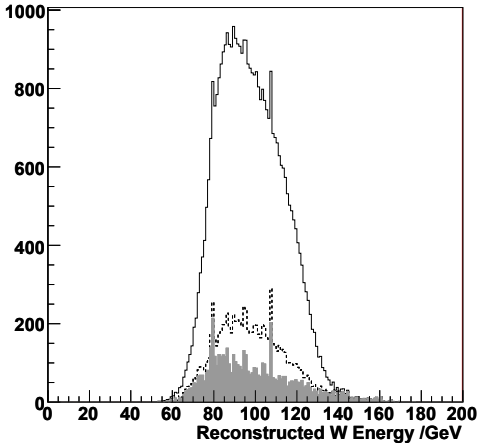
Reconstructed W Energy /GeV

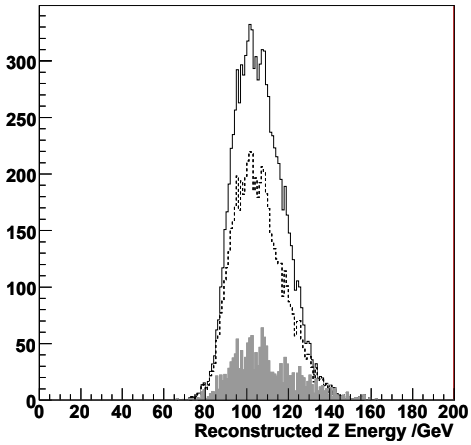
Reconstructed Z Energy /GeV

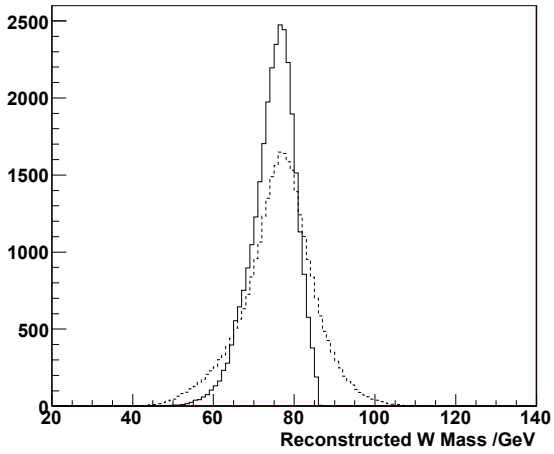
2500
2000
1500
1000
500
0
20
40
60
80
100
120
140
Reconstructed W Mass /GeV

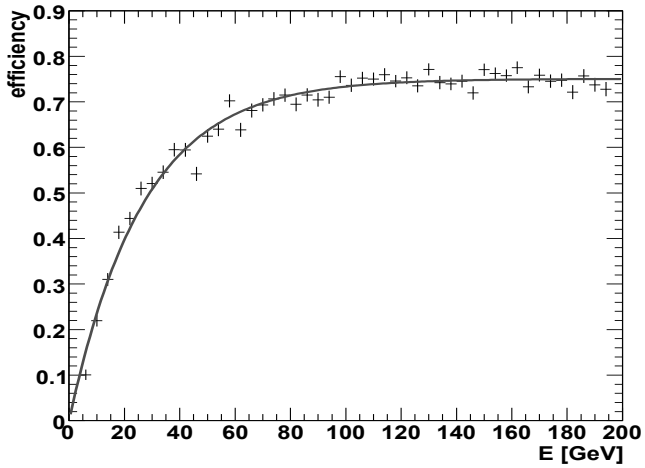
efficiency
0.9
0.8
0.7
0.6
0.5
0.4
0.3
0.2
0.1
0
0
20
40
60
80
100
120
140
160
180
200
E [GeV]

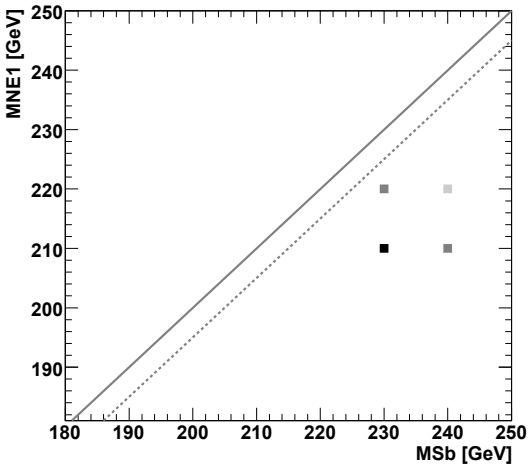
MNE1 [GeV]
250
240
230
220
210
200
190
180
190
200
210
220
230
240
250
MSb [GeV]

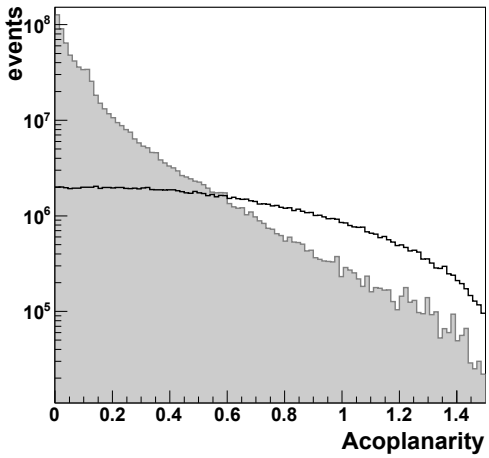
events
10^8
10^7
10^6
10^5
0
0.2
0.4
0.6
0.8
1
1.2
1.4
Acoplanarity

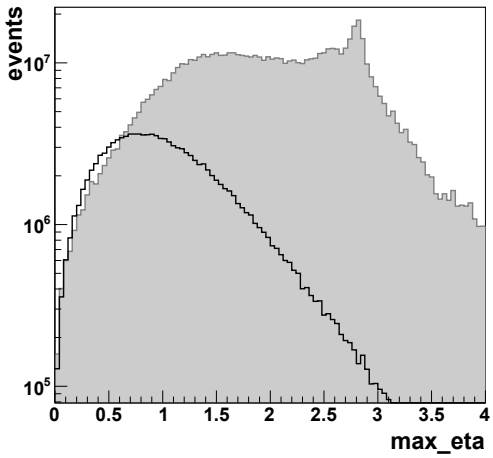
events
10^7
10^6
10^5
0
0.5
1
1.5
2
2.5
3
3.5
4
max_eta

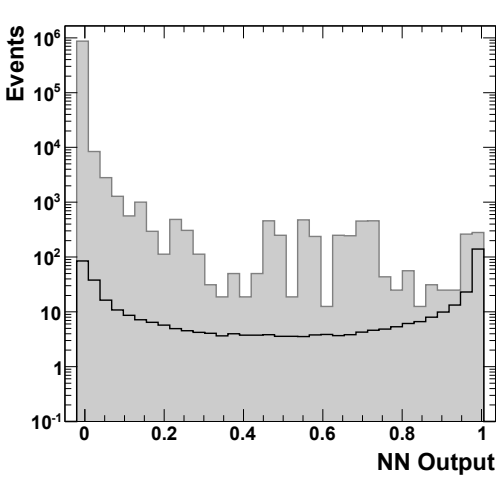
Events
10^6
10^5
10^4
10^3
10^2
10
1
10^{-1}
0
0.2
0.4
0.6
0.8
1
NN Output

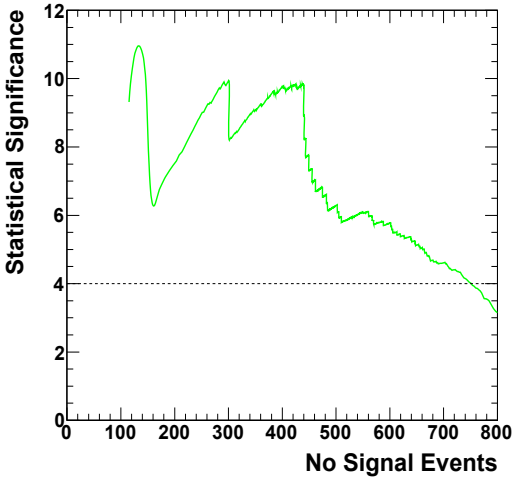
Statistical Significance
12
10
8
6
4
2
0
0
100
200
300
400
500
600
700
800
No Signal Events

1.1.3	Tracker	1 each	@CF=Tracker	15,446,950	5,869,383	11,473,252	4,015,638	36,805,223
1.1.3.1	Tracker ED&I	1 each		0	0	7,761,320	2,716,462	10,477,782
1.1.3.1.1	Mechanical Engineer	20 man year		0	0	140,000	49,000	3,780,000
1.1.3.1.2	Mechanical Designer	10 man year		0	0	91,520	32,032	1,235,520
1.1.3.1.3	Mechanical Tech	40 man year	WAG	0	0	101,153	35,404	5,462,262
1.1.3.2	Tracker Mechanics	1 each		2,900,000	1,375,000	1,200,325	420,114	5,895,439
1.1.3.2.1	Tracker Space Frame, Barrel	1 lot		1,250,000	625,000	0	0	1,875,000
1.1.3.2.2	Outer Endcap Frame[0]	2 lot		250,000	125,000	0	0	750,000
1.1.3.2.3	Tracker Cooling	1 lot		150,000	150,000	0	0	300,000
1.1.3.2.4	Tracker Alignment System	1 each		1,000,000	350,000	0	0	1,350,000
1.1.3.2.5	Mechanical Engineer	3 man year		0	0	140,000	49,000	567,000
1.1.3.2.6	Mechanical Designer	3 man year		0	0	91,520	32,032	370,656
1.1.3.2.7	Mechanical Tech	5 man year		0	0	101,153	35,404	682,783
1.1.3.3	Tracker Silicon Detectors	1 each		11,546,950	4,244,383	2,511,607	879,063	19,182,003
1.1.3.3.1	Barrel	1 each		6,340,450	2,341,108	1,531,015	535,855	10,748,428
1.1.3.3.1.1	Tracker Barrel Module	8,130 each	Parametric	665	248	188	66	9,487,528
1.1.3.3.1.1.1	Tracker Silicon	0.01 Sq.m.		30,000	10,500	0	0	405
1.1.3.3.1.1.2	Tracker Module Mechanics Barrel	1 each		65	23	0	0	88
1.1.3.3.1.1.3	Tracker KPiX	2 each		100	35	0	0	270
1.1.3.3.1.1.4	Tracker Cable	1 each		100	50	0	0	150
1.1.3.3.1.1.5	Mechanical Tech	2 man hour		0	0	54	19	145
1.1.3.3.1.1.6	Procurement Officer	1.5 man hour		0	0	54	19	109
1.1.3.3.1.2	Level 1 Concentrator, Tracker	467 each		2,000	700	0	0	1,260,900
1.1.3.3.1.3	Level 2 Concentrator, Tracker	1 each		0	0	0	0	0
1.1.3.3.2	Endcaps	2 each		2,603,250	951,638	490,296	171,604	8,433,575
1.1.3.4	Tracker Integration	1 lot		1,000,000	250,000	0	0	1,250,000

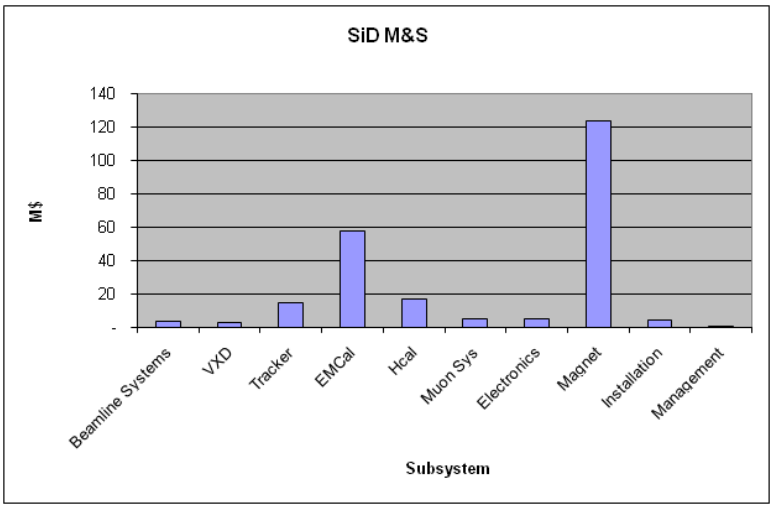
SiD M&S
M$
140
120
100
80
60
40
20
-
Beamline Systems
VXD
Tracker
EMCal
Hcal
Muon Sys
Electronics
Magnet
Installation
Management
Subsystem

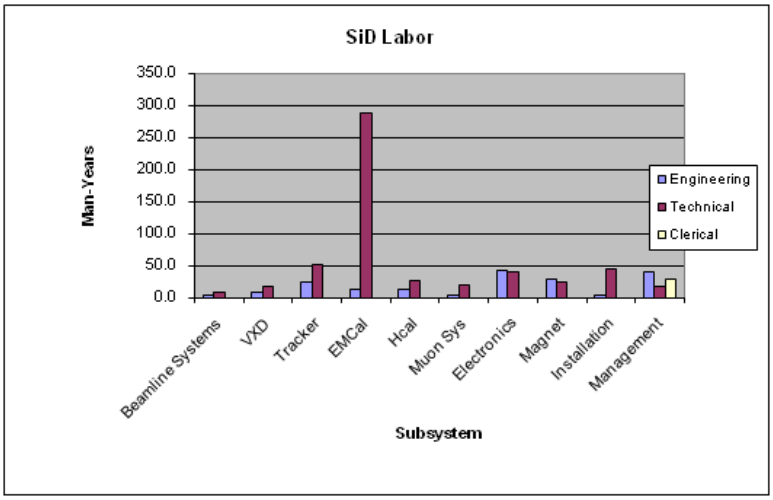
SiD Labor
Man-Years
350.0
300.0
250.0
200.0
150.0
100.0
50.0
0.0
Engineering
Technical
Clerical
Beamline Systems
VXD
Tracker
EMCal
Hcal
Muon Sys
Electronics
Magnet
Installation
Management
Subsystem

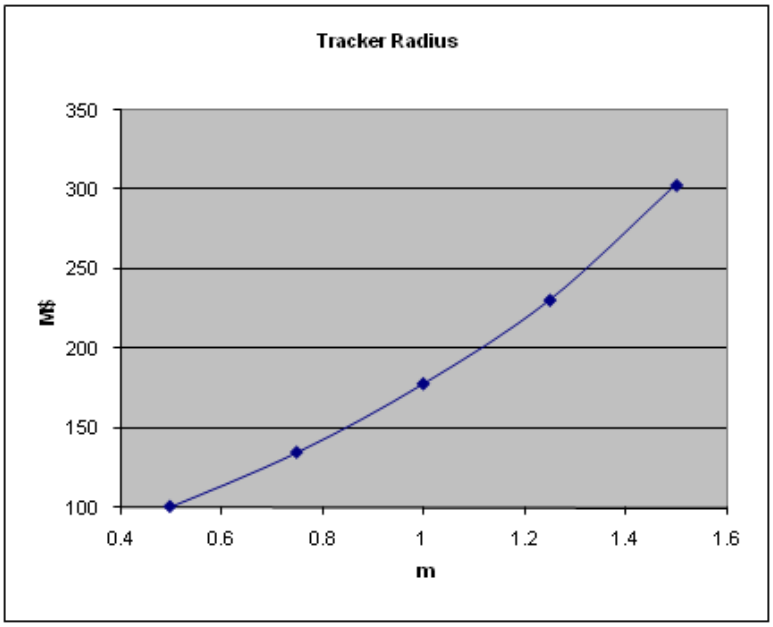
Tracker Radius
M$
350
300
250
200
150
100
0.4
0.6
0.8
1
1.2
1.4
1.6
m

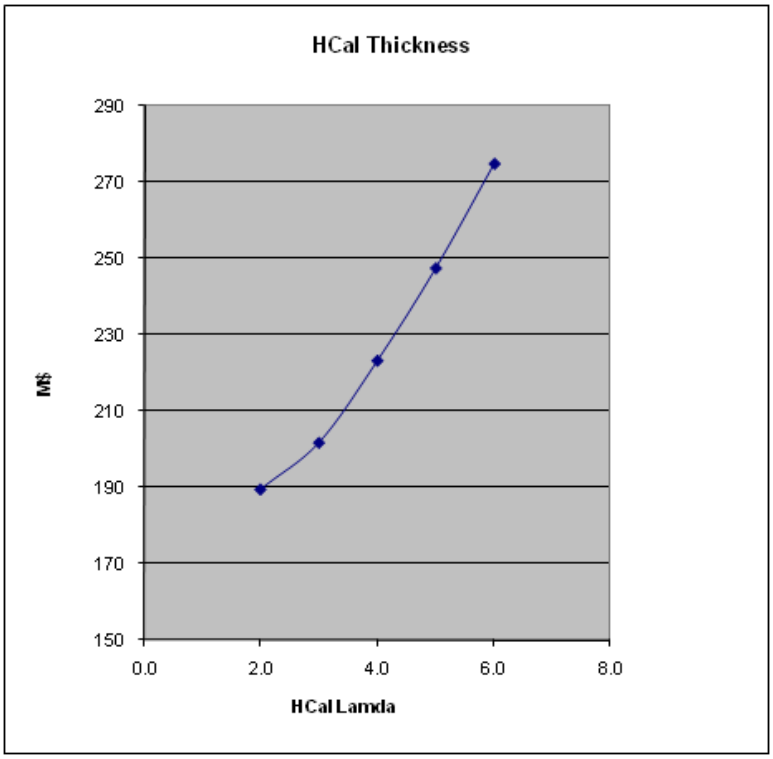
HCal Thickness
290
270
250
230
210
190
170
150
M$
0.0
2.0
4.0
6.0
8.0
HCal Lamda

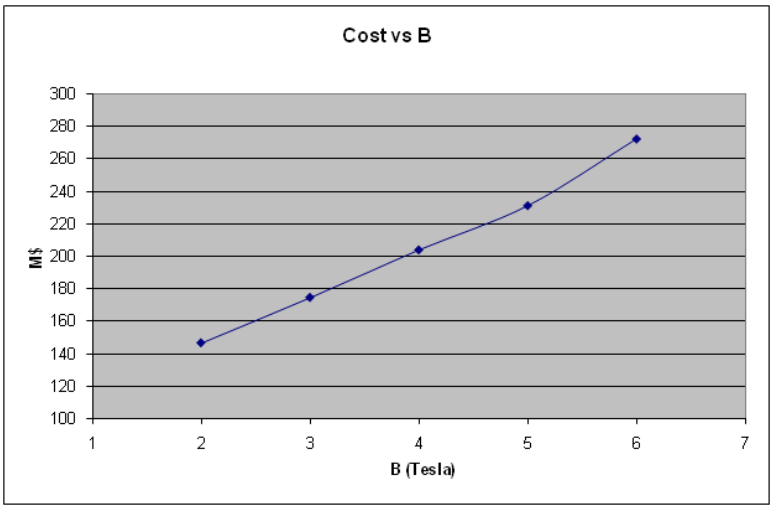
Cost vs B
300
280
260
240
220
200
180
160
140
120
100
M$
1
2
3
4
5
6
7
B (Tesla)

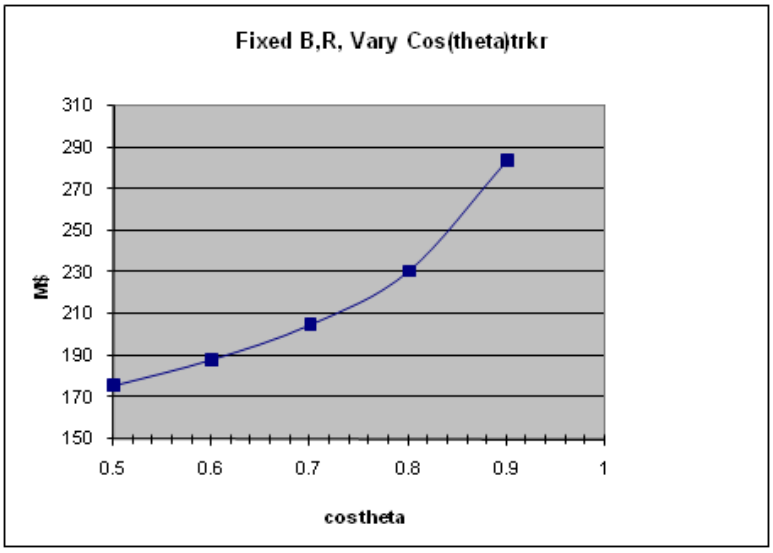
Fixed B,R, Vary Cos(theta)trkr
310
290
270
250
230
210
190
170
150
M$
0.5
0.6
0.7
0.8
0.9
1
costheta

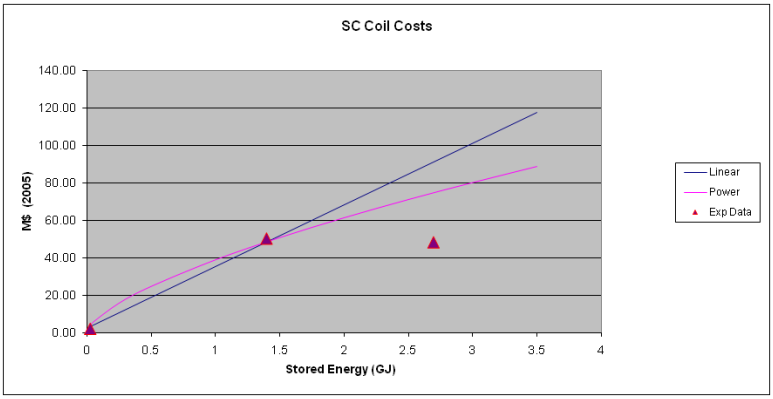
SC Coil Costs
140.00
120.00
100.00
80.00
60.00
40.00
20.00
0.00
M$ (2005)
0
0.5
1
1.5
2
2.5
3
3.5
4
Stored Energy (GJ)
Linear
Power
Exp Data

Editors:

H. Aihara, P. Burrows, M. Oreglia

Cosigners:

E. L. Berger, V. Guarino, J. Repond, H. Weerts, L. Xia, J. Zhang
Argonne National Laboratory, USA

Q. Zhang
Argonne National Laboratory and IHEP, Beijing, PR China

A. Srivastava
Birla Institute for Technology and Science, Pilani, India

J. M. Butler
Boston University, USA

J. Goldstein, J. Velthuis
Bristol University, UK

V. Radeka
Brookhaven National Laboratory, USA

R.-Y. Zhu
California Institute of Technology, USA

P. Lutz
CEA-Saclay (IRFU), France

A. de Roeck, K. Elsener, A. Gaddi, H. Gerwig C. Grefe, W. Klempt, L. Linssen,
D. Schlatter, P. Speckmayer
CERN, Switzerland

J. Thom
Cornell University, LNS, USA

J. Yang
Ewha Womans University, South Korea

D. C. Christian, S. Cihangir, W. E. Cooper, M. Demarteau, H. E. Fisk, L. A. Garren, K. Krempetz, R. K. Kutschke, R. Lipton, A. Para, R. Tschirhart, H. Wenzel, R. Yarema
Fermi National Accelerator Laboratory, USA

M. Grunewald
Ghent University, Belgium

A. Pankov
Gomel State Technical University, Belarus

T. Dutta
GSI, Germany

P. D. Dauncey
Imperial College London, UK

J.P. Balbuena, C. Fleta, M. Lozano, M. Ullán
Insitute of Microelectronics of Barcelona IMB-CNM (CSIC), Spain

G. B. Christian
Institute of Nuclear Research (ATOMKI), Hungary

A. Faus-Golfe, J. Fuster, C. Lacasta, C. Marinñas, M. Vos
Instituto de Fisica Corpuscular, IFIC CSIC-Univ. Valencia, Spain

J. Duarte, M. Fernandez, J. Gonzalez , R. Jaramillo, A. Lopez-Virto, C. Martinez-Rivero, D. Moya, A. Ruiz-Jimeno, I. Vila
Instituto de Fisica de Cantabria (IFCA), CSIC-Univ. Cantabria, Spain

C. Colledani, A. Dorokhov, C. Hu-Guo, M. Winter
IPHC-IN2P3/CNRS, Strasbourg, France

G. Moortgat-Pick
IPPP, Durham, UK

D. V. Onoprienko
Kansas State University, USA

G. N. Kim, H. Park
Kyungpook National University, South Korea

C. Adloff, J. Blaha , J.-J. Blaising, S. Cap, M. Chefdeville, C. Drancourt, A. Espargiliare, R. Gaglione, N. Geffroy, J. Jacquemier, Y. Karyotakis, J. Prast, G. Vouters
Laboratoire d'Annecy-le-vieux de Physique des Particules, Universite de Savoie, CNRS/IN2P3, France

J. Gronberg, S. Walston, D. Wright
Lawrence Livermore National Laboratory, USA

L. Sawyer
Louisiana Tech University, USA

M. Laloum
LPNHE, Faculte des Sciences de Paris VI et VII, France

C. Ciobanu, J. Chauveau, A. Savoy-Navarro
LPNHE, Universite Pierre et Marie Curie, Paris, France

L. Andricek, H.-G. Moser
Max-Planck-Institute for Physics, Munich, Germany

R. F. Cowan, P. Fisher, R. K. Yamamoto
MIT, LNS, USA

C. J. Kenney
Molecular Biology Consortium, USA

E. E. Boos, M. Merkin
Moscow State University, Russia

S. Chen
Nanjing University, China

D. Chakraborty, A. Dyshkant, D. Hedin, V. Zutshi
Northern Illinois University, USA

V. Galkin, N. D'Ascenzo, D. Ossetski, V. Saveliev
Obninsk State Technical University for Nuclear Power Engineering, Russia

F. Kapusta
LPNHE, Univ. VII, Paris, France

R. De Masi
PHC-IN2P3/CNRS, Strasbourg, France

V. Vrba
Institute of Physics, Prague, Czech Republic

C. Lu, K. T. McDonald, A. J. S. Smith
Princeton University, USA

D. Bortoletto
Purdue University, USA

R. Coath, J. Crooks, C. Damerell, M. Gibson, A. Nichols, M. Stanitzki, J. Strube, R. Turchetta, M. Tyndel, M. Weber, S. Worm, Z. Zhang
Rutherford Appleton Laboratory, UK

T. L. Barklow, A. Belymam, M. Breidenbach, R. Cassell, W. Craddock, C. Deaconu, A. Dragone, N. A. Graf, G. Haller, R. Herbst, J. L. Hewett, J. A. Jaros, A. S. Johnson, P. C. Kim, D. B. MacFarlane, T. Markiewicz, T. Maruyama, J. McCormick, K. Moffeit, H. A. Neal, T. K. Nelson, M. Oriunno, R. Partridge, M. E. Peskin, T. G. Rizzo, P. Rowson, D. Su, M. Woods
SLAC National Accelerator Laboratory, USA

S. Chakrabarti,
SUNY, Stony Brook, USA

A. Dieguez, Ll. Garrido
University of Barcelona, Spain

J. Kaminski
University of Bonn, Germany

J. S. Conway, M. Chertok, J. Gunion, B. Holbrook, R. L. Lander, S. M. Tripathi
University of California, Davis, USA

V. Fadeyev, B. A. Schumm
University of California, Santa Cruz, USA

M. Oreglia
University of Chicago, USA

J. Gill, U. Nauenberg, G. Oleinik, S. R. Wagner
University of Colorado, USA

K. Ranjan, R. Shivpuri
University of Delhi, India

G. S. Varner
University of Hawaii, USA

R. Orava
University of Helsinki, Finland

R. Van Kooten
University of Indiana, USA

B. Bilki, M. Charles[1], T. J. Kim, U. Mallik, E. Norbeck, Y. Onel
University of Iowa, USA

B. P. Brau, S. Willocq
University of Massechusetts, Amherst, USA

G. N. Taylor
University of Melbourne, Australia

K. Riles, H.-J. Yang
University of Michigan, USA

R. Kriske
University of Minnesota, USA

L. Cremaldi, R. Rahmat
University of Mississippi, USA

G. Lastovicka-Medin
University of Montenegro, Montenegro

S. Seidel
University of New Mexico, USA

M. D. Hildreth, M. Wayne
University of Notre Dame, USA

J. E. Brau, R. Frey, N. Sinev, D. M. Strom, E. Torrence
University of Oregon, USA

Y. Banda, P. N. Burrows, E. Devetak, B. Foster, T. Lastovicka, Y.-M. Li, A. Nomerotski
University of Oxford, UK

J. Riera-Babures, X. Vilasis-Cardona
Universitat Ramon Llull, Spain

S. Manly
University of Rochester, USA

B. Adeva, C. Iglesias Escudero, P. Vazquez Regueiro, J. J. Saborido Silva, A. Gallas Torreira
University of Santiago de Compostela (IGFAE), Spain

D. Gao, W. Jie, Y. Junfeng, C. Li, S. Liu, Y. Liu, Y. Sun, Q. Wang, J. Yi, W. Yonggang, Z. Zhao
University of Science and Technology of China

K. De, A. Farbin, S. Park, J. Smith, A. P. White, J. Yu
University of Texas at Arlington, USA

X. C. Lou
University of Texas at Dallas, USA

T. Abe, H. Aihara, M. Iwasaki
University of Tokyo, Japan

H. J. Lubatti
University of Washington, Seattle, USA

H. R. Band, F. Feyzi, R. Prepost
University of Wisconsin, Madison, USA

P. E. Karchin, C. Milstene
Wayne State University, USA

C. Baltay, S. Dhawan
Yale University, USA

Y.-J. Kwon
Yonsei University, Japan

Contents

Chapter 1

Introduction

This document presents the current status of SiD's effort to develop an optimized design for an experiment at the International Linear Collider. It presents detailed discussions of each of SiD's various subsystems, an overview of the full GEANT4 description of SiD, the status of newly developed tracking and calorimeter reconstruction algorithms, studies of subsystem performance based on these tools, results of physics benchmarking analyses, an estimate of the cost of the detector, and an assessment of the detector R&D needed to provide the technical basis for an optimised SiD.

1.1 The ILC Physics Menu

The Silicon Detector (SiD) has been designed to address questions of fundamental importance to progress in particle physics:

- What is the mechanism responsible for electroweak symmetry breaking and the generation of mass?
- How do the forces unify?
- Does the structure of space-time at small distances show evidence of extra dimensions?
- What are the connections between the fundamental particles and forces and cosmology?

These questions are addressed through precision measurements by SiD at the International Linear Collider (ILC) of the following:

- Higgs boson properties;
- Gauge boson scattering;
- Effects resulting from the existence of extra dimensions;

- Supersymmetric particles; and
- Top quark properties.

The Higgs boson studies will measure in detail the properties of the Higgs boson in order to determine its consistency with Standard Model expectations, and the nature of any deviations. These measurements will include the mass, width, spin, branching ratios and couplings, and the Higgs self-coupling. The estimated precision in these measurements is sufficient to discriminate between competing theories for electroweak symmetry breaking. With the decay-independent detection of Higgstrahlung events by Z tagging, sensitivity to a wide range of models is possible. Such measurements would establish the role of the Higgs boson in electroweak symmetry breaking, and the generation of mass. Should Nature choose a Higgs-less scenario, it could be addressed by studying the coupling of gauge bosons. If additional Higgs bosons beyond that of the Standard Model exist, they can be detected and studied with SiD, even if they have very large masses. For example, in the MSSM, the additional four Higgs bosons can be detected if they are within the kinematic reach of the ILC.

If supersymmetric particles are produced at the ILC, their masses and couplings will be measured by SiD, allowing studies of the evolution of the strength of the fundamental forces and experimentally testing their unification at very high energies. SiD has a reach up to $\sim$3 TeV in Higgs-less strong coupling scenarios. Such models include those with strongly-interacting W and Z and some with dimensions. A universe with extra dimensions of a scale within reach of the ILC can be probed, with high-precision sensitivity to the separate parameters of scale and number of dimensions. By observing masses and widths of excited graviton states, the length scale and the curvature in an additional fifth dimension of space-time can be determined. SiD plans to study the top quark, including the precise measurement of its mass and Yukawa coupling. Finally. a number of connections to issues of interest in cosmology would be realized through many of the measurements described above. These focus on two fundamental issues, namely the mechanism behind the present day baryon asymmetry and the nature of the cold dark matter

1.2 Detector Overview

SiD is a linear collider detector concept designed to make precision measurements, and at the same time be sensitive to a wide range of possible new phenomena at the ILC. A plan view of one quadrant of the detector is shown in Figure 1.1. SiD is based on silicon tracking, silicon-tungsten electromagnetic calorimetry, highly segmented hadronic calorimetry, and a powerful silicon pixel vertex detector. SiD also incorporates a high field solenoid, iron flux return, and a muon identification system. Particle Flow Analysis (PFA) (see below) is an important consideration for the basic philosophy and layout of the detector.

The choice of silicon detectors for tracking and vertexing ensures that SiD is robust with respect to beam backgrounds or beam loss, provides superior charged particle momentum resolution, and eliminates out of time tracks and backgrounds. The main tracking detector and

calorimeters are "live" only during a single bunch crossing, so beam-related backgrounds and low mass backgrounds from 2-photon processes will be reduced to the minimum possible levels. The SiD design has been cost-conscious from the beginning, and the present global design represents a careful balance between cost and physics performance. The SiD proponents are convinced that two detectors are required scientifically, technically, and sociologically to exploit fully the ILC physics potential. Therefore SiD is engineered to make the push pull process efficient and to minimize the time required for alignment and calibration after a move.

Figure 1.1: Illustration of a quadrant of SiD (dimensions in mm).

The key parameters of the SiD design starting point are listed in Table 1.1. The innermost tracking sub-system is the Vertex Detector (VXD), which comprises 5 cylinders and 4 sets of endcaps, composed of pixilated sensors closely surrounding the beampipe. The impact parameter resolution will surpass $\sigma_{r\phi} = \sigma_{rz} = 5 \oplus 10/(\mathrm{p}\ \sin^{3/2}\theta)$ [μm]. SiD has chosen a 5 T solenoidal field in part to control the e^+e^- pair background, and the cylinder and disk geometry is chosen to minimize scattering and ensure high performance in the forward direction. The VXD sensor technology is not yet chosen because the relatively high luminosity per train at the ILC makes integration through the train undesirable, and optimal technologies for separating the train into small temporal segments, preferably bunches, have not been determined. This is not a problem, since this choice will have almost no effect on the rest of the SiD design, and the VXD can be built and installed after many of the main detector components are complete.

SiD has chosen Si strip technology, arrayed in 5 cylinders and 4 endcaps for precision tracking and momentum measurement. Particular attention has been given to fabricating the endcaps with minimal material to enhance forward tracking. The sensors are single sided

SiD BARREL	Technology	Inner radius	Outer radius	Z max
Vertex detector	Pixel	1.4	6.0	± 6.25
Tracker	Silicon strips	21.7	122.1	± 152.2
EM calorimeter	Silicon-W	126.5	140.9	± 176.5
Hadron calorimeter	RPCs	141.7	249.3	± 301.8
Solenoid	5 Tesla	259.1	339.2	± 298.3
Flux return	RPCs	340.2	604.2	± 303.3

SiD FORWARD	Technology	Inner Z	Outer Z	Outer radius
Vertex detector	Pixel	7.3	83.4	16.6
Tracker	Silicon strips	77.0	164.3	125.5
EM calorimeter	Silicon-W	165.7	180.0	125.0
Hadron calorimeter	RPCs	180.5	302.8	140.2
Flux return	RPCs	303.3	567.3	604.2
LumCal	Silicon-W	158.0	173.0	19.0
BeamCal	Silicon-W	295.0	320.0	14.5

Table 1.1: Key parameters of the baseline SiD design. (All dimension are given in cm.)

Si, approximately 15 cm square, with a pitch of 50 μm. With an outer cylinder radius of 1.25 m and a 5 T field, the charged track momentum resolution will be better than $\sigma(1/p_T) = 5$ x 10^{-5} (GeV/c)$^{-1}$ for high momentum tracks. The endcaps utilize two sensors bonded together for small angle stereo measurements. Highly efficient track finding has been demonstrated in simulation using the integrated tracking system.

SiD calorimetry is optimized for jet energy measurement, and is based on a Particle Flow strategy, in which charged particle momenta are measured in the tracker; neutrals are measured in the calorimeter, and then the charged and neutral components are added. The challenge is identifying the energy which charged particles deposit in the calorimeters, and discriminating it from the energy photons and neutral hadrons deposit, so it can be removed. This requires highly segmented readout, both transversely and longitudinally, and in the ECAL puts a premium on minimizing the spread of electromagnetic showers. SiD calorimetry begins with an exceptionally dense, highly pixilated Silicon – Tungsten electromagnetic section. The ECAL has alternating layers of W and silicon pixel detectors; there are 20 layers of 2.5 mm tungsten followed by 10 layers of 5 mm tungsten. The silicon detector layers are only 1.25 mm thick. This results in a Moliere radius for the thin section of 13.5 mm. The sensor is divided into 1024 hexagonal pixels, forming an imaging calorimeter with a track resolution of $\sim$1 mm. The ECAL has a total of 26 X_0. The same technology is used in the endcaps. Silicon detector technology is used in the vertex detector, tracker, and ECAL because it is robust against machine backgrounds, only sensitive to backgrounds in a single bunch crossing, and has high precision.

The Hadronic Calorimeter (HCAL) is made from 4.5 λ of Stainless Steel, divided into

40 layers of steel and detector. The baseline detectors are RPCs with 1 cm square pixels, inserted into 8 mm gaps between the steel layers. The same technology is used for the endcaps. The jet energy resolution has been studied with Pandora PFA and also with SiD PFA (see online appendices for details); it is $\Delta E/E = 4\%$. Further improvement is expected as the algorithm matures. Having such superb jet energy resolution will allow, for the first time, the invariant masses of W's, Z's, and tops to be reconstructed with resolutions approaching the natural widths of these particles.

The calorimetric coverage is completed in the forward direction by a LumCal and a BeamCal. The LumCal overlaps the endcap ECAL, and is designed for a ΔL/L precision of 1×10^{-3}. The Lumcal is Si-W, with the pixilation designed to optimize the luminosity measurement precision. The BeamCal is the smallest angle calorimeter and is mounted to the inboard side of QD0. The BeamCal sensor technology may be diamond or low resistivity Si. Both calorimeters are designed for a 14 mrad crossing angle and an anti-DID correction winding on the main solenoid (see Section 2.3).

The SiD 5 T superconducting solenoid is based on the CMS design, but has 6 layers of conductor. The stored energy is $\sim$1.6 GJ. The critical cold mass parameters, such as stored energy/Kg, are similar to CMS. The CMS conductor is the baseline choice, but SiD is developing an advanced conductor that would eliminate the e-beam welding of structural alloy and be easier to wind. SiD will carry all the solenoid utilities (power supply, quench protection, etc) except for the He liquefier, which will be connected by a vacuum insulated flex line.

The flux is returned with an iron structure, configured as a barrel with movable endcaps. The present design limits field leakage to <100 G at 1 m. The flux return is 11 layers of 20 cm iron. The flux return also is the absorber for the muon identifier and is an important component of SiD self shielding. The barrel is composed of full length modules to help keep the structure stable during push pull and to enable full length muon detectors. The endcaps support the final-focus QD0 magnets, with provision for transverse alignment of the quads and vibration isolation. A platform fixed to the barrel supports the 2K cryogenic system for the QD0s. SiD is designed for rapid push pull and rapid recovery after such motion. Precision alignment will utilise a geodetic network of frequency scanning interferometers.

1.3 Polarimeters and Energy Spectrometers

The ILC physics program demands precise polarization and beam energy measurements [1], and SiD will have major responsibilities for these. The ILC baseline configuration is defined in the RDR [2] and specifies many key features of the machine that impact these measurements and the related physics program. These features are summarized in Reference [3] and include:

- a highly polarized electron beam with $P > 80\%$;
- a polarized positron beam with an initial polarization of $\sim 30 - 45\%$;
- spin rotator systems for both electron and positron beams to achieve longitudinal polarization at the collider IP;

- polarimeters and energy spectrometers upstream and downstream of the IP for both beams. The polarimeters utilize Compton scattering and aim to measure the polarization with an accuracy of $\Delta P/P = 0.25\%$. The energy spectrometers aim to achieve an accuracy of 100-200 parts per million (ppm);

- capability to rapidly flip the electron helicity at the injector using the source laser. (The possibility of fast positron helicity flipping is not included in the baseline configuration, but a scheme for fast positron helicity flipping has been proposed).

The baseline ILC provides beam energies in the range 100-250 GeV; precise polarization and energy measurements are required for this full range. The baseline also provides for detector calibration at the Z-pole with 45.6 GeV beam energies, but does not require accurate polarimetry or energy spectrometer measurements at the Z-pole. As discussed in References [3] and [4], accurate polarization and energy measurements at the Z-pole would allow important cross-checks and calibration of the polarimeters and energy spectrometers. SiD endorses making polarimetry and energy measurement checks and calibrations at the Z.

The polarimeter and energy spectrometer systems need to be a joint effort of the ILC Beam Delivery System (BDS) team and the Detector collaborations as summarized in Reference [3]. SiD intends to take significant responsibility for the design, development, operation and performance of these systems. SiD participants are already active in making significant contributions to their design and development. Data from the polarimeters and spectrometers must be delivered to the SiD DAQ in real time so as to be logged and permit fast online analysis. Fast online analysis results must also be provided to the ILC controls system for beam tuning and diagnostics. Details for integrating the polarimeter and energy spectrometer data with the SiD DAQ remain to be worked out, but SiD experts will assume responsibility for integrating the polarimeter and spectrometer data streams with the DAQ.

1.4 SiD Detector Optimization

It is the design of the calorimeters, more than other subsystems, which determines the global parameter choices for the whole detector. The calorimeters are costly, and their performance and costs depend critically on how far from the interaction point they are placed and how thick they must be to contain most of the energy of jets, and therefore how big and costly the detector must be. The problem of optimizing the global detector design simplifies, crudely, to optimizing the parameters of the calorimeters and solenoid. Bigger is more performant, but also more costly. A balance must be struck.

Optimizing SiD's global parameters required three tools. First, a parametric cost model was developed which could calculate the total cost based on the choice of global parameters, assumptions about what materials and detectors comprised each detector element, and per unit cost assumptions appropriate for the materials and detectors chosen.

Secondly, algorithms to estimate the jet energy resolution of the detector or the momentum resolution and impact parameter resolution of the tracker were needed to evaluate

the subsystem performance as a function of the global parameters. The key parameters include the outer radius of the tracker, R, the tracker's length, z, the magnetic field, B, and the thickness of the hadronic calorimeter absorber λ. SiD utilized its own algorithms to estimate the tracking and vertexing performance, and employed parameterizations of the PFA performance derived from Pandora PFA studies [5, 6], to estimate the jet energy resolution as a function of the key parameters.

Thirdly, the ultimate physics performance of SiD was studied as a function of the jet energy resolution. Fast Monte Carlo studies of these and other important physics measurements were conducted for a full range of possible jet energy resolutions, and the resulting measurement accuracy determined as a function of input jet energy resolution. Figure 1.2 shows an example.

These studies confirmed the results of earlier studies that showed slow improvements in physics measurement capability as jet energy resolution is improved. For several possible measurements, improving the jet energy resolution (i.e. $\Delta E/E$) by a factor of two, from $60\%/\sqrt{E}$ to $30\%/\sqrt{E}$, reduced the error in the measurement by about 30%, equivalent to roughly 60% more luminosity. This is a significant improvement, but not enough to make night and day differences in measurement capability.

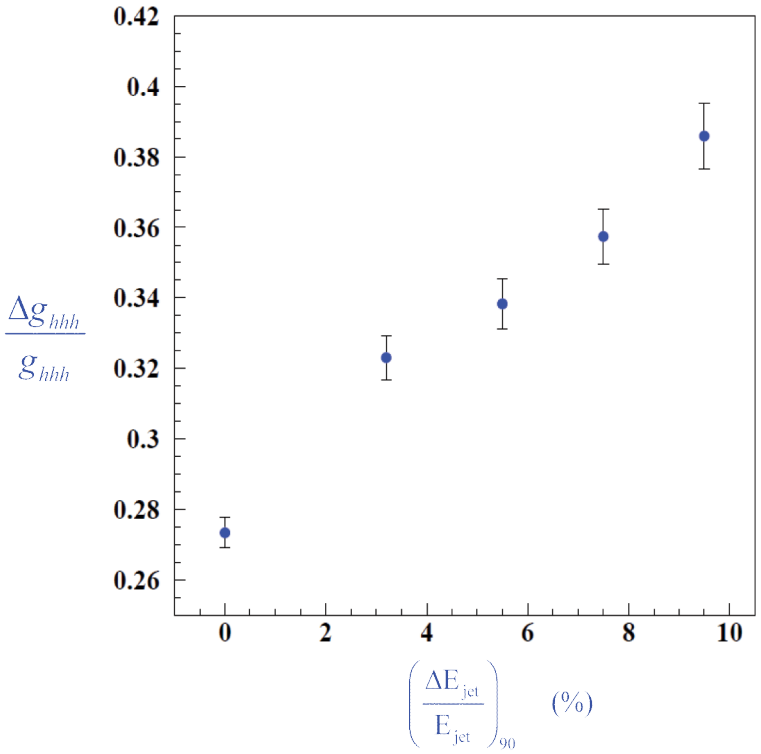

Figure 1.2: Fractional error in the triple Higgs coupling, g_{hhh}, as a function of the jet energy resolution, $\Delta E/E$ [%], from a fast Monte Carlo study of the measurement of the cross section for $e^+e^- \to ZHH \to qqqqbb$ at 500 GeV with an integrated luminosity of 2000 fb^{-1}.

Given these tools, it is possible to choose what set of global parameters minimize the cost of the detector for a desired jet energy resolution. Figure 1.3 shows an example. This

study, and a similar study based on jet energy resolutions for 100 GeV jets, lead to the choices of $R = 1.25$m, $B = 5$T, and $\lambda = 5$ interaction lengths.

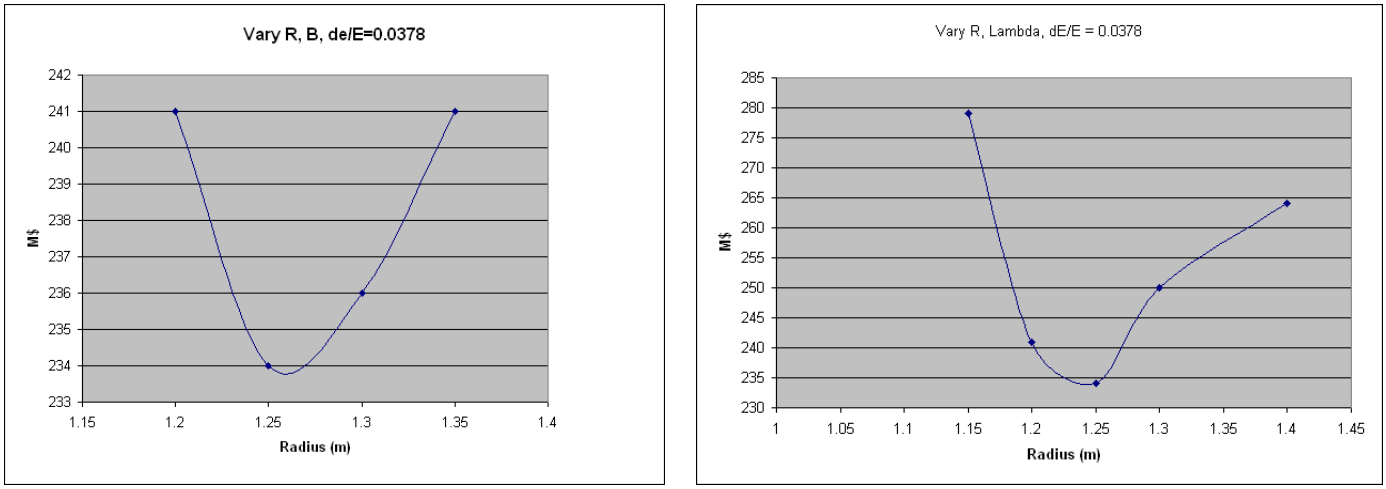

Figure 1.3: SiD cost vs radius. In the plot at left, the radius and B field are varied in such a way that a fixed value of jet energy resolution, $\Delta E/E = 0.0378$, is maintained. At right, the radius and HCal depth, λ, are varied. In both cases, Thomson's parameterization of the jet energy resolution for 180 GeV jets is used, along with the SiD costing model. The cost optimal point in this case is near the SiD baseline, with R=1.25 m, B=5 T, and λ=4.5.

This exercise can of course be repeated for a full range of jet energy resolutions, yielding an optimal cost (and selection of R,B, λ) for each jet energy resolution.

The final step is to use the cost vs. jet energy resolution and the physics performance vs. jet energy resolution inputs, to see how errors in a measured physics quantity change as the cost of the detector is varied. An example is shown in Figure 1.4. What performance is good enough? Obviously, the detector performance must be adequate for making measurements to the accuracy motivated by the physics. Once that is satisfied, it is desirable to pay as little for such performance as possible. Ideally, the chosen design should sit near the "knee" of the performance vs cost plot.

The parameters selected for the SiD baseline place SiD's cost somewhat beyond the cost vs performance "knee"; this fact reflects the existence of additional performance constraints and some conservatism. The optimization process outlined above has been based solely on jet energy resolution. Of course other detector characteristics must be optimized as well, especially track momentum resolution and impact parameter resolution. The choice of B = 5T does improve the jet energy resolution compared to choices of lower B, and it helps to optimize the cost by making the detector compact, but it also provides superb track momentum resolution. Furthermore, since it allows the smallest possible beam pipe radius by constraining the orbits of beamstrahlung-produced e^+e^- pairs, it optimizes vertex detector resolution as well. While less expensive detectors, with poorer jet energy resolution, may still be adequate for ILC jet physics, their tracker radii are typically below the chosen value of 1.25 m. Such trackers would not deliver the desired tracking performance, so more compact designs have not been chosen. Technical uncertainties restrict the maximum B field to 5T and the maximum R to 1.25 m in the case where B=5T.

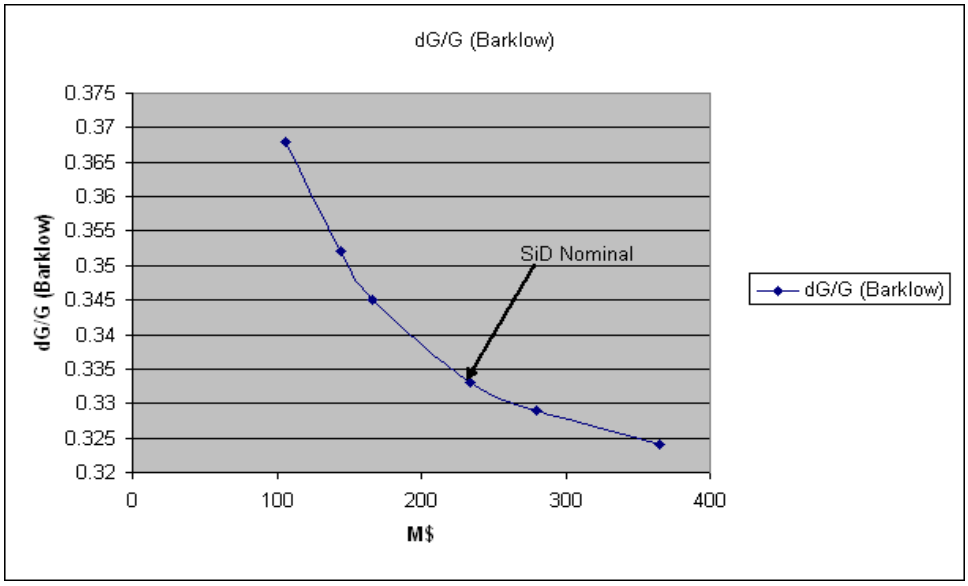

Figure 1.4: Fractional error in the measurement of the triple Higgs coupling in SiD, as a function of the cost of the detector. The SiD baseline is the point at \$238M (ILC units), slightly beyond the "knee". Similar curves can be generated for other physics measurements.

The optimization process will be iterated in tandem with ongoing consideration of improvements to the detector design.

1.5 ILC Environmental Concerns

The ILC beams comprise trains consisting of 2820 bunches, separated by 308ns; the train repetition rate is 5 Hz. Consequently, the bunch trains are about one millisecond long, separated by intervals of 199 milliseconds. The resulting machine backgrounds can be classified as being either directly due to the beam collisions or non-collision-related. Events contributing to the first category are:

- disrupted primary beam exiting the IP
- beamstrahlung photons
- e^+e^--pairs from beam-beam interactions
- radiative Bhabha events
- hadrons or muons from $\gamma\gamma$ interactions.

The second category is populated with events from:

- direct beam losses

- beam-gas interactions
- collimator edge scattering
- synchrotron radiation
- neutron back-shine from the beam dump
- extraction line losses

Each of these sources has been studied. GUINEAPIG [7] was used to simulate the beam-beam interaction and to generate pairs, radiative Bhabhas, disrupted beams and beamstrahlung photons. The ILC nominal 500 GeV beam parameters were used for the simulation. Table 1.2 summarizes the number of particles per bunch and their average energy. $\gamma\gamma$ interactions were included without a transverse momentum cut so as to provide sensitivity to the entire cross sections for these processes. The $\gamma\gamma$ hadronic cross section was approximated in the scheme of Peskin and Barklow [8].

Table 1.2: Background sources for the nominal ILC 500 GeV beam parameters.

Source	#particles/bunch	<E> (GeV)
Disrupted primary beam	2×10^{10}	244
Beamstrahlung photons	2.5×10^{10}	4.4
e^+e^- pairs from beam-beam interactions	75K	2.5
Radiative Bhabhas	320K	195
$\gamma\gamma \quad \rightarrow$ hadrons/muons	0.5 events/1.3 events	-

The backgrounds impose a number of constraints on the detector technologies and on the readout electronics. The e^+e^- pairs are produced at the IP, interact with the beam pipe, inner vertex detector layers, mask and beamline magnets, and produce a large number of secondary e^+e^-, photons and neutrons which in turn contribute background in the vertex detector and in the Si tracker and calorimeter at large radius. Furthermore, the two-photon processes yield about 200 hadronic events per bunch train. High energy interactions comprise only one event in about every ten bunch trains. Therefore, the pile up of the two-photon events could significantly confuse detection of the principal signal of interest unless the detector can cleanly select single bunch crossings, which SiD is designed to do.

The silicon microstrip and pixel detectors used in the vertexing, tracking, and electromagnetic calorimetry can be made sensitive to ionization which is deposited within just 1 μs of the interaction time, and the resultant hits can be uniquely associated with a single bunch crossing. A channel–by-channel buffer, which is 4 deep in current designs, will store hits over the course of the entire bunch train, and record each responsible bunch crossing. Consequently, SiD is sensitive only to the physics and backgrounds of a single bunch crossing, in contrast to detectors with longer inherent livetimes, which can be sensitive to $\sim$150 bunch crossings or more. Figure 1.5 contrasts the $\gamma\gamma$ backgrounds when the detector livetime is short or long. Pattern recognition benefits tremendously from this cleanest possible environment, and physics ambiguities are minimized. Channel-by-channel deadtime inefficiencies are

minimal, and the event buffering insures that essentially no physics data is lost because of noise hits.

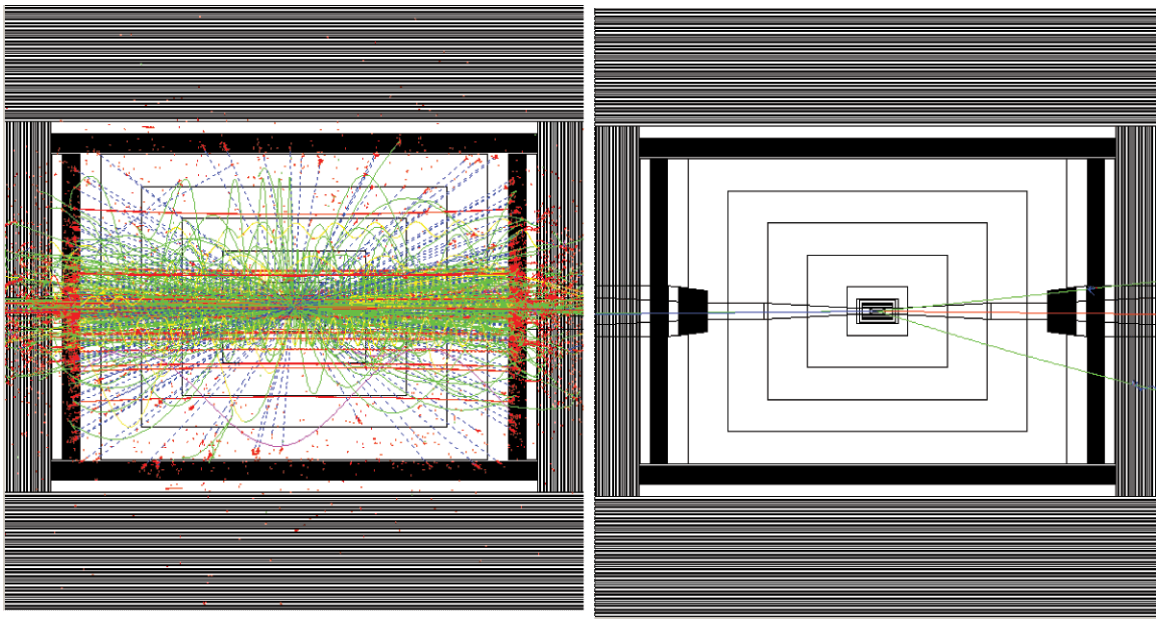

Figure 1.5: Physics backgrounds from $\gamma\gamma$ produced e^+e^- pairs, muon pairs, and hadronic events integrated over 150 bunch crossings (left) and a single bunch crossing (right).

A further complication comes from lessons learned at the first linear collider, the SLC. There, bunch-to-bunch variations in the beam parameters were large, and hard to predict, model, and control. Individual bunches with anomalous backgrounds were problematic to operation of the SLD. Significant precautions are being taken at ILC to deal with this, but experience suggests the need for robust detectors. SiD's reliance on silicon sensors for vertexing, tracking, and electromagnetic calorimetry promises the needed robustness.

1.6 SiD Organization

The SiD Design Study was initiated in 2004 at the Victoria LCWS meeting, and introduced in subsequent regional meetings at Durham and Taipei. The organization, shown in its present form in Figure 1.6, was put in place during this period. Working groups were created, leaders recruited, and plans debated on how to proceed toward the first major SiD Design Study Meeting, which was held in conjunction with the ALCPG Snowmass Meeting in 2005. That gathering marked the first opportunity for the Design Study participants to meet and interact for a protracted period, and it was the first meeting where the design had been captured completely in GEANT4, and made available for detailed study.

Since then the organization has expanded considerably. A series of Workshops has been conducted at Fermilab, SLAC, RAL, and Colorado, in addition to informational meetings conducted at the regional linear collider workshops at Vienna, Valencia, Beijing, Sendai, and Warsaw. The computing infrastructure developed for the ALCPG, org.lcsim, has been

adopted and expanded with new reconstruction codes, detector descriptions, and a repository of simulated data for detailed study. The Design Study has assembled several major documents leading up to the production of this Letter of Intent. In 2006, SiD produced a Detector Outline Document, followed the next year with major contributions to the Detector Concept Report. SiD also produced reports in 2007 to the Tracking, Calorimetry, and Vertex Detector Reviews which were organized by the World Wide Study.

Since its inception, the various SiD Working Groups have conducted regular meetings to monitor progress and organize activities. These meetings and the other Design Study activities are summarized on the SiD website: `http://silicondetector.org/display/SiD/home` . The meetings are of course open to all interested participants. From time to time, SiD has found it useful to organize SiD Collaboration Phone Meetings to discuss important issues when face-to-face meetings are inconvenient. These meetings are conducted on Webex.

The SiD Executive Board is ultimately responsible for making design and policy decisions for SiD, but it actively seeks input from the SiD Advisory Board, those attending SiD workshops, and the SiD Collaboration proper. Major decisions are reviewed by all SiD collaborators, and all voices are heard, before actions are taken.

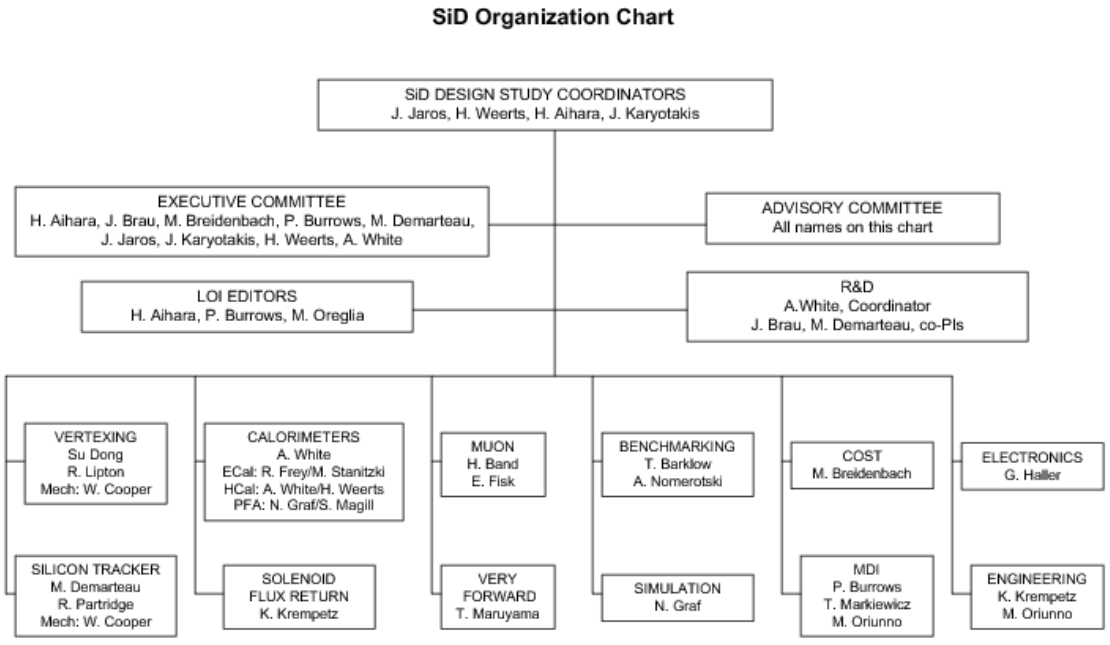

Figure 1.6: Organization chart for the Silicon Detector Design Study.

Besides the linear collider detector R&D support enjoyed by some SiD collaborators, SiD has received significant support from the US national laboratories ANL, FNAL, and SLAC, as well as Bristol, Imperial College, Oxford University, and the Rutherford Appleton Laboratory in the UK, and LAPP-Annecy in France. At the request of the US funding agencies, SiD (along with the other concepts) has recently taken on responsibility for organizing and presenting linear collider detector R&D proposals from US universities, and is optimistic that this support for linear collider detector R&D, well aligned with the needs of the concept, can grow.

References

[1] G. Moortgat-Pick et al. The role of polarized positrons and electrons in revealing fundamental interactions at the linear collider. *Phys. Rept.*, 460:131–243, 2005.

[2] N. Phinney, N. Toge and N. Walker Editors, *International Linear Collider Reference Design Report - Volume 3: Accelerator*, http://www.linearcollider.org/cms/?pid=1000437 (2007).

[3] S. Boogert et al., *Polarimeters and Energy Spectrometers for the ILC Beam Delivery System*, ILC-NOTE-2009-049.

[4] B. Aurand et al., *Executive Summary of the Workshop on Polarisation and Beam Energy Measurement at the ILC*, DESY-08-099, ILC-NOTE-2008-047, SLAC-PUB-13296 (2008); Workshop website is https://indico.desy.de/conferenceDisplay.py?confId=585.

[5] Mark Thomson. Particle flow calorimetry. *J. Phys. Conf. Ser.*, 110:092032, 2008.

[6] Mark A. Thomson. Progress with Particle Flow Calorimetry. 2007.

[7] D. Schulte. Study of electromagnetic and hadronic background in the interaction region of the TESLA Collider. DESY-TESLA-97-08.

[8] P. Chen, T. L. Barklow, and Michael Edward Peskin. Beamstrahlung and minijet background from gamma gamma collisions in linear colliders. Prepared for 2nd International Workshop on Physics and Experiments with Linear e+ e- Colliders, Waikoloa, Hawaii, 26-30 Apr 1993.

Chapter 2

Subsystems

2.1 Vertex and Tracking System

2.1.1 Introduction

The tracking system of the SiD detector uses a barrel-disk layout. Five cylindrical layers of pixel detectors surround the interaction point, complemented by four disks of pixel sensors on either end. These inner layers are followed by a set of five barrels of silicon strip sensors in the central region, capped by four nested disks of silicon strip sensors at both ends. To provide uniform hit coverage, three disks with pixel sensors are provided in the transition region between the inner and outer disks in both the forward and backward region.

Within the SiD detector concept the tracking system is regarded as an integrated tracking system. Although individual detector components can be identified in the vertexing and tracking system, the overall design is driven by the combined performance of the pixel detector at small radius, the outer strip detector at large radius and the electromagnetic calorimeter for the identification of minimum ionizing track stubs. The physics at the ILC requires good track reconstruction and particle identification for a wide array of topologies. The main elements for the pattern recognition are the highly pixellated vertex detector and the low occupancy outer strip detector.

Early track finding studies relied on identifying tracks in the vertex detector, where pattern recognition is simplified by the fact that precise three-dimensional information is available for each hit. Tracks found in the vertex detector are then propagated into the outer tracker, picking up additional hits. While good performance was achieved using this approach, an important class of events, notably highly boosted b-quarks, will decay at radii that do not allow for pattern recognition in the vertex detector alone. To provide additional flexibility, a more general tracking algorithm has been developed that can seed tracks using any three layers in the tracker, either from the outer tracker, the vertex detector or a combination of both. Tracks produced by the decay products of long-lived particles, however, can leave too few hits in the tracker to be reconstructed using only hits in the tracking volume. Obvious examples are long-lived particles such as K_s^0's and Λ's. The detector should also be

capable of detecting new physics signatures that would include long-lived exotic particles like those predicted by some gauge-mediated supersymmetry breaking scenarios. There are also issues of reconstructing kinked tracks produced by particles that lose a substantial portion of their energy in the tracker, as well as reconstructing backscatters from the calorimeter. To capture the tracks from these event topologies a calorimeter-assisted tracking algorithm has been employed. This algorithm uses the electromagnetic calorimeter to provide seeds for pattern recognition in the tracker. The very fine segmentation of the EM calorimeter allows for detection of traces left by minimum ionizing particles. These can be used to determine the track entry point, direction, and sometimes curvature with a precision sufficient for extrapolating the track back into the tracker. This set of complementary algorithms provides for very robust pattern recognition and track finding and it is the performance of this integrated tracking system that determines the overall physics reach of the detector. In this section the design and performance of the overall tracking system will be described. More details can be found in the companion documentation.

2.1.2 Vertex Detector Design

The vertex detector integrates with the outer tracker and remainder of the detector to provide significantly extended physics reach through superb vertex reconstruction – primary, secondary and tertiary. To date, all vertex detectors at collider experiments are silicon based, and the vertex detector for the SiD concept is no exception. The vertex detector consists of a central barrel section with five silicon pixel layers and forward and backward disk regions, each with four silicon pixel disks. Three silicon pixel disks at larger $\mid z \mid$ provide uniform coverage for the transition region between the vertex detector and the outer tracker. Barrel layers and disks are arranged to provide good hermeticity for $\cos\vartheta \leq 0.984$ and to guarantee good pattern recognition capability for charged tracking and excellent impact parameter resolution over the whole solid angle. A side-view of the vertex detector is shown in Fig. 2.1. For clarity, the silicon support structures have not been drawn in the right hand side of this figure.

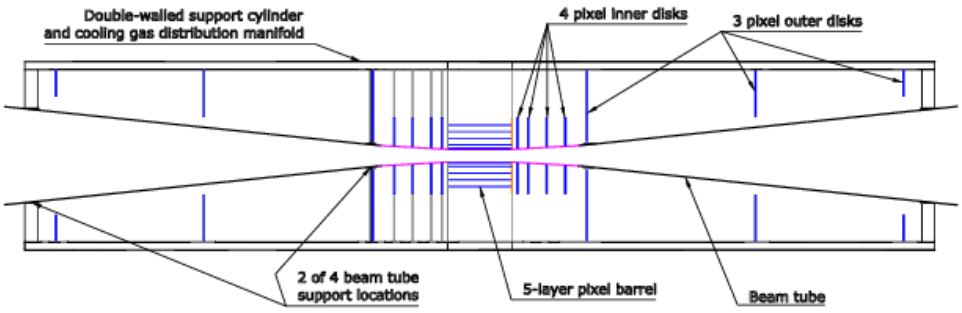

Figure 2.1: R-z view of the vertex detector. The right hand side has been drawn without the support structures.

Vertex detectors are generally plagued by a mismatch in thermal expansion coefficients between the silicon and its support structures. Moreover, these supports in general add to the material budget in a region of physics phase space where it is least desired. To

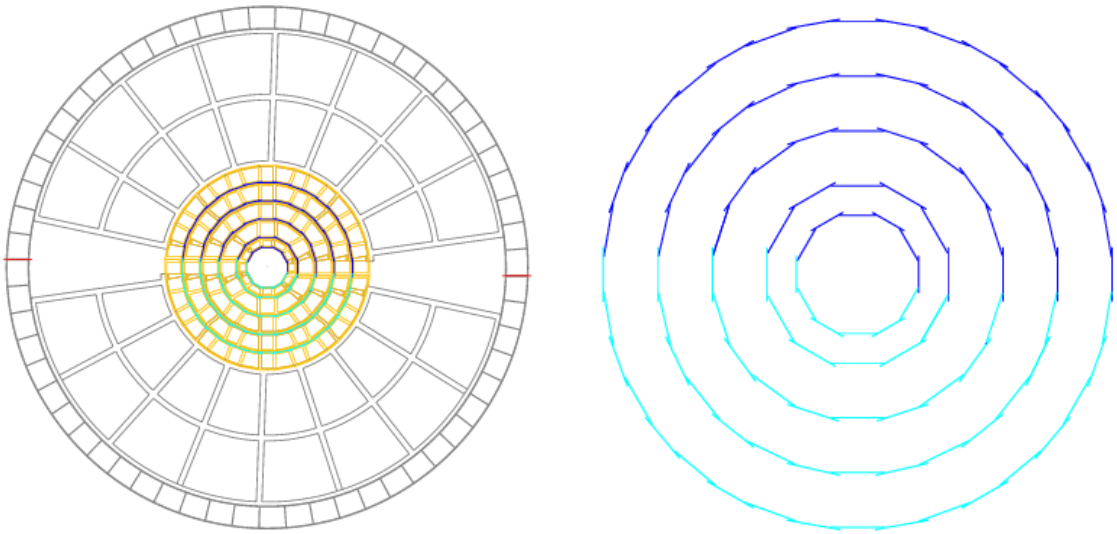

Figure 2.2: Barrel end view of the vertex detector (left) and layer arrangement of the silicon sensors only (right).

partially address those considerations, an 'all-silicon' structure is proposed for the vertex detector barrel. In this context, 'all-silicon' means that sensors of each barrel layer are joined along their edges with adhesive to approximate an arc of a circular cylinder, and no other structural materials are present in that limited region. Thermal distortions are reduced by limiting material to that of the sensors themselves and adhesive, which has a low elastic modulus relative to silicon. Longitudinal deflection of a layer is controlled by the cylindrical shape, thereby minimizing additional material. The quasi-cylindrical shape of a layer is maintained by annular, flat rings at each end. In turn, the end rings are joined to one another and connected to an outer support cylinder via web-like support disks. Though various possibilities are still under consideration for the end ring and support disk material, we would like a material, such as carbon fiber laminate or silicon-based foam, which has a longer radiation length than that of silicon. Because other materials than silicon are used for external mechanical connections, the term "all-silicon" is placed in quotes.

At this time, many sensor options remain under investigation and we have yet to choose a specific sensor technology. The design presented here makes the assumption, independent of sensor technology, that fabrication and assembly of the detector occur at room temperature and that the sensors are operated at a temperature $>$ -10 ^{0}C. Because sensors are used as a structural element and other material has been minimized, our design favors relatively thick sensors. The sensor thickness has been taken to be 75 μm. Sensor cut width is 8.68 mm in the innermost layer and 12.58 mm in all other layers. The cut sensor length for all layers is 125 mm.

To allow assembly about the beam pipe and later servicing, all barrels, disks, and support elements of the vertex detector are split about approximately the horizontal plane into top and bottom sub-assemblies. Once mated, the two sub-assemblies are supported from the beam pipe and stiffen the portion of the beam pipe passing through them. Fig. 2.2 is an

end view of the barrel region, showing the five silicon barrel layers and their spoked support disk. The outer rings indicate the double-walled carbon fiber support tube. Since the silicon is very thin on the scale of this drawing, the layer arrangement of the individual sensors is shown in the right drawing in Fig. 2.2 for clarity.

The five layers are arranged at radii ranging from 14 to 60 mm. The vertex detector also has four disk layer sensors which are attached to carbon fiber support disks at z positions ranging from about 72 to 172 mm. The innermost disk covers radii from 14 mm out to 71 mm; the outermost, from 20 mm to 71 mm. Forward tracking continues beyond the vertex detector proper with three additional small pixel disks, extending in z from about 207 to 834 mm. Their inner radii range from 29 to about 117 mm, and their outer radius is about 166 mm.

The beam pipe through the central portion of the vertex detector has been taken to be all-beryllium. Within the barrel region of the vertex detector, the beryllium beam pipe has been taken to be a straight cylinder with inner radius of 1.2 cm and a wall thickness of 0.04 cm. At $z = \pm 6.25$ cm, a transition is made to a conical beam pipe with a wall thickness of 0.07 cm. The half angle of the cone is 3.266^o. Transitions from beryllium to stainless steel are made beyond the tracking volume, at approximately $z = \pm 20.5$ cm. The initial stainless steel wall thickness is 0.107 cm; it increases to 0.15 cm at approximately $z = \pm 120$ cm. The half angle of the stainless steel cone is $5.329°$. The inner profile of the beam pipe is dictated by the need to avoid the envelope of beam-strahlung produced e^+e^--pairs.

To prevent bending of the small-radius portion of the beam pipe and ensure good stability of vertex detector position, the outer vertex detector support cylinder is coupled to the beam pipe at four longitudinal locations: ± 21.4 and ± 88.2 cm. Inner and outer support cylinder walls are 0.26 mm thick. They are made from four plies of high modulus carbon fiber, resin pre-preg. Wall separation is 15 mm. We propose to deliver cooling air via the vertex detector outer support cylinder. To allow that, the two walls of the cylinder would be separated by radially-oriented ribs running the full cylinder length. Calculations assumed ribs at 60 azimuths. Openings, each approximately 12.2 mm x 15 mm, at 18 z-locations in the inner cylinder wall distribute flow to the various disk locations and to the barrel.

During silicon servicing, the vertex detector and beam pipe remain fixed while the outer silicon tracker rolls longitudinally (see Fig. 2.3). To allow that motion, to enable placement of the outer silicon tracker elements at the smallest possible radius, and to leave space for any additional thermal insulation which might be needed, the outer radius of the vertex detector, including its support structures, has been limited to 18.5 cm. To maximize physics potential, the inner radius of vertex detector elements has been chosen to be as small as practical consistent with beam-related backgrounds and the beam pipe profile. In the barrel region, the minimum radius to a sensor surface is 1.4 cm, governed by the beam backgrounds as discussed earlier.

The number of radiation lengths represented by vertex detector structures, averaged over φ in most cases, and the vertex detector hit pattern are shown in Fig. 2.4. Shown are the contributions of the individual subdetectors to the total number of hits on a particle track with infinite momentum. The irregular features correspond to the transition regions. Overall there are more than five pixel hits on a particle trajectory down to angles of about 10°.

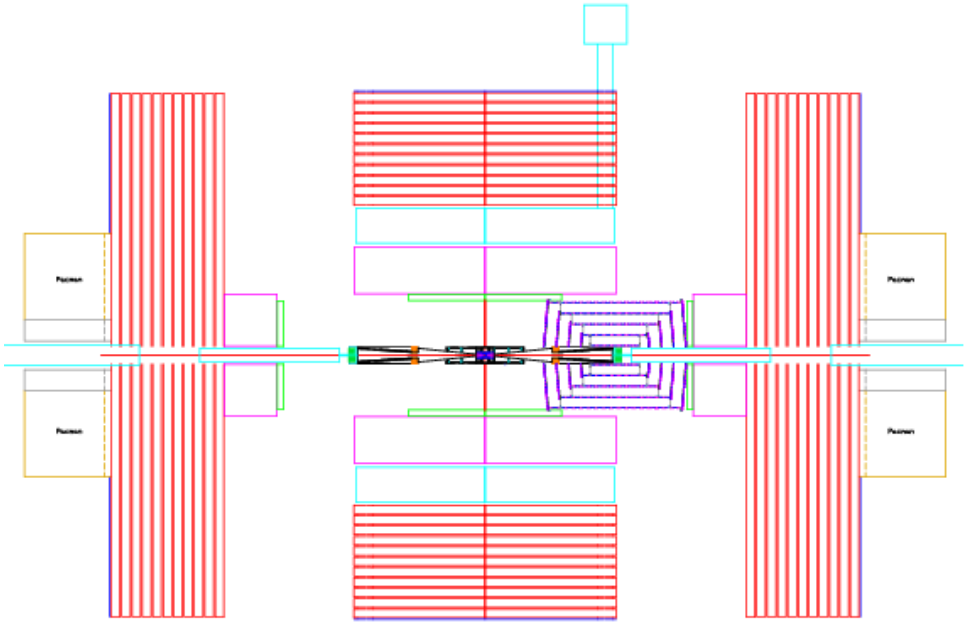

Figure 2.3: Tracker in the open position for servicing of the vertex detector.

The irregular features of the readout and service contributions to the material budget are due to discrete elements at the end of the sensors. Most of the readout material is beyond the first few layers of the vertex detector, so that their influence on the impact parameter resolution is limited. The fact that the amount of material in these elements is comparable to that of the sensors or mechanical supports calls for close attention to the design of low mass power delivery and signal transmission components. If the readout and service material can indeed meet what is in the current model, the material balance would be more favorable for a considerable portion of the endcap region compared to the $1/\sin\vartheta$ growth for a long barrel geometry. With this material balance, the benefit of the endcap geometry in spatial resolution with a better track entrance angle and smaller radial alignment effect, is a meaningful advantage. Table 2.1 summarizes the main parameters of the vertex detector.

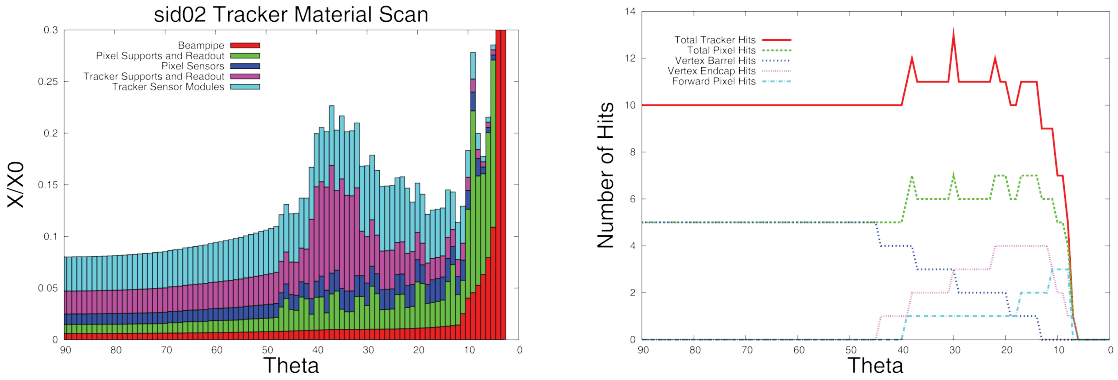

Figure 2.4: Material budget of the tracking system (left) and number of hit layers in the tracking system as a function of polar angle (right).

Barrel Region	R (mm)	Length (mm)	Number of sensors in φ
Layer 1	14	125	12
Layer 2	21	125	12
Layer 3	34	125	20
Layer 4	47	125	28
Layer 5	60	125	36
Disk	R_{inner}	R_{outer}	z_{center}
Disk 1	15	75	76
Disk 2	16	75	95
Disk 3	18	75	125
Disk 4	21	75	180
Forward Disk	R_{inner}	R_{outer}	z_{center}
Disk 1	28	166	211
Disk 2	76	166	543
Disk 3	118	166	834

Table 2.1: Parameters of the vertex detector. Units are mm.

2.1.3 Tracker Design

The ILC experiments demand tracking systems unlike any previously envisioned. In addition to efficient and robust track-finding, the momentum resolution required to enable precision physics at ILC energies must improve significantly upon that of previous trackers. The design must minimize material in front of the calorimeter that might endanger particle-flow jet reconstruction. Even with the largest feasible magnetic field, the tracking volume is quite large so that tracker components must be relatively inexpensive and easily mass-produced. Finally, the tracker must be robust against beam-related accidents and aging. These requirements have led to the choice of silicon microstrip detectors for the tracker. The outer silicon tracker design consists of five nested barrels in the central region and four cones in each of the end regions. The support material of disks follows a conical surface with an angle of 5-degrees with respect to the normal to the beamline. Sensors on the disk modules are normal to the beam line. The barrel supports are continuous cylinders formed from a sandwich of pre-impregnated carbon fiber composite around a Rohacell core. The support cones are also double-walled carbon fiber structures around a Rohacell core. Each support cone is supported off a barrel. Spoked annular rings support the ends of each barrel cylinder from the inner surface of the next barrel out. It is expected that openings will be cut in the support structures to reduce material, once module mounting locations are known. These openings not only reduce the number of radiation lengths, but also reduce the weight to be supported. Openings may also be needed for an optical alignment system. It is envisioned that the electronics and power cables that supply entire segments of the detector are mounted

on these spoked rings. The dimensions of the barrels and cones are given in Table 2.2. Fig. 2.5 shows an elevation view of the tracking system.

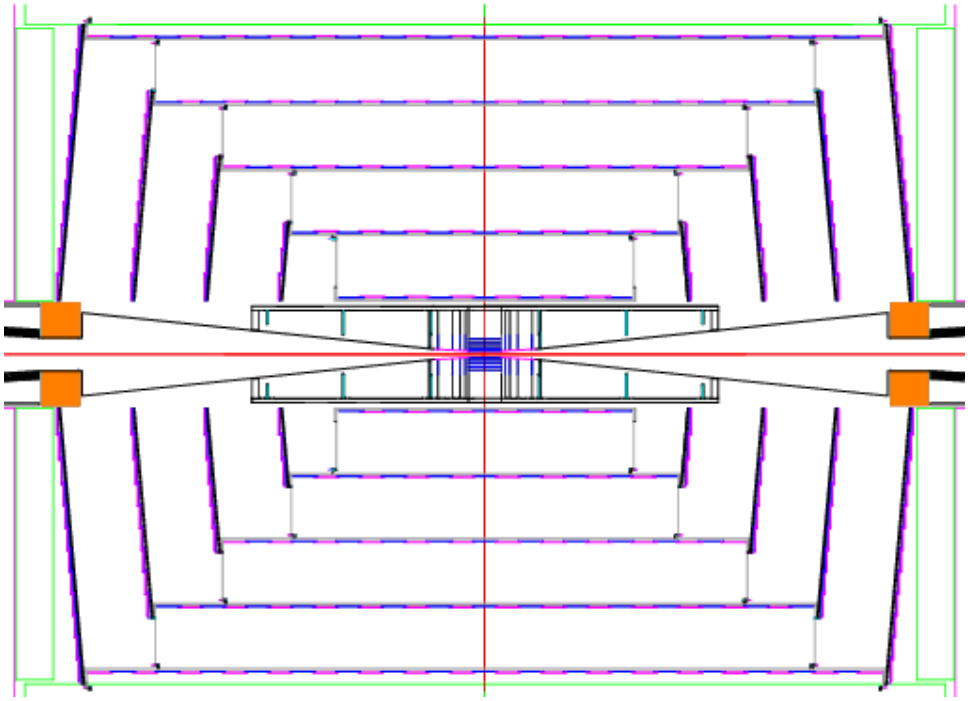

Figure 2.5: R-z view of the whole tracking system.

Because of the very low occupancies in the outer barrel, the nominal design for the outer tracker employs only axial readout in the barrel region. In the baseline design, the barrels are covered with silicon modules. Modules are comprised of a carbon fiber composite frame with rohacell/epoxy cross bracing and have one single-sided silicon sensor bonded to the outer surface. Sensors are obtained from one single 6-inch wafer and are approximately 10 cm $\times$ 10 cm. This size sets the longitudinal readout segmentation of the barrel detectors. The sensors are 300μm thick with a readout pitch of 50 μm and intermediate strips. Full coverage is obtained by ensuring small overlap both longitudinally and azimuthally. Azimuthal overlap is obtained by slightly tilting the sensors. The angle by which the sensor is tilted partially compensates for the Lorentz angle of the collected charge in the 5T field of the solenoid. Longitudinal overlap is obtained by placing alternate sensors at slightly different radii.

Modules are attached to the cylinder using a PEEK (Poly Ether Ether Ketone) mounting clip. The readout chips and cables are mounted directly to the outer surface of the silicon sensors. The cables supply power and control to the readout chip from electronics located at the ends of the barrel.

Fig. 2.6 shows an Rφ-view of the barrel region. The outermost disk is projected onto the barrel layout in this figure. For pattern recognition in the disks, small angle stereo will provide 3d-space points. The current design has two single-sided wedge detectors back-to-back, with strips at $\pm 6^\circ$ with respect to the long axis of the wedge for a stereo angle of 12°. Please note that in Fig. 2.4 the hits from a pair of sensors, corresponding to one 3d-space point, is represented as one hit. Two types of sensors are needed to tile the disks, one type

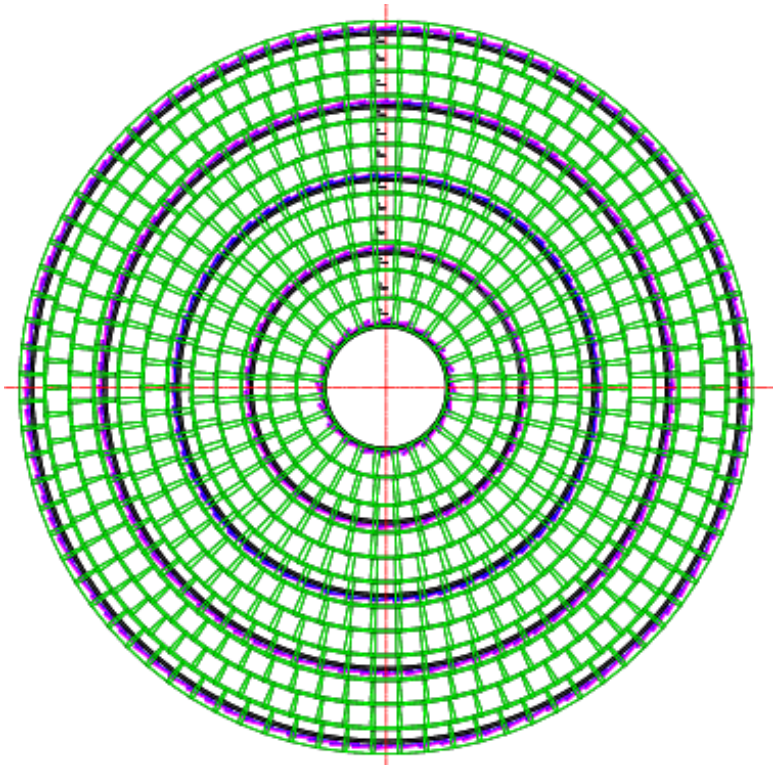

Figure 2.6: Rφ projection view of the tracker barrels and disks.

at the inner radii and a second sensor type to populate the area at the outer radii. Also in the forward region sensors will be 300μm thick with intermediate strips. The conical support disk design ("lampshade design") provides an elegant way to implement module overlaps, eliminating any dead areas, and allows for easy module mounting and cable routing.

The inner radius of the outer tracker is set by forward, beam-monitoring calorimetry and beamline elements, over which the tracker is intended to slide. Once the tracker inner radius is set, the outer radius of vertex detector structures follows. During servicing, the vertex detector and beam pipe remain fixed while the outer silicon tracker rolls longitudinally, as shown in Figure 2.3. To allow that motion, no element from the outer tracker can be at a radius smaller than the radius of the vertex detector outer support cylinder. To allow for good acceptance and pattern recognition, the small angle region is covered by three small silicon disks at each end with radius below 20 cm, which has been described in the section on the mechanical layout of the vertex detector. Figure 2.4 shows the cumulative amount of material as a function of polar angle as modeled in the Monte Carlo. The lowest curve shows the contribution from the beampipe followed by the contribution of the support and readout structures for the pixel detector. The material corresponding to the various readout elements has conservatively been assumed to be uniformly distributed in the tracker volume. The next curve indicates the material due to the active vertex detector elements. The outer two curves give the amount of material of the tracker supports and readouts and the silicon modules, respectively. It should be noted that the material corresponding to the silicon modules includes the module supports in addition to the silicon.

Overall a material budget of about 0.8% X_0 per layer is achieved for the outer tracker. Table 2.2 lists some of the parameters of the tracker for the current design. There are 8130 modules in the barrel region and 2848 modules for the end regions combined.

Barrel Region	$\langle R \rangle$ (cm)	Length of sensor coverage (cm)	Number of modules in φ	Number of modules in z
Barrel 1	21.95	111.6	20	13
Barrel 2	46.95	147.3	38	17
Barrel 3	71.95	200.1	58	23
Barrel 4	96.95	251.8	80	29
Barrel 5	121.95	304.5	102	35
Disk Region	z_{inner} (cm)	R_{inner} (cm)	R_{outer} (cm)	Number of modules per end
Disk 1	78.89	20.89	49.80	96
Disk 2	107.50	20.89	75.14	238
Disk 3	135.55	20.89	100.31	428
Disk 4	164.09	20.89	125.36	662

Table 2.2: Parameters of the tracking detector.

The central component of the readout architecture proposed for the SiD tracker is the 1024-channel KPiX readout chip. The KPiX chip is designed for pulsed power, minimizing the input current between bunch trains. This reduces the power consumption to 20 mW on average for a 1024-channel KPiX chip, or 40 mW for a single-sided module allowing for gas cooling of the tracker. The chip has four time-stamped analog buffers per channel that store signals from the detector until the inter-train period for digitization and readout. As a result, the only digital activities on KPiX during the bunch train are a synchronous LVDS clock and individual comparators firing when a channel crosses the readout thresholds. This low-noise mode of operation during the bunch train allows KPiX to be mounted directly to the sensor without inducing large RF pickup on the strips.

2.1.4 Simulation Infrastructure

The vertex detector and tracker designs have been incorporated in the compact *xml* detector description that drives our simulation studies. This detector description serves as an input both to *slic.org*, the GEANT4-based detector simulation used by SiD, as well as the event reconstruction software.

The current detector description includes both the active sensing elements, as well as our estimates of the dead material required to provide mechanical support, beam tube, readout electronics, and required services (including power and cooling). For the tracking studies reported here, the barrel sensors have been approximated by thin cylinders, while the

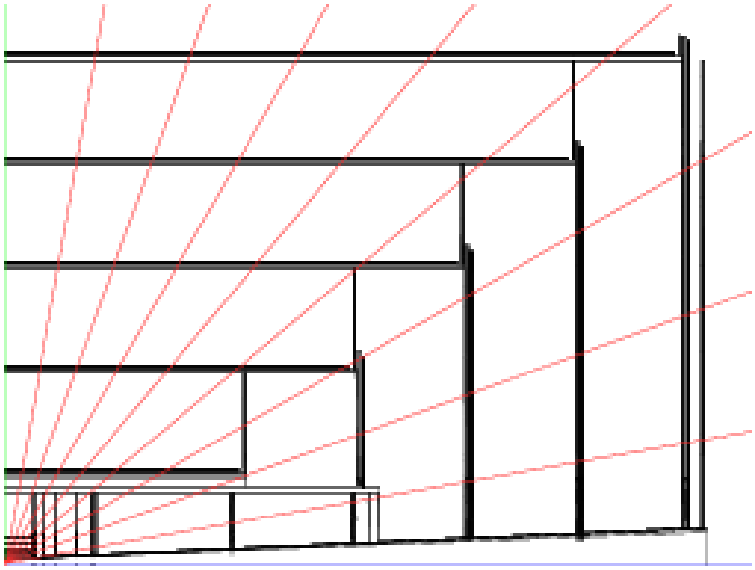

Figure 2.7: R-z view of the simplified tracking system as implemented in SiD02.

disk sensors have been approximated by planar disks perpendicular to the beamline. The dead material is modeled as a cylinder, planar disk, or cone as appropriate. Fig. 2.7 shows an x-y quarter view of the tracking system as implemented in this simplified geometry. This model has also been used to simulate the detector response for the large number of events generated for the physics benchmarking.

We have also developed a fully detailed tracker description that closely matches the engineering designs. It incorporates each individual sensor as a planar device with its mounting hardware. The fully segmented tracker description provides a highly realistic model of the tracker geometry, allowing us to study the effects of sensor overlaps and gaps, sensor mis-alignment, support material and more generally improve the precision of our detector modeling. Having the complete geometry fully defined and configurable at runtime (using a plain-text file), and immediately available to the reconstruction software, provides enormous flexibility to the design and optimization process.

We do not include the individual pixels and strips in the GEANT4 simulation, preferring to defer this to the reconstruction stage. Instead, we store the full Monte Carlo information about the particle's interaction with the sensitive sensor material (e.g. track ID, deposited energy, time, position). Hit digitization is the process of transforming these GEANT4 energy deposits into strip and pixel charge depositions, and then clustering these charge depositions to form tracker hits. This allows us to study different readout configurations without the overhead of having to rerun the full simulation.

2.1.5 Track Reconstruction

The standard pattern recognition algorithm developed by SiD is designed to efficiently find tracks using pixel and strip hits in the tracker. The pattern recognition algorithm treats the tracker as a single integrated device that is "agnostic" as to the origin of the hits (pixel or strip, barrel or endcap). This approach provides uniform pattern recognition throughout the tracking volume, effortlessly handling transitions between the different parts of the detector. Typically, 6-7 hits are sufficient for finding a track, which allows the standard pattern recognition algorithm to efficiently track particles originating near the interaction point with $p_T > 200$ MeV.

Since pattern recognition is of utmost importance in a sparse hit environment, additional track finding algorithms are explored. Of particular note is the calorimeter assisted track finder, which uses the tracking capability of the electromagnetic calorimeter to associate hits in the outer tracker with calorimeter "track stubs". Calorimeter assisted tracking is particularly well suited to reconstructing tracks that originate outside the vertex detector, as often occurs in K_s and Λ decays. Both the standard pattern recognition and calorimeter assisted tracking algorithm are described below.

2.1.5.1 Standard Pattern Recognition Algorithm

The standard pattern recognition algorithm is explicitly designed for the task of optimizing the design of an all-silicon tracker. Variations in tracker geometry and layout can be easily studied with no change to the software. The algorithm bases all its decisions on a global χ^2. A high level of user control over the tracking "strategies" is available if desired, but more typically a "strategy builder" tool is used to automate the process of developing an optimized set of strategies for a given detector configuration.

The first step in track finding is to convert the digitized hits into a common hit format. This format encapsulates all the information needed by the standard pattern recognition algorithm, while insulating the track finding from differences and changes in the digitization algorithms.

Three types of hits are supported: pixel hits that have two measured coordinates, axial strip hits that have one measured coordinate and one bounded coordinate, and stereo hits formed from a pair of strip hits. The pixel and stereo hits may be associated with either barrel or disk geometries, while the axial strip hits have the bounded coordinate parallel to the beam axis and are intrinsically associated with barrel geometries. One further limitation is placed on stereo hits: the planes of the two strip sensors must be parallel to each other.

Track finding is controlled by a set of strategies. A strategy consists of the list of detector layers to be used, the role of each layer (seed, confirm, or extend), kinematic constraints (p_T, impact parameters), requirements on the number of hits, and the χ^2 cut. Multiple strategies can be processed by the track finding algorithm, and the resulting tracks are the collection of all distinct tracks found. The set of strategies is contained in an *xml* file that is easily understood and can be viewed/edited with a text editor.

The track finding algorithm is exhaustive in the sense that all combinations of hits that could potentially lead to a successful track fit are considered. The algorithm proceeds in four steps:

1. The first step is to form a 3-hit track seed candidate by taking all 3-hit combinations possible among the 3 seed layers. A helix fit is performed on the seed candidate, and those seeds that fail the χ^2 cut are eliminated.

2. The second step tries to "confirm" the seed by adding additional hit(s) from the confirm layer(s). A helix fit is performed on the new seeds and those that fail the χ^2 cut are eliminated. Typically, it is found that good performance is achieved with one confirmation layer.

3. The third step seeks to "extend" a confirmed seed by trying to add additional hits from the extend layers. Each time a new hit is considered, a helix fit is performed and the hit is discarded if it fails the χ^2 cut. If no hits in a given extend layer give a satisfactory helix fit, then the original track seed is kept and the next extend layer is tried.

4. Track seeds that meet the strategy's requirement on the minimum number of hits are merged to form a list of distinct tracks. Two track candidates are allowed to share a single hit, but if a track candidate shares more than one hit with another candidate, an arbitration scheme is used to select the better candidate. Precedence is given to the candidate with the greatest number of hits, while the candidate with smaller χ^2 is selected when the number of hits is equal.

Consistency checks and hit sorting algorithms are used to minimize the number of helix fits performed, substantially improving the performance of the algorithm. Furthermore, a "bad hit χ^2" cut is used to identify track candidates with an outlier hit and allows preference to be given to track candidates without an outlier hit.

A key component of the pattern recognition algorithm is a fast helix fitter. The helix fitter takes as input 3 or more tracker hits. The hits can be any combination of pixel, axial strip, or stereo hits in the barrel and/or endcap detectors. The fitter is the one place in the tracking code that distinguishes between the various types of hits. The fast fitter is used to estimate the helix parameters and helix fit χ^2. First, a circle fit to the x,y coordinates of all hits is performed using the Karimäki algorithm to determine the helix parameters ω, ϕ_0, and d_0. If there are two or more pixel/stereo hits, then a line fit in the $s-z$ plane is used to determine the z_0 and $\tan\lambda$ helix parameters. In order to provide full helix fits for the case where there are fewer than two pixel/stereo hits, a new fitting algorithm was developed.

While an axial strip does not measure the z coordinate, it has well defined bounds that impose the constraint $z_{min} < z < z_{max}$. These bounds lead to each axial strip having an allowed band in the z_0-$\tan\lambda$ plane. For two or more axial strips, the intersection of these bands will produce a polygonal allowed region, the centroid of which is taken to be the measured values for z_0 and $\tan\lambda$. If there is no region of intersection, the hits are inconsistent with being from a helix and the fit fails. For the case of a single pixel/stereo hit, the pixel/stereo hit is treated like a very short strip and the above algorithm is used.

For all but the highest momentum particles, the multiple scattering errors will exceed the intrinsic hit resolution. Multiple scattering errors for both the active and dead materials are estimated and included in the helix fit. Correlations in the multiple scattering errors are ignored, leading to an under-estimate of the helix parameter errors by a factor of ≈ 1.5. For stereo hits, full account is taken for the separation between the two stereo layers in the calculation of both the hit position and hit covariance matrix.

The performance of the standard pattern recognition algorithm is shown in the section on tracker performance and is also reflected in the benchmarking studies. Unless otherwise noted, the tracking strategies require 1 confirmation hit, a total of at least 7 hits (6 hits for barrel-only tracks), $p_T > 0.2$ GeV, xy distance of closest approach $d_0 < 10$ mm, and distance of closest approach along the beam direction $z_0 < 10$ mm.

2.1.5.2 Calorimeter-Assisted Tracking

The development of the calorimeter assisted track finding algorithm was primarily motivated by the need to reconstruct non-prompt tracks and long-lived particles in the SiD detector. As will be shown later, the standard track finding algorithm achieves excellent efficiency in reconstructing prompt tracks that originate close to the interaction point. However, using the same algorithm for finding non-prompt tracks is difficult because those tracks often do not produce enough hits in the vertex detector to seed the track finder, and creating seeds from 3-hit combinations in outer layers without limiting combinatorics by constraining the track origin to the interaction region can be problematic.

The calorimeter assisted tracking solves the problem by seeding the track finder from traces left by charged particles in the electromagnetic calorimeter - so called MIP stubs. The standard SiD track finder is run first, and the found tracks are then propagated through the calorimeter. Clusters are created and attached to the tracks. After that, topological clustering is applied to the remaining calorimeter hits. Those of the created clusters that include hits in inner electromagnetic calorimeter layers are analyzed for consistency with being produced by minimum ionizing particles. Clusters that pass the test are converted into track seeds that contain information about the track position and direction at the calorimeter entry point. Depending on the MIP stub quality, the seed can also contain a track curvature estimate. The seeds are propagated back into the tracker, picking up hits that are not attached to any existing tracks. The search window in each tracker layer is calculated based on the trajectory parameters uncertainties, and the track parameters are re-evaluated after attaching every new hit. If more than one hit can be attached to the track in a certain layer, multiple track candidates are created. Once all seeds have been processed, the newly created tracks are rated based on quality, and duplicates are removed. This algorithm is essential for reconstructing all kinds of non-prompt tracks - K_s^0 and Λ decay products, new physics signatures that might include long-lived particles, kinked tracks, and calorimeter backscatters. It also performs high purity, topologically linked initial clustering in the calorimeter, and associates clusters with tracks.

2.1.5.3 Track Fitting

The track fitting results presented here use the fast helix finder described before. Two more precise approaches to track fitting have been developed by SiD. The first of these is based on a track fitting algorithm originally used by SLD and used in previous studies of the performance of the SiD tracking system. It solves minimization equations for χ^2, calculated from the matrix of residual weights. This weight matrix takes into account multiple scattering derived from the amount of material passed by a track, correlations between track deviations in the subsequent detector layers and independent measurement errors due to the sensors spatial resolution. Solving the matrix equation for 5 track parameters gives the parameter values corresponding to the best fit; the inverse of the weight matrix of the parameters gives the covariance matrix of parameter errors. Comparison of the expected parameter errors derived from the covariance matrix with real track parameter residual distributions shows agreement to within a few percent. This fitter may be slow for a large number of layers, as it requires a matrix inversion with a matrix dimension equal to the number of layers. For the SiD concept, however, it works fine as total number of layers crossed by a track rarely exceeds 10. A Kalman filter, which treats multiple scattering close to optimally, is under development and updated results using that Kalman filter will be presented at a later time. The Kalman filter will be used as a final fitter to refit tracks that are currently fitted by the simple fitter.

2.1.6 Tracking Performance

In this section the performance of the vertex and tracking detector will be described, along with its associated track-parameter fitter. The goal of these studies is to evaluate the overall performance of the SiD tracking system with the most realistic simulation available. The standard tracking algorithm was tuned for the benchmark processing to find tracks having $p_T > 0.2$ GeV that originate from near the interaction region. The strategies used generally required at least 7 hits to be associated with a track. An additional strategy that required 6 barrel hits in the vertex detector and first layer of the outer tracker was put in place to provide low-p_T coverage for central tracks that may not pass through 7 different layers before curling back around. Additionally, for the benchmark processing the strategies placed a 1 cm constraint on the x-y and z distances of closest approach.

We can break down tracking efficiency into two parts: (1) the fraction of Monte Carlo charged particles that are in principle "findable" given the set of strategies used, and (2) the track reconstruction efficiency for the findable tracks. The starting point for the tracking efficiency measurement is the set of long-lived charged particles identified as being "final state particles" by the event generator. Final state particles include short-lived particle decay products (e.g. $\pi^{\pm}$ from $K_S \to \pi^+\pi^-$), but does not include long-lived particle decay products (e.g. $\pi^{\pm}$ decay products) or secondaries produced by GEANT as the result of interactions in the detector.

Among the final state particles in $e^+e^- \to t\bar{t}$ collisions at $\sqrt{s} = 500$ GeV, 6.5% of the tracks are below the 0.2 GeV p_T cutoff in the standard tracking algorithm. Of the tracks satisfying the p_T constraint, 9.1% of the tracks have fewer than 6 hits, which is the

Selection	Selection Efficiency	Cumulative Efficiency
All Tracks	-	100%
$p_T \geq 0.2$ GeV	$(93.54 \pm 0.11)\%$	$(93.54 \pm 0.11)\%$
$N_{hit} \geq 6$	$(90.91 \pm 0.13)\%$	$(85.04 \pm 0.16)\%$
Seed Hits Present	$(99.78 \pm 0.02)\%$	$(84.85 \pm 0.17)\%$
Confirm Hit Present	$(99.95 \pm 0.01)\%$	$(84.84 \pm 0.17)\%$
$\lvert d_0 \rvert \leq 1$ cm	$(99.80 \pm 0.02)\%$	$(84.65 \pm 0.17)\%$
$\lvert z_0 \rvert \leq 1$ cm	$(99.69 \pm 0.03)\%$	$(84.39 \pm 0.17)\%$
Track Reconstruction	$(99.32 \pm 0.04)\%$	$(83.81 \pm 0.17)\%$

Table 2.3: Fraction of findable tracks

minimum number of hits for the standard tracking algorithm. Some of these tracks are from sources, such as K_s decay, that are potentially recoverable by the calorimeter assisted tracking algorithm. Findable tracks must also satisfy the requirements for having seed and confirmation hits and satisfy the 1 cm constraint on the x-y (d_0) and z (z_0) distances of closest approach. Taken together, 84.4% of the final state particles are findable by the standard tracking algorithm. The breakdown of these contributions to the findable track efficiency can be found in Table 2.3.

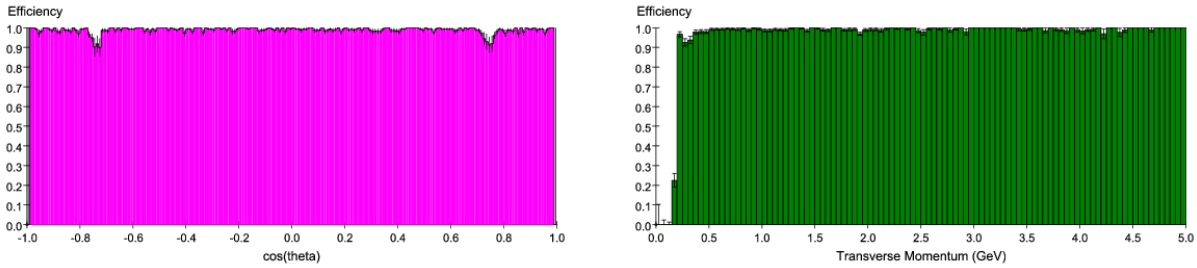

Figure 2.8: Track finding efficiency as a function of track $\cos\vartheta$ (left) and p_T (right).

The track reconstruction efficiency measures the fraction of findable tracks that are found by the standard tracking algorithm. Using the sample described above, the track reconstruction efficiency is found to be 99.3%. Fig. 2.8 shows the efficiency as a function of $\cos\vartheta$ and p_T. The track finding efficiency drops in the transition region between barrels and disks. Fig. 2.9 shows the efficiency as function of $\cos\vartheta$ for two p_T bins. The left plot is for tracks with $p_T < 500$ MeV and the right plot is for tracks with $p_T > 500$ MeV. All the inefficiency is due to low momentum tracks in this transition region. It is thought that the inefficiency is due to tracks just beyond the pixel barrel acceptance that curl by more than 180 degrees before they get to the seed layers that cover this acceptance region. As such, this may be an artifact of the current tracking algorithm and could be improved upon.

Tracking algorithms must balance track finding efficiency against the probability of finding "fake tracks" that are not associated with a Monte Carlo particle. A key indicator

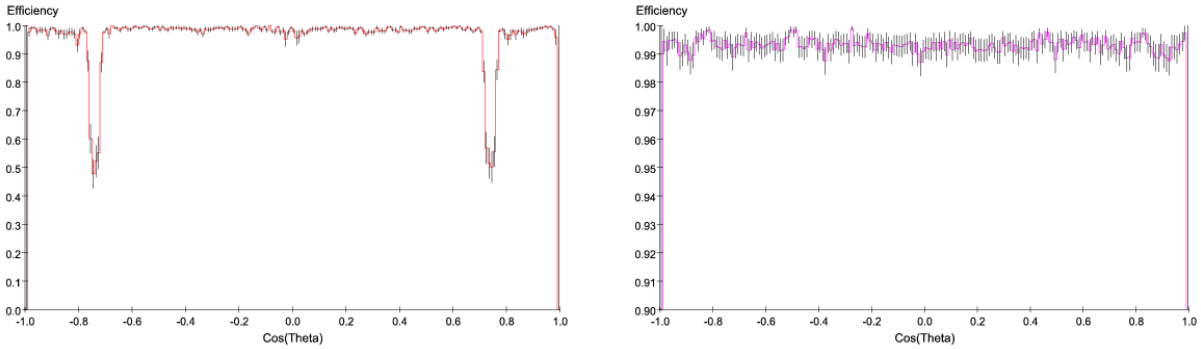

Figure 2.9: Track finding efficiency as a function of track $\cos\vartheta$ for tracks with $p_T < 500$ MeV (left) and $p_T > 500$ MeV (right). Please note the different vertical scales in the two figures.

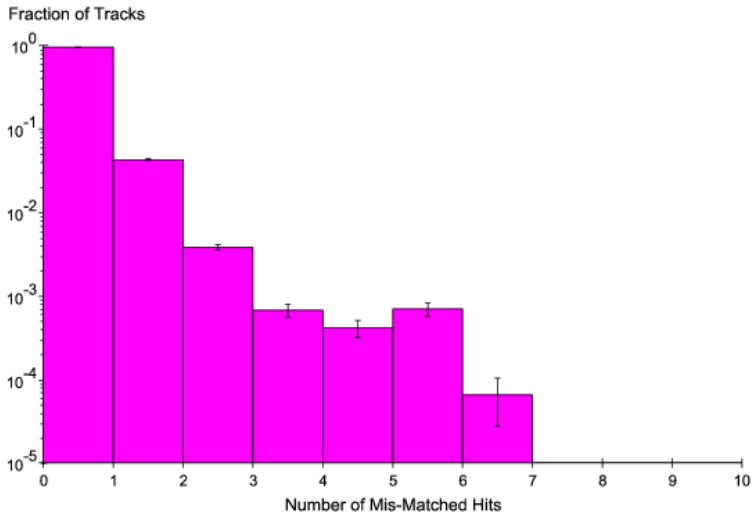

Figure 2.10: Fraction of tracks versus the number of mis-assigned hits.

for the number of fake tracks is the number of mis-assigned hits on a track. These hits are generated by a different Monte Carlo particle than the one with the preponderance of hits on the track. More than 99% of tracks have at most one wrong hit on the track, as seen from Fig. 2.10. Fake tracks, where no single Monte Carlo particle is responsible for the majority of hits, make up only 0.07% of the tracks found.

The momentum resolution of the tracker is shown in the top plot in Fig. 2.11 as a function of momentum for various track angles. The bottom figure shows the impact parameter resolution for various track angles. An impact parameter resolution of 4 μm is obtained in the high momentum limit.

How the tracking performs in higher occupancy environments is summarized in Fig. 2.12. Two studies have been carried out. First, the performance of the track finder has been studied in the environment of dense jets. The plot in the upper left corner in Fig. 2.12 shows

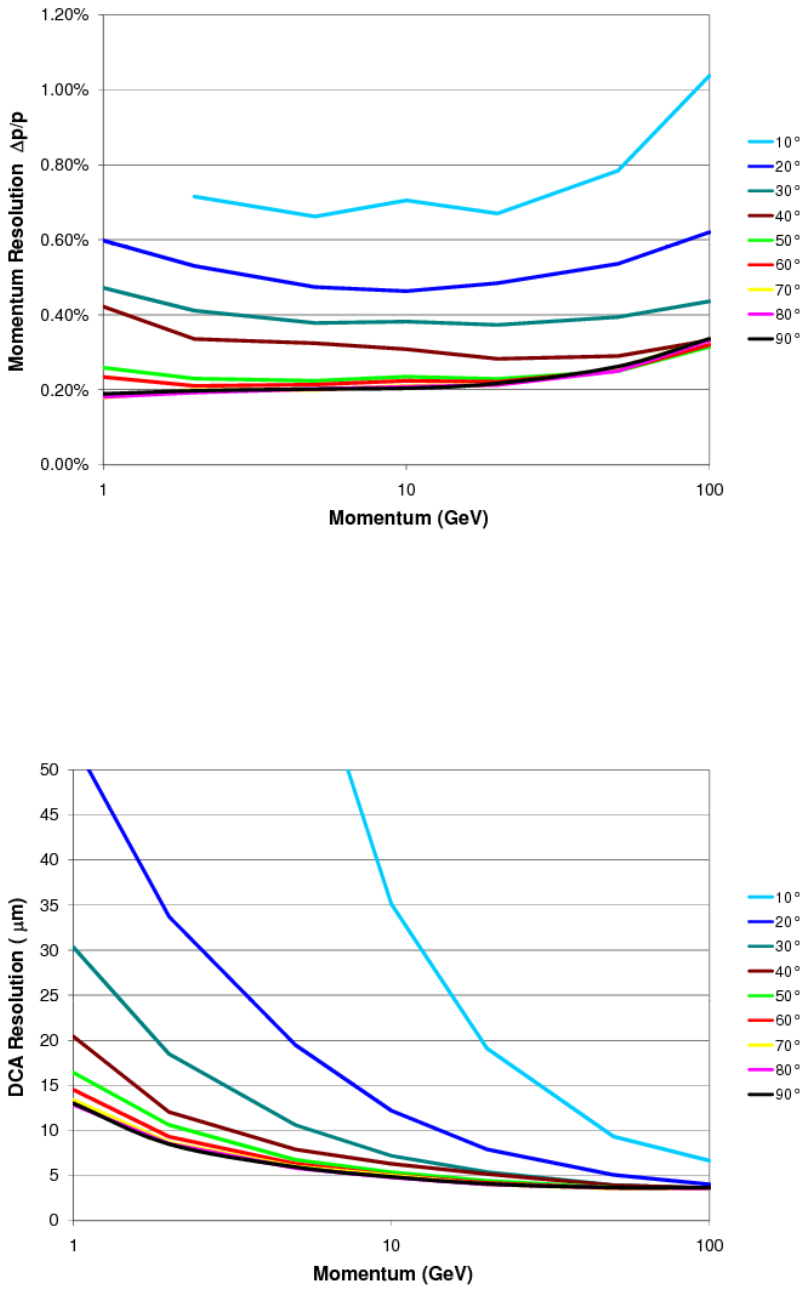

Figure 2.11: Resolution in momentum (top) and $r - \varphi$ distance of closest approach, DCA (bottom), as function of track momentum at various angles.

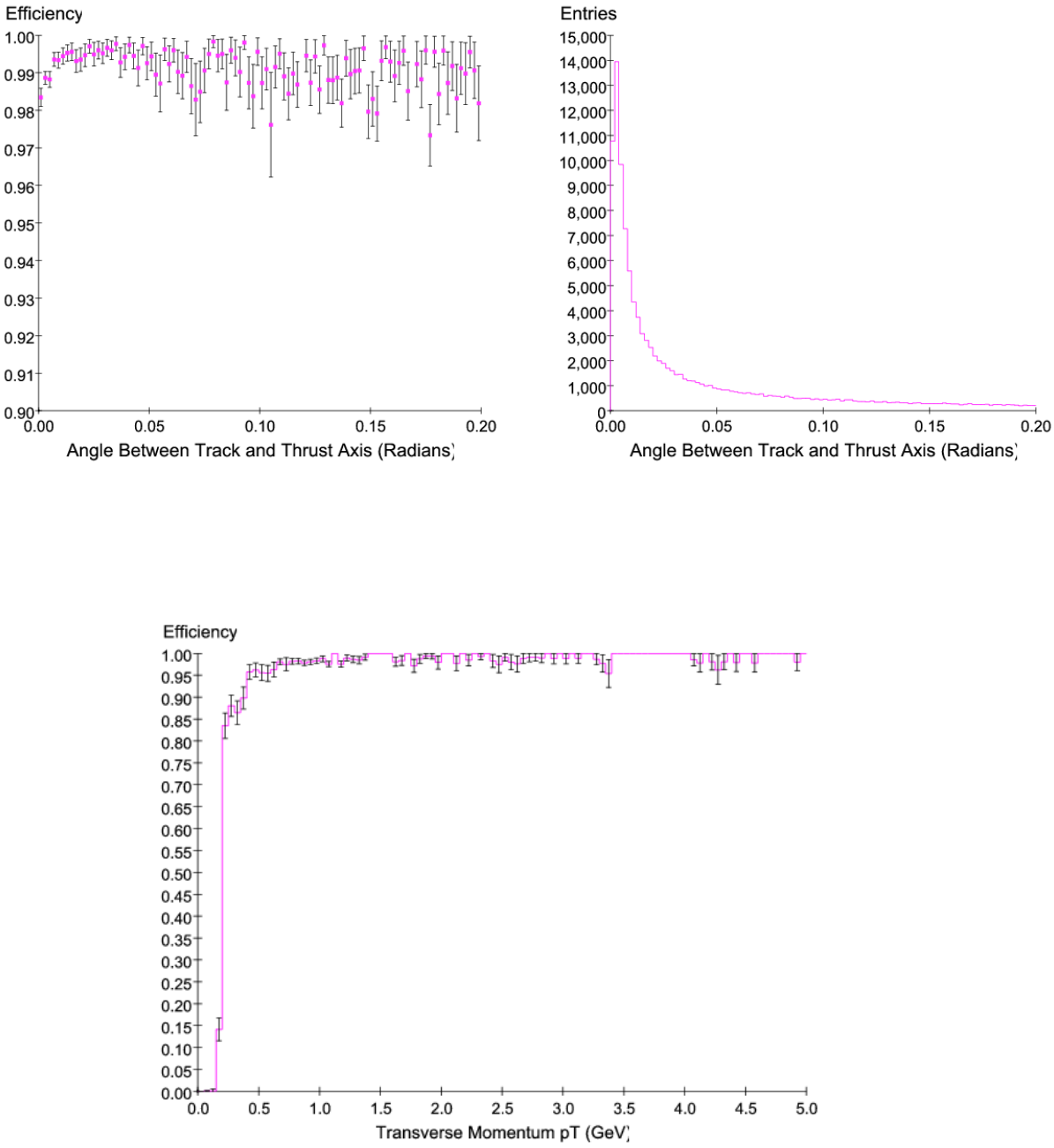

Figure 2.12: Tracking efficiency as function of α (upper left) and distribution in α (upper right) for $e^+e^- \to q\bar{q}$ events at $\sqrt{s} = 1$ TeV. The bottom figure shows the tracking efficiency for $e^+e^- \to b\bar{b}$ events at $\sqrt{s} = 500$ GeV with the background from 10 bunch crossings overlaid.

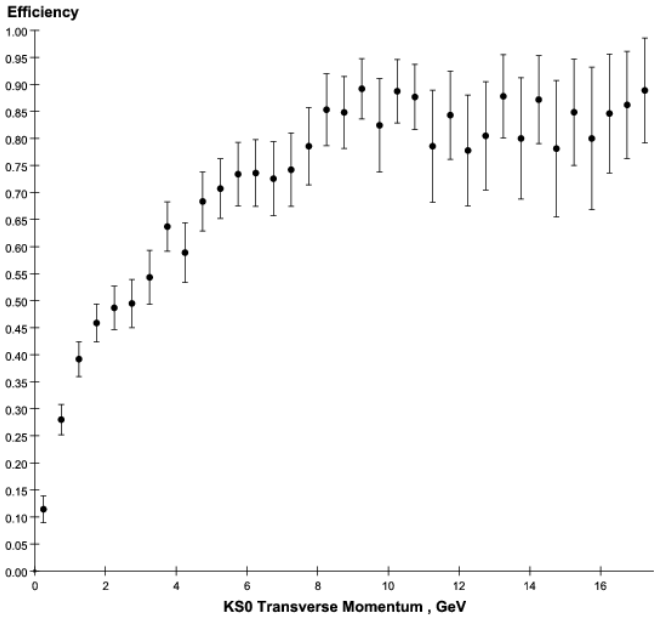

Figure 2.13: K_s^0 finding efficiency as function of its transverse momentum.

the track finding efficiency as function of the angle between the track and the jet thrust axis for $e^+e^- \to q\bar{q}$ events at $\sqrt{s} = 1$ TeV. The efficiency holds up rather well, dropping by about 1% for tracks within 2mrad of the jet core. The distribution in α, the angle of charged particles with respect to the jet thrust axis, is shown in the upper right corner in Fig. 2.12. The bottom figure shows the track finding efficiency as a function of track p_T for $e^+e^- \to b\bar{b}$ events at $\sqrt{s} = 500$ GeV with the backgrounds from 10 bunch crossings overlaid. In this study the effect of accumulating beam backgrounds over 10 crossings has been mimicked by adding these hits to all pixel devices in the detector. Hits in the silicon strip tracker were added only for a single bunch crossing, in-time of course with the physics event. There is a small loss in efficiency at low p_T, as anticipated. Also the fake track rate is higher, about 0.6%. Most of the fake tracks seem to be due to combinatorics.

An often-voiced concern of a tracker with relatively few measurements on a charged particle trajectory is the efficiency for the reconstruction of long-lived particles. The SiD detector should be viewed as an integrated detector where the overall performance derives from a combination of all the subdetectors. As described in section 2.1.5.2 a calorimeter assisted track finding algorithm was developed to reconstruct non-prompt tracks and long-lived particles. Fig. 2.13 shows the K_s^0 reconstruction efficiency for $t\bar{t}$-events, obtained by running the standard tracking algorithm followed by the calorimeter assisted tracking algorithm. The efficiency is defined as the ratio of the number of successfully reconstructed K_s^0's to the total number of K_s^0's that decayed into a charged pion pair inside the third layer of the outer tracker. The efficiency reaches 85% for K_s^0's with transverse momenta above 8 GeV. The result represents the current status of the software and significant improvements, particularly for low momentum K_s^0, are anticipated.

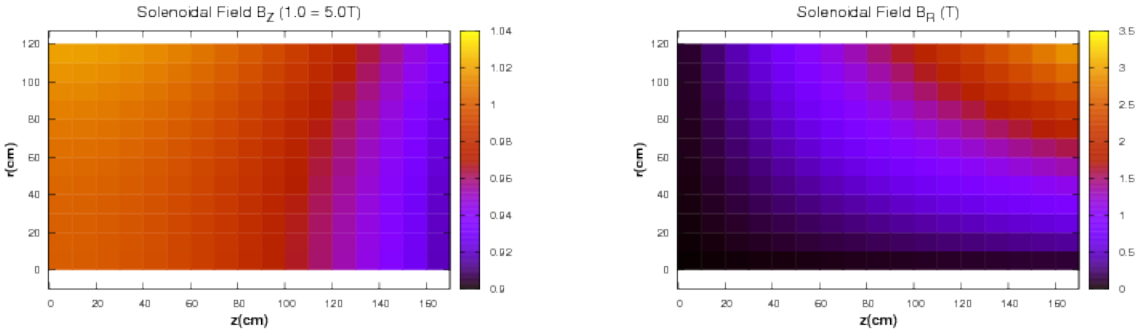

Figure 2.14: Map of the magnetic field components inside the tracking volume: B_z in fractional deviation from the nominal magnetic field (left) and B_R in absolute values (right)

All the simulations are performed using a uniform 5 Tesla magnetic field with no radial component. ANSYS simulations of the solenoid and the return flux show that the field is not uniform. Fig. 2.14 shows the distribution inside the tracking volume of the longitudinal (left) and radial (right) component of the magnetic field. The SiD detector having a 5 T magnetic field is defined as the field at $(R, z) = (0, 0)$ being 5 T. In Fig. 2.14 B_z is given as fraction of the nominal 5 T field. In the center of the detector B_z increases slightly with increasing radius. There is a drop of about 6% when reaching the end of the tracker volume. The field component B_R, given in absolute values in Fig. 2.14, is not negligible. The effect of a non-uniform magnetic field was studied by simulating particle trajectories with the field map as shown in Fig. 2.14 and reconstructing the trajectories assuming a perfect uniform field configuration. Preliminary studies indicate the effect on the pattern recognition to be minor. Studies are ongoing to investigate how it affects the fitted track parameters and whether the field uniformity must be improved.

2.1.7 Tracker Alignment

The unprecedented track momentum resolution contemplated for linear collider detectors demands minimizing systematic uncertainties in sub-detector relative alignments. At the same time, there is a strong impetus to minimize the amount of material in the tracking system, which might compromise its stability. These two requirements put a premium on accurate alignment of the various elements of the tracker. The short time scales on which alignment could change (e.g., from beam-driven temperature fluctuations) may preclude reliance on traditional alignment schemes based on detected tracks, where it is assumed the alignment drifts slowly, if at all, during the time required to accumulate sufficient statistics.

The prospect of two ILC detectors swapping places in the beamline only increases the importance of *in situ* alignment monitoring that does not depend on tracks. It will be important to monitor tracker distortions during the push-pull operations, not only for later track reconstruction, but also to ensure that no damage-inducing stresses are inadvertently applied to the tracker components. Alignment systems that can also be used during tracker

assembly to monitor strains would also be useful.

A system that can monitor alignment drifts in real time would be highly desirable in any precise tracker and probably essential to an aggressive, low-material silicon tracker. The trade-off one would make in the future between low material budget and rigidity will depend critically upon what a feasible alignment system permits. The SiD tracker is considering two alignment methods, one based on Frequency Scanned Interferometry (FSI), and one based on Infrared Transparent Silicon Sensors (IRSS).

The FSI system incorporates multiple interferometers fed by optical fibers from the same laser sources, where the laser frequency is scanned and fringes counted, to obtain a set of absolute lengths. With a test apparatus the state of the art in precision DC distance measurements over distance scales of a meter under laboratory-controlled conditions has been reached and even extended. Precisions better than 100 nm have been attained using a single tunable laser when environmental conditions are carefully controlled. Precisions under uncontrolled conditions (e.g., air currents, temperature fluctuations) were, however, an order of magnitude worse with the single laser measurements.

Hence a dual-laser FSI system is foreseen for the tracker, that employs optical choppers to alternate the beams introduced to the interferometer by the optical fibers. By using lasers that scan over the same wavelength range but in opposite directions during the same short time interval, major systematic uncertainties can be eliminated. Bench tests have achieved a precision of 200 nm under highly unfavorable conditions using the dual-laser scanning technique.

It should be noted that complementary analysis techniques of FSI data can be used either to minimize sensitivity to vibrations in order to determine accurate mean shape distortion or to maximize sensitivity to vibrations below the Nyquist frequency of data sampling. The latter algorithm could prove especially useful in commissioning in assessing vibration effects, such as might arise from pulse powering in a magnetic field.

The second method exploits the fact that silicon sensors have a weak absorption of infrared (IR) light. Consecutive layers of silicon sensors are traversed by IR laser beams which play the role of infinite momentum tracks. Then the same sophisticated alignment algorithms as employed for track alignment with real particles can be applied to achieve relative alignment between modules to better than a few microns. This method employs the tracking sensors themselves, with only a minor modification to make them highly transparent to infrared light. Only the aluminum metalization on the back of the sensor needs to be swept away in a circular window with a diameter of few millimeters to allow the IR beam to pass through. Since IR light produces a measurable signal in the silicon bulk, there is no need for any extra readout electronics.

A key parameter to understand the ultimate resolution of this method is the transmittance of a silicon sensor and the diffraction of the light. As a first approximation a silicon sensor is viewed as a stack of perfectly homogeneous plano-parallel layers, each characterized by its index of refraction and thickness. The layers are, however, not continuous but present local features, so that diffraction phenomena will appear if the size of the obstacle is comparable to the wavelength used. For instance, the strips of the detector with 50 μm readout

pitch, are good examples of an optical diffraction grating for an incoming beam in the IR. It has been determined that a key parameter that determines the overall transmittance of a microstrip detector is the pitch to strip width ratio, that is, the fraction of the sensor covered by aluminum. The smaller the strip width, the more light is transmitted. It was determined that good transmittance was achieved when the strip width was set to 10% of the pitch. Tuning of sensor thickness was found to contribute up to 5% over the layout optimized value. In bench tests, based on CMS strip detectors, a relative alignment of a few microns has been achieved.

2.2 Calorimeters

2.2.1 Introduction

The SiD baseline design uses a Particle Flow Algorithm-based approach to Calorimetry. PFAs have been applied to existing detectors, such as CDF and ZEUS and have resulted in significant improvements of the jet energy resolution compared to methods based on calorimetric measurement alone. However, these detectors were not designed with the application of PFAs in mind. The SiD baseline design on the other hand considers a PFA approach necessary to reach the goal of obtaining jet energy resolutions of the order of about $\Delta E/E = 3 - 4\%$ or better. SiD is therefore optimized assuming the PFA approach and the major challenge imposed on the calorimeter by the application of PFAs is the association of energy deposits with either charged or neutral particles impinging on the calorimeter. This results in several requirements on the calorimeter design:

- To minimize the lateral shower size of electromagnetic clusters the Molière radius of the ECAL must be minimized. This promotes efficient separation of electrons and charged hadron tracks.
- Both ECAL and HCAL must have imaging capabilities which allow assignment of energy cluster deposits to charged or neutral particles. This implies that the readout of both calorimeters needs to be finely segmented transversely and longitudinally.
- The calorimeters need to be inside the solenoid to be able to do track to cluster association; otherwise, energy deposited in the coil is lost and associating energy deposits in the calorimeter with incident tracks becomes problematic.
- The inner radius of the ECAL should match the outer radius of the tracking system, within the requirements of access and removal.
- The calorimeter needs to be extendable to small angles to ensure hermeticity, and be deep enough to contain hadronic showers.

Following is a short description of the baseline designs and options for the ECAL and the HCAL, as defined in December 2008. More details are available in the appendices and references. After that, the performance of the calorimeter system is discussed together with the implications of running at 1 TeV center-of-mass energy. Finally this leads into the discussion of an alternative approach to calorimetry for SiD based on dual readout.

2.2.2 Electromagnetic Calorimeter

The PFA approach of SiD is the main driver for the calorimetry design. For the ECAL, this implies that electromagnetic showers be confined to small volumes in order to avoid overlaps. Effective shower pattern recognition is possible if the segmentation of readout elements is small compared to the shower size. This level of transverse segmentation then also facilitates

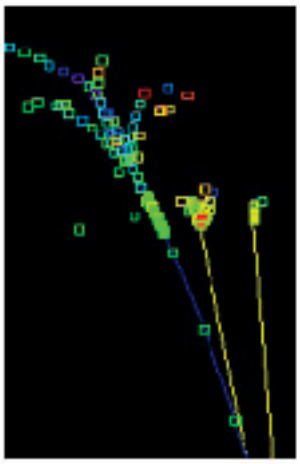

Figure 2.15: Simulated $\rho^+ \rightarrow \pi^+\pi^\circ$ decay in the SiD detector.

separating electromagnetic showers from the tracks of hadrons which haven't interacted or muons. The longitudinal segmentation is chosen not only to achieve the required electromagnetic energy resolution, but also to provide discrimination between electromagnetic showers and hadronic interactions which may occur in the ECAL. Finally, there should be a sufficient number of longitudinal readout layers to provide charged particle tracking in the ECAL. This is important not only for the PFA algorithms, but also to provide calorimeter-assisted track pattern recognition (see Section 2.1 Vertex and Tracking System). An important benefit of an ECAL which meets these requirements is that it is an *imaging* calorimeter. This is illustrated in Figure 2.15, which shows a simulated $\rho^+ \rightarrow \pi^+\pi^\circ$ decay in SiD. The photons are clearly distinguished from each other and from the charged track in the ECAL.

The ECAL described in this section according to the qualitative description above is expected to have capabilites including:

- Precise measurement of beam-energy electrons and positrons (and photons) from (radiative) Bhabha scattering. This is sensitive to contact terms and the angular distribution provides important information on electroweak couplings, e.g. in interference terms between Z, γ, and a new Z'. The Bhabha acollinearity distribution provides a key input for the measurement of the differential luminosity spectrum[1], which is needed for precision mass determinations coming from cross-section measurements at threshold.

- Identification of electrons from semileptonic decays, Dalitz decays, and photon conversions.

- EM energy resolution of $17\%/\sqrt{E}$, which is more than adequate to contribute negligibly to the overall jet energy resolution.

- PFA reconstruction of photons in jets with high (95%) efficiency and photon vertexing. The impact parameter resolution for photons of ~ 1 cm would be important for identifying decays where photons are the only visible decay products, such as predicted from some gauge-mediated SUSY-breaking models.

- PFA tracking of charged particles in jets and ECAL-assisted tracking (especially of V_0's)
- π° reconstruction in jets and τ decays, to improve the jet energy resolution[2] and to discriminate different τ final states.

2.2.2.1 Global ECAL design

A sampling ECAL provides the required energy resolution for ILC physics, as discussed above. Because of its small radiation length (X_0) and Molière radius, as well as its mechanical suitability, we have chosen tungsten as absorber/radiator. Due to practical considerations for ease of production of large plates and machining, the tungsten will be a (non-magnetic) alloy. This currently chosen alloy includes 93% W which has X_0 of 3.9 mm and Molière radius 9.7 mm. An additional benefit of tungsten is that it has a relatively large interaction length, which helps to minimize confusion between electromagnetic and hadron showers in the ECAL.

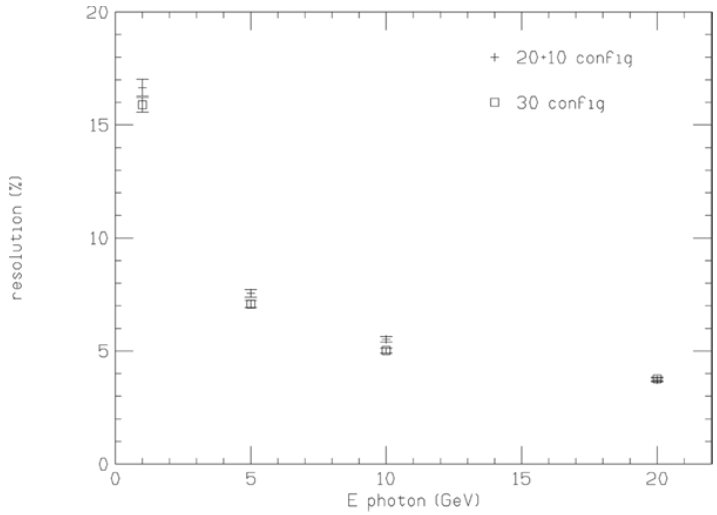

Figure 2.16: Energy resolution at low energy for two longitudinal configurations. The "20+10" configuration is our chosen design.

The longitudinal structure has 30 total layers. The first 20 layers each have 2.5 mm tungsten thickness and 1.25 mm readout gap. The last 10 layers each have 5 mm tungsten thickness plus the same 1.25 mm readout gap. This configuration attempts to compromise between cost, shower radius, sampling frequency, and shower containment. The cost is roughly proportional to the silicon area, hence the total number of layers. Finer sampling for the first half of the total depth improves the energy resolution for showers of typical energy. The total depth is 26 X_0, providing reasonable containment for high energy showers. Figure 2.16 shows that the energy resolution at low energy does not suffer relative to a design with 30 layers all having the thinner radiator. The resolution of the baseline design is well fit by the function $17\%/\sqrt{E}$. These simulations were made with EGS4, but have been verified by GEANT4 [3] simulations. For both technology options (described below) we have chosen a transverse

Inner radius of ECAL barrel	1.27 m
Maximum z of barrel	1.7 m
Longitudinal profile	(20 layers × 0.64 X_0) + (10 layers × 1.3 X_0)
EM energy resolution	$17\%/\sqrt{E}$
Readout gap	1.25 mm
Effective Molière radius ($\mathcal{R}_{eff}$)	14 mm

Table 2.4: Nominal parameters of the silicon-tungsten ECAL for SiD.

segmentation much smaller than the typical shower radius. As discussed above, the scale for this is set by the shower size, which we wish to be as small as feasible. Since showers will spread in the material between tungsten layers, it is crucial to keep the readout gaps as small as possible. We can scale the shower radii by a simple factor to provide a figure of merit. In our case, this factor is $(2.5 + 1.25)/2.5 = 1.5$ for the crucial first 20 layers. We can then define the *effective* Molière radius, $\mathcal{R}_{eff}$, as the Molière radius of the radiator multiplied by this factor. In our case, this is about 14 mm. A crucial driving force in our design has been to provide as small a $\mathcal{R}_{eff}$ as feasible, along with a transverse segmentation of the readout which is well below $\mathcal{R}_{eff}$. Table 2.4 summarizes the basic ECAL parameters.

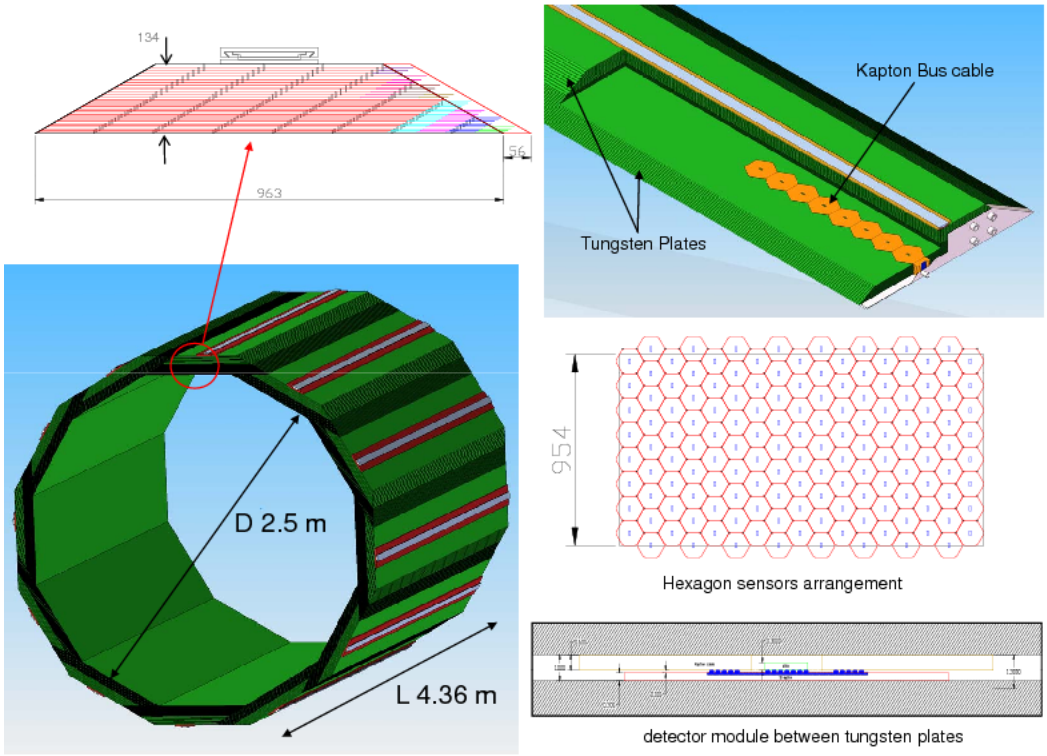

Figure 2.17: Overall mechanical layout of the ECAL.

The mechanical design of the ECAL consists of 12 independent wedges, fixed by rails on the inner radius of the HCAL. Each wedge is made of a stack of tungsten plates with a readout gap of 1.25 mm. Tungsten plates are available with a maximum size of 1 x 1 m, therefore, the wedge assembly is done interconnecting the plates by a screw-and-insert network, which transfers the load from the bottom of the stack to the rail. Such a design allows also to optimize the number of different silicon sensor sizes required to tile up each tungsten plate surface. The mass of one wedge is about 5000 kg. Data concentrator boxes are mounted on both sides of the wedge, reducing locally the number of the services to be interfaced outside the detector and all the services and cables run along the z-axis. Figure 2.17 shows the overall mechanical structure of the ECAL barrel, including sensor layout (for the baseline) and readout gap.

2.2.2.2 Technology choice

The technologies under consideration both use silicon sensors. Silicon will provide excellent transverse segmentation, while providing readout in a thin gap, which is a crucial performance criterion, as discussed above. The baseline design uses silicon sensors segmented into pixels of area 13 mm^2. The alternate option uses the CMOS-based Monolithic Active Pixel Sensor (MAPS) technology with 50 x 50 μm pixels. Both options are discussed below. An important feature of the SiD ECAL mechanical design is that it can accommodate either technology option without change to the basic mechanical configuration.

2.2.2.3 Baseline Design

In the baseline design, the ECAL readout layers are tiled by large, commercially feasible silicon sensors (presently from 15 cm wafers).

The sensors are segmented into pixels which are individually read out with a wide dynamic range. The complete electronics for the pixels is contained in a single chip (the KPiX ASIC) which is bump bonded to the wafer. The low beam-crossing duty cycle allows a reduction of the heat load by power pulsing, which permits passive thermal management within the ECAL modules. The realization of this technology has been the subject of an intensive, ongoing R&D program. The main parameters associated with the baseline technology choice are given in Table 2.5. Some details of the design and R&D results are given below. Further details can be found in the references [4] [5] [6]. Figure 2.18 shows a sensor with 1024 pixels. Not shown in the drawing are the signal traces, part of the second layer metalization of the sensors, which connect the pixels to a bump-bonding pad at the center of the sensor for input to the KPiX readout chip. The pixels are DC-coupled to the KPiX, requiring only two metalization layers. The pixels near the bump-bonding array at the center are split to reduce capacitance from the large number of signal traces near the sensor center. The electronic noise due to the resistance and capacitance of the traces has been minimized within the allowed trace parameters. The cutouts at the corners of the sensor are to accommodate mechanical standoffs which support the gaps between the tungsten layers. Figure 2.19 depicts a cross-sectional view of the readout gap in the vicinity of the center of

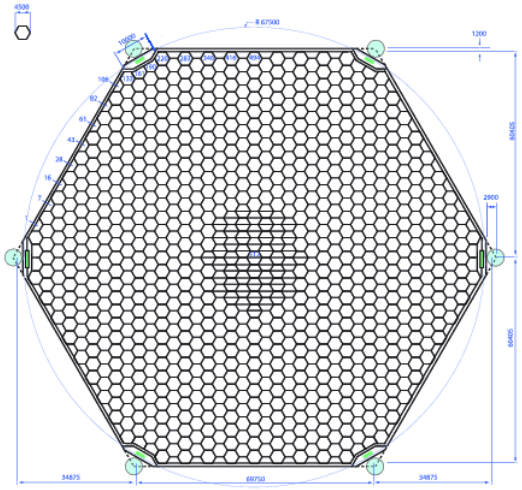

Figure 2.18: Drawing of a silicon sensor for the ECAL as delivered in 2008. The sensors are segmented into 1024 13 mm^2 pixels.

the sensor. The silicon sensor is about 320 μm thick. The KPiX is bump-bonded to the silicon sensor at an array of 32 x 32 bump pads which are part of the second metalization layer from sensor fabrication. Polyimid (kapton) flex cables connect near the center of the sensors. The cables bring power and control signals into the KPiX chip and bring out the single digital output line for the 1024 channels.

	Baseline	MAPS option
Pixel size	13 mm^2	50 x 50 μm
Pixels per silicon sensor	1024	1,000,000
Channels per KPiX readout chip	1024	-
Pixel dynamic range requirement	$\sim$ 0.1 to 2500 MIPs	1 MIP (digital)
Heat load requirement	20 mW per sensor	20 mW per sensor

Table 2.5: Parameters of both the baseline and MAPS options

Thermal management is a crucial feature of this design. The most power hungry elements of the KPiX chip, particularly the analog front end, are switched off for most of the interval between bunch trains. Our requirement is to hold the average power dissipation per wafer to less than 40 mW. This will allow the heat to be extracted purely passively, providing a much simpler design, less subject to destructive failure modes. The design of the KPiX chip in fact gives average power less than 20 mW per wafer, which would not be possible without power pulsing.

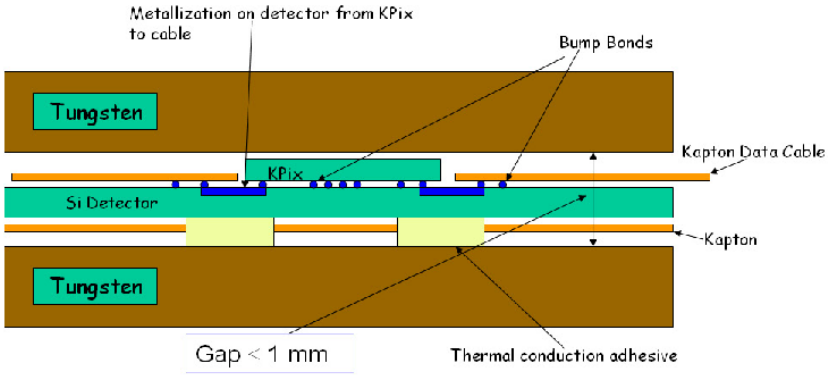

Figure 2.19: View into a readout gap in the vicinity of the KPiX readout chip. Representative bump bond connections are indicated by the small blue circles. Traces (dark blue lines) connect the KPiX serial readout stream, control signals, and power to the polyimide.

2.2.2.4 MAPS option

The Monolithic Active Pixel Sensor option [7] uses 50x50 μm silicon pixels as readout material. The main difference here is the usage of digital electromagnetic calorimetry where the ECAL is operated as a shower particle counter. Simulated performance [9] is illustrated in Figure 2.20. These sensors could be manufactured in a commercial 180 nm mixed-mode CMOS process using 300 mm wafers. This is an industrial and widely available process, so pricing for these wafers should be competitive.

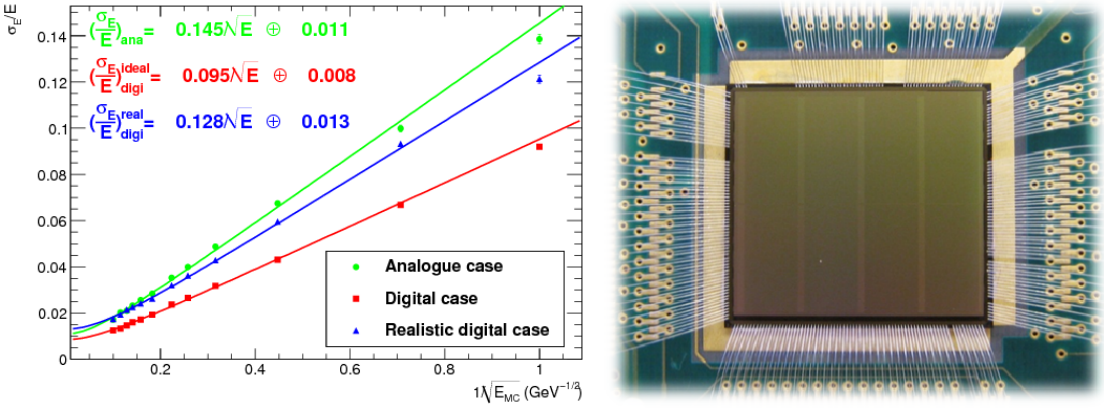

Figure 2.20: Left: The energy resolution as a function of the incident energy for single electrons for both analog and digital readout using a GEANT4 simulation. The realistic digital cases includes effects of saturation and charge sharing, leading to a degradation of 35% [9]. Right: a picture of a bonded TPAC sensor.

We have manufactured and tested two first-generation sensors for digital electromagnetic calorimetry, TPAC 1.0 and 1.1 [8] which both consists of 168x168 pixels with the required size of 50x50 μm and TPAC 1.1 will be described in a bit more detail. It uses a the pre-Shaper architecture and consists of a charge preamplifier, a CR-RC shaper which gen-

erates a shaped signal pulse proportional to the amount of charge collected and a two-stage comparator which triggers the hit-flag. The sensor supports single-bunch time stamping with up to 13 bits. Each pixel has a 6 bit trim to compensate for pedestal variations and each pixel can be masked off individually. A bank of forty-two pixels shares nineteen memory buffers to store the hits during the bunch train. The sensor also supports power-pulsing already and is able to power off its front-end in the quiet time between bunch trains. As the active sensor area is only about 20 μm thick, it allows backthinning of the wafers down to 100 μm or less. Both sensors have been tested using sources and lasers[8]. The MAPS option is designed to fit in the same mechanical structure as the baseline option and we foresee a sensor size of 5 x 5 cm (baseline) for a final system. The main parameters for the MAPS option are summarized in Table 2.5.

2.2.2.5 Calibration and Alignment

Silicon detectors are inherently insensitive to gain variations with time and should not have significant inter-pixel gain differences. Pixel to pixel gain differences in the electronic readout are calibrated by dedicated calibration circuitry within the KPiX and TPAC chips. Perhaps the main calibration issue will be sensor to sensor gain differences. These are not expected to be large, but we are investigating different options for this calibration. For mechanical alignment, the ECAL detector sensor locations will be optically measured and related to external fiducials on the modules. The modules will be located inside the HCAL using these fiducials to 1 mm or better, and the positions measured to approximately 100 micrometers.

2.2.3 Hadronic Calorimeter

2.2.3.1 HCAL barrel geometry

The PFA-based HCAL is a sandwich of absorber plates and instrumented gaps with active detector elements. It is located inside the magnet and surrounds the electromagnetic calorimeter, the latter being fixed to it. The total absorber depth amounts to 4.5 λ, made of stainless steel, divided into 40 layers, separated by 8mm gaps. Thus the HCAL internal and external radii are respectively: R_{int}=1419 mm and R_{ext}=2583 mm. The overall length is 6036mm long, centered on the interaction point.

The HCAL is divided into twelve azimuthal modules. In order to avoid cracks in the calorimeter, the module boundaries are not projective with respect to the interaction point. Consequently, in order to keep a symmetric shape two types of modules are used: 6 rectangles and 6 pseudo-trapezoids, as illustrated in Fig. 2.21. Each module covers the whole longitudinal length. Chambers are inserted in the calorimeter along the Z-direction from both ends and can eventually be removed without taking out the absorber structure from the magnet. Special care of the detector layout has to be taken into account to avoid a 90 degree crack.

The absorber plates are supported by several stringers fixed radially on both sides of the modules. Stringers of two consecutive modules are shifted in order to maximise the active

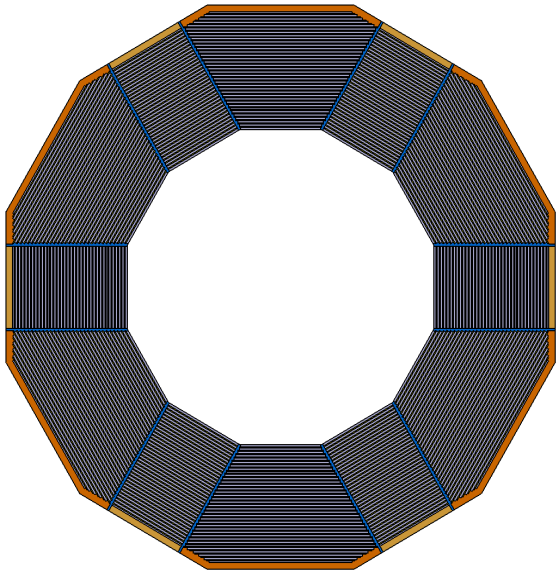

Figure 2.21: Cross-section of the HCAL barrel.

detector area. Although the space between two consecutive modules is not instrumented, it is however filled by the absorber material. The barrel will be fixed on the magnet at 3 and 9 o'clock or 5 and 7 o'clock.

2.2.3.2 Forward HCAL

Each endcap forms a plug that is inserted into an end of the barrel calorimeter. The layer structure of the end cap calorimeters is the same as for the barrel. Fig. 2.22 shows a view of one endcap.

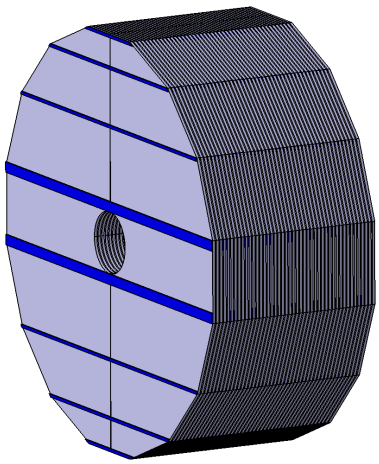

Figure 2.22: Face and top views of the Hcal forward.

2.2.3.3 Baseline Design (RPC)

Resistive Plate Chambers (RPCs) are gaseous detectors primarily in use for the large muon systems of colliding beam detectors. The detectors feature a gas volume defined by two resistive plates, typically Bakelite or glass. The outer surface of the plates is coated with a layer of resistive paint to which a high voltage is applied. Depending on the high voltage setting of the chamber, charged particles crossing the gas gap initiate a streamer or an avalanche. These in turn induce signals on the readout strips or pads located on the outside of the plates.

In recent years RPCs have seen a wide range of applications. Using glass as resistive plates, these detectors have shown excellent long-term stability and reliability. The assembly of the chambers is straightforward and does not require special skills or tools. The materials needed for their construction are readily available and cheap.

Current designs of the active layer

Various chamber designs have been investigated [10]. Of these two are considered particularly promising: a two-glass and a one-glass plate design. Schematics of the two chamber designs are shown in Figs. 2.23 and 2.24. The thickness of the glass plates is 1.1 mm and the gas gap is maintained with fishing lines with a diameter of 1.2 mm. The overall thickness of the chambers, including layers of Mylar for high voltage protection, is approximately 3.7 mm and 2.6 mm, respectively.

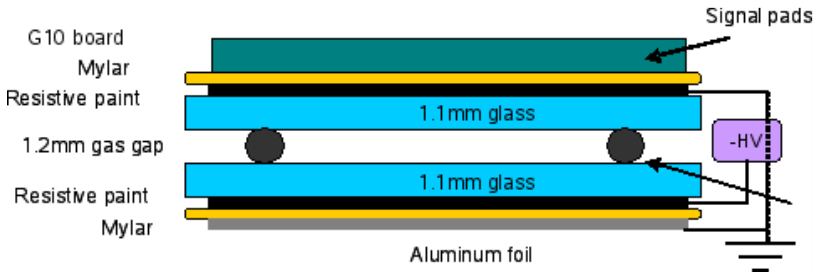

Figure 2.23: Schematic of the RPC design with two glass plates. Not to scale.

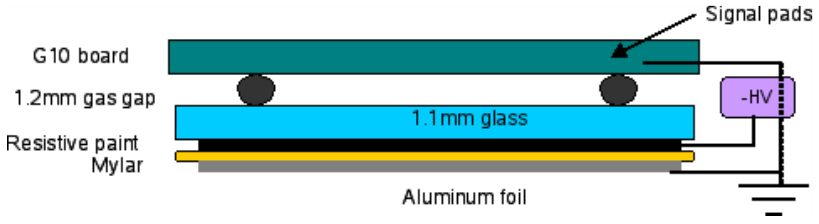

Figure 2.24: Schematic of the RPC design with one glass plate. Not to scale.

The chambers are operated in saturated avalanche mode with an average high voltage setting around 6.3 kV. The gas mixes three components: Freon R134A (94.5%), isobutane (5.0%) and sulfur-hexafluoride (0.5%).

The readout of the chambers consists of a pad board with 1×1 cm^2 pads, read out

individually. In such a calorimeter the energy of incident particles is reconstructed as a function of the number of pads with signals above threshold.

As part of the program of the CALICE collaboration [11], the ANL group [12] built and tested about 20 chambers. The tests included extensive characterization of the chambers with a 14-bit (analog) readout system. The size of the signal charges, the MIP detection efficiency and the pad multiplicity (as function of operating conditions) were measured with cosmic rays [10].

A test calorimeter consisting of up to 10 chambers, each with an area of 20×20 cm^2, was assembled and tested with cosmic rays and in the Fermilab test beam. The active media were interleaved with 20 mm thick Steel plates. As an example, Fig. 2.25 shows the pad multiplicity versus MIP detection efficiency [13]. Note the constant pad multiplicity at 1.1 (shown as open black squares), independent of efficiency, for the one-glass design.

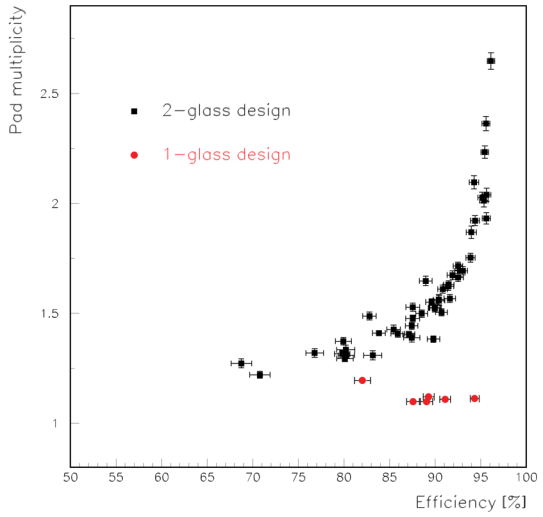

Figure 2.25: Pad multiplicity versus MIP detection efficiency for 2-glass RPC and 1-glass RPC. The results were obtained with a broadband muon beam

As an example of the results obtained with showering particles, Fig. 2.26 shows the response to 1, 2, 4, 8, and 16 GeV positrons.

Note that the response is highly non-linear, due to substantial leakage out the back of the calorimeter (with a depth of 6.8 X_0) and the high density of electromagnetic showers. The response is adequately reproduced by Monte Carlo simulations based on GEANT4. The results have been submitted for publication [14]. Additional tests with pions of various momenta were performed and showed the expected results [15].

The stack was also exposed to 120 GeV protons at various beam intensities to study the rate capability of RPCs. The results show no evidence of a dead time in excess of 0.3 ms. For rates above 100 Hz/cm^2 the MIP detection efficiency drops exponentially (with a time constant depending on the beam intensity) until reaching a constant level. The results have been submitted for publication [16].

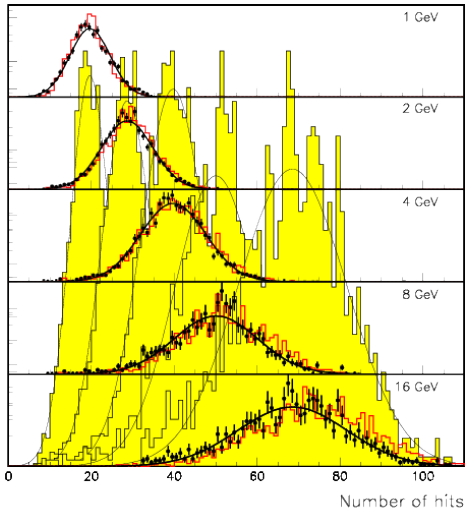

Figure 2.26: Response of a small size prototype calorimeter to positrons with energies of 1, 2, 4, 8 and 16 GeV. The red histograms are the results of a GEANT4 based simulation.

The stack has now been operational for over 18 months. During this time period, measurements of the noise rate, MIP detection efficiency and pad multiplicity were performed using cosmic rays. Fig. 2.27 shows the results as a function of time. It is seen that the noise rate and the pad multiplicity fluctuate over time. This is due to changing environmental conditions (temperature and barometric pressure). The efficiency of the chambers remains constant. Within the time period of these studies there is no evidence of long-term aging effects. Additional details on the long-term studies can be obtained from [17].

The group is currently assembling a larger prototype calorimeter with 40 planes and approximately 400,000 readout channels. The completed calorimeter will be tested in the Fermilab test beam in standalone mode and also together with the CALICE Silicon-Tungsten electromagnetic calorimeter [11]. The tests will validate the concept of a digital hadron calorimeter with RPCs as active medium and the proposed technical approach presented here. The prototype calorimeter will provide precision measurements of hadronic showers with unprecedented spatial resolution. These measurements will be compared to predictions of various hadron shower models.

The analysis of the data from the small scale prototype is close to complete. Two additional publications are planned: *Hadron Showers in a Digital Hadron Calorimeter* and *Measurement of the Environmental Dependence of the RPC Performance*. The group is currently assembling a one meter cube prototype calorimeter. Its completion is expected sometime during CY 2009, to be followed by tests in the Fermilab test beam. The data analysis will be carried through 2011. The projected R&D for the module/technical prototype will initiate in 2010, after the completion of the construction of the one meter cube prototype calorimeter. This phase is expected to last 2 – 3 years

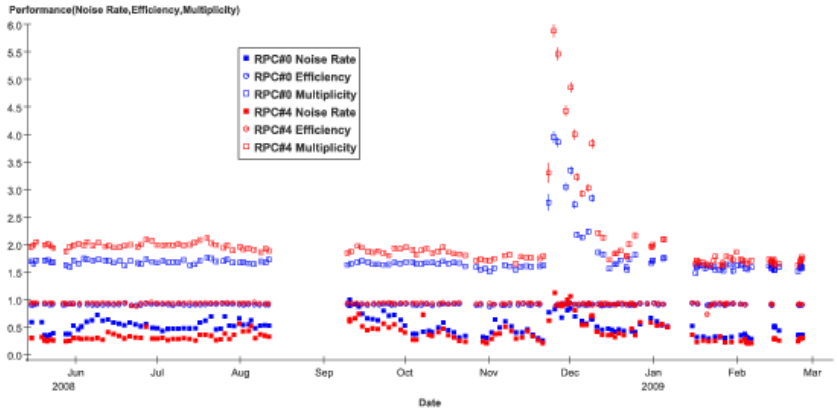

Figure 2.27: Noise rate, MIP detection efficiency and pad multiplicity as a function of time for two 2-glass RPCs. Periods without measurements are due to safety reviews and re-stacking of the chambers. The large increase in noise rate and pad multiplicity seen in December 2008 are due to tests with various gas flow rates.

2.2.3.4 GEM Option

We have been developing a digital hadronic calorimeter (DHCAL)[18] using GEM as the sensitive gap detector technology. GEM can provide flexible configurations which allow small anode pads for high granularity. It is robust and fast with only a few nano-second rise time, and has a short recovery time which allows a higher rate capability than other detectors. It operates at a relatively low voltage across the amplification layer, and can provide high gain using a simple gas (ArCO2), which protects the detector from long term degradation issues, and is stable. The ionization signal from charged tracks passing through the drift section of the active layer is amplified using a double GEM layer structure. The amplified charge is collected at the anode layer with pads at zero volts. The GEM design allows a high degree of flexibility with, for instance, possibilities for microstrips for precision tracking layer(s), variable pad sizes and shapes, and optional ganging of pads for finer granularity of future readout, if allowed by cost considerations and demanded by physics requirements. Fig. 2.28 depicts how the double GEM approach can be incorporated into a DHCAL scheme.

Status of GEM Chambers development

A number of double GEM chambers have been built and tested with cosmic rays sources, and test beam. Initial studies were conducted on signal characteristics and gain from a small prototype GEM detector read out using the QPA02 chip developed by Fermilab for Silicon Strip Detectors. The gain of the chamber, with a 70% Ar/20% CO_2 gas mixture, was determined to be of the order 3500, consistent with measurements done by the CERN GDD group. The MIP efficiency was measured to be 94.6% for a 40 mV threshold, which agrees with a simulation of chamber performance. The corresponding hit multiplicity for the same threshold was measured to be 1.27, which will be beneficial for track following and cluster definition in a final calorimeter system. A gas mixture of 80% Ar/20% CO_2 was shown to work well and give an increase in gain of a factor of three over the original mixture. A minimum MIP signal size of 10 fC and an average size of 50 fC were observed

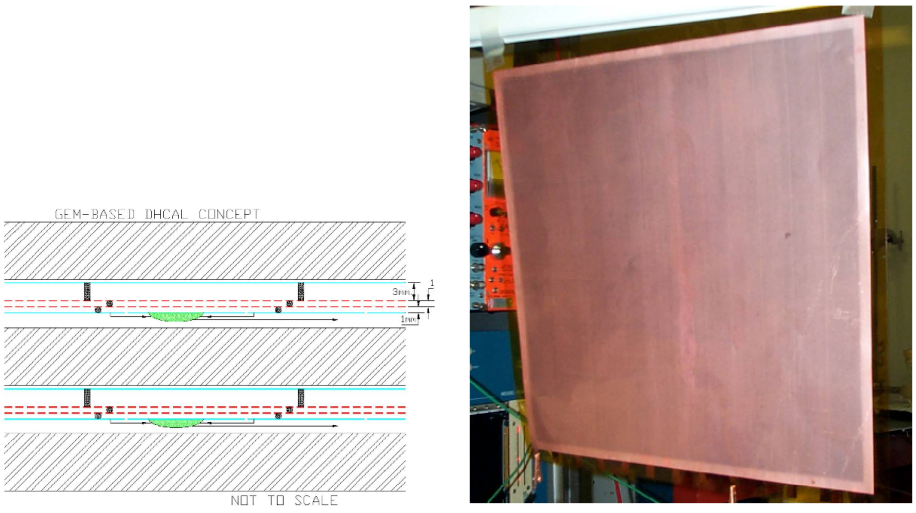

Figure 2.28: Left: GEM DHCAL Concept. Right: A 30 cm x 30 cm foil from 3M Corporation.

from the use of this new mixture. The prototype system has proved very stable in operation over many months, even after deliberate disassembly and rebuilding, returning always to the same measured characteristics.

Recently we have been using the SLAC KPiX chip to read out our chambers, and will continue this using the expected 128 and eventual 1024 channel KPiX versions. Our plans to build several 1m×1m layers and expose them to a testbeam in the CALICE 1 m^3 stack, are described in the appendices along with more details of recent cosmic ray, source and test beam data.

2.2.3.5 MICROMEGAS Option

A very interesting alternative for the DHCAL active medium is the MICRO MEsh GAseous Structure (MICROMEGAS) [22] based on micro-pattern technology. Our prototypes consist of a commercially available 20 μm thick mesh which separates the drift gap (3 mm) from the amplification gap (128 μm). This simple structure provides good gas gain uniformity over the whole area and allows full efficiency for MIPs. The rate obtained is not constrained, as is the case of glass RPCs. Moreover, the tiny size of the electron avalanches results in fast signals without physical crosstalk and leads to low hit multiplicity. The chosen bulk technology, based on industrial PCB processes, offers a robust detector with working voltages lower than 500 V. MICROMEGAS, with anode pads as small as 1 cm^2, is therefore a very appealing option for a DHCAL optimized for a PFA.

Different kinds of prototypes were developed, built and tested at LAPP: one type with analog readout for characterization (see Fig. 2.29) and two types with embedded digital ASICs. The next step is a 1 m^2 assembly of six bulks with 24 ASICs each, closed by two plates of 2 mm thick stainless steel which delimit a 6 mm active medium. Its construction is on-going and it should be available for 2009 beam tests. This design is foreseen for large quantity production in order to build a 1 m^3 DHCAL prototype.

Using an ^{55}Fe X-ray source, the measured gain comes to 10^4 with an energy resolution down to 8.5 % corresponding to 19.6 % FWHM. The gain and the resolution were measured as a function of the drift field, amplification field, gas flow and pressure variables. Our prototypes were tested at CERN in 2008. With 200k muons, the Landau distribution obtained on each pad has a Most Probable Value (MPV) around 45 fC. The chamber mapping was performed in terms of pedestal mean and sigma, Landau distribution MPV and sigma. The pedestal gaussian fits showed an average standard deviation of 0.6 fC. The MPV relative variation is about 11 % RMS (see Fig. 2.29), the efficiency 97 % and the multiplicity 1.08. For the first time, a bulk was laid on a PCB with embedded electronics, the DIRAC chip [25], and could be exposed to pions. With a threshold of 19 fC the beam profile was obtained. The next prototypes, with four HARDROC chips [24] are read out with the Detector InterFace board (DIF), designed at LAPP in the framework of the DHCAL CALICE data acquisition system [26]. More details of this options and future plans may be found in the appendices.

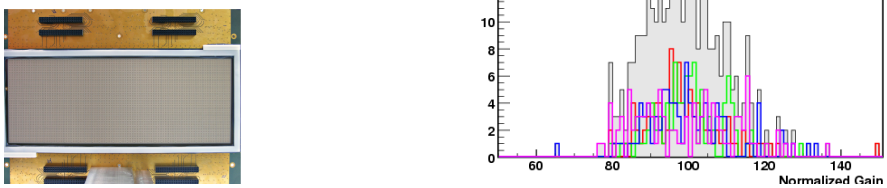

Figure 2.29: MICROMEGAS 12×32 cm^2 analog readout prototype with 1 cm^2 pads. MPV dispersion normalized to 100 % for four prototypes

2.2.3.6 Scintillator with SiPM Option

The CALICE Collaboration has been pursuing the design and prototyping of a fine granularity scintillator-based hadron calorimeter. This option capitalizes on the marriage of proven detection techniques with novel photodetector devices. The main challenge for a scintillator-based calorimeter is the architecture and cost of converting light, from a large number of channels, to electrical signal. Studies demonstrate that small tiles (4-9 cm^2) interfaced to Silicon Photomultipliers (SiPMs)/Multi Pixel Photon Counter (MPPC) photodetectors [27], [28] offer an elegant solution. SiPM/MPPCs are multi-pixel photo-diodes operating in the limited Geiger mode. They have distinct advantage over conventional photomultipliers due to their small size, low operating voltages and insensitivity to magnetic fields. The *in situ* use of these photodetectors opens the door to integration of the full readout chain to an extent that makes a high channel count scintillator calorimeter entirely plausible. Also, in large quantities the devices are expected to cost a few dollars per channel making the construction of a full-scale detector instrumented with these photo-diodes financially feasible.

A scintillator-SiPM prototype of about 1 m^3 has been designed, constructed and exposed to a test beam during the 2006-2008 period at CERN and Fermilab (see Fig. 2.30). The active layers of the HCAL prototype consist of 5 mm thick scintillator tiles sandwiched

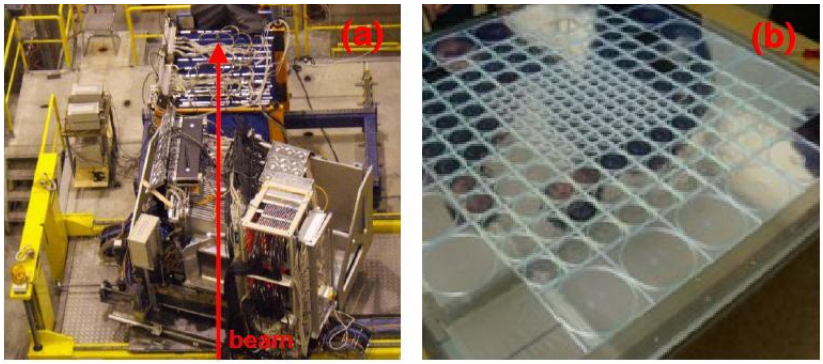

Figure 2.30: CALICE test beam setup at CERN (left) and an active layer of the scintillator-SiPM prototype (right)

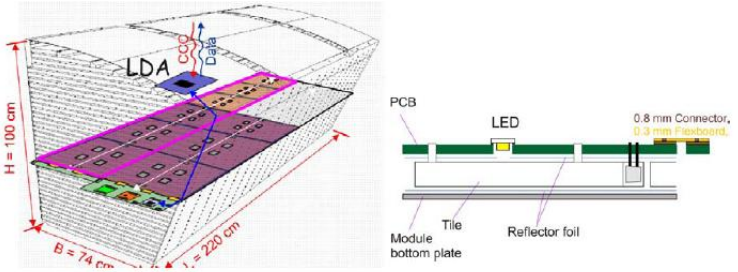

Figure 2.31: Barrel wedge intrumented with IRL planes (left) and conceptual design of an IRL (right).

between 2 cm thick steel absorber plates. Each tile comes with its own 1 mm diameter WLS fiber mated to a SiPM embedded in it. Over six run periods millions of electron, pion and proton events in the 2-180 GeV/c range were written to disk. Ongoing analysis of the data collected, has gone a long way in establishing the scintillator-SiPM option as a calorimeter technology, benchmarking hadron shower Monte Carlo's and testing the particle-flow paradigm using hadrons from real data [29].

The focus of the current R&D effort is the development of an Integrated Readout Layer (IRL). In general for the IRL, it is proposed to have a printed circuit board (PCB) inside the detector which will support the scintillator tiles, connect to the silicon photodetectors and carry the necessary front-end electronics and signal/bias traces (see Fig. 2.31). This can however be achieved in a number of ways and different groups are working on complementary approaches (e.g. fiber vs. direct or fiberless coupling of SiPMs to the tiles) in a coordinated fashion. It is planned that the R&D being carried out on the scintillator-SiPM hadron calorimeter option in America, Asia and Europe will be brought together for a next-generation EUDET/CALICE 'technology' prototype in 2010. This 'wedge' will be intrumented with IRL planes. Complementary versions of the IRL planes being pursued by different groups in the collaboration will be tested and compared.

2.2.4 Calorimeter Performance

The SiD detector is designed to take advantage of the expected improvement in jet energy resolution deriving from the use of a Particle Flow Algorithm (PFA). The SiD PFA is described in the online appendices and was used in the physics benchmarking reported in Chapter 4. This section first describes the necessary software calibrations, which were then applied to check calorimeter/PFA performance. Three results were compared: calorimeter only/no PFA, a perfect pattern recognition (PPR) PFA, and the SiD PFA.

Full Geant4 simulations using SLIC [31] and the SiD simplified detector geometry (SiD02) were performed on test samples. The test samples were qq events ($q = uds$) at fixed E_{cm}, and $ZZ \rightarrow qq\nu\nu$ at 500 GeV E_{cm}. The qq events have no beamstrahlung, no bremsstrahlung, and no gluon radiation, so each event contained exactly 2 equal energy back-to-back quark jets. The ZZ events were generated with all these effects, and allow mass reconstruction without jet finding algorithms.

Software calibrations were performed separately for photons and hadrons using the ZZ test sample, to relate the simulated detector response to the incident energy. Details of the calibration procedure may be found in the appendices . The calibrations were then applied to a sample of particles not used in the calibration ($t\bar{t}$ events at 500 GeV E_{cm}). For photons a single calibration constant was determined for each of the calorimeters, ECAL (barrel and endcap) and HCAL (barrel and endcap). This was sufficient to give a maximum nonlinearity of less than 0.5% and full rms of 0.5% + 18%/$\sqrt{E}$ for single photons in the $t\bar{t}$ sample. See Fig. 2.32.

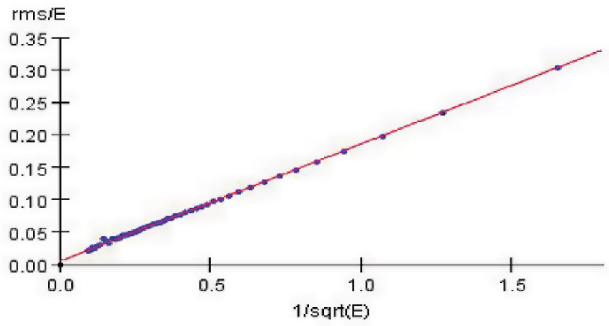

Figure 2.32: Resolution plot for single photons from ttbar events. The line in the resolution plot represents a fit to the data, 0.5% + 18%/$\sqrt{E_{Gen}}$.

For neutral hadrons, one calibration constant was determined per calorimeter, as was a polar angle correction for the hadron calorimeters (barrel and endcap). After combining the deposits in different calorimeters, an energy correction was applied. This resulted in a maximum nonlinearity of less than 3% and full rms of 65%/$\sqrt{E}$ for single neutral hadrons in the $t\bar{t}$ sample Fig. 2.33 .

The test sample events were then reconstructed using particle flow algorithms (PFA's) with this calibration. Several PFA algorithms are being developed, and the one yielding the best energy resolution for the test samples was chosen for the benchmark analyses.

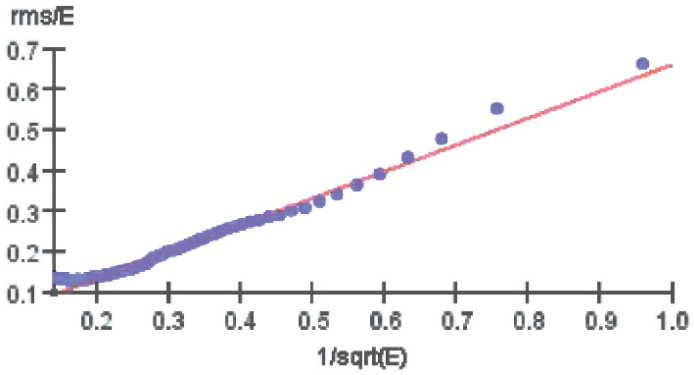

Figure 2.33: Resolution plot for single neutral hadrons from ttbar events. The line in the resolution plot represents 65%/EGen.

The calorimeter only/no PFA reconstruction calculated a single parameter for each calorimeter with no assumption as to the type of particle depositing energy. For the digital hadron calorimeter, a polar angle correction was applied. Using this calibration, event energy was measured using only the calorimeters. In the PPR PFA reconstruction, the Monte Carlo truth information was used to associate calorimeter hits to the appropriate particles, showing the potential of a PFA with the SiD detector.

Each of these two reconstructions was run on the qq test samples. Since the samples contain two jets of equal energy, $dE_{jet}/\sqrt{E_{jet}} = dE_{event}/\sqrt{E_{event}}$. The standard for comparing results has become rms90, where rms90 is the rms of the 90% of the events yielding the smallest rms. Defining α_{90} with the expression rms90/E $= \alpha_{90}/\sqrt{E}$, α_{90} vs E_{jet} is shown in Fig. 2.34 for the reconstructions. Although the PPR PFA jet energy resolution remains relatively constant with jet energy, Fig. 2.34 shows that the calorimeter-only resolution degrades somewhat, and the SiD PFA resolution degrades significantly as the jet energy increases. Future studies must determine if the SiD PFA performance can be improved at the higher energies, if it can be complemented with calorimeter-only measurements, or if a new approach, like that using dual-readout crystals, described below, is superior.

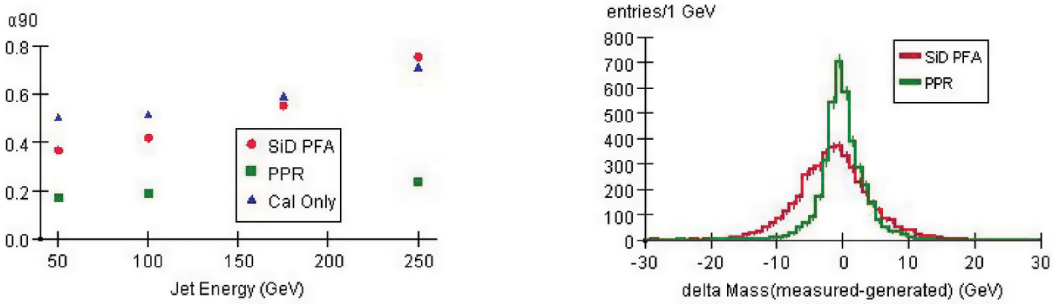

Figure 2.34: Left: α_{90} vs jet energy for the 3 different reconstructions. Right: Mass residuals in the ZZ test sample. For PPR rms90 = 2.2 GeV. For SiD PFA rms90=4.0GeV

Finally, the ZZ test sample was reconstructed with the PFA's. The mass residuals

($M_{measured}$ - $M_{generated}$) are shown in Fig. 2.34. Using the rms90 of the distributions, dM/M = 2.5% for the PPR, and dM/M = 4.5% for the full PFA. This demonstrates that the SiD PFA has already approached the desired mass resolution. Further improvements are expected as work continues refining the SiD PFA.

2.2.4.1 Homogeneous Crystal Dual-readout Option

SiD is studying an alternative to particle flow calorimetry based on the dual readout approach. The principal limitations of the hadron energy resolution in traditional total absorption calorimetry come from two sources:

- The sampling nature of the conventional hadron calorimeters
- A significant and fluctuating fraction of the incoming hadron energy is converted into non-observable forms of energy (primarily nuclear binding energy).

Good jet energy resolution requires a calorimeter where both of these factors are eliminated or largely reduced. This can be accomplished with a homogenous, totally active calorimeter with dual readout, i.e. readout of scintillation and Cherenkov light. A dimensionless anti-correlation function may be derived using these components and is shown in Fig. 2.35, based on a Monte Carlo simulation. Application of an event-by-event correction to a sample of hadron induced showers improves the energy resolution and makes the average hadron response equal to the beam energy (hence equal to the response to electrons on neutral pions of the same energy), as shown in Fig. 2.35.

The construction of a practical hadron calorimeter, especially with the hermeticity required in the colliding beam environment, is now possible by two technological breakthroughs:

- The development of affordable, high density crystals
- The advent of compact, inexpensive silicon-based photodetectors (APD's and SiPM's) capable of operating in a string magnetic field.

A high resolution calorimeter is designed to fit into the space occupied by the ECAL and HCAL of the baseline design. It is constructed of optical "crystals" equipped with two sets of compact silicon photodetectors at the back. One set, equipped with the low pass optical filter and short integration gate electronics, is used to detect and measure the Cherenkov light. The other set, equipped with high pass filter and long integration gate electronics is used to detect and measure the scintillation component.

Further details of the use of the dual-readout, specifications of a viable calorimeter, and the required R&D tasks may be found in Chapter 6.

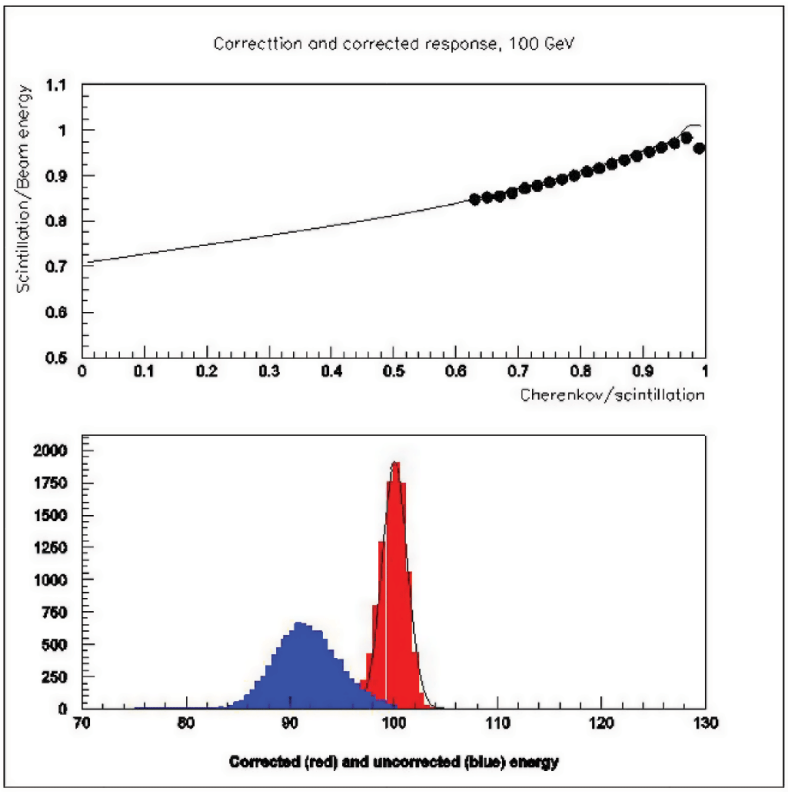

Figure 2.35: Based on a Monte Carlo simulation, The correlation between the average fraction of the beam energy detected via scintillation and the ratio of responses measured with the Cherenkov and the scintillation light (top); A response of the total absorption calorimeter to 100 GeV pion beam (blue) and the same response corrected on the event-by-event basis using the correlation (bottom).

References

[1] S. T. Boogert and D. J. Miller, arXiv:hep-ex/0211021.

[2] G.W. Wilson, "pi0 Reconstruction in Jets", Jet and Photon Energy Measurements session, ALCPG 2007, Fermilab, http://ilcagenda.linearcollider.org/conferenceDisplay.py?confId=1556

[3] S. Agostinelli *et al.* [GEANT4 Collaboration], Nucl. Instrum. Meth. A **506** (2003) 250.

[4] R. Frey, *et al.*, *Proc. 10th International Conference on Calorimetry in High Energy Physics, pg. 54*, World Scientific, 2002.

[5] World-wide Study review of Calorimeter R&D program, talks by D. Strom, agenda URL: http://ilcagenda.linearcollider.org/sessionDisplay.py?sessionId=38&slotId=22&confId=1296

[6] DoE/NSF review of the U.S. ILC R&D program, talk by R. Frey, agenda URL: http://ilcagenda.linearcollider.org/conferenceDisplay.py?confId=1640

[7] N. K. Watson *et al.*, "A MAPS-based readout of an electromagnetic calorimeter for the ILC," J. Phys. Conf. Ser. **110** (2008) 092035.

[8] J. A. Ballin *et al.*, "Monolithic Active Pixel Sensors (MAPS) in a quadruple well technology for nearly 100factor and full CMOS pixels", Sensors 2007 Journal, arXiv:0807.2920

[9] J. A. Ballin *et al.*,"A digital ECAL based on MAPS," arXiv:0901.4457 [physics.ins-det].

[10] G.Drake et al., Nucl. Instrum.Meth.,A578, 88-97(2007).

[11] https://twiki.cern.ch/twiki/bin/view/CALICE/WebHome

[12] http://www.hep.anl.gov/repond/DHCAL_US.html

[13] B.Bilki et al., JINST **3** P05001 (2008).

[14] B.Bilki et al., "Measurement of Positron Showers with a Digital Hadron Calorimeter", ArXiV 0902.1699, submitted to JINST.

[15] B.Bilki et al., "Hadron Showers in a Digital Hadron Calorimeter", to be submitted for publication.

[16] B.Bilki et al., "Measurement of the Rate Capability of Resistive Plate Chambers", ArXiV 0901.4371, submitted to JINST.

[17] See talk by Q. Zhang at the 2008 Linear Collider Workshop LCWS2008, Chicago, IL.

[18] For an early discussion of the GEM DHCAL concept please see: http://www-hep.uta.edu/~white/SiD/LOI/GEM_DHCAL_FNAL_092205.ppt

[19] KPiX, An Array of Self Triggered Charge Sensitive Cells Generating Digital Time and Amplitude Information. D. Freytag et al. SLAC-PUB-13462, Dec 11, 2008. 4pp. Presented at 2008 IEEE Nuclear Science Symposium (NSS) and Medical Imaging Conference (MIC) and 16th International Workshop on Room-Temperature Semiconductor X-Ray and Gamma-Ray Detectors (RTSD), Dresden, Germany, 18-25 Oct 2008.

[20] R. Chechik, A. Breskin, C. Shalem, D. Mormann, "Thick GEM-like hole multipliers: Properties and possible applications," Nucl.Instrum.Meth.**A535**, 303 (2004).

[21] V Peskov et al. 2007 Vienna Conference on Instrumentation, `http://vci.oeaw.ac.at/2007/`.

[22] Y, Giomataris, Ph. Rebourgeard, J.P Robert and G. Charpak, "MICROMEGAS: A High granularity position sensitive gaseous detector for high particle flux environments", NIM A376, 1996, pp 29-35

[23] D. Roy, "CENTAURE Acquisition Program", http://www-subatech.in2p3.fr/ electro/infoaq/CENTAURE/main_centaure.html

[24] S. Callier, F. Dulucq, Ch. de La Taille, G. Martin-Chassard, N. Seguin-Moreau, R. Gaglione, I. Laktineh, H. Mathez, V. Boudry, J-C. Brient, C. Jauffret, "HARDROC1, readout chip of the Digital HAdronic CALorimeter of ILC", IEEE-NSS Conference Record, vol 3, 2007, pp 1851-1856

[25] R. Gaglione, "DIRAC: Digital Readout ASIC for hAdronic Calorimeter", IEEE-NSS/MIC 2008

[26] B. Hommels, "Data Acquisition Systems for Future Calorimetry at the International Linear Collider", IEEE-NSS/MIC 2008

[27] B. Dolgoshein et. al, NIM A504:48-52, 2003.

[28] Hamamatsu Photonics K. K., Solid-state Division, 1126-1 Ichino-cho, Hamamatsu City, 435-8558, Japan.

[29] https://twiki.cern.ch/twiki/bin/view/CALICE/CaliceAnalysisNotes

[30] "A high granularity scintillator hadronic-calorimeter with SiPM readout for a linear collider detector." V. Andreev et al, NIM A540, 2005.

[31] http://www.lcsim.org/software/slic/doxygen/html/.

2.3 SiD Magnet Subsystem

The magnet consists of the following subsystems:

1. a large 5 T superconducting solenoid with a separated iron plate flux return that is integral with the muon tracking system,
2. a power supply, a pressurized water cooled dump resistor, and a conventional mechanical dump switch that move with the detector,
3. a helium liquefier that supplies 4.5 K LHe to both the solenoid and to a pair of 2 K cold boxes for each of the superconducting focusing quadrupoles,
4. oil flooded helium screw compressors with oil removal and helium gas storage, all located on the surface,
5. a superconducting Detector Integrated "anti" Dipole (antiDID), and
6. two superconducting final focus quadrupoles (not discussed here).

2.3.1 Superconducting Solenoid

The superconducting solenoid is an expensive and technically challenging component to procure. Its design is based on the engineering philosophy, experience and details used for the successful 4 T CERN CMS superconducting solenoid, the largest in the world. Thus a direct comparison is warranted, with major parameters listed Table 2.6. The now standard high-purity aluminum superconductor stabilization, with indirect LHe cooling, technique will be used. The CMS individual self-supporting winding turn design philosophy is used for SiD, and is even more important due to the higher field and the increased radial softness of six layers versus four layers. Figure 2.36 shows a cross section of the SiD magnet.

The SiD solenoid has a stored energy per unit cold mass of 12 kJ/kg, which is only slightly larger than the CMS value. This value is close to the upper bound in which this type of large aluminum dominated magnet can be operated in a fail-safe manner if the quench detection or energy extraction circuit were to fail. This specific energy density yields an average magnet temperature of 130 K. Prudent engineering for the SiD solenoid dictates that the total volume of aluminum stabilizer/structure cannot be reduced significantly relative to the present baseline design.

The present flux return design has assumed that field uniformity will not require shims or size-graded conductors, but this issue will be revisited once forward tracking studies have been conducted with a realistic field map. Fringe field requirements are set at 100 Gauss at 1 m from the iron surface. Two-dimensional and three-dimensional ANSYS magnetic field calculations of the magnet were performed; the resulting field shape in the central region of the detector is shown in Figure 2.37. Eleven 20 cm thick iron plates with 4 cm gaps form both the barrel and endcap portions of the flux return. There is also a 4 cm gap between the

Table 2.6: SiD and CMS superconducting solenoid comparison.

Quantity	**SiD**	**CMS**	**Units**
Central field	5.0	4.0	T
Stored energy	1.56	2.69	GJ
Stored energy per unit cold mass	12	11.6	kJ/kg
Operating current	17.75	19.2	kA
Inductance	9.9	14.2	H
Fast discharge voltage to ground	300	300	V
Number of layers	6	4	
Total number of turns	1457	2168	
Peak field on superconductor	5.75	4.6	T
N° CMS superconductor strands	36	32	
% of short sample	32	33	
Temperature stability margin	1.6	1.8	K
Total mass of solenoid	125	220	Metric ton
Rmin cryostat	2.591	2.97	m
Rmin coil	2.731	3.18	m
Rmax cryostat	3.392	3.78	m
Rmax coil	3.112	3.49	m
Zmax cryostat	$\pm$3.033	$\pm$6.5	m
Zmax coil	$\pm$2.793	$\pm$6.2	m
Operating temperature	4.5	4.5	K
Cooling method	Forced flow	Thermosiphon	

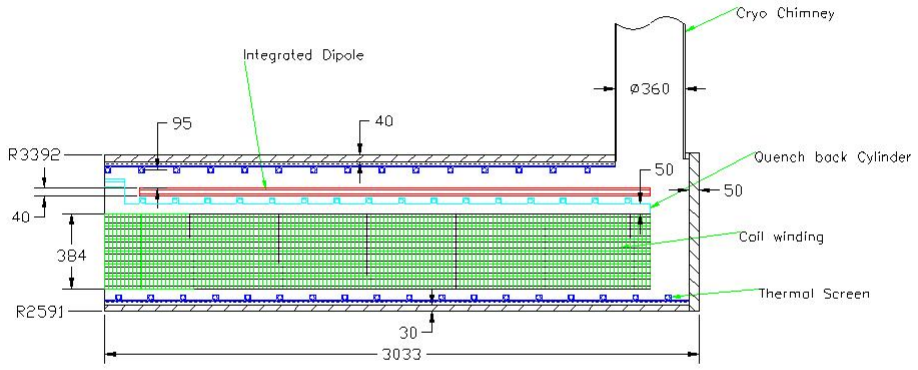

Figure 2.36: Longitudinal half-section view of SiD superconducting solenoid with winding/quench-back cylinder/LHe cooling tubes, cryostat, thermal shields, and anti-DID.

barrel and endcaps. Magnet field optimization studies are underway to improve uniformity while meeting the fringe field requirements.

The CMS conductor forms a fall-back option for SiD. All magnet ANSYS finite element stress analysis to date has been with this conductor. However a more advanced, and most likely cheaper, conductor is being pursued and is proposed here. It is based on dilute high-purity aluminum alloys, such as Al-0.1%Ni, which have been studied more extensively since CMS and were used in the ATLAS central solenoid. Figure 2.38 shows a photo of the CMS conductor and an advanced SiD conductor design using Al-0.1%Ni and a novel internal high strength stainless steel reinforcement. An ANSYS coupled transient electromagnetic and thermal diffusion model is being used to evaluate conductor stability. With large-size high-purity aluminum-stabilized superconductors, the current is slow to diffuse into the aluminum during a temperature excursion. Thus a higher resistivity, and therefore higher strength, aluminum stabilizer can have stability margins equal to a conductor with lower resistivity aluminum. A stability margin similar to CMS will be used. ANSYS is also being used to evaluate strength and bending stiffness for coil winding. Compared to CMS this advanced conductor has reduced bending stiffness that facilitates winding. Other conductor stabilizer possibilities are also under consideration and study. These include TiB2 grain refinement, aluminum matrix composites, and cold working via the equal area angle extrusion process.

The superconductor will be internally wound onto two precise aluminum 5083-H321 mandrels. All CMS winding procedures such as conductor milling to size, cleaning, and taping will be employed. CMS epoxy vacuum impregnation and mandrel joining techniques will be

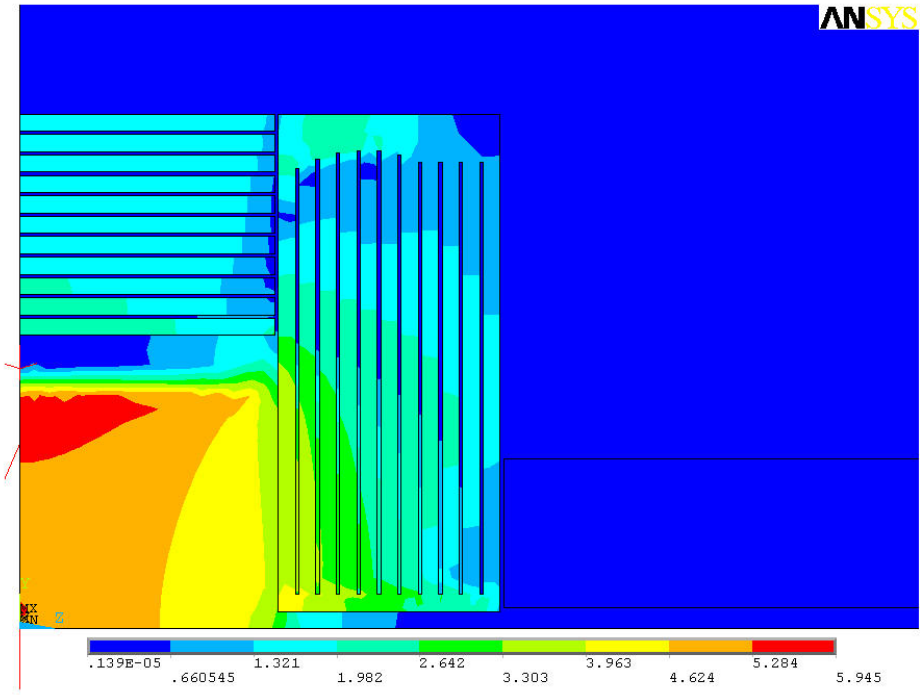

Figure 2.37: SiD central field contours in |B|, shown by intensity scale. The iron Pacman is included and shown as the rectangle in the lower right.

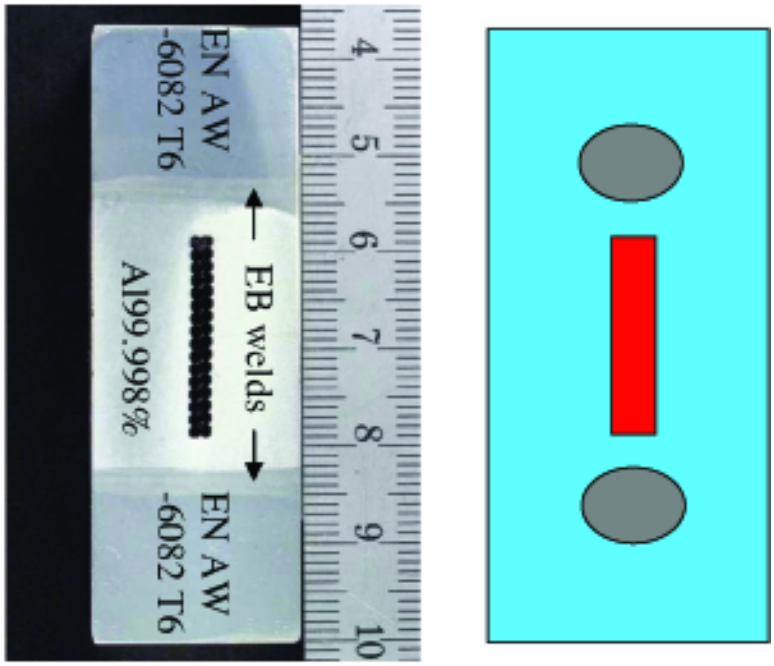

Figure 2.38: Photo of CMS conductor and proposed SiD conductor.

used. CMS conductor splicing methods shall also be used. CMS coil-winding experience will significantly reduce SiD time and expense for setting up and commissioning the coil winding facility, and vacuum impregnation will take place at the vendor's facility. The vendor will probably also perform the initial assembly, cool down, and low-current checkout. The magnet will be shipped as two separate coils and a vacuum shell.

A comparison was made via ANSYS studies of the SiD and CMS solenoid stresses, deflections and forces. All stresses are evaluated after cool down and energization. For this comparison the CMS conductor was used in the SiD analysis. Note that all stress and deflections are very similar for the two coils.

Table 2.7: Mechanical Comparison of SiD and CMS Solenoids.

Quantity	**SiD**	**CMS**	Units
Von Mises stress in high-purity aluminum	22.4	22	MPa
Von Mises Stress in Structural Aluminum	165	145	MPa
Von Mises Stress in Rutherford cable	132	128	MPa
Maximum radial displacement	5.9	~ 5	mm
Maximum axial displacement	2.9	~ 3.5	mm
Maximum shear stress in insulation	22.6	21	MPa
Radial decentering force	38	31	kN/mm
Axial decentering force	230	85	kN/mm

The power supply, dump resistor and dump switch are attached on the side of the detector near the top. These three components are arranged to be in line with the solenoid current leads, thereby minimizing the buswork. The power supply and mechanical dump switch are standard components which will be procured from outside vendors. A novel, compact, pressurized-water-cooled dump resistor will be used instead of a very large air-cooled resistor, such as the type used for CMS and other large superconducting magnets. In the worse case, in which all 1.56 GJ of stored energy are deposited as heat in the water of the resistor, an ASME-coated vessel, holding 3100 l of water, will rise in temperature to a conservative design value of 150 degC at 0.48 MPa. Correct dimensioning of the stainless steel resistor element ensures that boiling heat transfer is only 1/3 of the peak nucleate boiling flux at the metal/water interface. A 1.50 m diameter $\times$ 3.5 m tall cylindrical tank could be used. This design concept eliminates long runs of 18 kA cable to an air cooled resistor, or long vent pipes to the surface of boiling water vapor. Internal connections will provide for both fast dump and normal slow dump modes. A center tap grounding wire is attached to the electrical center of the resistor.

Quench protection safety will less stringent than for the CMS coil due to the lower stored energy and inductance. A conservative 300 V to center-tapped ground is chosen. Experimental tests and computer simulations show that the CMS quench propagation velocity around one complete turn is faster than turn to turn quench propagation through the insulation. Because we have chosen identical CMS conductor size and insulation thickness, with very similar conductor electrical and thermal properties, peak temperatures will be less than

the CMS design of 80 K with dump resistor, but equal to the CMS design of 130 K with dump breaker failure. Both SiD and CMS safety rely on the winding mandrel serving as a quench-back cylinder for spreading the load on the outer layer and absorbing some of the stored energy.

2.3.2 Cryostat and Magnet Iron

The cryostat, $\sim$ 60 K thermal shield, current leads, tie rods, and instrumentation will all be designed using standard cryogenic techniques. Current leads will be very similar to the CMS design. Vacuum shells will be built according to the ASME pressure vessel code design rules. Two separate iron penetrations will be used, a 70 cm $\times$ 40 cm chimney for the current leads and 36 cm diameter chimney for the cryogenic plumbing. Vacuum pump-down will take place through both chimneys. Tie rods will be segmented into three different systems based on direction (axial, vertical and radial), as in the CMS and BaBar cases. They will be manufactured from Inconel 718 or Ti-5Al2.5Sn ELI. Radial and vertical loads will be carried to the cryostat outer wall. Axial loads will be carried to the cryostat end plates. In all cases, the tie rod systems are substantially stiffer than the magnetic spring constant.

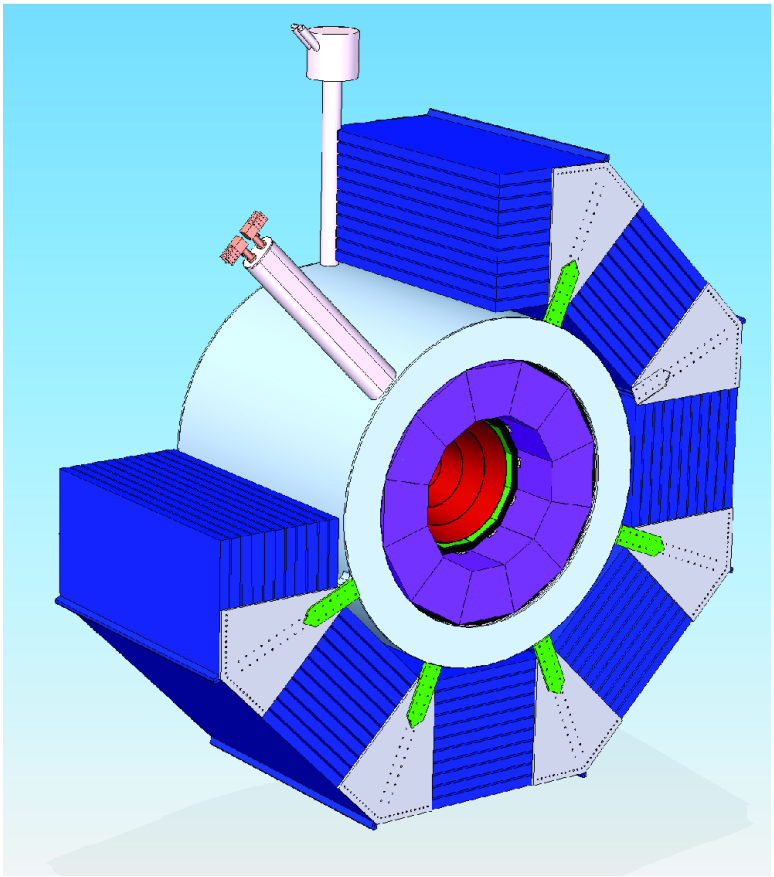

Figure 2.39: Solenoid shown with valve box, current leads and attachments to barrel iron plates.

A helium refrigerator/liquefier is required to provide approximately 1 kW of refrigeration at 4.5 K. Flexible transfer lines connect the liquefier to the detector valve box to enable push-pull motion. In order to minimize the length of the transfer line, the liquefier will be mounted at the same level as the top of the solenoid. The liquefier supplies forced flows of 4.5 K saturated LHe and 40-80 K helium gas. The latter flow is for the thermal shield and for the thermal intercepts of the support rods. The liquefier is a custom-built commercial product whose detailed design and construction will be carried out by industry as part of the complete cryo plant procurement. A 5000 LHe storage dewar is stationed next to the refrigerator liquefier and can almost be considered part of the liquefier. It serves as a pressure buffer for forced flow operation and as a LHe supply reservoir during liquefier down times. This technique was used successfully for a decade of running the SC solenoid for the BaBar detector.

The detector valve box (Figure 2.39)is used to minimize flexible connections between the detector and the refrigerator. It also serves as the distribution point for supply of LHe to the two final-focus magnet 2 K cold boxes that are fixed on the detector.

It is expected that both ILC detectors will require similar size cryogenic plants. In order to maintain flexibility, we propose that each detector have its own complete cryogenic system which includes all the components discussed above. However, the design should allow connections between these plants at both the warm compressor level and at the output of the main cold boxes. These cross connects establish a redundant system for operations and could provide additional refrigeration capacity when cooling one of the magnets down from room temperature.

The redundant 1250 kW helium compressors will be oil-flooded screw compressors. Compressors and their associated oil removal equipment are commercially available (though typically custom modified). The compressors will be on the surface to minimize vibration and noise as well as to allow easier access. The compressors will be connected to the Cold Box by a 14 -16 bar helium supply and ∼1.05 bar helium return lines. Necessary LN2 and helium gas buffer/storage tanks will be located near the compressors.

2.3.3 Detector Integrated anti-Dipole (anti-DID)

The 550 kA turn Detector Integrated "anti" Dipole (DID) generates a ∼600 G dipole field from each of the coils. These dipole coils are to be mounted between the end flanges of the outer winding mandrel of the solenoid. They will be placed just above the solenoid LHe cooling pipes. Solenoid conductor splices will be secured in the open spaces of the dipole coils. The most likely method of fabrication is to flat wind the dipole pancakes in an aluminum case, then bend them to the correct radius and impregnate the vacuum with a filled epoxy resin. Dozens of bolted connections to the winding mandrel, with additional thermal straps, will guarantee mechanical restraint and adequate cooling.

The dipole coils are to be wound with co-extrusion of a high-purity aluminum and a CMS single superconducting strand. Four layers of 197 turns of 3 mm × 4 mm superconductor are proposed, with 0.5 mm of fiberglass cloth between each turn and each layer. They operate at 700 A, corresponding to 1/3 of the critical current. The stored energy for an independently

powered anti-DID is in the range of 150 kJ. Because the stored energy is so small, the volume fraction of high-purity aluminum, relative to superconductor, needed for safe energy extraction during a quench has been reduced from the CMS value (12.4) to 10.3. Forces on each of the four coils are rather large in sum (4100 kN radial and 7800 kN axial) but they are spread uniformly and are manageable. Figure 2.40 shows the dipole size, location and magnetic field profile.

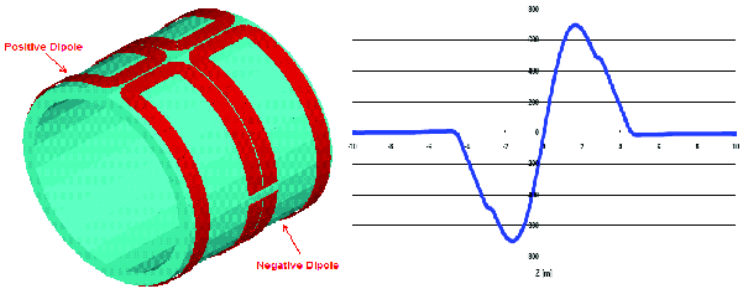

Figure 2.40: Anti-DID (left) with magnetic field profile (right); the dipole field is horizontal.

On the basis of the CMS experience are no show stoppers for the superconducting solenoid or any other magnet system component. It remains to implement the CMS construction techniques, examine other possible conductor choices, and refine decisions to reduce cost and complexity and improve safety margins.

2.4 Muon System

2.4.1 Overview

The SiD muon system is designed to identify muons from the interaction point with high efficiency and to reject almost all hadrons (primarily pions and kaons). The muon detectors will be installed in the gaps between steel layers of the solenoid flux return. The required position and rate capabilities of the detectors are modest and can be met by several different detector technologies. The baseline design uses double layers of resistive plate chambers(RPC). Also under consideration are extruded scintillator strips read out by silicon photomultipliers (SiPMS). Cost, reliability and physics capabilities will determine the preferred choice.

2.4.2 Design

The muon system will start outside of the highly segmented electromagnetic and hadronic calorimeters and the 5T solenoid cryostat at a radius of 3.40 m. In the baseline design shown in Figure 2.41a the flux return is divided into eleven layers of 20 cm steel in an octagonal barrel geometry. Endcaps of eleven 20 cm thick steel octagons will cap both ends of the barrel. The muon detectors will be inserted in the 4 cm gaps between the plates. In the barrel a detector layer is also inserted between the solenoid and the first steel plate. The first barrel layer is approximately 2.8 m by 6.0 m and the last layer is ∼4.8 m by 6.0 m. The total detector area needed in the barrel is ∼2050 m^2. As shown in Figure 2.41b, the endcap detectors will be subdivided into rectangular or trapezoidal modules ∼2 m by 6 m. Each endcap has a total detector area of 1220 m^2.

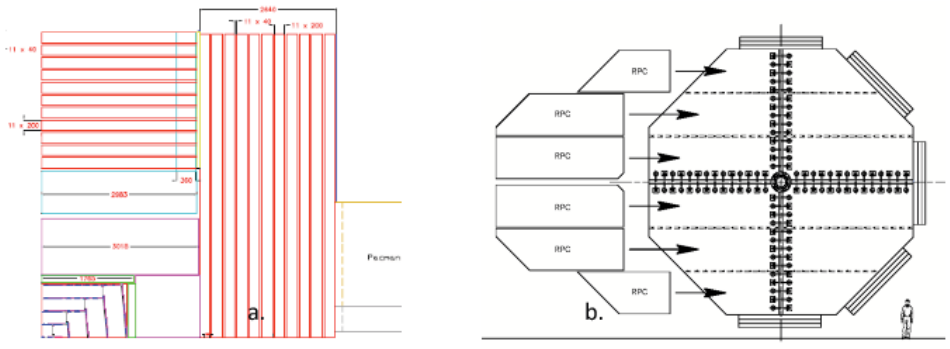

Figure 2.41: (a) Quarter-section of the SiD flux return. (b) Sub-division of the endcap into RPC modules.

2.4.3 Function

SiD muon selection will combine information from the central tracker, calorimeter, and muon detectors to construct 3-dimensional tracks through the entire detector for each muon candidate. Candidates will be required to penetrate a number of interaction lengths consistent

with the muon momentum. In addition, the observed number and position of hits along the fitted track length can be used to further discriminate against hadrons. The first layers of the muon system may also be useful as a tail-catcher for the hadronic calorimeter.

2.4.4 Requirements

To date, physics benchmark/detector studies have been carried out for single muons and pions, Smuon pair production (see Chapter 4) and b-pair production at 500 GeV. The single particle studies were done to develop algorithms to use in determining muon ID efficiency and hadron punch-through probability vs. momentum[1]. The results of these studies show that muon identification efficiency is greater than 96% above a momentum of 4 GeV/c. Muons perpendicular to the e+e- beamline reach the SiD muon system when their momentum exceeds ∼3 GeV/c.

2.4.5 Detector Design

Muon systems characteristically cover large areas and have active layers that are difficult to access or replace. Reliability and low cost are major requirements. Over 2.2 meters of steel thickness will be required for the solenoid flux return, providing 13.2 hadron interaction lengths to filter hadrons emerging from the hadron calorimeter and solenoid. Since the central tracker will measure the muon candidate momentum with high precision, the muon system only needs sufficient position resolution to unambiguously match calorimeter tracks with muon tracks. Present studies indicate that a resolution of ∼1-2 cm is adequate. This can be achieved by two layers of extruded scintillators or RPC pickup strips of ∼4 cm width.

Full optimization of the muon system design has not been completed. Although the total steel thickness is set by the solenoid requirements, the optimum number of detector layers is being studied. We have studied the mis-identification rate of pions between 10-50 GeV/c as a function of the depth in the flux return[2] to check that the present design is thick enough. As shown in Figure 2.42, requiring that the track makes hits in some of the outer layers is sufficient to reduce the pion mis-identification rate to 0.25 %, consistent with the expected level of pion to muon decays. Pending further R&D it may be possible to eliminate detector layers without compromising either performance or reliability of the system.

2.4.6 Backgrounds

Backgrounds in the muon system are expected to come primarily from beam losses upstream of the detector. The muon system is shielded from backgrounds generated at the collision point or along the internal beam lines by the calorimeters, which are greater than 5 absorption lengths thick. Therefore only penetrating backgrounds, such as high-energy muons or neutrons, affect the barrel muon detectors. Calculations by N. Mokhov et al[3] of the expected background from muons produced by collimators near the detector hall predict a rate of 0.8 muons/cm^{2}per pulse train (∼1 ms) without muon spoilers, which is reduced to 3*10^{-3}/cm^2

per pulse train with the addition of muon spoilers. These background rates are significantly higher than the typical RPC noise rate of 1 kHz/m^2(10^{-4}/cm^2 per pulse train). Physics backgrounds from two-photon processes producing hadrons or muon pairs significantly increase the expected signal rate in the endcap detectors near the beam-line. At a radius of 30 cm the expected rate from muons above 2 GeV is < 0.03/cm^2 per pulse train. The endcap detectors can in addition be hit by electromagnetic shower debris from local beam losses and may require additional shielding around the beam-line.

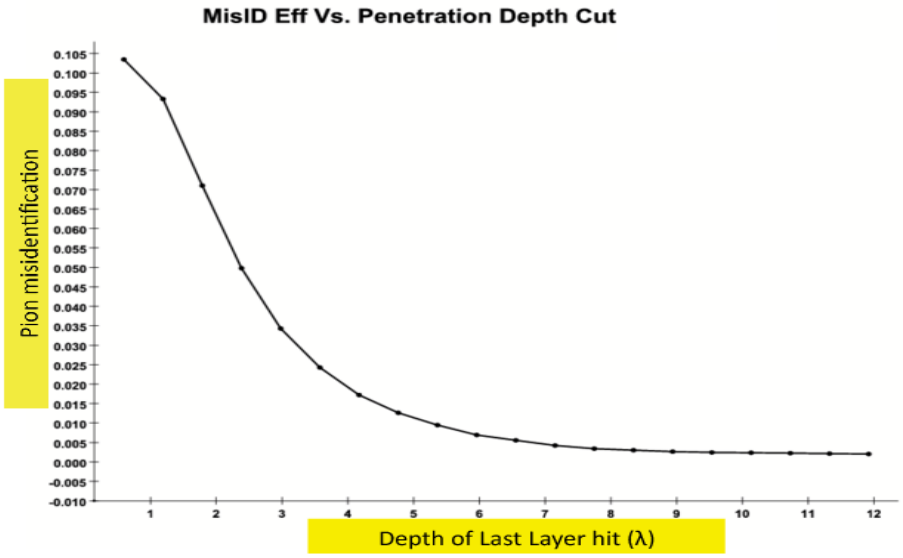

Figure 2.42: Fraction of pions between 10-50GeV/c that produce a hit as a function of the number of interaction lengths traversed in the muon system.

2.4.7 Resistive Plate Chambers

RPCs have often been used as muon detectors (BaBar and BELLE) and will be used in ATLAS ans CMS. RPCs are inexpensive to build and can be easily constructed in a variety of shapes and sizes. RPCs use fluorocarbon gases which may be regulated in the future as they are greenhouse warming gases and require nontrivial gas delivery systems. The major concern with RPCs are their aging characteristics (BaBar was forced to replace its original RPCs and BELLE had startup problems). However, significant progress has been made in recent years in understanding aging mechanisms. Many of the aging processes are proportional to current passing through the gas gap. LHC detectors will run in avalanche mode which has much lower charge per track. Aging studies of LHC prototypes have shown good stability even at the high background rates expected (100 Hz/cm^2) at the LHC.The 2^{nd} generation BaBar RPCs and the Belle RPCs have preformed reliably at low signal rates (<0.2 Hz/cm^2). SiD RPCs will run in avalanche mode and be subjected to backgrounds of <0.15 Hz/cm^2 near the beamline and <0.015 Hz/cm^2 elsewhere.

The baseline RPC detector planes will be made by assembling single gap RPC HV chambers(∼1m by 2 m) into modules of the required size to fill each slot in the octagonal

barrel or endcaps. Each barrel layer will be split into three full length modules to allow removal even if the gusset plates holding the steel octants are in place. The supports for the endcap modules will be staggered at different heights to reduce projective dead spaces. If the single gap efficiency is 90%, then an average layer efficiency of 93% can be achieved. Orthogonal pickup strips of a ∼3 cm pitch will cover the sides of each HV module producing two x-y positions per layer. Muon hits will be digitized by a lower channel count(64-128) version of the KPIX chip mounted on a transition board containing circuit protection diodes. The strip area will be limited to < 300 cm^2 so less than 1 background hit is expected per train under the worst background conditions. Use of the KPIX time information will reduce the expected background occupancy per strip to $< 0.04\%$. Smaller segmentation maybe necessary near the beamline to keep the occupancy in this region equally low. One KPIX chip will digitize a side of a module. Since the total area of double layer chambers will be ∼4500 m^2 and the average module is ∼2 m^2 about 4500 RPC modules and 9000 KPIX chips will be needed. One KPIX concentrator board will collect all of the KPIX data from one layer of each barrel octant or endcap quadrant. High voltage, gas, low voltage, and fiberoptic lines will be routed to the end of the barrel or to the periphery of the endcaps and connected to gas manifolds or trunk lines.

2.4.8 Scintillating Strips with SiPM Readout

The MINOS experiment has shown that a strip-scintillator detector works well for identifying muons and for measuring hadronic energy in neutrino interactions. A MINOS type scintillator detector design would provide muon identification and could be used to measure the tails of late developing or highly energetic hadron showers. However, the MAPMT readout design utilized by MINOS is a poor match to the geometry of an ILC detector and would require long runs of optical fiber to get signals to MAPMTs outside of the detector B field. The recent development of Silicon PhotoMultipliers (SiPM or Si avalanche photo-diodes) allows a much simpler design in which the SiPM is directly coupled to the wave-length shifting fiber embedded in the scintillating strip. SiD is pursuing a design with SiPMs as an alternate technology for the muon system detector. The quantum efficiency of SiPM detectors is about twice that of vacuum tube photomultipliers, yielding 25 photoelectrons per minimum-ionizing particle (mip) in recent beam tests. This high efficiency makes possible the use of long scintillating strip/fibers with readouts at only one end which reduce the total number of channels.

A possible layout of a forward muon scintillator system divides each layer into quadrants of two strip planes rotated by 90^o relative to each other. Each strip plane would contain ∼ 142 strips 4.1 cm wide. There would be 59 strips 5.28m in length and 83 strips that vary in length from 5.8 m to 2.4 m. The 20 double planes, ten forward and ten backward, would result in 22,700 forward/backward single ended readout strips.

Muon scintillator-strip detectors located in the Fe barrel octant gaps could be arranged in planes of u-v strips which are oriented at $\pm\ 45^o$ to the long axis of the barrel or, alternatively, parallel to the edges in x-y fashion. With the SiPM yield of photoelectrons per mip it may be possible to reduce the multiplicity of observed particles in the z-direction axial strips by cutting the axial strips into two pieces, each 3.03m in length, which results in 16,300

signal sources. In the perpendicular direction, with an octagonal barrel geometry it takes eight strips to circumscribe the beam line. With 10 concentric gaps in the barrel Fe and one inner layer of detectors there would be 13,000 circumferential strips. Thus there would be a total of 29,300 barrel single-ended readout strips. The total forward/backward and barrel signals with this geometry would result in 52,000 electronic channels.

2.4.9 Muon System R&D

The primary aim of the muon system R&D is to validate both possible detector choices and to develop cost-effective read-out designs. The RPC R&D effort is focused on adapting the KPIX ADC to digitize RPC signals[4]. Other studies will measure the aging characteristics of IHEP RPCs and search for gas mixtures or cathode materials with better aging properties[5]. The groups involved with the scintillating strip option will evaluate SiPM devices from different manufacturers and develop mounting, temperature control, and calibration designs[6]. Both the KPIX and SiPM efforts will be applicable to the HCAL RPC and scintillator detector options. Further details of the Muon System R&D plans can be found in the online appendices and the individual R&D proposals [4, 5, 6].

References

[1] Milstene, C. , H.E. Fisk, A. Para (Fermilab), "Tests of the Charged Particle Stepper with Muons", **FERMILAB-TM-2274-E**, Oct 2004. 17pp.

[2] Q. Zhang, "Primary Muon ID Results"
http://silicondetector.org/display/SiD/Muon+Talks (unpublished) 2008. Band, H. R. and H. E. Fisk,"SiD Muon System,"
http://silicondetector.org/download/attachments/33358377
SiD_Muon_Oxford_hrb.ppt,(unpublished) Apr 2008.

[3] Mokhov, N. V., A. I. Drozhdin, M. A. Kostin, "*Beam Collimation and Machine Detector Interface at the International Linear Collider*, " PAC 2005 Paper **Fermilab-Conf-05-154-AD** May 2005.

[4] H. R. Band,"*RPC/KPiX Studies for Use in Linear Collider Detectors*,"
http://silicondetector.org/download/attachments/37323762/RPC_Wisc.pdf

[5] C. Lu *et al.* "*Aging Study for SiD Hcal and Muon System RPCs*,"
http://silicondetector.org/download/attachments/37323762/
RPC_Princeton_k.pdf

[6] P. Karchin *et al.*,"*Scintillator Based Muon System & Tail-CatcherR&D*",
http://silicondetector.org/download/attachments/37323762/
ILC_Muon_2009_proposal_v2.pdf

2.5 Forward Detector

The forward region is defined as polar angles $|\cos\theta| > 0.99$ ($\theta < 140$mrad) forward of the SiD Endcap ECAL. The angular coverage is completed by two detectors, the Luminosity Calorimeter (LumiCal) and the Beam Calorimeter (BeamCal). The physics missions in this region are:

- precision measurement of the integrated luminosity using small-angle Bhabha scattering (LumiCal). To measure cross section of an event sample $O(10^6)$ expected for $e^+e^- \rightarrow W^+W^-$ in 5 years with 500 fb^{-1}, the goal is to measure the luminosity with an accuracy better than 10^{-3}.
- precise determination of the luminosity spectrum by measuring the acolinearity angle of Bhabha scattering (LumiCal). Due to the beamstrahlung emission the colliding beams loose energies before collision, and the center-of-mass energy is no longer monochromatic. The luminosity spectrum affects mass measurements and threshold scan.
- extend the calorimeter hermeticity into the small angles for physics searches (LumiCal and BeamCal). An excellent hermeticity is essential as many new-physics reactions are accompanied with a large missing energy.
- instantaneous luminosity measurement using beamstrahlung pairs (BeamCal).
- two photon veto for new particle searches (BeamCal).

The detector challenges are good energy resolution, radiation hardness, interfacing with the final focus elements, high occupancy rate requiring special readout, and performing the physics measurements in the presence of the very high background in the forward direction.

2.5.1 Design criteria

2.5.1.1 LumiCal Physics Requirements

The lowest order Bhabha cross-section for t channel one photon exchange is given by:

$$\frac{d\sigma}{d\Omega} = \frac{\alpha^2}{8E^2}\left(\frac{1+\cos^2\theta/2}{\sin^4\theta/2}\right)$$

We use this simple formula to estimate the polar angle coverage needed, although the complete electro-weak s and t channel cross-section will later be needed in order to do the physics. The number of Bhabha events per bunch crossing for a detector with minimum and maximum polar angle coverage θ_{min} and θ_{max} (in mrad) is:

$$N = 0.5\text{pb}\frac{\text{L}}{\text{R}}\int_{\theta_{\min}}^{\theta_{\max}}\frac{\text{dcos}\theta}{\sin^4\theta/2} \sim 8\left(\frac{1}{\theta^2_{\min}} - \frac{1}{\theta^2_{\max}}\right)$$

for $\sqrt{s}$=0.5 TeV, L=$2\times10^{34}\text{cm}^{-2}\text{s}^{-1}$, and bunch crossing rate R=$1.4\times10^4\text{s}^{-1}$. Our goal is to measure the luminosity normalization with an accuracy of several 10^{-4} for $\sqrt{s}$=0.5 TeV. To do this one needs $\approx 10^8$ events collected over $\approx 10^7$ s, or about ten events per second. One can then calculate the absolute luminosity with $\approx 10\%$ statistical error every several minutes during the run. With a bunch crossing rate of $1.4\times10^4\text{s}^{-1}$, we need $> 10^{-3}$ events per bunch crossing. To achieve this statistical accuracy, we start the fiducial region for the precision luminosity measurement well away from the beamstrahlung pair edge at θ_{min}=20mrad, with a fiducial region beginning at 46 mrad, which gives $\approx 2\times10^{-3}$ events per bunch crossing.

2.5.1.2 Luminosity precision and detector alignment

The integrated luminosity, L is measured using the number of Bhabha events N and the Bhabha scattering cross section σ in the detector fiducial region as $L = N/\sigma$. Since the Bhabha cross section is $\sigma \sim 1/\theta^3$, the luminosity precision can be expressed as

$$\frac{\Delta L}{L} = \frac{2\Delta\theta}{\theta_{min}},$$

where $\Delta\theta$ is a systematic error (bias) in polar angle measurement and θ_{min} is the minimum polar angle of the fiducial region. Because of the steep angular dependence, the precision of the minimum polar angle measurement determines the luminosity precision. To reach the luminosity precision goal of 10^{-3}, the polar angle must be measured with a precision $\Delta\theta <$ 0.02 mrad and the radial positions of the sensors must be controlled within 30 μm relative to the IP.

2.5.1.3 Monitoring the Instantaneous Luminosity with BeamCal

The colliding electron and positron bunches at the ILC experience intense electromagnetic fields as they pass each other. These fields generate large Lorentz forces, which cause radiation of gammas called beamstrahlung. A small fraction of the beamstrahlung gammas convert into pairs. Under the ILC Nominal beam parameters at $\sqrt{s} = 0.5$ TeV, approximately 75k e^+/e^- are generated. The BeamCal intercepts $\approx 3\times10^4$ beamstrahlung pairs of average energy ≈0.7 GeV per bunch crossing when the bunches have maximum overlap. Since the number of pairs is directly proportional to the beam overlap, the instantaneous luminosity can be monitored by detecting pairs in the BeamCal. Our goal is at the ten percent level per beam crossing.

The Detector Integrated Dipole (DID)[2] plays an important role in controlling the beamstrahlung pairs. The DID is a pair of coils wound on the detector solenoid, which

creates a dipole field whose intensity varies in z like a sine function. In the so-called Anti-DID configuration, the DID field effectively compensates the crossing angle for the outgoing beam and directs the low energy pairs into the extraction aperture, reducing the total pair energy hitting the BeamCal from 20 TeV to 10 TeV.

2.5.1.4 Detector Hermeticity

By hermeticity we mean complete solid angle coverage down to small polar angles, avoiding cracks and dead areas, which will enable accurate measurement of the transverse momentum balance in the event. This is achieved by good energy resolution, avoiding cracks, dead areas, and by covering down to small polar angles. The measurement of $e^+e^- \rightarrow slepton\ pairs$ in the presence of two photon background has been given as the performance detector design criteria for hermeticity[1]. In the stau production and decay,

$$e^+e^- \rightarrow \bar{\tau}\bar{\tau} \rightarrow \tau^+\chi^0\tau^-\chi^0$$

the χ^0 is the LSP and escapes the detector. Under the SUSY dark matter scenario, the mass difference between stau and the LSP becomes less than 10 GeV, the missing P_T is less and the measurements become more difficult. The main background comes from the two-photon process $e^+e^- \rightarrow e^+e^-X$, where X is ee, $\mu\mu$, or $\tau\tau$ for the slepton search. This background process has no missing P_T; however, if we miss both electrons then the missing $P_T < 2\theta_{min}E_{beam}$. This is the kinematic limit. Generally one photon is on-shell, so usually the missing $P_T < \theta_{min}E_{beam}$. The search region in the missing P_T is determined by how small angle the two-photon electrons are detected and thereby vetoed. The electron detection must be made in the BeamCal where the beamstrahlung pairs deposit 10 TeV of energy.

2.5.1.5 Dynamic range and mip sensitivity

While minimum ionizing particles (MIP) deposit 93 keV in a 320 μm-thick Si layer, a 250 GeV electron can deposit up to 160 MeV or 1700 MIP equivalents in a single cell near shower maximum. If we want a 100% MIP sensitivity, the S/N ratio for MIP should be greater than 10, and the dynamic range of electronics need to be at least 17,000. This dynamic range can be achieved by using a 10-bit ADC with two gain settings.

2.5.1.6 Radiation hardness

The beamstrahlung pairs will hit the BeamCal, depositing 10 TeV of energy every bunch crossing. Sensor electronics could be damaged by the energy deposition, and sensor displacement damage could be caused by the resulting neutrons. The radiation dose varies significantly with radius, and a maximum dose of up to 100 MRad/year is expected at near the beampipe. The main source of neutrons is from secondary photons in the energy range 5-30 MeV, which excite the giant nuclear dipole resonance. The neutron flux is approximately $5 \times 10^{13}\mathrm{n/cm}^2$ per year.

2.5.1.7 Occupancy

The issue here is how "deep" we need to make the readout buffer to hold one train of events for the LumiCal. The LumiCal occupancy is studied for the beamstrahlung pairs and two-photon events. The occupancy from the pairs still dominates. In the outer region of the Lumical, $R > 7.5$cm (the 'far LumiCal'), just outside the pair edge, the number of hits will reach 120 hits per bunch train. The number of hits per bunch train decreases to four at approximately $R \sim$10 cm (the 'near LumiCal').

2.5.2 Baseline Design

The layout of the forward region is illustrated in Figure 2.43. The LumiCal covers the polar angles from 40 mrad to 90 mrad, and the BeamCal from 3 mrad to 40 mrad. The conical mask made of 3cm-thick tungsten is located between the LumiCal and BeamCal. When the beamstrahlung pairs hit the BeamCal, low energy secondary particles are generated. The mask shields the SiD central detectors from low energy photons backscattered from the BeamCal. The Low-Z mask made of 13cm-thick Borated-Polyethylene is located in front of the BeamCal. The Low-Z mask reduces the low energy electron and positron albido from the BeamCal by more than an order of magnitude. Borated-Polyethylene also absorbs low energy neutrons produced in the BeamCal and directed toward the IP.

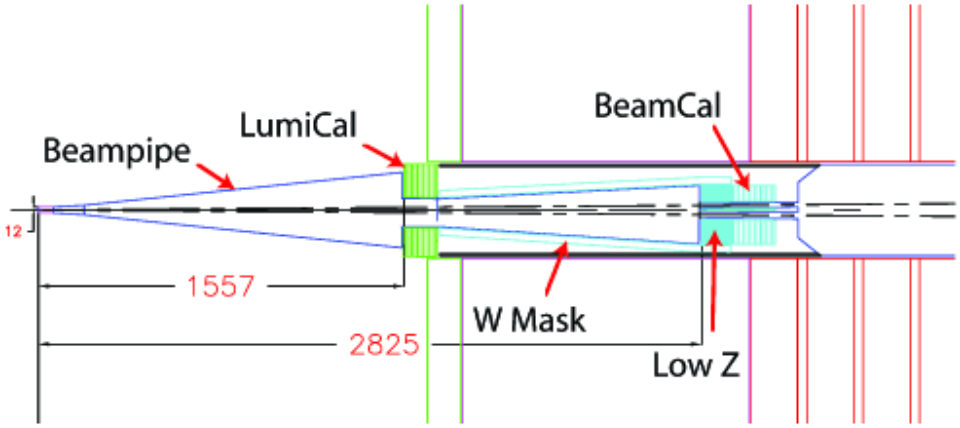

Figure 2.43: Forward region.

The beam pipe at the IP is made of beryllium to minimize multiple scattering. The inner radius is 1.2 cm, and the thickness is 400 μm. The conical section starts at R=1.2 cm, z=6.25 cm, with a cone angle of 103 mrad, which is outside the LumiCal fiducial region. The flared beam pipe design allows particles to exit the beam pipe at normal incidence before entering the LumiCal. The cylindrical beam pipe inside the LumiCal is 6 cm in radius, and is

centered on the extraction beam line. The beam pipe does not intercept the beamstrahlung pairs which are confined within 4 cm radius by the SiD 5 Tesla solenoid.

The entire forward region is supported by the support tube which is cantilevered from the QD0 cryostat. There is a 1 cm gap between the support tube and the endcap door to facilitate the door opening. To minimize the electromagnetic energy loss due to the gap, the LumiCal is 10 cm closer to the IP relative to the ECAL.

The LumiCal consists of two cylindrical C-shaped modules surrounding the beam pipe. The inner radius is 6 cm centered on the extraction beam line with a horizontal offset of $\Delta x = 1.0$ cm (158 cm $\times$ 0.007). The inner radius is dictated by the requirement that no detector intercepts the intense beamstrahlung pairs, which are confined within 4 cm radius by the 5 Tesla solenoid field. The longitudinal structure follows the ECAL design, consisting of 30 alternating layers of tungsten and silicon. The first 20 layers of tungsten each have thickness equivalent to 2.5 mm (or 5/7 radiation length) of pure tungsten. The last 10 layers have double this thickness, making a total depth of about 29 radiation length. The silicon sensors will be made from 6 inch wafers, and the segmentation is illustrated in Figure 2.44. The sensor is segmented in a $R - \phi$ geometry. A fine radial segmentation with 2.5 mm pitch is used to reach the luminosity precision goal of 10^{-3}. The azimuthal division is 36 with each sensor covering 10 degrees. Table 2.8 summarizes the LumiCal parameters.

z	158 - 173 cm
Inner radius	6 cm
Outer Radius	20 cm
Fiducial	46-86 mrad
Tungsten thickness	2.5 mm (20 layers), 5.0 mm (10 layers)
Silicon sensor thickness	320 μm
Radial division	2.5 mm pitch
Azimuthal division	36

Table 2.8: LumiCal Parameters

The BeamCal consists of two cylindrical C-shaped modules split in half horizontally to accommodate the incoming beam line. The inner radius is 2 cm centered on the extraction beam line and the outer radius is 13.5 cm. The longitudinal structure consists of 50 alternating layers of tungsten and silicon. The tungsten thickness is 2.5 mm, making a total depth of 36 radiation lengths. The silicon sensor design based on a 6 inch wafer is shown in Figure 2.45. The inner region less than $R < 7.5$ cm is the area where the beamstrahlung pairs would hit. The segmentation in this region is approximately 5mm $\times$ 5mm, which is roughly one half of the Molière radius. This segmentation is optimized so that tell-tale electrons or positrons from two-photon processes can can be detected in the high beamstrahlung pair background. The outer region $R > 7.5$ cm is the far LumiCal and has the same geometrical segmentation as shown in Figure 2.44.

Currently two electronic readout chips are being developed. The KPiX chip with 1024 channels is designed primarily for the ECAL. The chip has four hits per bunch train to be

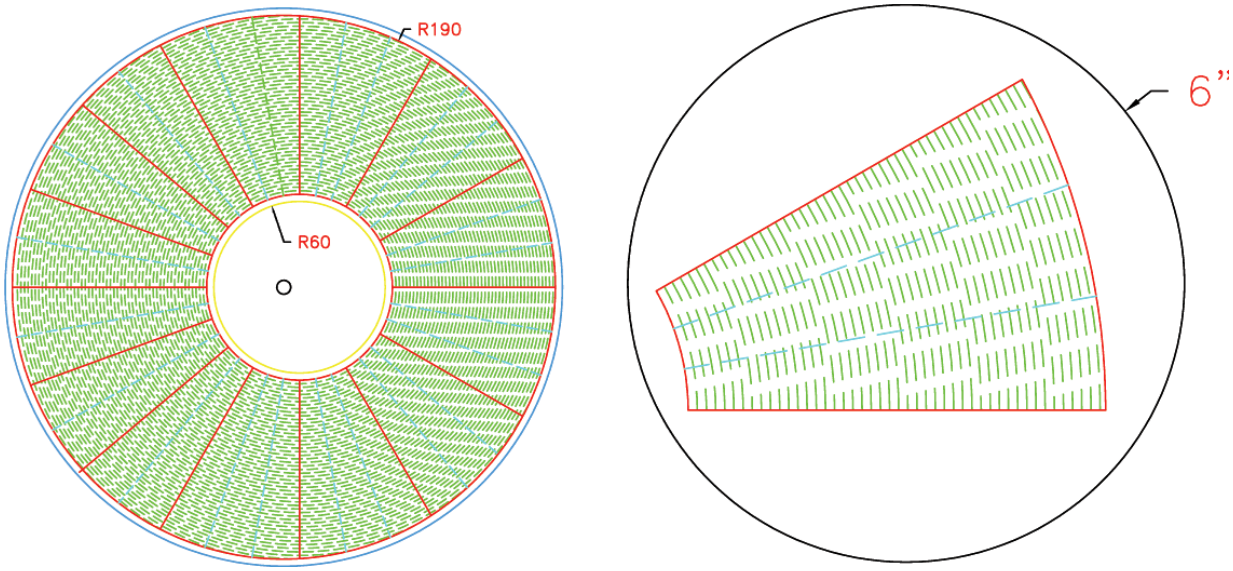

Figure 2.44: LumiCal sensor and segmentation.

stored for each channel. The FCAL chip with 64 channels is designed to handle the 100% occupancy in the BeamCal. The chip has 2820 buffer space so that a complete bunch train can be stored. Although the LumiCal occupancy is not 100%, the LumiCal region smaller than about 10 cm will have more than four hits per bunch train. Therefore, the LumiCal will use the FCAL chip in the inner region and the KPiX chip in the outer region.

2.5.3 Expected Performance

The detector performance has been studied using EGS5 [4], FLUKA [5], and GEANT4 [6] simulation packages. The ILC Nominal beam parameters at $\sqrt{s}$=500 GeV are used. Bhabha scattering is simulated using BHWIDE [7], and beamstrahlung pairs are generated using GUINEA-PIG [8]. The magnetic field map for the SiD 5 Tesla solenoid and the Anti-DID field are used.

2.5.3.1 Energy containment and energy resolution in LumiCal

One of the most important requirements for the LumiCal is the energy containment. If the energy of Bhabha events is not fully contained, some events will be classified as radiative Bhabhas and fail Bhabha event selection criteria, introducing a systematic error. Figure 2.46(a) shows the deposited energy (scaled by the incident energy) distribution as a function of the silicon layer from 1 GeV to 500 GeV electrons. At lower energies, the energy is mostly contained in the front 20 layers. Even at 500 GeV a significant deposition is in the front 20 layers, and the back 10 layers with double tungsten thickness accomplish the energy containment. Figure 2.46(b) shows the energy resolution parameter α in $\Delta E/E = \alpha/\sqrt{E}$ as a function of energy. The energy resolution improves at the lower energies, reaching $15\%/\sqrt{E}$

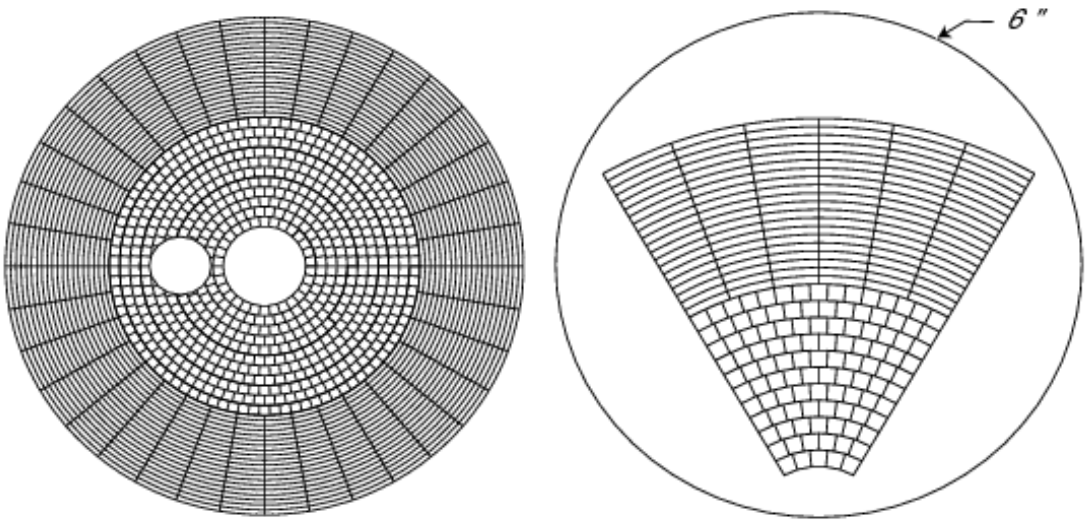

Figure 2.45: BeamCal sensor and segmentation.

at 1 GeV, and still maintains $20\%/\sqrt{E}$ at 500 GeV.

2.5.3.2 Luminosity precision and LumiCal segmentation

The polar angle bias ($\Delta\theta$) and achievable luminosity precision have been studied as a function of sensor segmentation. Each silicon layer is segmented equally in the radial and azimuthal directions, and energy depositions in individual cells are calculated. The polar angle is reconstructed by taking a weighted average of the polar angle θ_i of individual cells with a weight W_i as

$$\theta = \frac{\sum_i \theta_i W_i}{\sum_i W_i}.$$

It is well known that the electromagnetic shower development is non-linear and the weight in linear energy introduces a large bias in coordinate measurements[3] . The bias can be reduced by using so-called logarithmic weight,

$$W_i = \max\{0, \mathrm{C} + \ln(\mathrm{E_i}/\mathrm{E_{total}})\},$$

where E_i is energy deposition in each cell, E_{total} total energy deposition, and C is a constant. The constant provides an effective energy threshold, and only cells with a large enough energy deposition are used in the polar angle reconstruction.

The LumiCal is fully simulated using 250 GeV electrons with a $1/\theta^3$ angular distribution. The reconstructed polar angle, θ_{rec} is compared with the generated one θ_{gen}. The polar

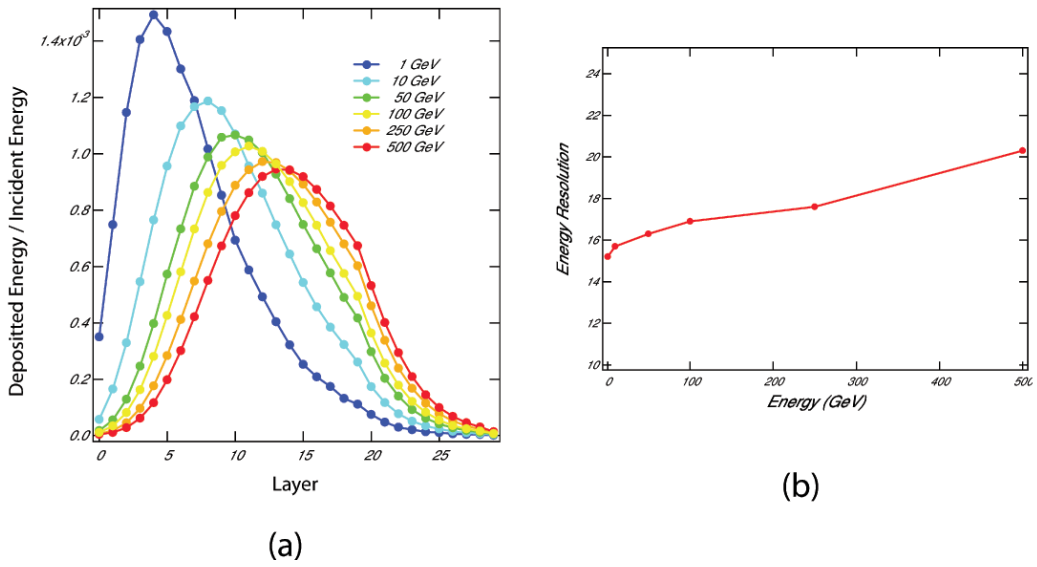

Figure 2.46: (a) Deposited energy in Si layers (b) Energy resolution

angle bias $\Delta\theta$ is calculated by an average value of $\theta_{rec} - \theta_{gen}$, and the angular resolution by the rms value. Table 2.9 shows the angular bias, angular resolution and the luminosity precision as a function of the radial segmentation. The azimuthal segmentation is fixed to 32. The luminosity precision improves as the radial segmentation decreases, and the luminosity precision goal of 10^{-3} can be reached when the radial segmentation is smaller than 3 mm. The dependence on the azimuthal segmentation is studied using a fixed 2.5 mm radial segmentation. Table 2.10 shows the result. The luminosity precision improves as the azimuthal segmentation is decreased, but the improvement is small. Finer azimuthal segmentation would be beneficial for cluster separation.

$\Delta r(mm)$	$\Delta\theta(mrad)$	$\sigma(\theta)(mrad)$	$\Delta L/L$
2.0	0.008	0.042	3.3×10^{-4}
2.5	0.017	0.046	7.9×10^{-4}
3.0	0.023	0.050	1.0×10^{-3}
4.0	0.036	0.058	1.7×10^{-3}
5.0	0.049	0.069	2.2×10^{-3}

Table 2.9: Radial segmentation

2.5.3.3 Bhabha scattering

The LumiCal performance is studied using Bhabha events at $\sqrt{s}$=0.5 TeV. A sample of 10,000 Bhabha events is generated in the CM system by the BHWIDE event generator[7]. Each event is transferred to the laboratory system with the 14 mrad crossing angle, and then processed through the LumiCal simulation. After energy and angle reconstructions,

$N\phi$	$\Delta\theta(mrad)$	$\sigma(\theta)(mrad)$	$\Delta L/L$
16	0.017	0.046	7.7×10^{-4}
32	0.017	0.046	7.9×10^{-4}
48	0.017	0.045	7.6×10^{-3}
64	0.014	0.045	6.6×10^{-3}

Table 2.10: Azimuthal segmentation

the event is transferred back to the CM system to understand the characteristics of Bhabha events. Figure 2.47(a) shows the total energy distribution of the reconstructed e^+ and e^-. The distribution has a peak at 500 GeV as expected, and has a long tail of radiative Bhabha events. The current cluster finder can reconstruct shower energies above 25 GeV. Figure 2.47(b) shows the correlation between the reconstructed e^- and e^+ polar angles. The 14 mrad crossing angle has been properly taken care of. The radial segmentation is visible at small angles.

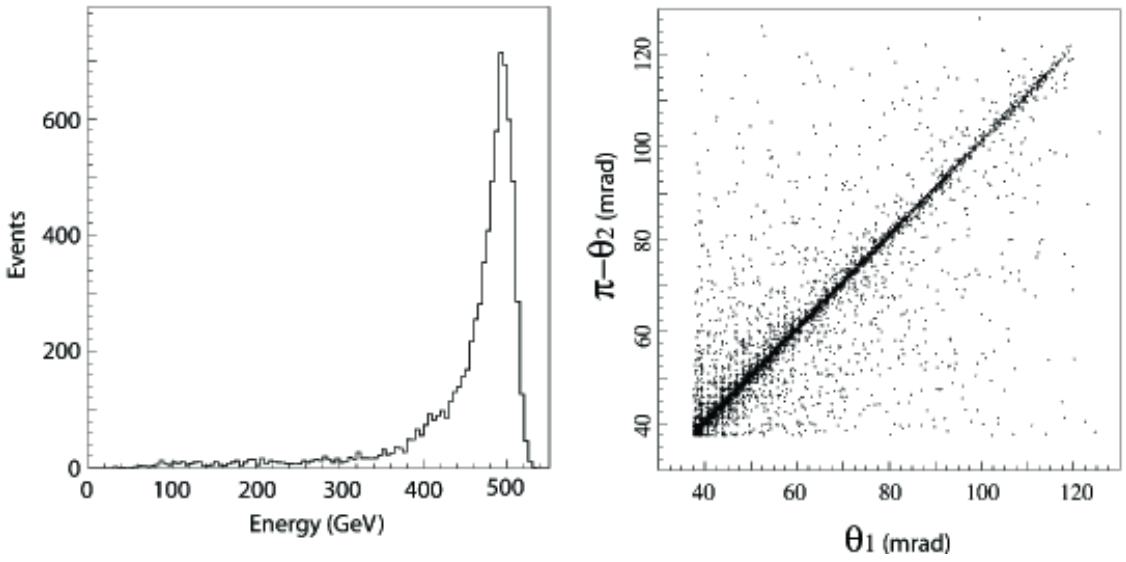

Figure 2.47: (a) Total energy distribution (b) Correlation of e+ and e- polar angles

2.5.4 High energy electron detection in BeamCal

We have studied the ability to identify and reconstruct high energy electron in the presence of beamstrahlung pair background in the BeamCal[9]. The analysis consists of three parts:

1. A lookup table which would correlate the energy and position of a shower on the BeamCal to an incident particle energy. This accounts for the θ and ϕ dependence of shower energy introduced by energy loss down the beampipe, and also incorporates the sampling fraction of the detector.

2. A lookup table of average beamstrahlung depositions which would be used to subtract the expected beamstrahlung energy from the shower of interest.

3. A cluster algorithm which would analyze the total signal on the BeamCal and attempt to isolate the part of the signal that is due to the high energy electron.

BeamCal signals are created by overlaying a high energy electron shower and one bunch crossing of beamstrahlung backgrounds randomly selected from the 10,000 crossings. After subtracting the average beamstrahlung energy, the cluster algorithm reconstructs the high energy electron if the subtracted energy is greater than three sigma of the beamstrahlung energy variation. Since the average energy of individual beamstrahlung pairs hitting the BeamCal is only 1.7 GeV, the beamstrahlung showers are shallower than the showers from high energy electrons. Much better electron detection efficiency is found possible when only energies deposited at depths of 3cm or greater are counted. As the beamstrahlung energy has a strong radial and azimuthal dependence, the detection efficiency is calculated as a function of the distance from the extraction beam axis at three azimuthal angles (0, 90, and 180 degrees). Figure 2.48 shows the detection efficiency as a function of radius in the BeamCal for 50, 100, and 150 GeV electrons. The inefficiency between 30 and 50 mm at phi=180° is due to the incoming beam hole. Since the beamstrahlung background energy is the highest at phi $\approx$ 90° (and 270°), the detection efficiency is lower at this angular region. The efficiency to detect more than 150 GeV electrons is almost 100% up to 8 mrad from the beam axis.

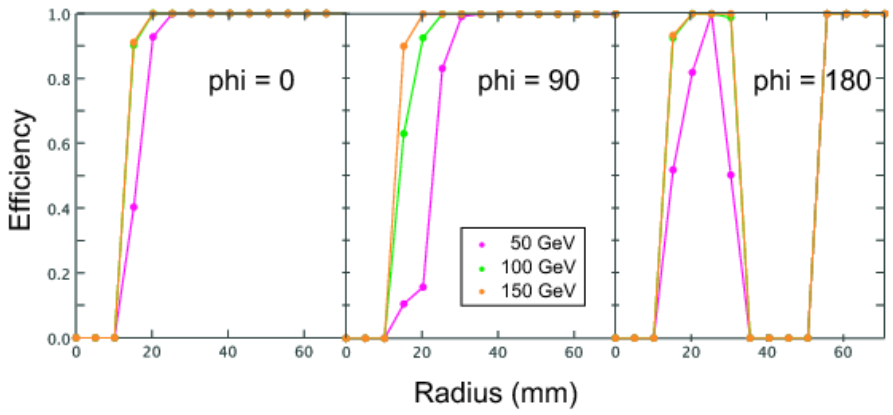

Figure 2.48: Efficiency to reconstruct high energy electrons at three azimuthal angles

2.5.4.1 Calorimeter hermeticity

Calorimeter hermeticity is surveyed using 250 GeV electrons. Figure 2.49 shows the total energy deposition in Silicon layers as a function of $\cos\theta$. The ECAL, LumiCal and BeamCal angular coverages are indicated in the figure. Five sets of simulation are made with different

LumiCal Z locations. When the LumiCal is at the same Z location as the ECAL, a significant energy is lost at $\cos\theta \sim 0.993$. To achieve calorimeter hermeticity, the LumiCal is moved 10 cm closer to the IP.

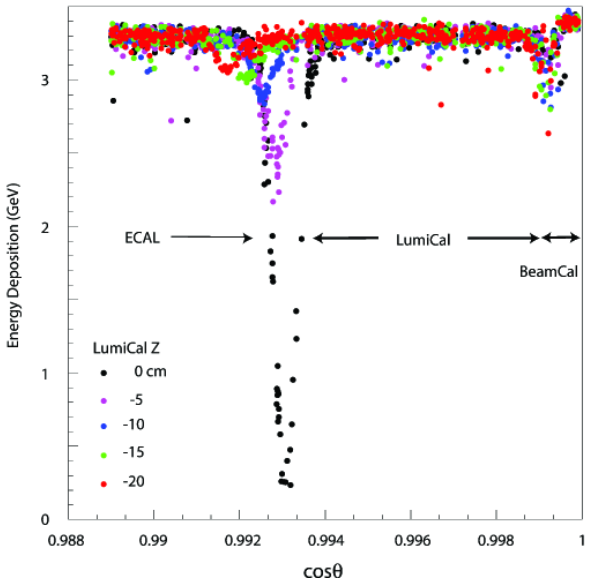

Figure 2.49: Energy deposition in Si layers as a functon of $\cos\theta$

2.5.4.2 Tungsten mask

When the beamstrahlung pairs hit the BeamCal, a large number of secondary photons are produced and about 35k photons per bunch crossing are back scattered. The tungsten mask is to shield the central detector from these low energy photons. Figure 2.50 shows the number of photons penetrating the tungsten mask as a function of the mask thickness. To eliminate the photons, a mask thicker than 6 cm is necessary. But such a thick mask takes up the space and significantly increases the weight. The mask thickness of 3 cm is chosen. Although about 1000 photons are penetrating the mask, they are low energy ($\sim$200 KeV) and are uniformly distributed over the inner surface of Endcap HCAL.

2.5.5 R&D

The radiation level in the forward direction implies that one will need to probably specify specialized Si material. One needs to select the materials and expose them to radiation levels equivalent to what will be seen at the ILC forward region over period of 5 years. Two possible radiation hard materials are oxygenated Float Zone Si wafers and magnetic Czochralski Si wafers.

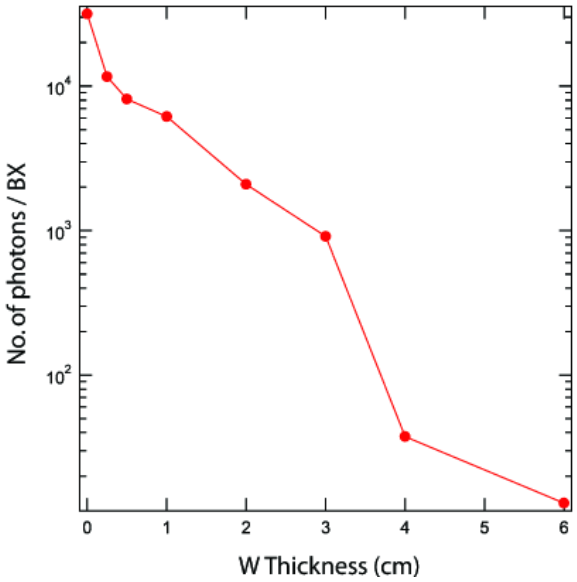

Figure 2.50: Number of photons penetrating the tungsten mask as a function of the mask thickness

References

[1] "Experimental implications for a linear collider of the SUSY dark matter scenario," P. Bambade et al., arXiv:hep-ph/0406010v1, june 2004.

[2] "IR Optimization, DID and Anti-DID," A. Seryi, T. Maruyama and B. Parker, SLAC-PUB-11662, Jan. 2006.

[3] "A simple method of shower localization and identification in laterally segmented calorimeters," Nucl. Instrum. Methods A, vol. 311, 130 (1992).

[4] "The EGS5 code system," H. Hirayama, Y. Namito, A.F. Bielajew, S.J. Wilderman and W.R. Nelson, SLAC-R-730 (2005)

[5] "FLUKA: a multi-particle transport code," CERN-2005-10 (2005), INFN/TC-05/11, SLAC-R-773.

[6] "GEANT4 developments and applications," IEEE Transactions on Nuclear Science, 53, 270 (2006)

[7] "$O(\alpha)$ YFS exponentiated monte carlo for Bhabha scattering at wide angles for LEP/SLC and LEP2," Phys. Lett. B390, 298 (1997)

[8] "Study of Electromagnetic and Hadronic Background in the Interaction Region of the TESLA Collider," D. Schulte, Ph.D Thesis, Hamburg University 1996.

[9] "Electron Identification in the BeamCal of the Silicon Detector at ILC," G. Oleinik, J. Gill and U. Nauenburg, ILC-SID-TechNote-003. For details, see http://hep-www.colorado.edu/~uriel/Beamstrahl_TwoPhoton-Process/grp_results.html .

2.6 Data Acquisition and Electronics

SiD has a coherent approach to the electronics architecture that seems to fit all the baseline subsystems. Figure 2.51 shows the simplified block diagram for the data-acquisition from the front-end electronics to the online-farm and storage system. The subsystems with the exception of the Vertex detector (for which the sensor technology is not yet selected) and the FCAL (which has approximately unit occupancy) are read out by variants of KPiX as the front-end Application-Specific Integrated Circuit (ASIC). KPiX is a multi-channel system-on-chip, for self triggered detection and processing of low level charge signals ("KPiX - An Array of Self Triggered Charge Sensitive Cells Generating Digital Time and Amplitude Information" D. Freytag et al, IEEE NSS Dresden 08).

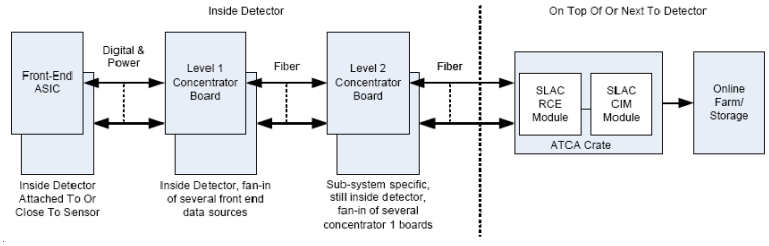

Figure 2.51: Simplified block-diagram of detector control and readout electronics using the SLAC ATCA RCE and CIM modules.

Figure 2.52 shows a simplified block diagram of the KPiX, processing signals from 1024 detector channels. The low level charge signal at the input is processed by the charge amplifier in two ranges with automatic range switching controlled by the range threshold discriminator. Calibration is provided covering the full range. Leakage compensation is available for DC-coupled detectors. Internal or external trigger options can be selected.

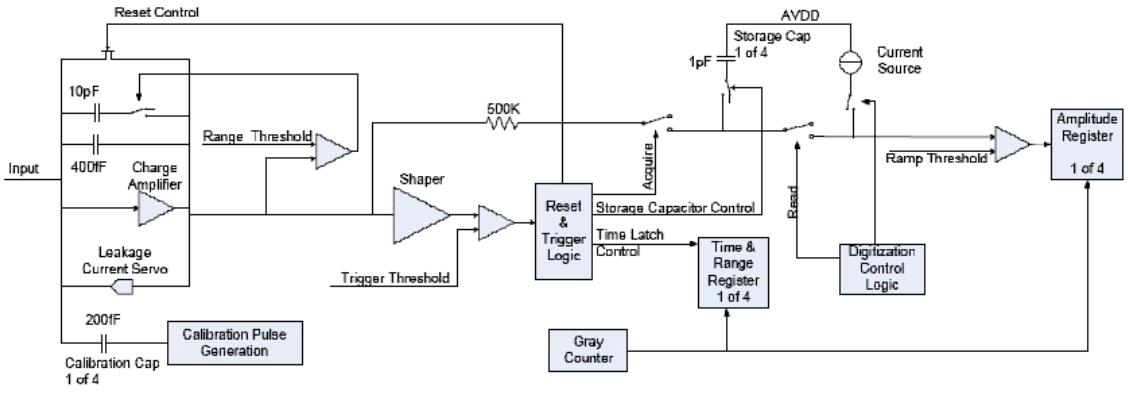

Figure 2.52: Simplified block-diagram of one channel of the 1024 channel KPiX Application Specific Integrated Circuit.

Up to four sets of signals for each channel can be stored in one acquisition cycle. Time is stored in digital format, the amplitude as a voltage on a capacitor for subsequent digitization in a Wilkinson-type ADC. At the end of the acquisition and digitization cycle nine words of

digital information are available for each of the 1024 cells of the KPiX chip. The data is read out serially from the ASIC before the next acquisition cycle begins.

Sub-System	KPiX Count	Channels/KPiX
Tracker	27464	1024
ECAL	99076	1024
HCAL	35412	1024
Muons	8834	64
Total	170786	

Table 2.11: Count of KPiX ASICs for each sub-system.

Table 2.11 lists the number of KPiX ASICs for each sub-system. Tracker, ECAL, and HCAL use 1024-channel ASICs while the Muon sub-system uses a 64-channel version.

As illustrated in Figure 2.51, several front-end ASICs (KPiX, FCAL or Vertex ASICs) are connected to a Level-1 Concentrator (L1C) board using electrical LVDS. The concentrator board main functions are to fan out upstream signals to the front-end modules, to fan-in data from the front-end modules for transmission to the Level 2 Concentrator (L2C) boards, and to perform zero-suppression and sorting of the event data. Just as an example, for the EMC Barrel a total of 96 1024-channel KPiX chips would be connected from 8 front-end cables with 12 KPiX's each to one Level-1 Concentrator board. The number of Level 1 concentrator boards in the detector depends on the sub-system, e.g for the EMC Barrel there would be 821 L1C boards and 52 L2C boards (80k KPiX, 96 KPiX for each L1C board, 16 L1C boards for each L2C board)

Figure 2.53 shows a block diagram and a prototype of the board.

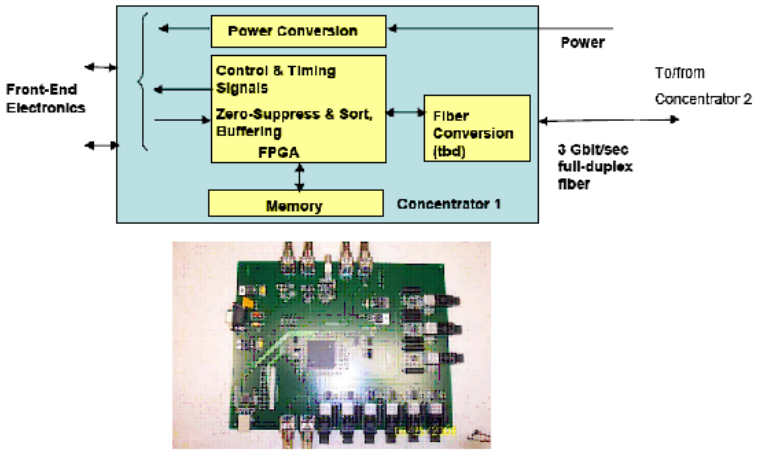

Figure 2.53: Level 1 Concentrator Board.

The Level 1 Concentrator boards are in turn connected via 3-Gbit/sec fibers to the Level-2 Concentrator boards. These are similar to the Level 1 Concentrator boards. They

fan out and fan in signals to/from the Level 1 Concentrator boards. In addition the data-streams of sorted event data received from each Level 1 Concentrator board are merged and sorted before transmission to the off-detector processor boards. The Level 2 boards are either located inside the detector or outside, depending on the sub-system. E.g. for the EMC Barrel there are 36 of such boards inside the detector volume.

The Level 2 Concentrator boards are connected via fibers to ATCA crates either on or next to the detector. ATCA stands for "Advanced Telecommunications Computing Architecture" and is the next generation communication equipment used by the telecommunication industry. It incorporates the latest trends in high-speed interconnect, processors and improved Reliability, Availability, and Serviceability (RAS). Essentially instead of parallel bus back-planes, it uses high-speed serial communication and advanced switch technology within and between modules, redundant power, plus monitoring functions. For SiD 10-G Ethernet is used as the serial protocol.

SLAC designed two custom ATCA boards, the Reconfigurable Cluster Element (RCE) Module and the Cluster Interconnect Module (CIM) as shown in Figure 2.51. Figure 2.54 shows the RCE which interfaces via eight 3-Gbit/s fiber links to sub-system detector electronics. It provides timing and configuration commands, and reads back configuration and event data. It contains 2 sets of the following: Virtex FPGA with embedded 2 PowerPC processors IP cores, 512 Mbyte low-latency RLDRAM, important 8 Gbytes/sec cpu-data memory interface, 10-G Ethernet event data interface, 1-G Ethernet control interface, RTEMS operating system, up to 512 Gbyte of FLASH memory or 1 TByte/board. The flash memory does not have to be fully loaded, it is implemented in SIMMS plug-in modules. One RCE connects to up to 8 detector cards via 8 3-Gbit/sec fibers connected into the Read Transition Module (RTM)

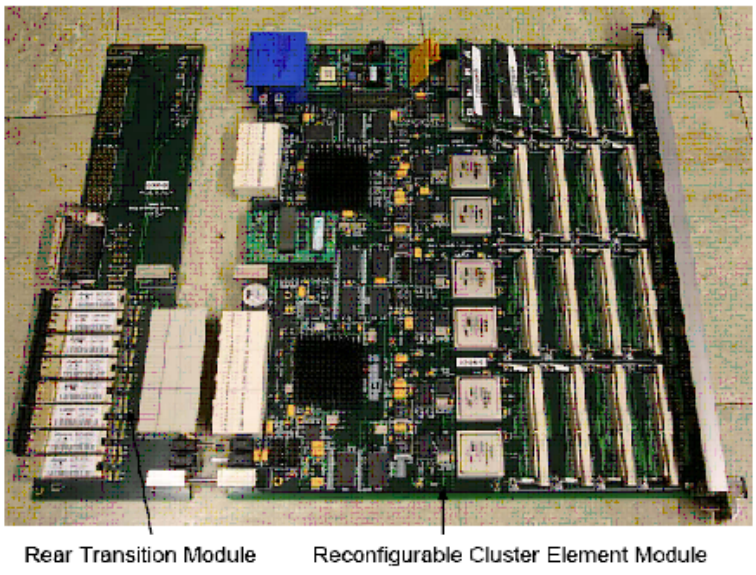

Figure 2.54: SLAC ATCA Reconfigurable Cluster Element.

Figure 2.55 shows a picture of the SLAC CIM. It is essentially a switch card with two 24-port 10-G Ethernet Fulcrum switch ASICs. The switch ASICs are managed via a Virtex

FPGA. The function of the CIM is to provide communication between all the RCE modules in a crate and to destinations external to the crate at 10Gbit/s data rates.

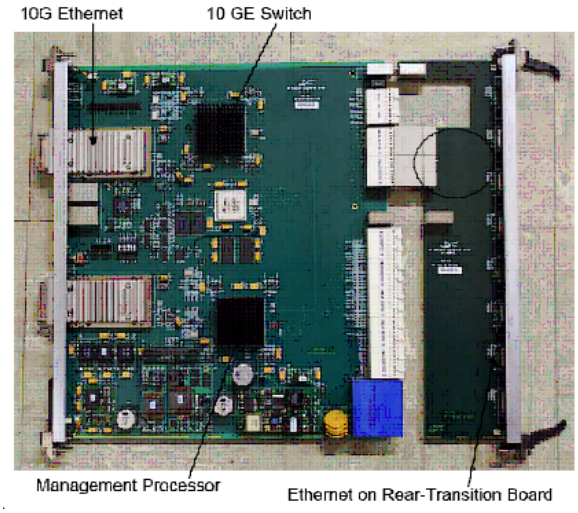

Figure 2.55: SLAC ATCA Cluster Interconnect Module.

One of those network cards serves up to 14 in-crate RCE modules. The data transfer rate is up to 480 Gbit/sec, more than the complete SiD data rate requirement.

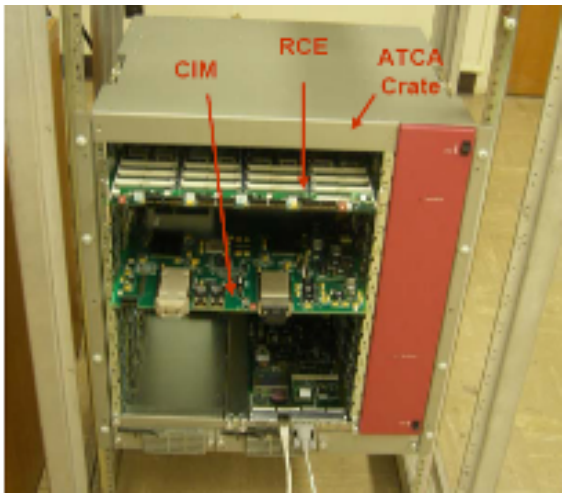

Figure 2.56: ATCA Crate with RCE and CIM.

Figure 2.56 shows an ATCA crate with one RCE and one CIM inserted. A total of 14 RCE's and 2 CIM's can be inserted into one crate providing connections to 8 x 14 = 112 3Gbit/sec fiber links into the detector for a 360 Gbit/sec IO. The estimate for the complete SiD detector is approximately 320 Gbit/sec including a factor of 2 margin, so in principle a single ATCA crate could serve the complete detector. However for partitioning reasons, the ability to run each of the sub-systems completely independently during commissioning is desired, and one crate for each sub-system is planned. The complete SiD DAQ only requires about 4 racks full of Data Acquisition electronics.

The data is further sorted by event in the ATCA system and sent to the online processing system for potential data reduction. Whether further data reduction is required is not determined yet, and the data may directly be forwarded to the offline system.

Note that the event data is zero-suppressed in the sub-systems without the need for a global trigger system. All data produced in the front-ends above a programmable threshold is read out. For diagnostics and debugging, the DAQ includes the ability to assert calibration strobe and trigger signals, transmitted to the front-ends via the Level-2 and Level-1 Concentrator boards using the fibers shown in Figure 2.51. The fiber transports encoded command, clock, and synchronization to all the front-ends.

Power Conversion circuits on the Level 2 and Level 1 Concentrator boards supply the power to the front-ends, starting with 48V or higher voltages from off-detector supplies. Alternatively, serial powering architectures are also under consideration. The power supplies are located in several racks on or next to the detector.

Environmental and health monitoring circuits are also included on the concentrator boards. In addition there may be additional monitoring boards in the detector, connected to RCE fiber interfaces. In addition there are crates of monitoring modules mounted in several racks on or next to the detector.

Most subsystems use the KPiX integrated circuit for reading out the detector signals. For the FCAL BeamCal subsystem a different custom integrated circuit has been designed due to its expected high occupancy (A. Abusleme et al., "Beamcal front-end electronics: Design and simulation", Proceedings of the Workshop of the Collaboration on Forward Calorimetry at ILC, 2008; http://www.vinca.rs/pub/FCAL Belgrade.pdf). Figure 2.57 shows a simplified block diagram of the integrated circuit. Input signals up to 40 pC are amplified, shaped, and digitized with 10-bit resolution. The amplifier gain can be configured for science (x1) and calibration (x50) mode. Each of the 32 channels in the device has its own Analog-to-Digital Converter and 2,820 memory cells to store the data which is then read out between bunch trains. A separate low-latency (¡ 1usec) output digitizing the sum of the 32 channels is provided to allow for fast feedback diagnostics.

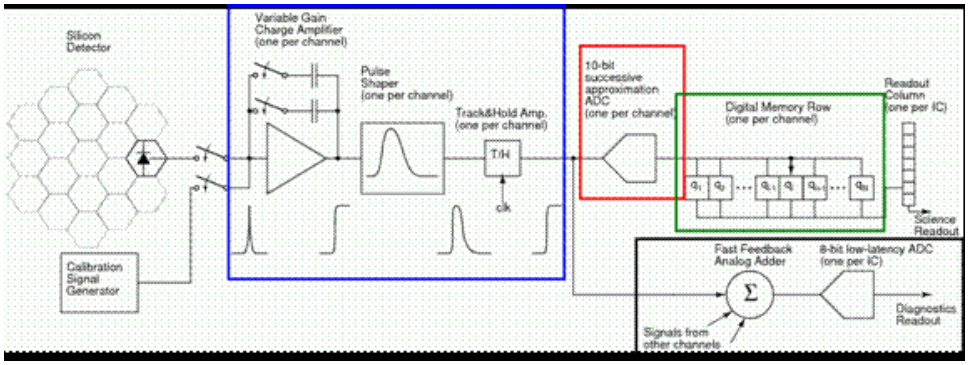

Figure 2.57: Block diagram of BeamCal Front-End Integrated Circuit.

Chapter 3

Machine-Detector Interface and Global Issues

SiD has contributed to the current definition of the machine-detector interface (MDI) specifications[1]. Here we describe our present plans for assembly of the detector, its alignment, and details of the push-pull operation.

3.1 SiD Assembly

SiD expects the VXD, ECAL, and HCAL modules to be built at collaborating labs and universities and transported to the ILC site. The iron will be built in sub modules with a mass suitable for transportation from an industrial site, and bolted together at the ILC. The solenoid would probably have two sections, and will be wound industrially.

The detailed strategy of final assembly must await site selection. A shallow site strategy will likely be different than one for several hundred meters underground. The optimal mass for steel modules will depend on transportation modes available between the factory and ILC, and sea, rail, or road limits will lead to different conclusions. (As a baseline, SiD is designing for road transportation and approximately 100 tonne maximum unit weight). The shape of an underground hall and the capacity for underground bridge cranes may depend on the site geology. In addition, an optimal strategy will depend on the ILC construction schedule.

A possible assembly procedure, for an underground site, is illustrated in Figure 3.1. The main steps are:

1. Underground assembly of Flux Return Barrel.
2. The Barrel Octants are lowered in pre-assembled pieces of 400t max.

[1] B. Parker et al, 'Functional Requirements on the Design of the Detectors and the Interaction Region of an e+e- Linear Collider with a Push-Pull Arrangement of Detectors'.

3. The Solenoid is lowered and inserted in the Flux Return Barrel.
4. Door are preassembled on surface and lowered in one piece 2500t max.
5. Flux Return Barrel moves between the doors. Doors close
6. The magnet (Iron+solenoid) is moved in garage position, hooked up to the cryogenics and commissioned.
7. Doors move leaving access on the barrel for the insertion of HCAL (380t), ECAL(60t) and Tracker(2t) (the other shaft is used for lowering)
8. Full assembled SiD barrel moves between the doors to close the detector
9. Full assembled SiD is moved in garage position, hooked up to the cryogenics and ready for the push pull operations.

The complete barrel assembly weighs approximately 4 Ktonnes, and each door weighs approximately 1.9 Ktonnes. Surface assembly and lowering of each with a substantial gantry crane is possible, as is assembly on the interaction region floor with a 300 to 400 tonne bridge crane. A possible alternative would be two approximately 200 tonne cranes on the same rails, one nominally for each experiment, with occasional coordinated use of both cranes for the larger lifts. Dedicated tooling is assumed for the insertion of the barrel detectors into the solenoid.

SiD expects to move on hardened steel rails, grouted and locked to the floor. Rail sets for transverse motion (push pull) and door opening in both the beamline and garage positions will be needed. SiD expects that locations for these rails can be found that either can be shared with the other detector, or not interfere with its system. If ILC is built in a seismic location, provision will be needed for locking SiD down in both the beamline and garage positions.

SiD subsystems will have few data and power connections compared to those for the LHC detectors because of the absence of a trigger and the low aggregate data rates. The subsystems will be integrated with their electronics and tested at their assembly points and at staging areas at the ILC site; final connection, integration and test should be relatively simple. The utility needs (electricity, water, LHe, compressed air, data fibers) needs of SiD are modest, and are expected to be via flexible connections to the wall.

3.2 Alignment

Detector Alignment and positioning is critical to the unprecedented momentum resolution and vertex detector performance expected of SiD. The positioning is critical for the push-pull model of ILC. Well defined positioning and measuring systems have not yet been designed but a general concept is described below.

SiD will be moved into the beam position as a single large unit, carrying the end doors with the barrel. It is expected that the detector will move on multi-roller supports,

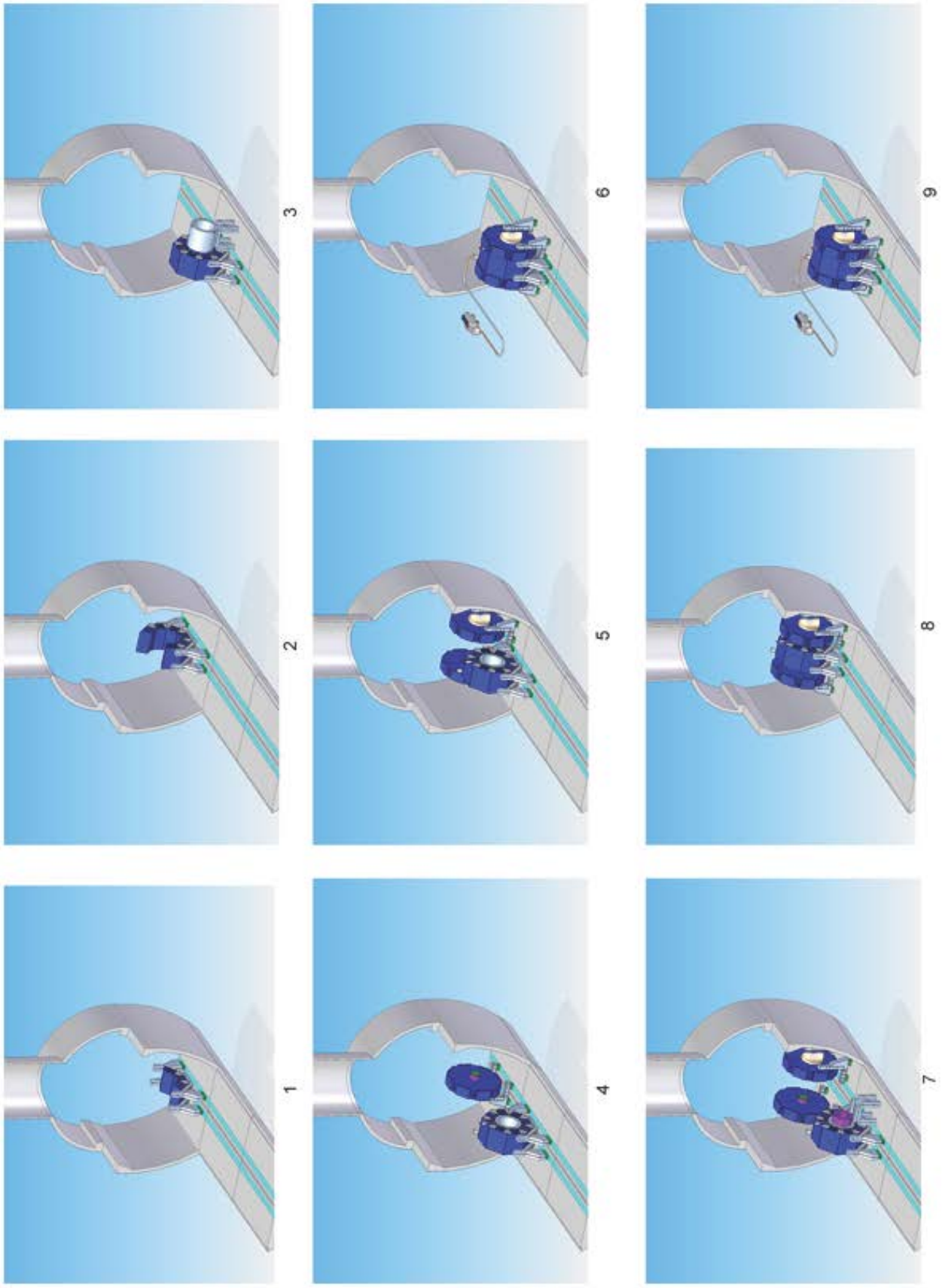

Figure 3.1: Schematic of steps in a possible assembly procedure.

each with an integrated drive, so that the steel structure is minimally stressed. The drive will accelerate and decelerate smoothly, and a maximum speed between 1 to 5 mm/sec is expected. It will be pushed up to permanent mechanical stops. Operating experience from other large detectors has shown that this method of positioning achieves position accuracy of +- 1 mm. This accuracy is acceptable for the positioning of the iron structure, muon system, solenoid, calorimetry and outer tracker. The QD0s will be moved onto the beamline defined by the two QFs by remotely-controlled motors. The QD0s carry the beam pipe and the vertex detector. The relative position of the beam pipe/vertex detector to the outer tracker needs to be known to a few microns. This relative position will be measured by a frequency scanning interferometer measuring system, and will be recorded periodically. It is expected that each launcher-corner reflector pair will measure with a precision of 1 micron over a range of several meters.

During movement concerns about distortions of the sub-detector systems need to be addressed so that permanent deformations are not observed. This will be achieved by kinetic mounts, progressively isolating the tracker from any external stress. The solenoid will be kinematically mounted to the iron structure. To be conservative, kinetic mounts will also be designed between the solenoid and the calorimetry and between the calorimetry and the outer tracker.

3.3 Push Pull

SiD strongly supports the notion of two detectors at the ILC, and considers the push-pull interchange of the two detectors on a frequent schedule necessary for a successful project. Consequently, SiD has made technical subsystem choices that support a rapid exchange of position and that will require minimal alignment and calibration time on beamline. It has also made engineering decisions to optimize these moves.

SiD assumes an interchange frequency of about a month, with a fixed (but adjusted) time allocation to each detector. This is long enough to make the lost data taking time reasonable if the transition time is approximately a day, and short enough to both avoid the possibility of significant data disparity opportunities, and to limit the time for any hardware changes that would require re-commissioning of the off-beamline detector. We assume that the time a detector takes to clear the beamline after the beginning of a transition will be subtracted from its next time allocation, and that a detector may take as long as it wants to set up on beamline, but that this time is part of its allocation. We assert that with a properly engineered detector and adequate experienced staff, the time from beginning detector exchange to beginning beam-based alignment of the final quadrupoles should be less than one day. We assume that except for unusual machine mishaps, both detectors take their chances with the machine luminosity.

3.3.1 Machine Detector Interface Assumptions

1. QD0 is located in SiD and moves with it. Supporting it with adequate vibrational stability is a responsibility of SiD. Its transverse position within SiD is remotely adjustable

to +- 1 mm.

2. QF1 is a fixed part of the machine, and is shared by the two detectors. Its support system includes a longitudinal anchor that will be used to stabilize the z position of the QD0 assembly when the SiD door is opened.

3. There is a warm removable spool piece between QD0 and QF1. It has two RF smooth, remotely operated high vacuum valves isolating the spool piece, and there is provision for purging, pumping to high vacuum, and leak checking this assembly (presumably permanently installed RGAs). There is a bellows system that will accommodate +- 1mm misalignment.

4. SiD will be self shielded. In addition to the SiD calorimeters and iron providing sufficient shielding in the event of an accident to the portion of the beamline approximately inboard of the QD0's, the rest of the beamlines are shielded by a system of portable iron and concrete (Pacmen). In a conceptual sense, each Pacman consists of a section fixed to the tunnel mouth wall, a pair of hinged shields that open to gain access to the beamline connection described above, and a section fixed to the detector door. It is expected that the hinged sections and the piece fixed to the tunnel wall will be common with the other detector, and that dimensional differences between the two detectors will be made up in the third section.

5. The 2K He cryogenic system for QD0 is carried on a support fixed to SiD and supplied from a 4K He system on SiD. All connections to QD0 are undisturbed during a move, and the magnet remains cold.

6. An automatic alignment system with an accuracy of at least +- 1 mm will relate the position of SiD to the beamline coordinates (when SiD is near the beamline).

3.3.2 Detector Assumptions

1. The superconducting solenoid has all of its services and utilities carried with SiD. The He liquefier is mounted on a hall wall, and supplies He to SiD by a flexible vacuum insulated line. (It is assumed that He compressors are located remotely for vibration isolation.) (It is assumed that each detector has its own liquefier, but that cross connect valves are incorporated in the cold boxes to allow mutual assistance.) SiD will have support platforms, attached above, aside, or adjacent to the detector. These platforms will support the solenoid power supply, dump resistor, quench protection system, and other auxiliaries.

2. The detector will receive utilities of ∼350 KW 480 VAC 3 phase power from a flexible line that remains connected during a move. Low Conductivity water, chilled water, and compressed air will also be provided by continuously connected flex lines.

3. Data will exit the detector via an optical fiber system continuously connected to the wall. Monitoring and control communications will also be via a fiber system. All detector subsystem power will come from supplies that travel with the detector. No subsystem signal cable will come off the detector.

4. The detector will roll on hardened steel rails using Hilman rollers or equivalent. SiD will carry its doors when moving in z, and will have rails in both the beam and garage position to open its doors. The drive mechanism will have minimal energy storage, possible a gear drive to a fixed cog rail. It is expected that a velocity between 1 and 5 mm/s is desirable and reasonable.

5. The detector transport system will deliver the detector to its appropriate position on the beamline to a precision of +- 1mm.

6. The detector is designed so that any stresses caused by the force required to move the detector are not transmitted to the calorimeter supports, and so the precision calorimeter and tracker systems will not be distorted from the moving process.

7. The detector will have an internal alignment system, probably based on frequency scanning interferometers that will provide high precision measurements of the relative positions of the barrel components, endcap systems, and beamline components.

8. The Sid beamline is supported by the inboard ends of the QD0s, and moves with them as they are moved to the ILC beamline during beam based alignment. The SiD Vertex Detector (VXD) is mounted to the beamline, and will remain coaxial to the beam during the alignment process.

9. The SiD flux return will limit leakage field to be less than 100 Gauss at 1m from the iron.

3.3.3 The Push Pull Process

SiD envisions the process as a series of rehearsed steps which are described here and in Microsoft Project Gantt chart format in Figure 3.3.3. The time units are hours, and SiD believes that with suitable experience and engineering, this is a rational schedule. Some of this belief is based on the experience with the 600 ton SLD doors, in which a door could be opened, the detector internals accessed for two hours, the door closed, and beam based alignment begun – in 8 hours.

1. Secure ILC Beams: This is the first step of the detector exchange process, and involves ensuring that ILC can not deliver a beam to the hall, and releasing the necessary keys (physical or otherwise) to permit opening of the shielding. This step would be very similar to that before a detector could open a door. (1 time unit)

2. De-energize magnets: At this time, it is not obvious whether the QD0s and solenoid should be (partly) de-energized. We assume here that the QD0s and solenoid will be run down, and that the time will be approximately equal to the charging time for the solenoid, which is 3 hours. If the ILC is built in a region with seismic requirements, this time can also be used to release seismic restraints.

3. Open Beamline Shielding: It is assumed that the beamline shielding is mechanically locked and requires the previously mentioned keys to unlock. The moving parts of the Pacmen are supported by hinges, and are activated by fixed mechanisms so that no

crane activity is required. It is assumed that all 4 Pacmen are opened together by coordinated but separate crews. (1 time unit).

4. Disconnect Beamlines: This process involves checking that the isolation valves have properly shut, venting the spool piece wit an appropriate purge, and disconnecting the flanges. It is assumed that separate crews work on each end. (2 time units).

5. Check Detector Transport System: The detector transport system should be carefully checked to see that it is ready to move the detector. It is assumed that the transport system is carefully maintained, and so this is a safety step rather than an opportunity for regular maintenance. (2 time units).

6. Transport Detector: The detector is moved in x for 15 to 20 m. The time, including a provision for acceleration and deceleration, would under 5 hours for a top velocity of 1 mm/s (15 m travel) and about 1 hour for 5 mm/s. (2 time units)

7. Transport other detector on beamline: It is assumed that the other detector has completed appropriate safety checks, and is ready to move when the first detector is fully off beamline. (This may be too conservative.) (2 time units).

8. Connect Beamlines: This process includes making up the spool piece flanges, pumping the spool piece with the in place pumping system, and He leak checking with the associated leak checker. Note that the beamline valves are remotely operable and can be opened when the spool piece vacuum is satisfactory. (2 time units)

9. Close Beamline Shielding: This step is the reversal of step 3. It is assumed that the Pacmen are engineered to handle +- 1mm misalignment with respect to the ideal beamline. (1 time unit)

10. Check Gross Detector Alignment: This step is the opportunity to check that the detector is within its tolerance to the beamline coordinates, and adjust the position if necessary. (2 time units).

11. Energize magnets: This step is the reversal of step 2. (3 time units)

12. Safety Checks before beams: This step consists of appropriate safety checks and the return of any outstanding "keys" to the machine. (1 time unit)

13. Begin Beam Based Alignment: This process consists of ILC using beams to move the quadrupoles to their desired positions. It is unknown how long this procedure will take, but 10 hours is assumed here, which is pessimistic compared to SLC experience.

The relation and overlap of these steps is indicated in Figure 3.3.3. It seems reasonable to us, that given the engineering assumptions, the luminosity-luminosity transition could take approximately a day. SiD expects that its internal alignment system, coupled with mechanically isolated but robust subsystems, will not need any calibration following the initial one.

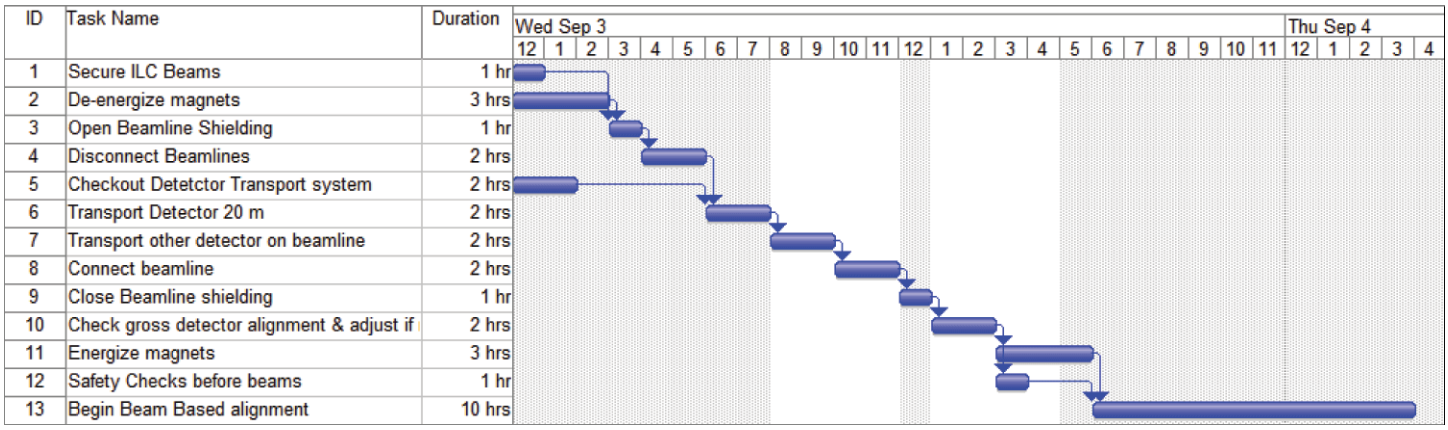

Figure 3.2: Summary chart of push-pull operational steps.

Chapter 4

Physics Performance and Benchmarking

4.1 Simulation of SiD

In order to design a detector which is capable of exploiting the full physics discovery potential of the ILC, a fairly sophisticated and mature simulation and reconstruction environment is needed. The Simulation & Reconstruction Working Group has concentrated its efforts on assembling a flexible framework to allow different detector designs to be simulated and multiple reconstruction algorithms to be implemented and used for physics and detector analyses. The code, binary executables, and documentation in the form of Application Programming Interface (API) and tutorials are all available online at http://lcsim.org.

4.1.1 Event Generation

A number of different event samples have been generated for detector design studies, ranging from single particles to inclusive Standard Model processes. The main focus of benchmarking analyses described in this section were complete sets of unbiased Standard Model processes at 500 and 250 GeV that were generated using the Whizard Monte Carlo program [1]. All 0, 2, 4 and 6 fermion final states, as well as top quark-dominated 8 fermion processes were generated. PYTHIA [2] was used for final state QED and QCD parton showering, fragmentation and decay to provide final-state observable particles. Included in this sample are backgrounds arising from interactions between virtual and beamstrahlung photons.

Samples were generated with electron and positron polarizations of 100%. Arbitrary polarization samples can be generated by properly combining events from the four data samples. For the purposes of the physics benchmark analyses, event samples were created which reflect the expected ILC baseline parameters of 80% electron and 30% positron polarization. Because of the large size of the full dataset, only a fraction of these events, about 80M, have been processed through the full detector simulation, with individual events weighted to reflect the statistical sampling.

4.1.2 Full Detector Simulation

The simulation of the response of the detector to the generated events is based on the Geant4 toolkit [5] [6], which provides the classes to describe the geometry of the detector, the transport and the interactions of particles with materials and fields. A thin layer of Linear Collider-specific code, SLIC [7], provides access to the Monte Carlo events, the detector geometry and the output of the detector hits. The geometries are fully described at runtime, so physicists can vary detector parameters without having to rebuild the simulation executable binaries. The output uses the standard LCIO format [8], so that detectors modeled using other simulation packages could be analyzed, and data generated using this system could be analyzed in other reconstruction and analysis frameworks.

All analyses described in this section use the full detector simulation.

4.1.3 Detector Variants

The XML format allows variations in detector geometries to be easily set up and studied, e.g. Stainless Steel vs. Tungsten hadronic calorimeter absorber material, RPC vs. scintillator readout, calorimeter layering (radii, number of layers, composition, ...), readout segmentation (pad size, projective vs. fixed cell size), tracking detector topologies ("wedding cake" vs. Barrel + Cap), magnetic field strength.

In addition to the baseline Silicon Detector (sid02), a number of variants have been developed in order to study the dependence of the performance on detector options. The option sid02 used for all analyses in this section is consistent with the detector described in the previous sections though some compromises had to be made to simplify the geometry in specific cases. A more detailed geometry description is available at **http://lcsim.org/detectors/#sid02**.

4.1.4 Analysis Tools

The jet finder used in most analyses is a simple y-cut algorithm usually run with a predetermined number of jets. Additionally the jet finder also provides y_{max} and y_{min}; these are the y-cut values that determine the separation between the one and two jet cases and between the N and N-1 jet cases; where N is the number of desired jets. Pattern recognition on hadronic final states is performed using a PFA algorithm devised for SiD; more details can be found in the online appendices.

The Marlin Kinematic Fitter (KinFit [9]) was used in several analyses to provide the most probable kinematic configuration of the event topology under specific, user defined constraints. A wide range of constraints can be selected: total energy, momentum, mass of selected jets and several other parameters. The fitter uses the method of Lagrange multipliers to determine the most probable value for the jet four-momentum given user specified uncertainties on the energy and on the angles of each jet. The algorithm can also select the most probable configuration of jets out of all possible permutations.

The vertexing package used for several analyses was developed by the LCFI collaboration [11]. The main algorithm of the package, the topological vertex finder ZVTOP, reconstructs vertices in arbitrary multi-prong topologies. It classifies events on number of found vertices and combines eight optimized variables for each type of event in a neural network which is then separately trained on samples of b-, c- and light quarks. The best discriminating variables are the corrected vertex mass, the joint probability, the secondary vertex probability, the impact parameter significance of the most significant track and number of vertices in the event. The joint probability is defined as the probability for all tracks in a jet to be compatible with hypothesis that they originate at the primary vertex. Typically nine networks are used with eight inputs, one hidden layer with 14 sigmoid neurons and one output.

The performance of the LCFI package optimised for the SiD detector is shown in Figure 4.1. The left plot shows dependence of purity on the efficiency for the di-jet sample at 500 GeV for b-tagging, c-tagging with b-only background and c-tagging. The SiD specific optimisation was performed by building a new neural network which used the same input parameters described above and training it using di-jet samples which passed through the full SiD simulation and reconstruction. The right plot of Figure 4.1 addresses the issue of integration of the beam-beam background in the vertex detector. It shows the dependence of b-tagging efficiency on the amount of beam-beam background integrated in the vertex detector expressed as the number of integrated beam crossing (BC). The dependence is minimal which confirms the robustness of the pattern recognition and vertexing in SiD. Bottom quark di-jet events at 500 GeV with beam-beam background events overlaid at the detector hit level were used for this study. In all cases the beam-beam background corresponding to one BC was overlaid with signal events in the Tracker.

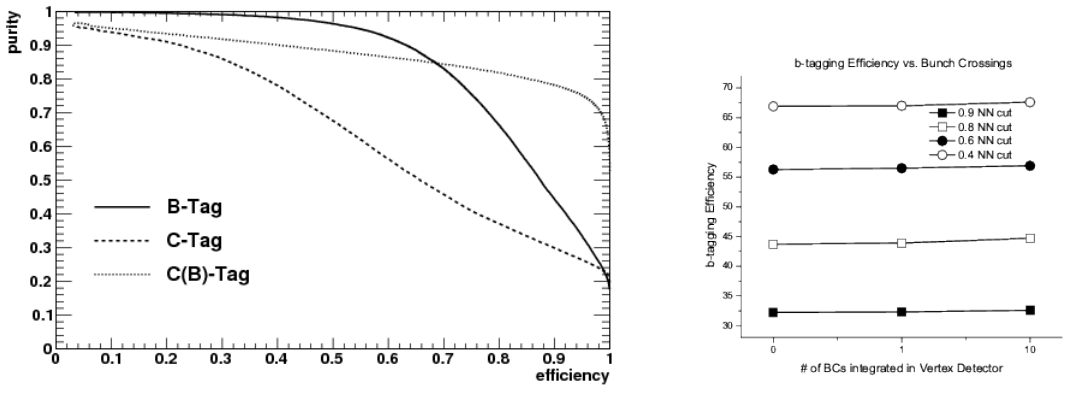

(a) (b)

Figure 4.1: Flavour tagging with LCFI package optimized for SiD (a) and dependence of b-tagging efficiency on the amount of beam-beam background integrated in the vertex detector (b).

In several analyses the event classification is based on the open source Fast Artificial Neural Network (FANN) [10] package. The package provides fast and reliable framework written in C programming language called from within a C++ wrapper. FANN was partially

modified in order to account for event weights during the Neural Network training.

4.2 Benchmark Reactions

Physics performance studies are needed to quantify the performance of SiD, revisit the performance requirements on the various ILC detector subsystems, and ultimately optimize the SiD design by studying how the performance changes as one varies the basic detector parameters. In a broader context, these studies further the physics case of the ILC.

A list of physics benchmark reactions [12] was presented to the ILC community at Snowmass 2005. This list of about 30 reactions provides comprehensive coverage of ILC physics topics and detector challenges, but is too long to be addressed by detector concept groups at this time. Thus, a reduced list of 6 reactions was specified by the ILCSC Research Director which is more appropriate for studies on the time scale of the LOI:

1. $e^+e^- \to e^+e^-H\,,\ \mu^+\mu^-H\,,\ \sqrt{s}$=250 GeV;
2. $e^+e^- \to ZH\,,\ H \to c\bar{c}\,,\ Z \to \nu\bar{\nu}\,, q\bar{q}\,,\ \sqrt{s}$=250 GeV;
3. $e^+e^- \to ZH\,,\ H \to \mu^+\mu^-\,,\ Z \to \nu\bar{\nu}\,, q\bar{q}\,,\ \sqrt{s}$=250 GeV;
4. $e^+e^- \to \tau^+\tau^-\,,\ \sqrt{s}$=500 GeV;
5. $e^+e^- \to t\bar{t}\,,\ t \to bW^+\,,\ W^+ \to q\bar{q'}\,,\ \sqrt{s}$=500 GeV;
6. $e^+e^- \to \tilde{\chi}_1^+\tilde{\chi}_1^-/\tilde{\chi}_2^0\tilde{\chi}_2^0\,,\ \sqrt{s}$=500 GeV.

In addition to these compulsory LOI benchmark reactions SiD also investigated the following process:

7. $e^+e^- \to \tilde{b}\tilde{b}\,,\ \tilde{b} \to b\tilde{\chi}_1^0, \sqrt{s}$=500 GeV.

The following sections describe these seven analyses.

4.2.1 $e^+e^- \to e^+e^-H\,,\ \mu^+\mu^-H\,,\ \sqrt{s}$=250 GeV

Studies of the Higgs Boson are expected to be center stage at the ILC. The production of the Higgs through "Higgs-strahlung" in association with a Z, will allow a precision Higgs mass determination, precision studies of the Higgs branching fractions, measurement of the production cross section and accompanying tests of SM couplings, and searches for invisible Higgs decays. When the associated Z decays leptonically, it is possible to perform a measurement of the Higgsstrahlung cross section and to reconstruct the mass of the Higgs recoiling against the Z with high precision, independent of how the Higgs boson decays.

A sample of three million Monte Carlo signal events of the type $e^+e^- \to e^+e^-H,\ \mu^+\mu^-H$ was used along with a $\sqrt{s} = 250$ GeV Standard Model Monte Carlo background event sample

of 47 million events for training and for estimating the statistical errors for the mass and the cross section. An independent signal sample of three million events was used as a testing sample to verify the statistical errors calculated with the larger training sample.

Event selection begins with the identification of electrons and muons by the SiD PFA algorithm. Following lepton identification the cuts for the the electron and muon channels are identical. An event must contain at least two oppositely charged electrons or muons with $|\cos\theta_{\rm track}| < 0.99$. The mass of the lepton pair must be in the range 87 GeV $< M_{l^+l^-} <$ 95 GeV and the angle $\theta_{l^+l^-}$ made by the vector sum of the momenta of the two leptons with the beam axis must satisfy $|\cos\theta_{l^+l^-}| < 0.85$. Finally the angle $\theta_{\rm missing}$ between the event missing momentum vector and the beam axis must satisfy $|\cos\theta_{\rm missing}| < 0.99$, in order to reject Bhabha and muon pair events. The last cut involves objects other than electron or muon pair; however we believe the l^+l^-H efficiency for this cut is independent of the Higgs decay mode, and so this analysis is model independent. The distributions for the Higgs signal following cuts is shown in Figure 4.2 assuming 250 fb^{-1} luminosity with the initial electron and positron polarization combination $e^-(80\%R)$ $e^+(30\%L)$ and 0 fb^{-1} with the combination $e^-(80\%L)$ $e^+(30\%R)$. These two polarization combinations will be referred to by their electron polarizations 80eR and 80eL.

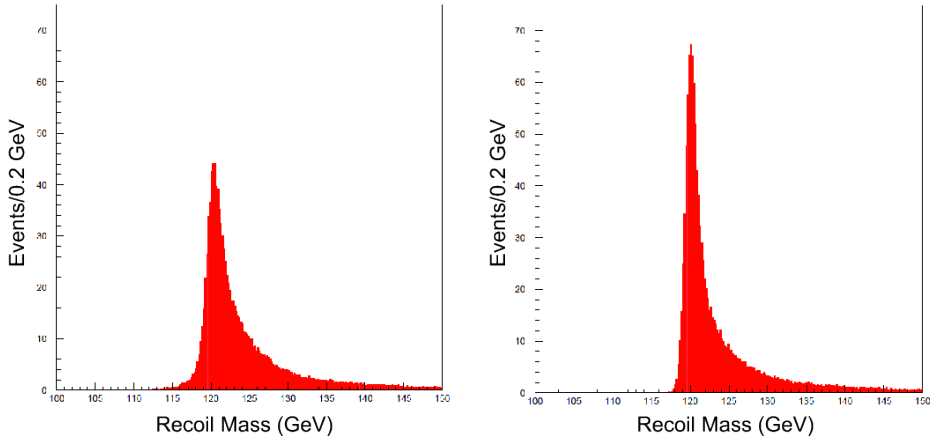

(a) (b)

Figure 4.2: Recoil mass distributions following selection cuts for eeH (a) and $\mu\mu H$ (b) assuming 250 fb^{-1} luminosity with 80eR initial state polarization. Background is not included.

The major backgrounds following the selection cuts are $e^+e^- \to \gamma\gamma l^+l^-$, $e^+e^- \to W^+W^- \to l^+\nu l^-\bar{\nu}$, $e^+e^- \to ZZ^* \to l^+l^- f\bar{f}$, and $e^-\gamma \to e^-e^+e^-$. The distributions for the Higgs signal with background included are shown in Figure 4.3. The W^+W^- background can be greatly reduced by running 100% of the time with the 80eR initial state polarization combination. This comes at a price, however, as the signal cross-section is reduced by 30% relative to the 80eL combination.

A linear least squares fit of the Higgs mass M_H and Higgs cross section σ_{ZH} near $(M_H, \sigma_{ZH}) = (120\ GeV, \sigma_H^{SM})$ is used to measure the mass and cross section. All recoil mass bins in the range of 117 GeV $< M_{\rm recoil} <$ 137 GeV are used. The dependence of the recoil mass bins on the Higgs mass and cross section is calculated by comparing the reconstructed

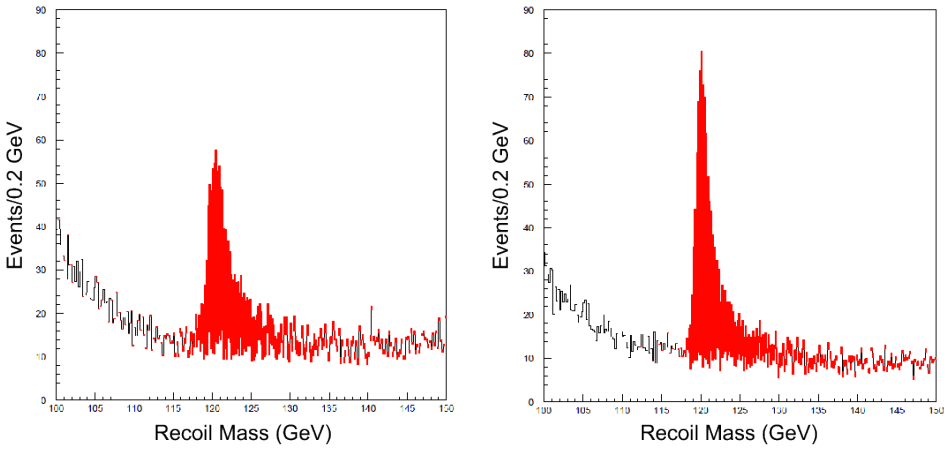

(a) (b)

Figure 4.3: Recoil mass distributions following selection cuts for eeH (a) and $\mu\mu H$ (b) assuming 250 fb^{-1} luminosity with 80eR initial state polarization. The signal in red is added to the background in white; background is assumed constant over 5 GeV sections.

recoil mass distributions for the training samples with $M_H = 119.7, 120.0, 120.3$ GeV. It is assumed that the background cross-section can be calculated to arbitrary accuracy, that the luminosity spectrum and polarization can be perfectly measured, and that there are no detector systematic errors. The errors on the Higgs mass and cross section are summarized in Table 4.1, assuming a recoil mass bin size of 0.2 GeV.

80eR lumi	80eL lumi	Mode	ΔM_H (GeV)	$\Delta\sigma_{ZH}/sigma_{ZH}$
250 fb^{-1}	0 fb^{-1}	e^+e^-H	0.078	0.041
250 fb^{-1}	0 fb^{-1}	$\mu^+\mu^-H$	0.046	0.037
250 fb^{-1}	0 fb^{-1}	$e^+e^-H + \mu^+\mu^-H$	0.040	0.027
0 fb^{-1}	250 fb^{-1}	e^+e^-H	0.066	0.067
0 fb^{-1}	250 fb^{-1}	$\mu^+\mu^-H$	0.037	0.057
0 fb^{-1}	250 fb^{-1}	$e^+e^-H + \mu^+\mu^-H$	0.032	0.043

Table 4.1: Summary of Higgs mass and ZH cross section errors for different channels and different luminosity assumptions. The error includes the measurement statistical error and the systematic error due to the finite statistics of the Monte Carlo training sample.

4.2.2 $e^+e^- \to ZH\,,\ H \to c\bar{c}\,,\ Z \to \nu\bar{\nu}\,, q\bar{q}\,,\ \sqrt{s}$=250 GeV

The measurement of the Higgs absolute branching ratios to all possible species is an important part of the ILC program, giving a precision test of the Standard Model prediction that the Higgs boson couples to each particle in proportion to its mass. These measurements also discriminate between different 'Beyond the SM' scenarios. The considered decay modes result

in two- and four-jet final states and exercise the tagging of charm quarks which is particularly sensitive to the vertex detector performance [15].

At the centre of mass energy $\sqrt{s} = 250$ GeV the Higgs boson with mass of 120 GeV is produced predominantly in the Higgsstrahlung process, $e^+e^- \rightarrow ZH$. The choice of energy maximizes the the cross-section value for Higgsstrahlung. The expected SM Higgs boson branching ratio to charm quarks is equal to 3.0% and one of the main difficulties of the analysis is to separate this signal from the background of Higgs decays to b-quarks which has a substantially larger Br of 68.2%. For the analysis we considered the signal and SM samples with total integrated luminosity of 250 fb^{-1} and +80% electron polarization, -30% positron polarization.

The analysis signature is dependent on the Z boson decay products (charged leptons, hadrons or neutrinos). The channels studied in this analysis are the neutrino mode (Z decaying to neutrinos) and the hadronic mode (Z decaying to hadrons). The selection of signal events is performed in three stages. The first step involves the classification of events into these two channels using the number of leptons and visible energy in the event. Visible energy is defined as the sum of energies of all reconstructed particles in the event. Leptons are defined as reconstructed electrons or muons with minimum momentum of 15 GeV. Figure 4.4 shows the distribution of the visible energy and the number of leptons for the signal, Higgs background and SM background before any selections. The neutrino mode is selected as events with no leptons and with visible energy in the 90 to 160 GeV interval. The hadronic mode is selected as events with no leptons and the visible energy above 170 GeV.

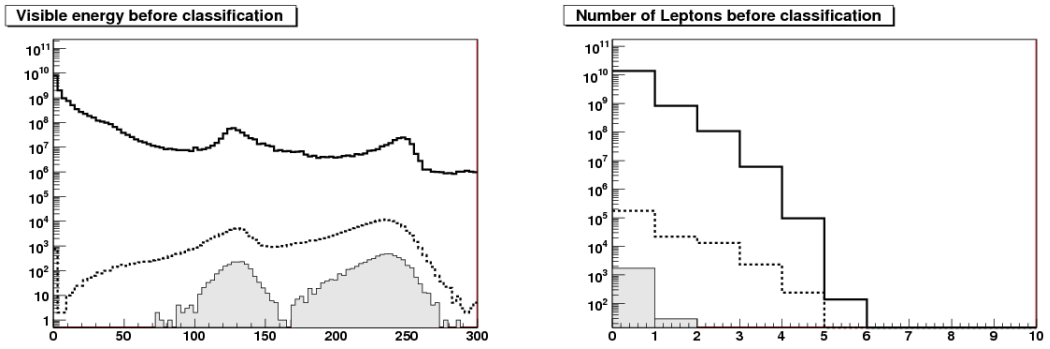

(a) (b)

Figure 4.4: Visible energy (a) and the number of leptons per event (b) used for channel classification. Solid curves are SM background, dashed curves are inclusive Higgs sample and filled histograms are the signal.

The second step is a cut based selection which reduces the backgrounds in the selected channel followed by a final stage using two neural network (NN) discriminants trained on signal and on two types of background samples, the SM and inclusive Higgs ones. The remaining events after the NN selection are used for the calculation of the cross sections and branching ratios.

4.2.2.1 The neutrino channel

The analysis starts with forcing all reconstructed particles to be clustered into two jets which for the signal are assumed to come from the Higgs boson recoiling against two neutrinos from the Z boson decay. The discrimination between the signal and background with different number of jets is achieved by selection on the y_{min} parameter. Another powerful discriminant, the reconstructed invariant mass of two hadronic jets, is expected to be consistent with the Higgs mass. Figure 4.5 shows distributions of di-jet invariant mass (a) and y_{min} (b) for the signal and backgrounds after classification. The background includes all SM processes but at this stage the most important are 2-fermion events, ZZ pairs decaying to neutrinos and hadrons and WW pairs where one W decays hadronically and the other W decays into a neutrino and a lepton which escapes undetected.

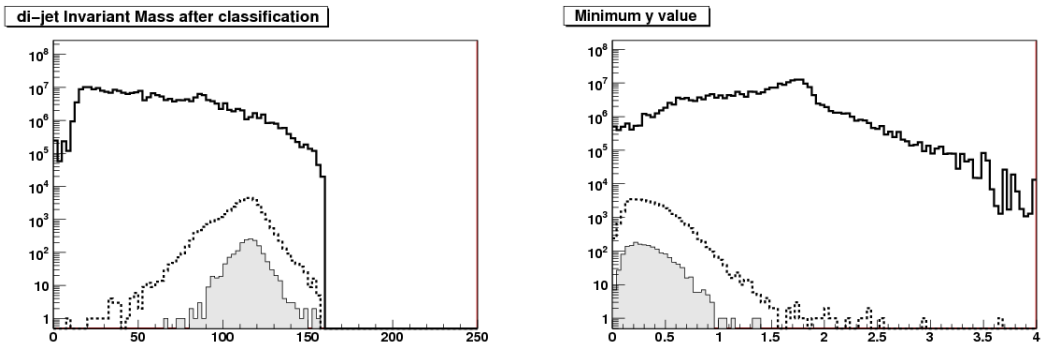

(a) (b)

Figure 4.5: Distribution of di-jet invariant mass (a) and y_{min} (b). Solid curves are SM background, dashed curves are inclusive Higgs sample and filled histograms are the signal.

The full list of selections is given in Table 4.2.

		selection	value
20	$<$	p_T of jet	< 90 GeV
		number of charged tracks in jet	> 4
		$-\log(y_{min})$	< 0.8
		thrust	< 0.95
		$\cos(\theta_{thrust})$	< 0.98
100°	$<$	angle between jets	$< 170^\circ$
100 GeV	$<$	di-jet invariant mass	< 140 GeV
		energy of isolated photon	< 10 GeV

Table 4.2: Selections for the neutrino channel

The remaining events are categorized using a neural network implemented in FANN [4]. The NN input variables include all the variables stated above with addition of the LCFI

flavour tag outputs for both jets. Figure 4.6 (a) shows the distribution of one of three possible flavour tags, 'c with b only background' for the first jet. This particular tag corresponds to the training to distinguish c-quarks from b-quarks without taking into account light quarks at all. The NN has been trained two times, the first time to distinguish the SM background from the inclusive Higgs sample and to produce the $\mathrm{NN}_{SM-Higgs}$ output; and, the second time to distinguish the signal from the inclusive Higgs sample and to produce the $\mathrm{NN}_{Higgs-signal}$ output, the latter shown in Figure 4.6 (b).

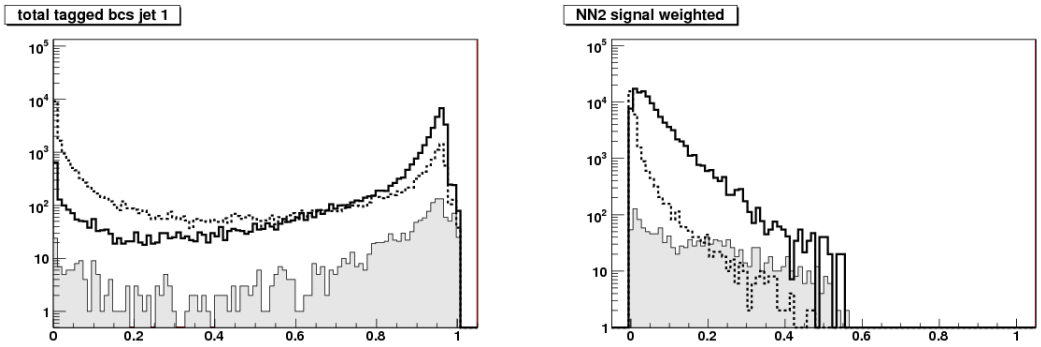

(a) (b)

Figure 4.6: Neutrino channel: (a) Flavour tag 'c with b only background' for the first jet; (b) $\mathrm{NN}_{Higgs-signal}$ output. Solid curves are SM background, dashed curves are inclusive Higgs sample and filled histograms are the signal.

The final signal sample is required to have $\mathrm{NN}_{Higgs-signal} > 0.2$ and $\mathrm{NN}_{SM-Higgs} > 0.3$. The sample includes 476 signal events with SM background of 570 events and inclusive Higgs background of 246 events. The signal efficiency is equal to 28%. This corresponds to the measured signal cross section of 6.8 ± 0.7 fb. The branching ratio of $3.3 \pm 0.4\%$ was determined by normalization to the Higgs inclusive cross section as measured in the Higgs recoil mass analysis. The relative accuracy of 11% is dominated by the precision of the $HZ \to c\bar{c}\nu\bar{\nu}$ cross section. Here and below the uncertainty accounts purely for statistical fluctuations of expected number of events with all other contributions considered negligible.

4.2.2.2 The hadronic channel

In this channel, events are forced to have four reconstructed jets and as in the two-jet case the y_{min} variable was chosen to differentiate from backgrounds with different number of jets. For the signal, two of the jets are assumed to have an invariant mass consistent with the Higgs boson and the other two having mass consistent with the Z boson. Kinematic fitting [3] is performed to improve the assignment of jets to decay products of the Higgs and Z bosons and therefore to reduce the combinatorial background. The main backgrounds for this channel are WW and ZZ pairs where the all the bosons decay to hadrons. Figure 4.7 shows the Higgs invariant mass before and after kinematic fitting (a) and thrust (b) of the signal and backgrounds after classification.

Selections used for further reduction of the background are presented in Table 4.3.

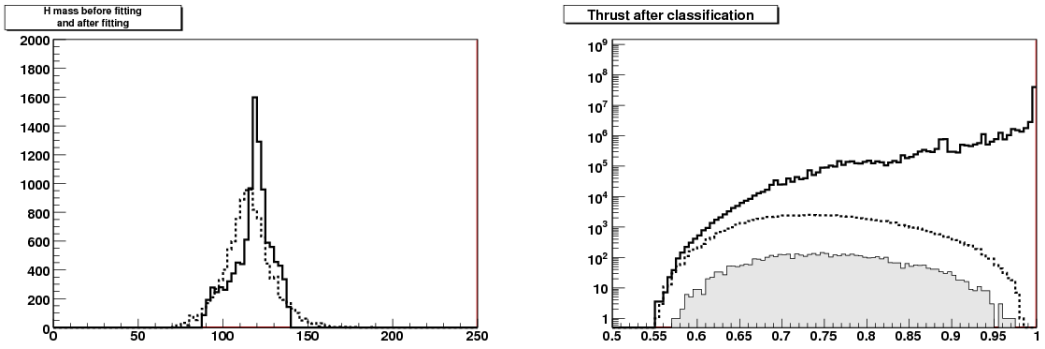

(a) (b)

Figure 4.7: Higgs invariant mass before and after kinematic fitting (a) and thrust of the signal and backgrounds after classification (b). Solid curves are SM background, dashed curves are inclusive Higgs sample and the filled histogram is the signal.

For the angular selections the jets were ordered in energy. The invariant mass selections

		selection	value
		number of charged tracks in jet	> 4
		$-\log(y_{min})$	< 2.7
		thrust	< 0.95
		$\cos(\theta_{thrust})$	< 0.96
75°	$<$	angle between jet 1 and 3	$< 165^\circ$
50°	$<$	angle between jet 2 and 4	$< 150^\circ$
95 GeV	$<$	invariant mass of Higgs candidate	< 145 GeV
45 GeV	$<$	invariant mass of Z candidate	< 105 GeV
		energy of isolated photon	< 10 GeV

Table 4.3: Selections for the four-jet analysis

were employed after the kinematic fitting which paired the four jets into the Higgs and Z candidates.

Similarly to the neutrino channel the variables above and also the three flavour tag outputs for all jets, are used in a neural network based selection employing the FANN package. Figure 4.8 (a) shows the distribution of one of three possible LCFI flavour tags, 'c with b only background' for the first jet. The NN has been trained two times, first to distinguish the SM background from the inclusive Higgs sample producing the $\mathrm{NN}_{SM-Higgs}$ output, and, second, to distinguish the signal from the inclusive Higgs sample producing the $\mathrm{NN}_{Higgs-signal}$ output, the latter shown in Figure 4.8 (b).

The final signal sample is required to have $\mathrm{NN}_{Higgs-signal} > 0.2$ and $\mathrm{NN}_{SM-Higgs} > 0.3$. The sample includes 814 signal events with SM background of 569 events and inclusive Higgs

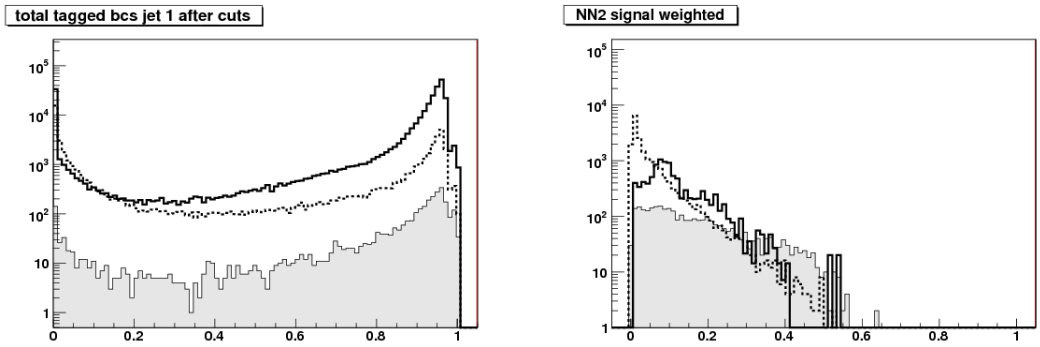

(a) (b)

Figure 4.8: Four jet channel: (a) Flavour tag 'c with b only background' for the first jet; (b) $\mathrm{NN}_{Higgs-signal}$ output. Solid curves are SM background, dashed curves are inclusive Higgs sample and filled histograms are the signal.

background of 547 events. The signal efficiency is equal to 47%. This corresponds to the measured $HZ \to c\bar{c}q\bar{q}$ cross section of 6.9 ± 0.4 fb. The branching ratio of $3.3 \pm 0.2\%$ was determined by normalization to the Higgs inclusive cross section as measured in the Higgs recoil mass analysis. The relative accuracy of 6% on the latter takes into account contributions from both cross sections and is dominated by the precision of $HZ \to c\bar{c}q\bar{q}$ cross section.

4.2.3 $e^+e^- \to ZH\,,\ H \to \mu^+\mu^-\,,\ Z \to \nu\bar{\nu}\,, q\bar{q}\,,\ \sqrt{s}$=250 GeV

The decay of Higgs boson into muons is one of the SM rare decays. Together with the $c\bar{c}$ final state it gives access to the Higgs coupling to the second generation fermions. The expected branching ratios are of the order of 0.01%. This decay channel will allow a precise direct determination of the Higgs mass as it only relies on the performance of the tracking and will also allow to set an upper limit on the Higgs decay width limited only by the resolution of tracking system. The challenge of the analysis is to extract the signal out of an overwhelming background from two-fermion and four-fermion processes.

For the signal we have a dedicated WHIZARD sample of $H \to \mu^+\mu^-$ with $Z \to f\bar{f}$ (including the fusion channels) with a Higgs mass of 120 GeV. The branching ratios for the final states are 67.0 % for the hadronic final states and 22.9 % for the neutrino final state. Contribution due to the WW fusion process to the neutrino channel, 16.1 %, complicates this analysis as this channel does not exhibit a peak in the missing mass. The integrated luminosity of the sample is 250 fb^{-1}.

The primary aim of this analysis are the hadronic channel and the neutrino channel. For both we require in each event a presence of two muons which are identified by associating a reconstructed track to a MIP segment in the calorimeter and a stub in the muon system. For the leading muon we require its energy to be larger than 50 GeV and for the second muon we require it to be larger than 30 GeV. The number of identified muons is shown in Figure 4.9 for the signal and background samples. The energy distribution of the most energetic muon

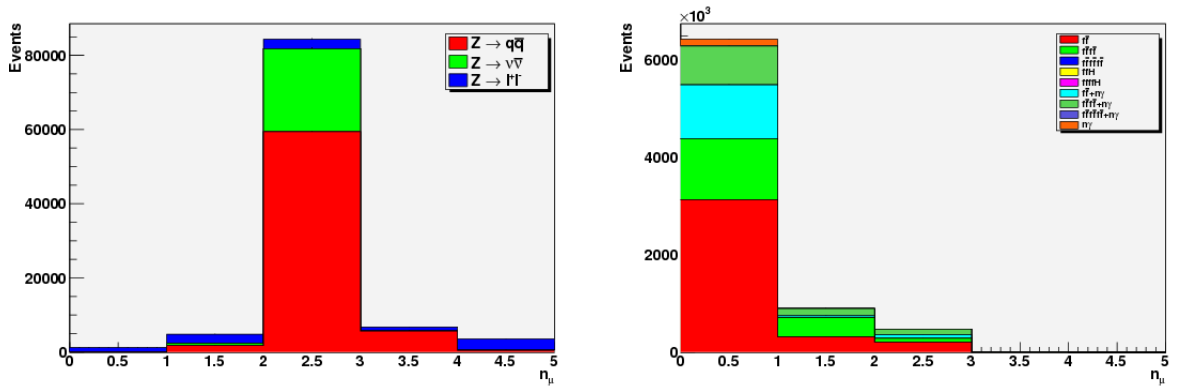

Figure 4.9: The Number of identified muons in the signal sample (left) and the background sample (right).

is shown in Figure 4.10. The signature of the hadronic channel consists of two high-energetic

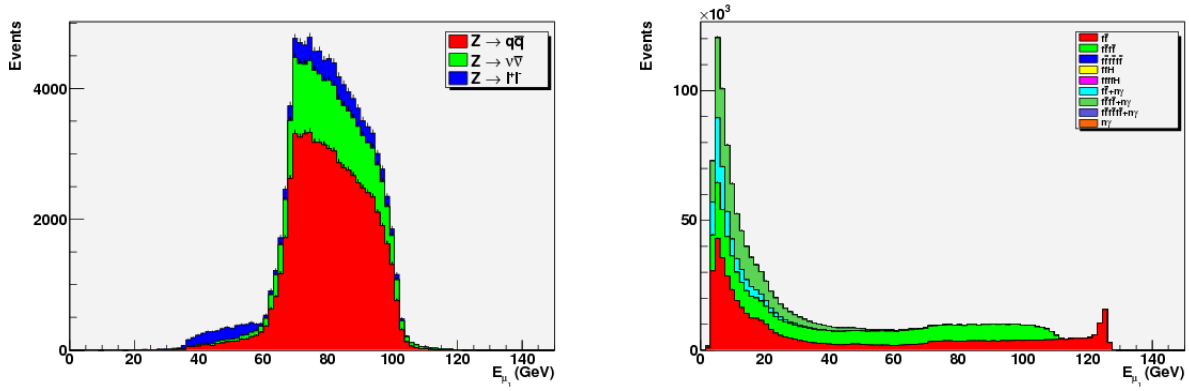

(a) (b)

Figure 4.10: The energy spectrum of the most energetic muon for the signal (a) and the SM background (b).

muons from the Higgs decay and two jets from the hadronically decaying Z boson. For this channel we force the event into two jets using the Durham algorithm, after excluding the previously identified muons. We require the y_{min} parameter of the jet clustering to be larger than 0.05.

Preselecting hadronic events compatible with the di-jet di-muon signature we require the number of charged tracks to be greater than 5 and the visible energy to be larger than 190 GeV. We then select events where the leading jet has an energy between 30 and 105 GeV and second jet has an energy between 10 and 70 GeV. We also require the jet P_T to be smaller than 90 and 60 GeV respectively. Finally we require the mass of the di-muon system to be compatible with the m_H=120 GeV $\pm$ 0.9 GeV.

We check the mass resolution for the signal both for the di-muon and the di-jet system

before any kinematic fitting and corrections for energy losses have been applied. We obtain 120.07 GeV with a width of 304 MeV for the di-muon system and 90.84 GeV with a width of 7.58 GeV for the di-jet system. The results are shown in Figure 4.11.

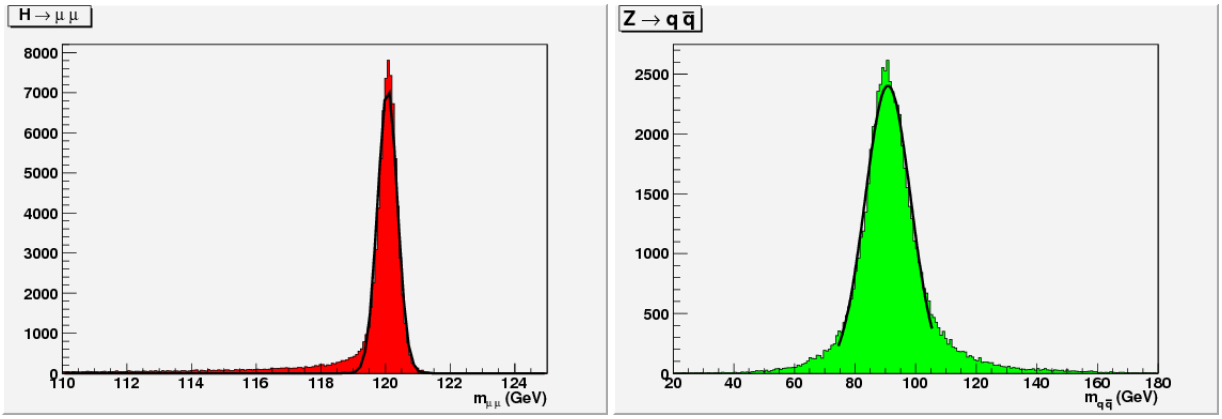

Figure 4.11: The mass resolution for the di-muon system (left) and the di-jet system(right) for the signal sample $Z \to q\bar{q}$; $H \to \mu^+\mu^-$.

After the preselection, the dominant background originates from four-fermion processes, mainly ZZ production with $e^+e^- \to ZZ \to q\bar{q}\mu^+\mu^-$. To select "good" muons, we cut on the muon opening angle, $\cos(\theta_{\mu\mu}) < -0.5$. The signal tends to be very back-to-back, and we exploit this fact by cutting on the angle between the two reconstructed bosons (from the di-jet and di-muon pairs) $\cos(\theta_{BB}) < -0.8$. Furthermore, we require the distance of any muon with respect to any jet to be at least 0.1 radians. Finally we select events with an acoplanarity in the reconstructed boson-boson system larger than 2.8 radians.

In order to test the compatibility of each event with either the HZ or ZZ hypothesis, we construct a χ^2 as follows

$$\chi^2_{ZZ} = \left(\frac{m_{JetJet} - m_Z}{\sigma_{m_{JetJet}}}\right)^2 + \left(\frac{m_{\mu\mu} - m_Z}{\sigma_{m_{\mu\mu}}}\right)^2 \tag{4.1}$$

$$\chi^2_{HZ} = \left(\frac{m_{JetJet} - m_Z}{\sigma_{m_{JetJet}}}\right)^2 + \left(\frac{m_{\mu\mu} - m_H}{\sigma_{m_{\mu\mu}}}\right)^2 \tag{4.2}$$

For the uncertainties we assume the resolutions derived above, but for the resolution the di-muon pair in the ZZ case we assume the natural width of the Z which is considerably larger than the muon resolution and we assume the Higgs mass to be known as 120 GeV. We then cut on $80 < \chi^2_{ZZ} < 120$ and $\chi^2_{HZ} < 20$. The number of events after each cut is summarized in Table 4.4. As a result of the selection above, we expect about 8 signal events with the background of 39 events in the final sample. The di-muon mass distributions after the final selections are shown in Figure 4.12.

The statistical significance of the abundance of events in the signal region $S/\sqrt{S+B}$ for this selection is equal to 1.1. The cross-section of the decay and its uncertainty can be computed accordingly as $\sigma = 0.074 \pm 0.066$ fb.

Cut	SM Background	$H \to \mu^+\mu^-$		
	Events	Events	$\epsilon_{H\to\mu^+\mu^-}$	$\epsilon_{H\to\mu^+\mu^- Z\to q\bar{q}}$
two muons required	4663389.3	17.18	0.928	0.960
Charged Tracks hadronic	26665.9	12.03	0.650	0.959
Evis hadronic Cut	19567.1	11.98	0.647	0.957
Jet Selection Cut	16683.6	11.82	0.638	0.944
Muon Mass Window	1519.3	11.49	0.621	0.918
MuonMuon Angle Cut	1297.9	11.32	0.612	0.905
BosonBoson Angle Cut	1129.3	10.90	0.589	0.872
Min Isolation Angle Cut	870.7	10.84	0.585	0.866
Boson Acoplanarity Cut	792.1	10.51	0.568	0.841
ZZ qqqmm chisquare Cut	260.7	10.04	0.543	0.804
HZ qqqmm chisquare Cut	60.7	8.64	0.467	0.692
Z mass cut	53.6	7.74	0.418	0.622
Higgs mass cut	39.3	7.66	0.414	0.616

Table 4.4: The event selection for hadronic channel.

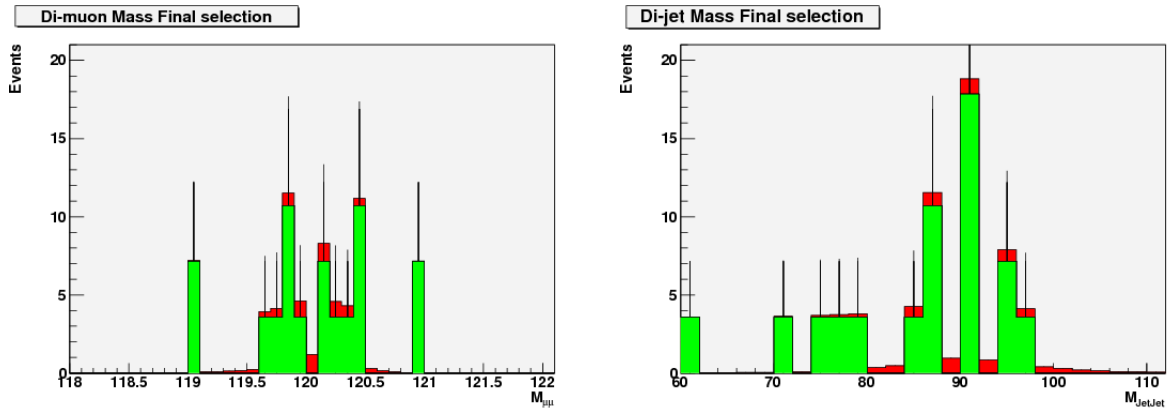

Figure 4.12: The mass of the di-muon pair (a) and the di-jet pair in the final sample.

Cut	SM Background	$H \to \mu^+\mu^-$		
	Events	Events	$\epsilon_{H\to\mu^+\mu^-}$	$\epsilon_{H\to\mu^+\mu^- Z\to\nu\nu}$
two muons required	4663389.3	17.18	0.928	0.960
number of Tracks	4376478.9	4.06	0.219	0.958
visible Energy	706483.1	3.42	0.185	0.806
charged Energy	356850.7	3.21	0.174	0.758
missing Momentum	26937.9	3.21	0.174	0.758
cos theta between muons	17238.6	3.20	0.173	0.756
muon energy cut	15952.1	3.17	0.171	0.747
chi2 cut	1314.3	2.72	0.147	0.641
missing Mass	1280.7	2.70	0.146	0.637
mass	1190.7	2.70	0.146	0.637

Table 4.5: Event selection for the missing energy channel.

For the neutrino channel we select events with a missing mass compatible with the Z mass, and with two high-energetic muons consistent with a $H \to \mu\mu$ decay. The analysis selections are listed in Table 4.5.

Based the numbers of signal and background events after the final selections we conclude that in the case of missing energy channel a cut-and-count analysis is insufficient to obtain a meaningful result. Multivariate classifiers can aid greatly in the separation of signal and background. A preliminary analysis employing these methods showed that a separation between signal and background of 1.8 sigma is achievable in the neutrino channel. Similarly, a considerable improvement could be expected in the hadronic channel.

4.2.4 $e^+e^- \to \tau^+\tau^-$, $\sqrt{s}$=500 GeV

The identification of 250 GeV taus and their decay modes is a challenge for the tracker and calorimeter. Low multiplicty but tightly collimated jets must be reconstructed in terms of the underlying charged hadron and π^0 constituents. Particle flow algorithms designed to measure jet energy may require modification to provide optimal tau mode identification.

Two sets of observables are used to quantify the ability of the SiD detector to reconstruct 250 GeV taus. First, tau decay mode efficiencies and purities are determined, and then the tau polarization is measured. Decay mode efficiencies are determined for the decays $\tau^- \to e^-\bar{\nu}_e\nu_\tau$, $\mu^-\bar{\nu}_\mu\nu_\tau$, $\pi^-\nu_\tau$, $\rho^-\nu_\tau$, $a_1^-\nu_\tau$. With the exception of $a_1^-\nu_\tau$ the same set of decay modes is used for the measurement of the tau polarization.

4.2.4.1 Cross Section and A_{FB} Precision

Full energy tau pair events were selected by clustering the PFA reconstructed particles into tau jets. Event cuts were $1 <$ #tracks < 7 and 40 GeV $<$ EVis $<$ 450 GeV. Exactly 2 jets were required, each with $|\cos\theta| < 0.95$. The opening angle between the jets was required to be greater than 178°. Events with both jets identified as electrons or both jets identified as muons were also rejected. The results of this selection are shown in Figure 4.13. The selection efficiency for all tau pair events is 17.9%, yielding 128708 events. Using the full SM data set, 3099 events were selected from non tau pair events, for a background of 2.4%.

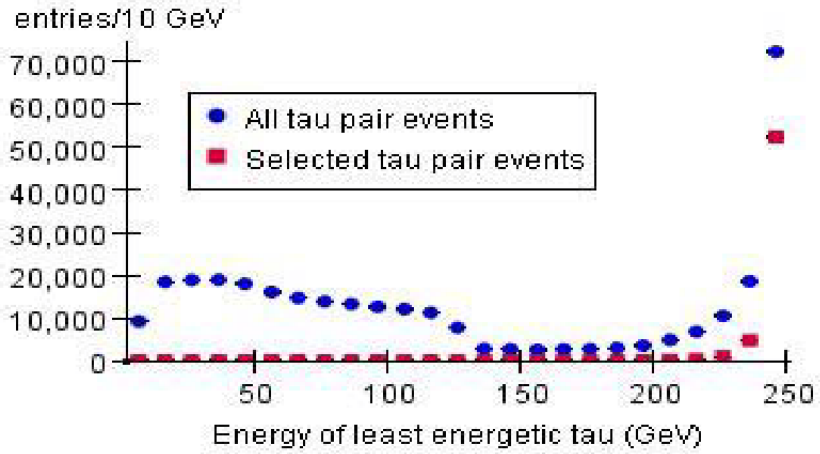

Figure 4.13: Energy of least energetic τ for full sample (blue) and following event selection (red).

Using these events the cross section was measured by counting, and the forward backward asymmmetry A_{FB} was measured by performing a least squares fit of the $\cos\theta$ distribution of the taus assuming $d\sigma/d\cos\theta \propto 1 + \cos\theta^2 + 8/3 \cdot A_{FB}\cos\theta$. The precision of the cross section is 0.28%. The forward backward asymmetry measurement was $A_{FB} = 0.5038 \pm 0.0021$ for a 250 fb^{-1} 80eL test sample and $A_{FB} = 0.4704 \pm 0.0024$ for a 250 fb^{-1} 80eR test sample (80eL and 80eR are defined in the discussion on tau polarization).

4.2.4.2 Tau Decay Mode Efficiencies and Purities

The tau decay modes were identified as follows. All calorimeter hits were clustered and assigned to the nearest tau jet. Photon identification was performed on EM clusters, and photons reconstructed. All remaining clusters were assigned to tracks. The total calorimeter energy assigned to the track was required to be no more than the sum of the track momentum and $n\sigma$, where $\sigma = 0.65\sqrt{E}$ and $n = 2.2$ or 2.5 (the EPcut). The selection cuts are summarized in Table 4.6 where a π^0 is a pair of photons satisfying 0.06 GeV $< M_{2\gamma} <$ 0.18 GeV.

Alternate photon reconstructions were attempted on tau jets that remained unidentified after this first pass at identification. The number of photons was changed by combining the 2 nearest photons, changing the identification of a photon cluster, or looking for possible

decay mode	# γ	# π^0	EPcut	other criteria
$e^-\bar{\nu}_e\nu_\tau$	0	0	-	HCAL energy $< 4\%$ of track energy.
$\mu^-\bar{\nu}_\mu\nu_\tau$	0	0	-	identified as μ by PFA
$\pi^-\nu_\tau$	0	0	2.5	-
$\rho^-\nu_\tau \to \pi^-\pi^0\nu_\tau$	1	0	2.2	0.6 GeV $< M_\rho <$ 0.937 GeV, $\quad E_\gamma > 10$ GeV
$\rho^-\nu_\tau \to \pi^-\pi^0\nu_\tau$	2	1	2.2	0.4 GeV $< M_\rho <$ 0.93 GeV
$a_1^-\nu_\tau \to \pi^-\pi^0\pi^0\nu_\tau$	3	1	2.2	0.8 GeV $< M_{a_1} <$ 1.5 GeV, $\quad E_\gamma > 10$ GeV
$a_1^-\nu_\tau \to \pi^-\pi^0\pi^0\nu_\tau$	4	2	2.2	0.8 GeV $< M_{a_1} <$ 1.5 GeV
$a_1^-\nu_\tau \to \pi^-\pi^+\pi^-\nu_\tau$	0	0	2.5	0.8 GeV $< M_{a_1} <$ 1.7 GeV

Table 4.6: Decay mode identification criteria.

missed photons. After a new set of photons was reconstructed the criteria in Table 4.6 were applied. If the tau jet remained unidentified after this second pass then further alternate photon reconstructions were attempted.

Using a test sample the purity of the mode identification was calculated separately for each of these photon reconstruction iterations. The purity was recorded for use in the polarization analysis. The decay mode purity and efficiency for all identified taus is shown in Table 4.7, while the purity and efficiency for taus identified with a photon reconstruction pass with purity greater than 85% is shown in Table 4.8. In all semi-leptonic modes, standard model backgrounds are below 2%.

decay mode	Correct ID	Wrong ID	ID eff	ID purity	SM bgnd
$e^-\bar{\nu}_e\nu_\tau$	39602	920	0.991	0.977	1703
$\mu^-\bar{\nu}_\mu\nu_\tau$	39561	439	0.993	0.989	1436
$\pi^-\nu_\tau$	28876	2612	0.933	0.917	516
$\rho^-\nu_\tau \to \pi^-\pi^0\nu_\tau$	55931	8094	0.790	0.874	1054
$a_1^-\nu_\tau \to \pi^-\pi^0\pi^0\nu_\tau$	18259	11140	0.732	0.621	847
$a_1^-\nu_\tau \to \pi^-\pi^+\pi^-\nu_\tau$	21579	2275	0.914	0.905	141

Table 4.7: Tau decay mode reconstruction for all events.

4.2.4.3 Tau Polarization

A measurement of the tau polarization P_τ for full energy taus at $\sqrt{s} = 500$ GeV would be an important part of a program, for example, to search for and measure the properties of multi-TeV Z' resonances at the ILC. The tau polarization measurement relies on the quality of the decay mode identification as well as the quality of the decay product four-vector reconstruction. It therefore serves as an excellent benchmark for detailed particle reconstruction by ILC detectors.

decay mode	Correct ID	Wrong ID	ID eff	ID purity	SM bgnd
$e^-\bar{\nu}_e\nu_\tau$	39602	920	0.991	0.977	1703
$\mu^-\bar{\nu}_\mu\nu_\tau$	39561	439	0.993	0.989	1436
$\pi^-\nu_\tau$	26599	491	0.859	0.982	387
$\rho^-\nu_\tau \to \pi^-\pi^0\nu_\tau$	41013	3056	0.579	0.931	674
$a_1^-\nu_\tau \to \pi^-\pi^0\pi^0\nu_\tau$	2720	272	0.109	0.909	23
$a_1^-\nu_\tau \to \pi^-\pi^+\pi^-\nu_\tau$	17328	1153	0.734	0.938	111

Table 4.8: Tau decay mode reconstruction for the high purity sample of tau decays.

The optimal observable technique[3] is used to measure the mean tau polarization $< P_\tau >$ over all tau production angles. The following decay modes are used: $e^-\bar{\nu}_e\nu_\tau$, $\mu^-\bar{\nu}_\mu\nu_\tau$, $\pi^-\nu_\tau$, and $\rho^-\nu_\tau \to \pi^-\pi^0\nu_\tau$. For lepton and single pion decays the optimal observable ω is simply x, the ratio of the energy of the lepton or pion and the beam energy. For the rho decay ω is a complicated function[4] of the angles of the rho in the tau rest frame and of the charged pion in the rho rest frame.

The average polarization is measured separately for initial electron and positron polarization combinations of $e^-(80\%L)\ e^+(30\%R)$ and $e^-(80\%R)\ e^+(30\%L)$. These two polarization combinations will be referred to in the following by their electron polarizations 80eL and 80eR. In the Standard Model the true tree-level average tau polarizations at $\sqrt{s} = 500$ GeV are $< P_\tau >$= -0.625 and 0.528 for initial state polarizations of 80eL and 80eR, respectively.

A linear least squares fit of $< P_\tau >$ over all the bins of all the reconstructed ω distributions for $e^-\bar{\nu}_e\nu_\tau$, $\mu^-\bar{\nu}_\mu\nu_\tau$, $\pi^-\nu_\tau$, and $\rho^-\nu_\tau \to \pi^-\pi^0\nu_\tau$ is used to measure $< P_\tau >$. The Monte Carlo tau pair sample is divided in half with one half used for training and the other for testing. The dependence of the reconstructed ω distributions on $< P_\tau >$ is obtained by comparing the reconstructed ω distributions for the training samples for 80eL and 80eR initial state polarizations. The tau polarization of the testing sample is then measured.

The quality of the tau decay product kinematic variable reconstruction is exhibited in Figure 4.14. The reconstructed and true distributions for the cosine of the angle θ^* between the rho and the tau in the tau rest frame, and the cosine of the angle β between the charged pion and rho in the rho rest frame are shown. The true and reconstructed distributions for the optimal observable ω for the decay $\rho^-\nu_\tau$ are show in Figure 4.15.

The testing tau pair Monte Carlo sample corresponds to a luminosity of 250 fb^{-1} for each of the intial state polarizations 80eL and 80eR . After performing the least squares fits the mean tau polarizations are $< P_\tau >$=-0.611$\pm$0.009 stat.$\pm$0.005 sys. for the 80eL sample and $< P_\tau >$=0.501$\pm$0.010 stat.$\pm$0.006 sys. for the 80eR sample, where the systematic errors are due to the finite training sample statistics.

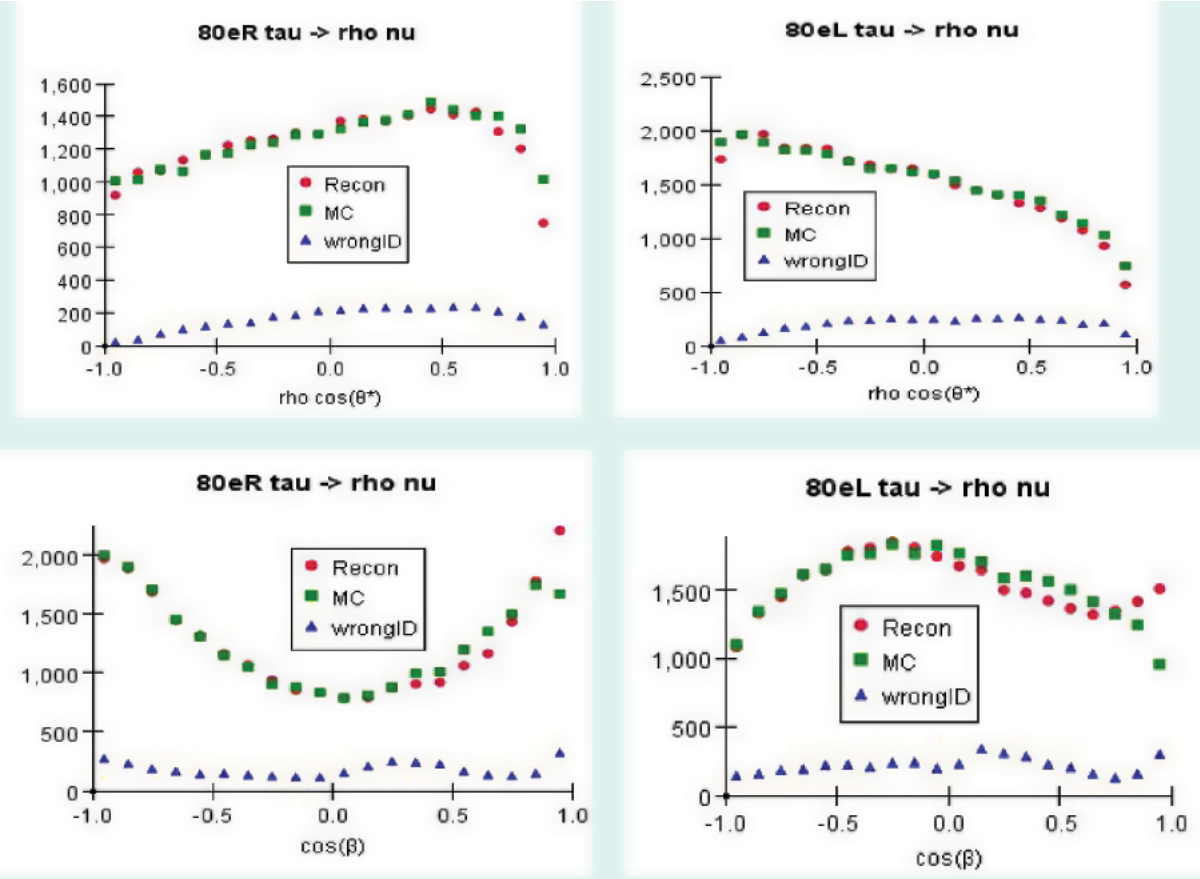

Figure 4.14: Reconstructed (red) and true (green) kinematic variables used in the definition of the optimal observable ω for the decay $\rho^-\nu_\tau$. The top two plots are $\cos\theta^*$ and the bottom two plots are $\cos\beta$ (see text). Also shown are distributions for incorrectly identified taus (blue).

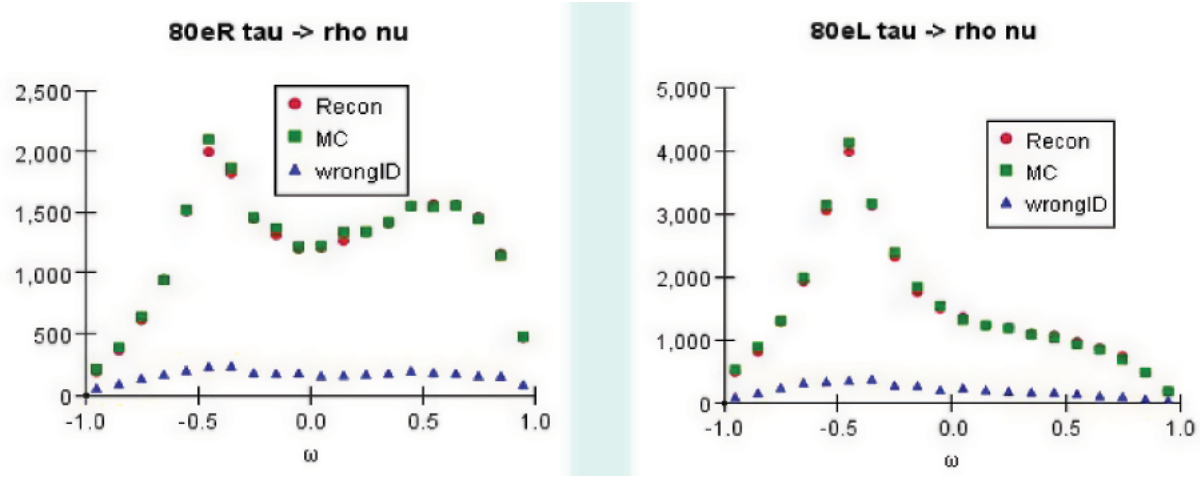

Figure 4.15: Reconstructed (red) and true (green) distributions for the optimal observable ω for the decay $\rho^-\nu_\tau$.Also shown are distributions for incorrectly identified taus (blue).

4.2.5 $e^+e^- \to t\bar{t}\,,\ t \to bW^+\,,\ W^+ \to q\bar{q'}\,,\ \sqrt{s}$=500 GeV

The top quark is substantially more massive than the rest of the observed quarks [16]. It is therefore important to search for the physical mechanism that introduces the mass difference and at the same time to use the top as a probe into new physics, which often couples to mass. In order to investigate such mechanisms it is essential to determine precisely the mass of top and its couplings to the SM bosons. The aim of the analysis is to measure the total top cross-section of the channel $e^+e^- \to t\bar{t}, t \to bW, W \to q\bar{q}$, the mass and the forward backward asymmetry (A_{FB}) of the top quark and also of the bottom quark from the top quark decay.

The sample used in the analysis is the inclusive SM sample which includes the top quark production with mass of 174 GeV. Two separate samples with the top mass 174 and 173.5 GeV have been generated to evaluate precision of the mass reconstruction.

The analysis considers only the hadronic decay modes with the largest available statistics. The six jet final state includes two b-quarks from the top decay. The first step of the analysis is to identify the hadronically decaying top quarks simultaneously rejecting the non-top SM background, leptonic top decays and poorly reconstructed hadronic top decays. The analysis starts with clustering of reconstructed particles in to six jets using the y-cut algorithm. All events with jets composed of a single reconstructed electron or muon are discarded. A list of further selections used in the analysis is given in Table 4.9.

	selection	value
	E_{total}	$>$ 400 GeV
	$\log(y_{min})$	$>$ -8.5
	number of particles in event	$>$ 80
	number of tracks in event	$>$ 30
50 GeV $<$	W mass	$<$ 110 GeV
	NN_{b-tag} output for the most b-like jet	$>$ 0.9
	NN_{b-tag} output for the 2^{nd} most b-like jet	$>$ 0.4
	Sum of NN_{b-tag} outputs for all jets	$>$ 1.5

Table 4.9: Selections for the top analysis.

In particular, the y_{min} variable is a good indicator that an event is topologically consistent with a six jet hypothesis. For example, in a case where two jets overlap in the detector, these jets will be merged by the jet clustering algorithm. However due to the six jet requirement another jet of the event will have to be separated into two reconstructed jets. This will result in the substantially lower y_{min} value and therefore the rejection of the event. Events with jets outside of the acceptance will have a substantial missing energy and will be rejected by the total energy requirement. Figure 4.16 shows examples of variables, y_{min} and $N_{particles}$, used in the top selections.

Another powerful selection criteria for the top events is tagging of two b-quarks necessarily present in the signal. This substantially reduces the combinatorial background in the top quark events by decreasing the number of possible jet permutations. Figure 4.17 shows

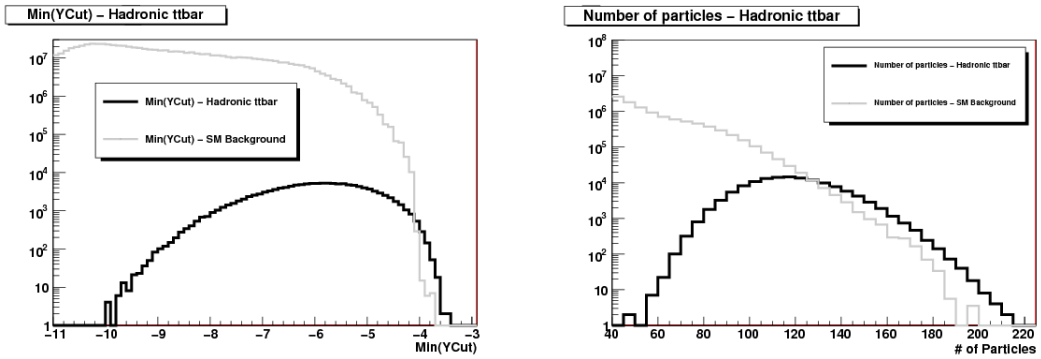

Figure 4.16: Distributions of y_{min} (a) and $N_{particles}$ (b) before the selection.

the sum of b-tagging NN outputs for all jets before (a) and after (b) the selections.

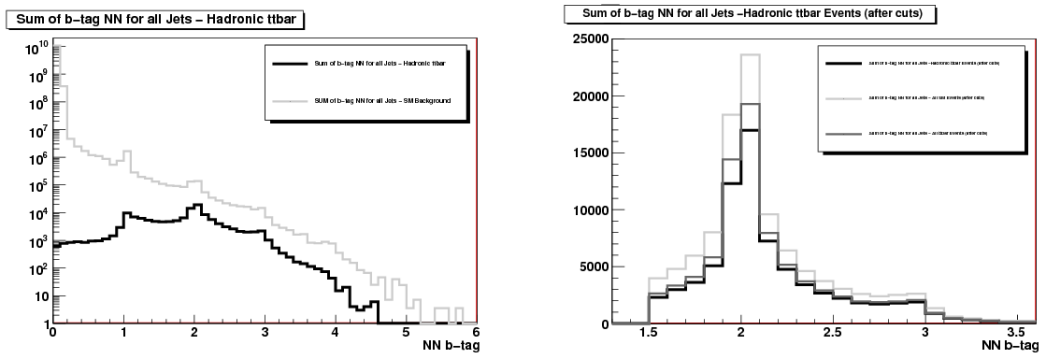

Figure 4.17: Sum of b-tagging NN outputs for all jets for top signal and background events before (a) and after (b) selections.

The signal efficiency of the above selections is equal to 51.2% which amounts to approximately 73000 signal events in the final sample. About 99.97% of di-lepton top decay channels and 93.9% single leptonic modes are rejected. The total remaining SM background comprises about 33000 events which corresponds to the purity of 68.8%, where purity is defined as number of events passing all cuts that originated from two b quarks and four other quarks at the parton level divided by all events that pass the cuts.

The next step of the analysis is the calculation of the top mass. A kinematic fitter was employed to reduce the combinatorial background of the six-jet environment and to take advantage of the existing kinematic constraints of top decays, see Table 4.10 for the full list of constraints used for this analysis.

The two most b-like jets were considered to be originating from b-quarks and therefore were not used in permutations for reconstruction of two W bosons. All the events that

mass(top1)	= mass(top2)
mass(W1)	= 80.4 GeV
mass(W2)	= 80.4 GeV
E_{total}	= 500 GeV
p_x; p_y; p_z	= 0

Table 4.10: Kinematic fitting constraints.

meet the fitting constrains with probability less than 10% were rejected. This requirement selects only well reconstructed top events and is quite sensitive to the jet energy and angular resolutions which are the input parameters for the fitter. Although this selection reduces the efficiency to 31.3%, but it also increases the purity to 85.1% and overall improves the precision of mass resolution.

It is now possible to perform a mass fit using an asymmetric double Gaussian convoluted with a Breit-Wigner as a signal fit function. The function is fitted on a separate signal sample in the mass range of 166 GeV - 200 GeV where the parameters of the Gaussians are determined keeping all other parameters fixed. The Standard Model background is then described by a second order polynomial function. The combined function is fitted on the data sample with all the parameters fixed for the exception of the top mass and the Breit-Wigner width. This method results in the top mass of 173.918 ± 0.053 GeV thus predicting the accuracy of about 50 MeV of the top mass determination with 500 fb^{-1}. The distribution of the top mass and the corresponding fit is shown in Figure 4.18. It is also possible to estimate the $t\bar{t}$ cross-section in the hadronic channel as 284.1 ± 1.4 fb.

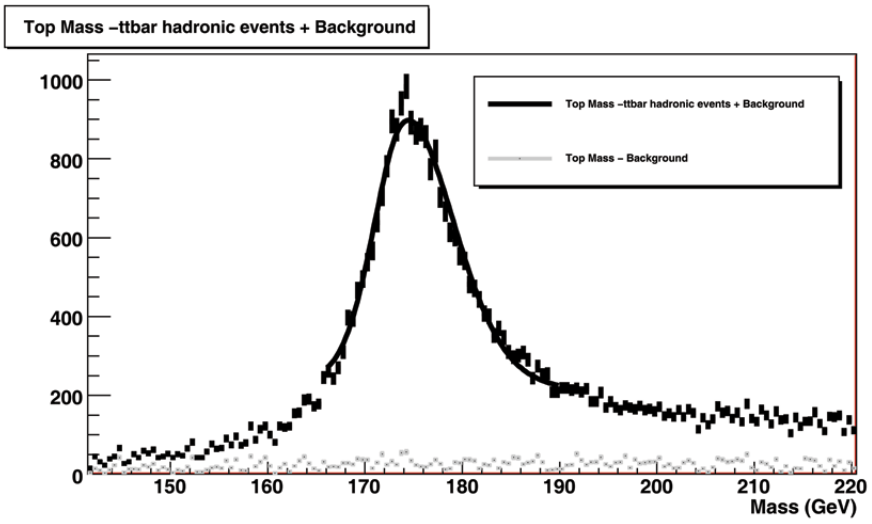

Figure 4.18: Distribution of the top invariant mass after the kinematic fitting and probability cut.

The determination of top quark mass uncertainty can be calculated also using a template method. The data sample, without the SM background, is compared with a template

produced at the same mass and with a template with the top mass shifted by 0.5 GeV. From the reconstructed top mass distribution the chi-square between the two can be calculated as:

$$\chi_1^2 = \sum_{i=0}^{Nbins} \frac{(y_{template1,i} - y_{data,i} + \delta_i)^2}{\sigma^2_{template1,i} + \sigma^2_{data,i} + \sigma^2_{SM,i}} \tag{4.3}$$

where $y_{...i}$ denotes the content of the ith bin. The δ term is added as a Gaussian smearing of the central value of $y_{template,i} - y_{data,i}$ to take the SM background into account. The calculated χ^2 divided by degrees of freedom is close to one and does not depend on the bin width.

Similarly we can obtain χ_2^2 between 'data' and the other template sample. From χ_1^2 and χ_2^2 we can fit a χ^2 parabola with respect to Δm_{top}, assuming χ_1^2 is the minimum [14]. The half width of the parabola where χ^2 equals $\chi_1^2 + 1$ gives the uncertainty of top mass. With the method described above it is possible to measure m_{top} with a resolution of 45 MeV. For this measurement the top candidate mass was restricted between 150 and 200 GeV. We note that the relation between the value of the measured top quark mass of this analysis and the mass that comes out of the measurement of the top quark threshold cross section are both expected to have a systematic bias. Both quantities can be related to $\mathrm{m}_t(\bar{M}S)$ by precise calculations [20].

Finally the last aim of the analysis is to determine the top couplings analyzing the forward-backward asymmetry of the top quark and of the b quark from the top decay. A precise measurement of both will allow to set limits on the anomalous couplings of Z$\rightarrow t\bar{t}$ and $t \rightarrow$Wb respectively [17].

For this purpose, one must be able to discriminate between b quarks and b anti-quarks. The conceptually simplest way to do this is by measuring the vertex charge, defined as the sum of the charges of all particles associated to a secondary vertex. However, there are other variables that are correlated with the primary quark charge, and these can be combined to make a more powerful discriminant. For this analysis, we use a discriminant built from the momentum-weighted vertex charge and the momentum-weighted jet charge [18]. The performance of this discriminant is shown in Figure 4.19 (a).

Figure 4.19(b) shows the reconstructed number of top candidates as function of $\cos\theta$ of the b-quark direction with respect to the direction of the electron beam. This information is used as input for calculation of the forward-backward asymmetry of b-quark in top decays which was determined using the combined quark charge method described above. By using this method the resulting b-quark forward-backward asymmetry in 500 fb^{-1} is determined to be $A^b_{FB} = 0.272 \pm 0.015$, consistent with the generated one.

Calculation of the top quark asymmetry represents another complication as the reconstructed b-quark must be correctly associated with its W boson. This pairing is done using the output of the kinematic fitter. We note that the flavour of the top quark is determined by the flavour of the b-quark so the charge determination does not change; however the flight direction of the quark may change. The resulting top quark forward-backward asymmetry is calculated to be equal to $A^t_{FB} = 0.342 \pm 0.015$.

The selection efficiency for events where the quark charge can be determined with

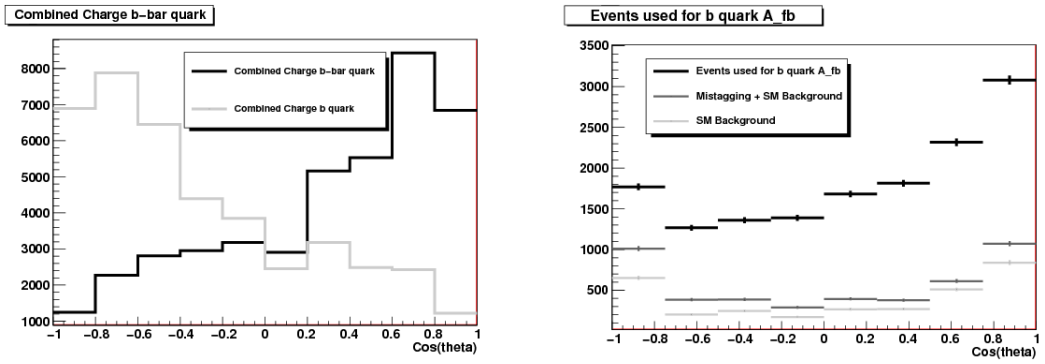

Figure 4.19: Combined quark charge discriminant for b and anti-b quarks (left). Number of events as function of $\cos\theta$ used for calculation of A_{FB} for the b-quark (right). The histograms are inclusive corresponding to the top signal with correct and incorrect charge assignment, and SM background.

sufficiently high purity is substantially lower, 7.1%, than the one previously presented for the top mass. This is due to the additional 155-195 GeV mass window selection and the fact that the selection on the combined charge effectively rejects a large sample of the B^0 mesons which have low purity of the quark charge determination and also rejects events in which a secondary vertex has not been reconstructed in both b-tagged jets. The selection on the top charge was done by requiring the product of combined charges of two b-quarks in the event to be smaller than -0.3.

4.2.6 $e^+e^- \to \tilde{\chi}_1^+\tilde{\chi}_1^-/\tilde{\chi}_2^0\tilde{\chi}_2^0$, $\sqrt{s}$=500 GeV

The masses of charginos and neutralinos are important parameters in supersymmetry which can be measured at ILC with high precision. In this analysis the following processes were used for the measurement:

$$\begin{aligned} e^+e^- &\to \tilde{\chi}_1^+\tilde{\chi}_1^- \to \tilde{\chi}_1^0\tilde{\chi}_1^0 W^+W^- \\ e^+e^- &\to \tilde{\chi}_2^0\tilde{\chi}_2^0 \to \tilde{\chi}_1^0\tilde{\chi}_1^0 Z^0Z^0 \end{aligned}$$

Here we only discuss the SUSY point at which the $\tilde{\chi}_1^\pm$ and $\tilde{\chi}_2^0$ decay by emission of on-shell W and Z bosons [13]. If we consider the all-hadronic decay of the gauge bosons in the final states, the above processes will both have a signature of four jets with large missing energy. Once the W or Z bosons are successfully reconstructed the shapes of their energy distributions will provide information on the chargino or neutralino masses. The uncertainty of the mass measurement is determined by the template fitting.

A Monte-Carlo SUSY sample with $\sqrt{s}$ of 500 GeV used for this study included the chargino/neutralino signals and SUSY backgrounds such as $e^+e^- \to \tilde{\chi}_1^0\tilde{\chi}_2^0$ and slepton pair production. Apart from this sample, six more samples with the same statistics were generated in order to estimate the uncertainty of these mass measurements, each with a corresponding

SUSY mass shifted by either ±0.5 GeV, see Table 4.11. All the samples have one polarization, namely 80% electrons left-handed and 30% positions right-handed and correspond to the integrated luminosity of 500 fb^{-1}. The production cross-section of chargino events with all hadronic final state is 57 fb which is considerably larger than that of the neutralino, 11 fb.

sample	$m_{\tilde{\chi}_1^0}$ (GeV)	$m_{\tilde{\chi}_1^\pm}$ (GeV)	$m_{\tilde{\chi}_2^0}$ (GeV)
Reference	115.7	216.7	216.5
$m_{\tilde{\chi}_1^0}$ + 0.5	116.2	216.7	216.5
$m_{\tilde{\chi}_1^\pm}$ + 0.5	115.7	217.2	216.5
$m_{\tilde{\chi}_2^0}$ + 0.5	115.7	216.7	217.0
$m_{\tilde{\chi}_1^0}$ - 0.5	115.2	216.7	216.5
$m_{\tilde{\chi}_1^\pm}$ - 0.5	115.7	216.2	216.5
$m_{\tilde{\chi}_2^0}$ - 0.5	115.7	216.7	216.0

Table 4.11: Parameters of the MC SUSY samples.

To identify events of the all-hadronic channel all reconstructed particles are clustered into four jets and selections described in Table 4.12 are applied.

cut	value
E_{jet}	> 10 GeV
Fraction of EM energy in each jet	$< 80\%$
Number of tracks	> 20
Total visible energy	< 250 GeV
Thrust	< 0.85
$\cos\theta_{thrust}$	< 0.9
$\theta(1, 2)$	$> 60^\circ$
$\theta(1, 3)$, $\theta(1, 4)$, $\theta(1, 3)$	$> 40^\circ$
$\theta(2, 4)$, $\theta(3, 4)$	$> 20^\circ$
Acoplanarity of two reconstructed gauge bosons	$> 10^\circ$

Table 4.12: Pre-selection cuts. $\theta(i, j)$ defines the angle between the ith and jth jet. The jets are ordered in energy, e.g. jet 1 is the most energetic jet.

These selections efficiently suppress the Standard Model background as illustrated in Figure 4.20 which shows distributions of total visible energy and acoplanarity before the selections.

To reconstruct the two gauge bosons from four jets we have to determine the correct jet

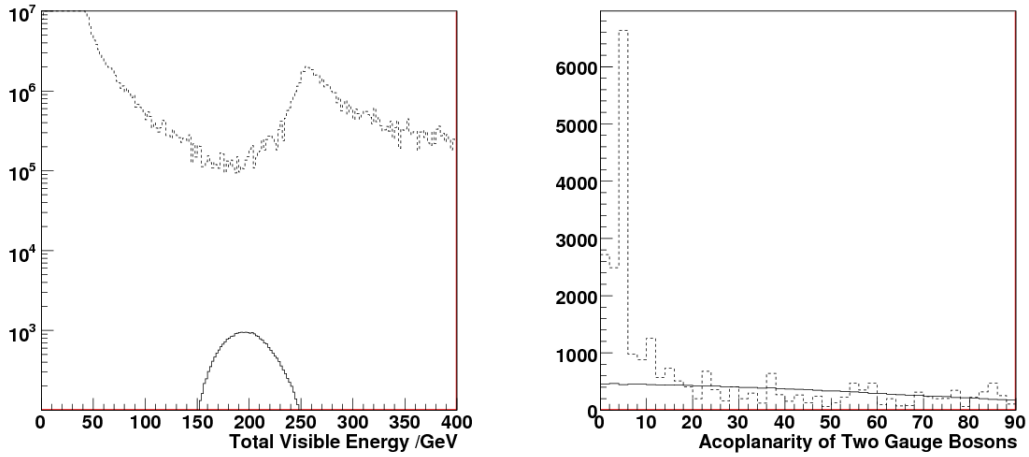

(a) (b)

Figure 4.20: Examples of selections for chargino analysis. Solid lines are chargino signal and dashed lines are SM background. (a)Total visible energy; (b)Acoplanarity of two reconstructed W bosons.

pairing. It is done by minimizing the quantity of $(m(j_1, j_2) - m_{W/Z})^2 + (m(j_3, j_4) - m_{W/Z})^2$, where $m(j_1, j_2)$ is the invariant mass of the jets j_1 and j_2 and all possible jet permutations are considered. W mass is used when selecting $\tilde{\chi}_1^+\tilde{\chi}_1^-$ events, and Z mass for $\tilde{\chi}_2^0\tilde{\chi}_2^0$ events. The correlation of the two reconstructed boson masses is shown in Figure 4.21. The chargino and neutralino events will populate different regions in the mass plane and therefore can be distinguished by a selection indicated by a thick line in Figure 4.21. Events above the line are classified as $\tilde{\chi}_1^+\tilde{\chi}_1^-$ events and below the line as $\tilde{\chi}_2^0\tilde{\chi}_2^0$ events. Another selection is applied for the chargino events to remove the events on the lower left corner of the mass plane, which are due to the remaining leptonic decays of the bosons.

After these selections the reconstructed boson energy distributions are shown in Figure 4.22. The chargino sample contains 15362 signal events with 1997 neutralino pair background and 2980 SM background events. Similarly the neutralino sample contains 1659 signal events with 2395 chargino and 865 SM background events. Contribution of other SUSY backgrounds are negligible in both cases. The uncertainty on the cross section measurement for chargino and neutralino pair production with all hadronic final state is 0.9% and 4.2% respectively neglecting the uncertainty on efficiency.

In the rest frame of $\tilde{\chi}_1^\pm/\tilde{\chi}_2^0$, $W^\pm/Z$ bosons are monochromatic and their energy is determined by $m_{\tilde{\chi}_1^\pm}/m_{\tilde{\chi}_2^0}$, $m_{W^\pm}/m_Z$ and $m_{\tilde{\chi}_1^0}$. For a boosted parent $\tilde{\chi}_1^\pm/\tilde{\chi}_2^0$, the boson energy distribution depends on the SUSY particle masses which will determine the edges of the energy spectrum. The masses can be measured comparing the energy spectrum in the 'data' to reference MC samples as in Table 4.11. Thus, the best possible energy resolution is required for a high precision mass measurement. Using the fact that the two bosons reconstructed from the four jets have the same mass in both $\tilde{\chi}_1^+\tilde{\chi}_1^-$ and $\tilde{\chi}_2^0\tilde{\chi}_2^0$ cases, kinematic fitting with one constraint ($m_{boson1} = m_{boson2}$) can be used for improving the energy distribution assuming

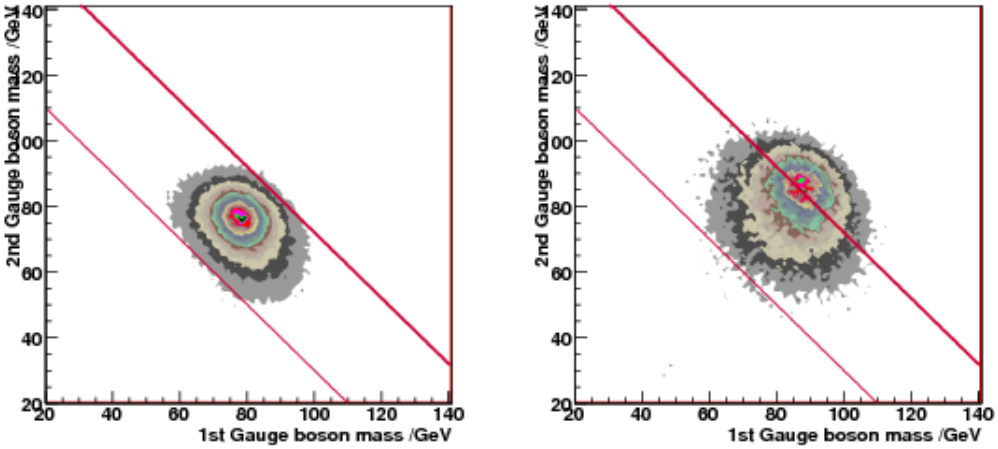

Figure 4.21: The reconstructed boson masses from the four jets, selecting chargino events. Left: pure chargino signal; right: pure neutralino signal. The region between the two straight lines shows the allowed chargino selection window.

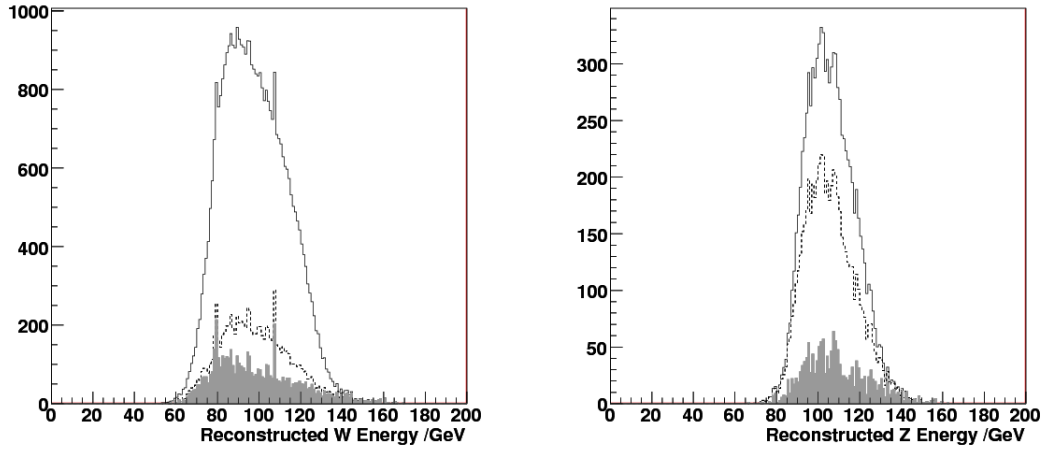

(a) (b)

Figure 4.22: (a) The stack histogram of reconstructed W energy for the chargino selection. The solid line shows the combined chargino signal and all backgrounds including neutralino, the dashed line is neutralino events and SM background, the solid grey line is the SM background only. (b) Reconstructed Z energy for neutralino selection, the solid line is the neutralino signal and all backgrounds including chargino, dashed line is the chargino events and SM background, the solid grey line is the SM background only. The spikes in (a) are due to the large weight of a few events in the SM background sample.

that the detector energy and angular resolution for jets is known. Kinfit in Marlinreco package is used for the fitting. The comparison of reconstructed W mass with and without fitting is shown in Figure 4.23.

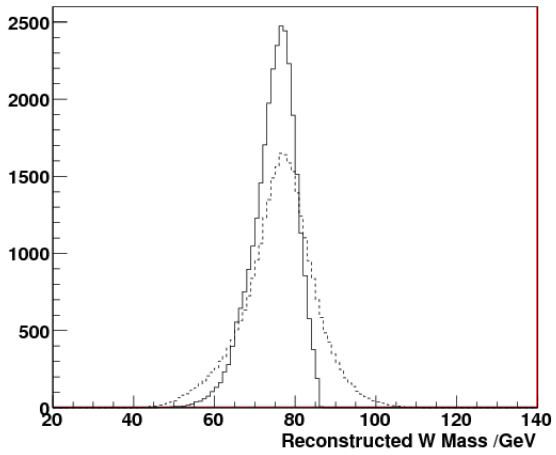

Figure 4.23: Mass distribution of reconstructed bosons before (dashed line) and after (solid line) kinematic fitting.

The determination of SUSY particle mass uncertainty is explained below on the example of $m_{\tilde{\chi}_1^\pm}$. The reference $\tilde{\chi}_1^+\tilde{\chi}_1^-$ sample (without SM background) is split into two unequal subsamples, 'data' and 'template 1', with the latter one having much higher statistics. From the normalized reconstructed W energy distribution the chi-square between the two can be calculated as:

$$\chi_1^2 = \sum_{i=0}^{Nbins} \frac{(y_{template1,i} - y_{data,i} + \delta_i)^2}{\sigma_{template1,i}^2 + \sigma_{data,i}^2 + \sigma_{SM,i}^2} \tag{4.4}$$

where $y_{...i}$ denotes the content of the ith bin. The δ term is added as a Gaussian smearing of the central value of $y_{template,i} - y_{data,i}$ to account for fluctuations of the SM background. The resulting χ^2/NDF is close to one and does not depend on the binning.

Similarly we can obtain χ_2^2 and χ_3^2 using template samples with $m_{\tilde{\chi}_1^\pm}$ shifted by $+0.5$ and -0.5 GeV, respectively. We fit a χ^2 parabola with respect to $\Delta m_{\tilde{\chi}_1^\pm}$, assuming that χ_1^2 is the minimum and using χ_2^2 and χ_2^2 as second and third points. The half width of the parabola where χ^2 equals $\chi_1^2 + 1$ gives the uncertainty on the chargino mass [14].

With the method described above for the $\tilde{\chi}_1^+\tilde{\chi}_1^-$ process we can measure $m_{\tilde{\chi}_1^\pm}$ and $m_{\tilde{\chi}_1^0}$ with uncertainties of 450 MeV and of 160 MeV respectively. The $\tilde{\chi}_2^0\tilde{\chi}_2^0$ process gives uncertainties of 490 MeV for $m_{\tilde{\chi}_2^0}$ and 280 MeV for $m_{\tilde{\chi}_1^0}$. The larger uncertainties for the latter are expected because of the smaller cross-section with respect to the $\tilde{\chi}_1^+\tilde{\chi}_1^-$ process, which yields lower statistics as well as inferior purity of the sample. A small improvement of the precision can be achieved by a simultaneous fit to the both chargino and neutralino samples.

4.2.7 $e^+e^- \to \tilde{b}\tilde{b}\,,\ \tilde{b} \to b\tilde{\chi}_1^0$

Recent measurements of the neutralino relic density suggest a small mass splitting between the neutralino and the next to lightest SUSY particle (NLSP) assuming that neutralino accounts for the measured dark matter content of the universe. The ILC has a potential to cover a large fraction of the parameter space motivated by this SUSY scenario. In this analysis we assume that the supersymmetric partner of b-quark, sbottom, is the NLSP [21]. Such a measurement is challenging due to very low energy of jets, below 20-30 GeV, which pushes the jet clustering and tagging algorithms to their limits. Figure 4.24 shows that while the b-tagging efficiency is about 75% above 60 GeV, it is falling steeply for lower jet energies.

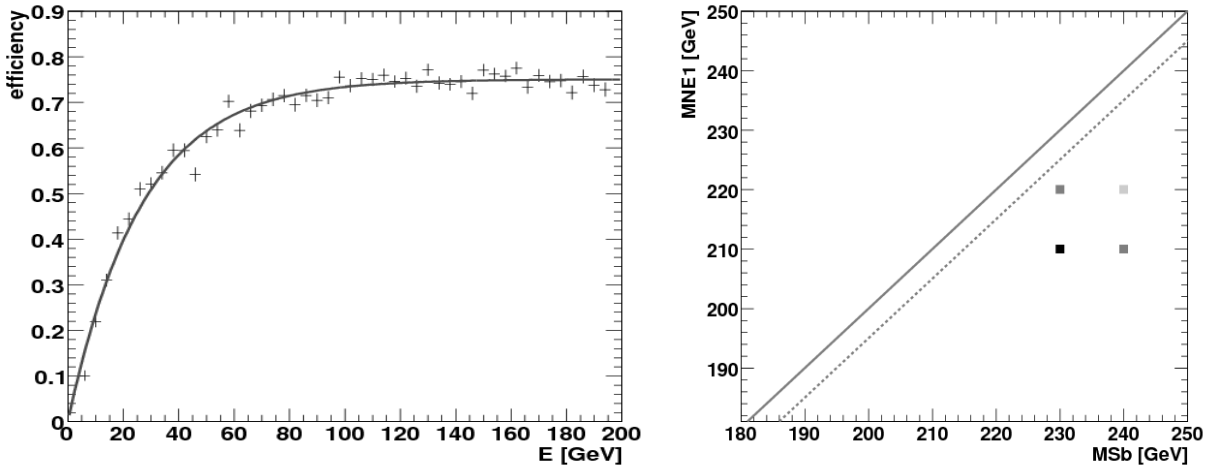

Figure 4.24: Jet b-tagging efficiency as a function of the jet energy for b-jets (left). Signal mass points selected for this analysis (right). The dashed line corresponds to the kinematic limit due to a small difference between $m_{\tilde{b}}$ and $m_{\tilde{\chi}_1^0}$.

In this study the CalcHEP event generator [19] was employed to generate SUSY signal events. The events were converted to Les Houches format, passed to Pythia for their fragmentation and particle decays and consequently to the usual SiD full simulation and reconstruction chain. The event classification is based on a Neural Network using the FANN package [10]. Several points in the MSSM parameter space were chosen close to kinematic limits in order to investigate the discovery potential. These points correspond to various masses of the sbottom quark and neutralino: (230, 210); (240, 210); (230,220); (240,220), all in GeV, see the right plot in Figure 4.24. For each signal point 200k events were generated, also accounting for ISR, FSR and beamstrahlung.

The mass of sbottom quark $m_{\tilde{b}}$ essentially determines the cross section of the process, 1.3 fb for $m_{\tilde{b}} = 230\,\text{GeV}$ but the cross section is 3.5 times smaller for $m_{\tilde{b}} = 240\,\text{GeV}$. The mass difference between $m_{\tilde{b}}$ and $m_{\tilde{\chi}_1^0}$, on the other hand, determines the energy of b-jets.

Jets were reconstructed by employing the Durham k_T algorithm with $k_T^{min} = 10\,\text{GeV}$ and limiting the maximum number of jets to two. Events with a single reconstructed jet were later rejected as well. The majority of the SM background is suppressed by the

$E_{visible} < 80\,\text{GeV}$ selection. Signal events are misbalanced in energy due to neutralinos while the dominant two-photon and $e^+e^- \to q\bar{q}$ backgrounds produce jets in back-to-back topology motivating the $\Delta R_{\eta\phi} < 3.0$ selection. To further suppress the background a selection $max(|\eta_1|, |\eta_2|) < 2.0$ is required, where η_1 and η_2 are jet pseudorapidities. Finally, the total number of particles in an event is required to be within $10 \leq N_{particles} \leq 60$ for the mass point (230,210) and it is adjusted for the other mass points individually.

Figure 4.25 shows distributions of acoplanarity and maximum pseudorapidity for the signal with $m_{\tilde{b}} = 230\,\text{GeV}$ and $m_{\tilde{\chi}^0_1} = 210\,\text{GeV}$ and inclusive SM background. The signal was scaled up by a factor of 100000 for the presentation purposes.

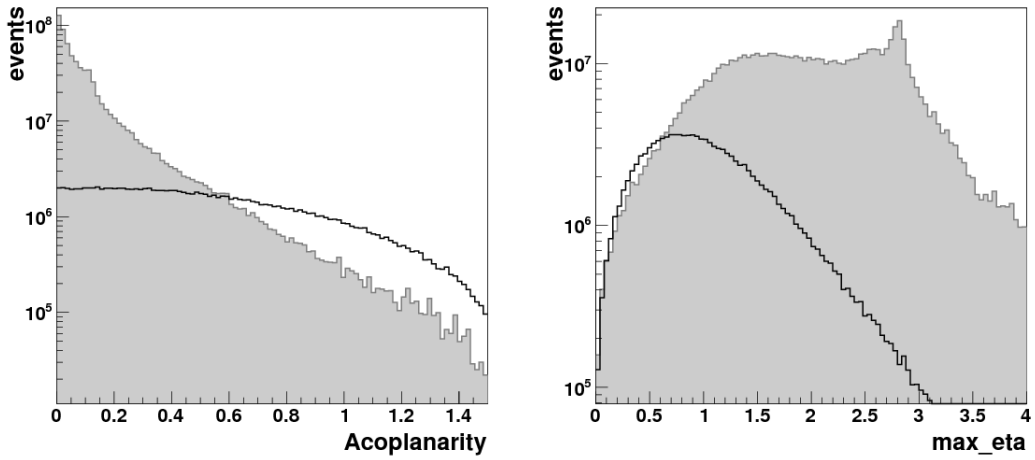

Figure 4.25: Examples of selection variables: acoplanarity (left) and maximum pseudorapidity (right) of jets. Signal with $m_{\tilde{b}} = 230\,\text{GeV}$ and $m_{\tilde{\chi}^0_1} = 210\,\text{GeV}$ (black) is shown together with the inclusive SM background (filled histogram). The signal was scaled up by a factor of 100000.

An important ingredient in this analysis is an electromagnetic veto using the forward detector at very low polar angles, above $\theta = 10\,\text{mrad}$. This is used to suppress the two-photon background as well as other backgrounds with a large ISR contribution. The forward detector acceptance was estimated using a simple geometrical model. An event is rejected if a photon or electron with $E > 300\,\text{MeV}$ is detected within the acceptance.

For the final event selection a Neural Network based on the above variables was defined and trained on independent signal and background samples. The Neural Net inputs were completed by adding the flavour tag information for both jets, momentum isotropy, acoplanarity and the total number of charged particles. The resulting NN output is shown in the left plot of Figure 4.26. The measurement is interpreted in terms of signal significance calculated as $S/\sqrt{S+B}$, where S is the number of selected signal events and B is the number of selected background events. The event numbers are normalised to the total luminosity of 1000 fb^{-1}. Figure 4.26 shows a distribution of $S/\sqrt{S+B}$ as function of the number of selected signal events with each bin corresponding to a particular cut on the NN classifier output. Big variations are caused by the SM events with large weights. Based on the above the signal cross section statistical uncertainty was calculated to be equal to 15% for the (230,210)

mass point. The mass points (240, 210); (230,220); (240,220) all can be excluded at the 95% CL. We conclude that the exclusion region can be extended very close to the ILC kinematic limits and, in case of discovery, the sbottom production cross section can be measured with a resonable statistical precision. This measurement relies on good performance of the forward detector used to veto two-photon background events and soft di-jet events with a dominant ISR contribution.

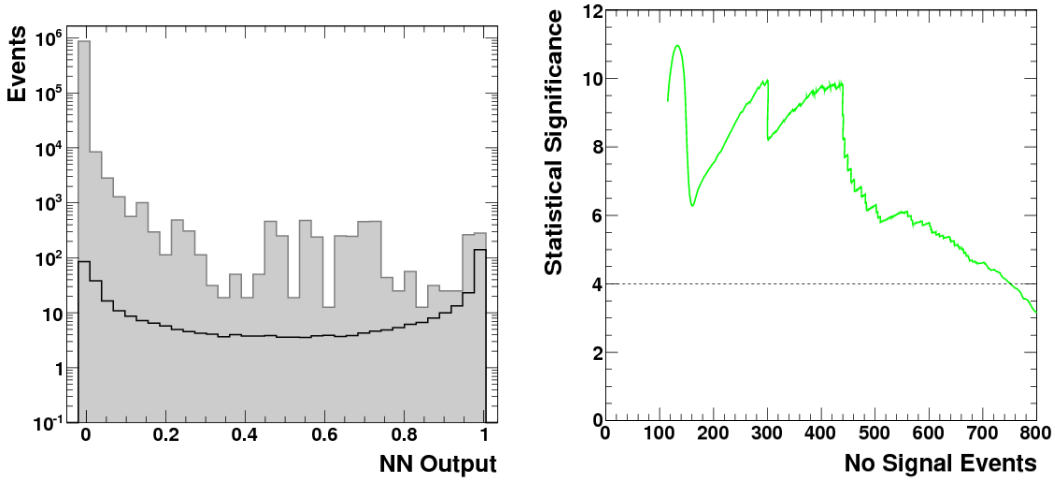

Figure 4.26: Neural Network output (left) is shown for events which passed the basic selections for signal with $m_{\tilde{b}} = 230\,\text{GeV}$ and $m_{\tilde{\chi}_1^0} = 210\,\text{GeV}$ (black) and inclusive SM background (filled histogram). Statistical significance (right) is shown as a function of number of selected signal events. Dashed line shows a limit of four standard deviations. Big variations are caused by SM events with large weights.

References

[1] W. Kilian, T. Ohl and J. Reuter, "WHIZARD: Simulating Multi-Particle Processes at LHC and ILC," arXiv:0708.4233 [hep-ph].

[2] T. Sjostrand, S. Mrenna and P. Skands, "PYTHIA 6.4 physics and manual," JHEP **0605**, 026 (2006) [arXiv:hep-ph/0603175].

[3] M. Davier, L. Duflot, F. Le Diberder and A. Rouge, Phys. Lett. B **306**, 411 (1993).

[4] L. Duflot, "New method of measuring tau polarization. Application to the tau → a1 tau-neutrino channel in the ALEPH experiment", LAL-93-09.

[5] S. Agostinelli et al, "GEANT4a simulation toolkit", *Nuclear Instruments and Methods in Physics Research A 506 (2003) 250-303.*

[6] J. Allison et al, "Geant4 developments and applications", *IEEE Transactions on Nuclear Science 53 No. 1 (2006) 270-278.*

[7] http://www.lcsim.org/software/slic/doxygen/html/ .

[8] F. Gaede, T. Behnke, N. Graf and T. Johnson, LC-Note LC-TOOL-2003-053.

[9] B. List, J. List, "MarlinKinfit: An Object–Oriented Kinematic Fitting Package", LC-TOOL-2009-001.

[10] http://leenissen.dk/fann/ [leenissen.dk]

[11] http://hepwww.rl.ac.uk/LCFI/; LCFI Collaboration, "LCFIVertex package: vertexing, flavour tagging and vertex charge reconstruction for the design of an ILC vertex detector", NIM paper in preparation.

[12] M. Battaglia, T. Barklow, M. E. Peskin, Y. Okada, S. Yamashita and P. M. Zerwas, "Physics benchmarks for the ILC detectors," *In the Proceedings of 2005 International Linear Collider Workshop (LCWS 2005), Stanford, California, 18-22 Mar 2005, pp 1602* [arXiv:hep-ex/0603010].

[13] T. Tsukamoto et al. "Precision study of supersymmetry at future linear e^+e^- colliders", *Phys. Rev. D 51, 3153 (1995).*

[14] L. Lyons, *"Statistics for nuclear and particle physicists" Cambridge University Press, 1986.*

[15] T. Kuhl, K. Desch, *"Simulation of the measurement of the hadronic branching ratios for a light Higgs boson at the ILC"*, LC-PHSM-2007-001.

[16] C. Amsler *et al.* [Particle Data Group], Phys. Lett. B **667**, 1 (2008).

[17] E. Boos, M. Dubinin, M. Sachwitz and H. J. Schreiber, Eur. Phys. J. C **16**, 269 (2000) [arXiv:hep-ph/0001048].

[18] V. M. Abazov *et al.* [D0 Collaboration], Phys. Rev. D **74**, 112002 (2006) [arXiv:hep-ex/0609034].

[19] A. Pukhov, arXiv:hep-ph/0412191v1.

[20] S. Fleming *et al.*, PR D77, 114003 (2008).

[21] S. Profumo, Phys.Rev. D68 (2003) 015006.

Chapter 5

Cost Estimate

The SiD cost estimate is a construction cost estimate; it does not include R&D, commissioning, operating costs, or physicist salaries.

The SiD design incorporates a parametric cost model, which has been essential for ongoing detector optimization. Detector parameters (e.g. dimensions or masses) have been transferred to a Work Breakdown Structure (WBS) where a subsystem can be described to an arbitrary level of detail. Here we describe the LOI version of SiD as such a point design.

The parametric model of the detector comprises a large set of Excel spreadsheets that encapsulate a self-consistent model of SiD. It is straightforward to vary parameters ranging from the most basic, such as the tracker radius and aspect ratio, to parameters such as the number of tracking layers, the number and thickness of HCAL layers, and calorimeter radiator material. The tracking layers and disks are adjusted to fit the allocated space. The calorimeters are adjusted to nest properly with the tracker. The solenoid model is adjusted for its radius and field, and the flux return is adjusted to roughly contain the return flux. For each system, the cost driving component count, such as tungsten plates, silicon detectors, and readout chips for the ECAL, are calculated. The model has tables for material costs and estimates both materials and services (M&S) and labor costs that are associated with the actual scale of SiD. Costs that are approximately fixed, for example engineering, fixturing, or solenoid He plants, are imported from separate Work Breakdown Structure programs. A set of macros are used to calculate the costs of SiD as parameters are varied.

The WBS facilitates the description of the costs as a hierarchical breakdown with increasing levels of detail. Separate tables describe cost estimates for purchased M&S and labor. These tables include contingencies for each item, and these contingencies are propagated through the WBS. The cost tables have been reviewed by the subsystem groups. The quality of the estimate is considered roughly appropriate for a Letter of Intent; it would not be defensible for a construction readiness review. For illustration, sample of the WBS, for the tracker, is shown in Figure 5.1.

The M&S costs are estimated in 2008 US $. Labor is estimated in man-hours or man-years as convenient. For this estimate labor types are condensed to engineering, technical,

1.1.3	Tracker	1 each	@CF=Tracker	15,446,950	5,869,383	11,473,252	4,015,638	36,805,223
1.1.3.1	Tracker ED&I	1 each		0	0	7,761,320	2,716,462	10,477,782
1.1.3.1.1	Mechanical Engineer	20 man year		0	0	140,000	49,000	3,780,000
1.1.3.1.2	Mechanical Designer	10 man year		0	0	91,520	32,032	1,235,520
1.1.3.1.3	Mechanical Tech	40 man year	WAG	0	0	101,153	35,404	5,462,262
1.1.3.2	Tracker Mechanics	1 each		2,900,000	1,375,000	1,200,325	420,114	5,895,439
1.1.3.2.1	Tracker Space Frame, Barrel	1 lot		1,250,000	625,000	0	0	1,875,000
1.1.3.2.2	Outer Endcap Frame[0]	2 lot		250,000	125,000	0	0	750,000
1.1.3.2.3	Tracker Cooling	1 lot		150,000	150,000	0	0	300,000
1.1.3.2.4	Tracker Alignment System	1 each		1,000,000	350,000	0	0	1,350,000
1.1.3.2.5	Mechanical Engineer	3 man year		0	0	140,000	49,000	567,000
1.1.3.2.6	Mechanical Designer	3 man year		0	0	91,520	32,032	370,656
1.1.3.2.7	Mechanical Tech	5 man year		0	0	101,153	35,404	682,783
1.1.3.3	Tracker Silicon Detectors	1 each		11,546,950	4,244,383	2,511,607	879,063	19,182,003
1.1.3.3.1	Barrel	1 each		6,340,450	2,341,108	1,531,015	535,855	10,748,428
1.1.3.3.1.1	Tracker Barrel Module	8,130 each	Parametric	665	248	188	66	9,487,528
1.1.3.3.1.1.1	Tracker Silicon	0.01 Sq.m.		30,000	10,500	0	0	405
1.1.3.3.1.1.2	Tracker Module Mechanics Barrel	1 each		65	23	0	0	88
1.1.3.3.1.1.3	Tracker KPiX	2 each		100	35	0	0	270
1.1.3.3.1.1.4	Tracker Cable	1 each		100	50	0	0	150
1.1.3.3.1.1.5	Mechanical Tech	2 man hour		0	0	54	19	145
1.1.3.3.1.1.6	Procurement Officer	1.5 man hour		0	0	54	19	109
1.1.3.3.1.2	Level 1 Concentrator, Tracker	467 each		2,000	700	0	0	1,260,900
1.1.3.3.1.3	Level 2 Concentrator, Tracker	1 each		0	0	0	0	0
1.1.3.3.2	Endcaps	2 each		2,603,250	951,638	490,296	171,604	8,433,575
1.1.3.4	Tracker Integration	1 lot		1,000,000	250,000	0	0	1,250,000

Figure 5.1: Example of WBS.

and clerical. The statement of base M&S and labor in man-years by the three categories results in a cost which we believe is comparable to that used by the ILC GDE, and is referred to here as the ILC cost.[1]

While contingency is not used in the ILC value system, it does give some idea of the uncertainties in the costs of the detector components. Items which are close to commodities, such as iron, have seen wild cost swings over the last few years. It is also difficult to estimate silicon detector costs for such large quantities.

There are a substantial set of interfaces in the IR hall. For the purpose of this estimate, the following has been assumed:

- The hall itself, with finished surfaces, lighting, and HVAC are provided.
- Utilities, including 480 VAC power, LCW, compressed air, and internet connections are provided on the hall wall.
- An external He compressor system with piping to the hall is provided. The refrigeration and associated piping is an SiD cost.
- Any surface buildings, gantry cranes, and hall cranes are provided.
- Data storage systems and offline computing are provided.
- Detector motion rails, for push-pull and opening in the beamline and garage positions, are installed by SiD in suitably prepared areas in the concrete floor.
- The QD0s and their cryogenic systems are provided. The beampipe is an SiD cost.

The subsystem level summary is shown in Table 5.1, the M&S costs are plotted in Figure 5.2, and the labor costs are shown in Figure 5.3. The costs are dominated by the Magnet and the ECAL. The magnet has roughly equal costs for the superconducting coil and the iron. The ECAL is dominated by the silicon detectors. The ECAL manpower is dominated by the operations associated with handling and testing the Si detectors and their associated KPiX and cable. The ECAL has relatively complex cables related to the thin gap between radiators. At this time, it is uncertain whether significant fractions of the handling and testing can be automated, so the estimate is conservative. Also, the tungsten plate assembly is complex, with a large number of spacer columns. This is again conservatively estimated.

[1] To expand this to U.S. DOE style costs, the following steps are made:

Contingencies are assigned to M&S and Labor. The purpose of the contingency is primarily to make funding available to hold a schedule in the face of unforeseen problems; to fund items that were forgotten in the estimate; and to provide some relief from underestimates.

Labor is transformed to a dollar value by using SLAC salaries that include benefits but not overhead.

Indirects are computed as a fraction of the M&S and Labor. SLAC large project values are used.

Escalation is computed assuming a start date, a 6 year construction cycle, and an inflation rate. For this study, a start date of 2016 and an inflation rate of 3.5%/year is assumed. The escalation is both quite substantial and uncertain.

	M&S Base (M$)	M&S Contingency (M$)	Engineering (MY)	Technical (MY)	Administrative (MY)
LumCal and BeamCal	3.68	1.42	4.0	10.0	0.0
VXD	2.80	2.04	8.0	17.7	0.0
Tracker	14.45	5.71	24.0	53.2	0.0
ECAL	57.74	23.02	13.0	287.8	0.0
HCAL	16.72	6.15	13.0	28.2	0.0
Muon System	5.35	1.65	5.0	20.1	0.0
Electronics	4.90	1.65	44.1	41.7	0.0
Magnet	123.74	42.58	29.2	25.0	0.0
Installation	4.10	1.08	4.5	46.0	0.0
Management	0.92	0.17	42.0	18.0	30.0
Totals	234	85	187	548	30

Table 5.1: Subsystem summary of costs. Labor contingency is not shown.

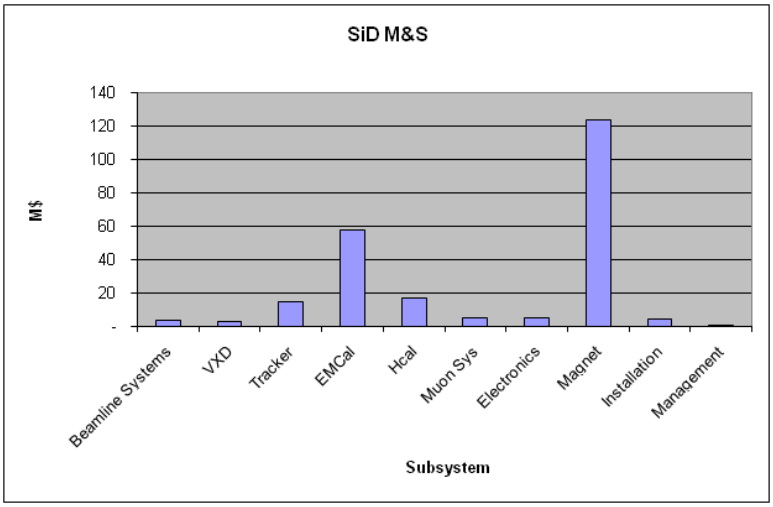

Figure 5.2: Subsystem M&S Costs.

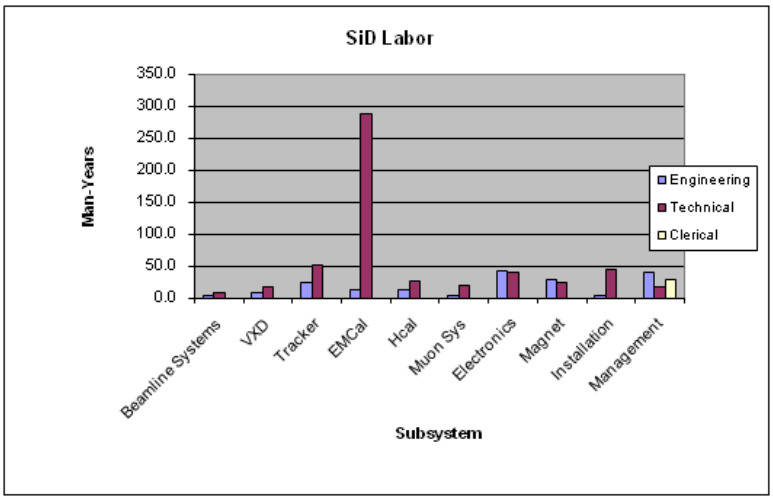

Figure 5.3: Subsystem Labor.

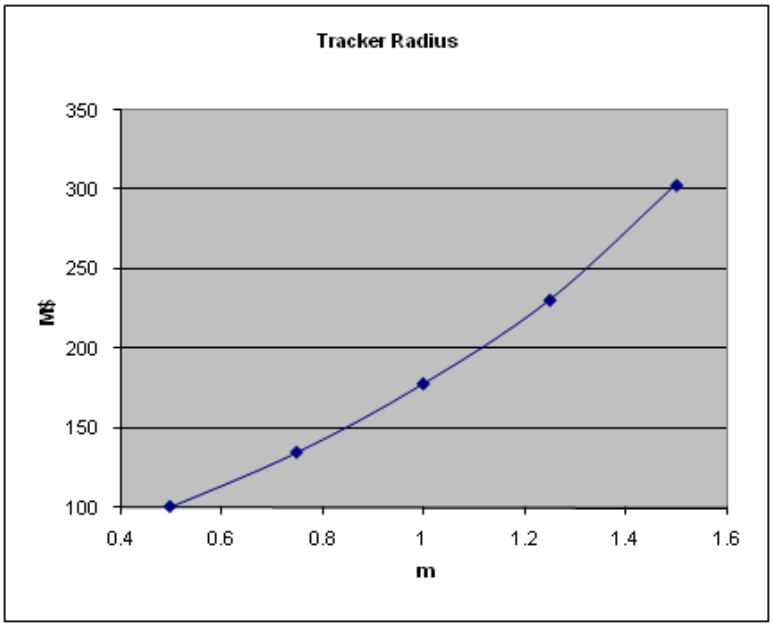

Figure 5.4: SiD Base M&S Cost vs Tracker Radius.

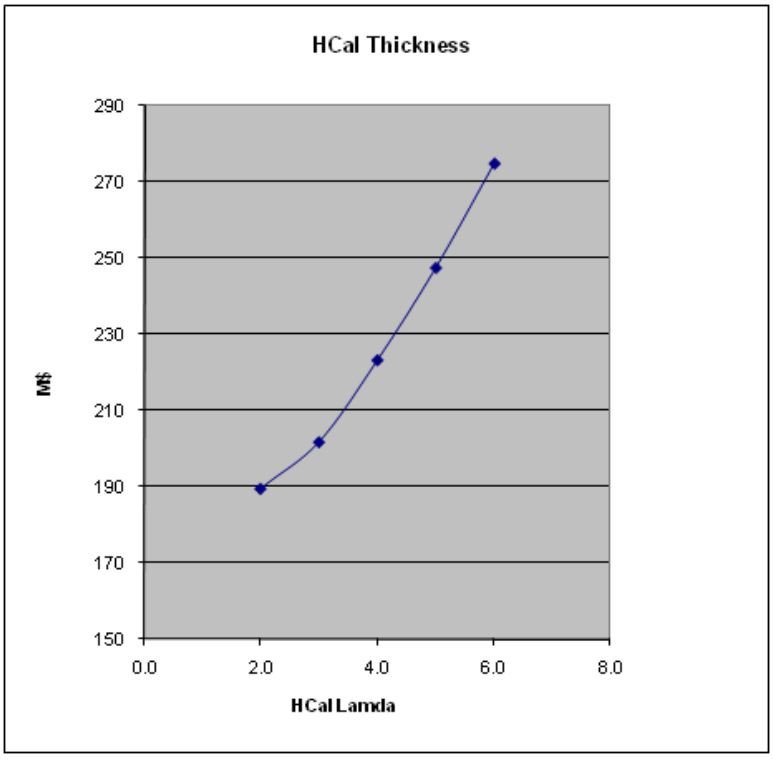

Figure 5.5: SiD Base M&S Cost vs Hadronic Calorimeter Thickness.

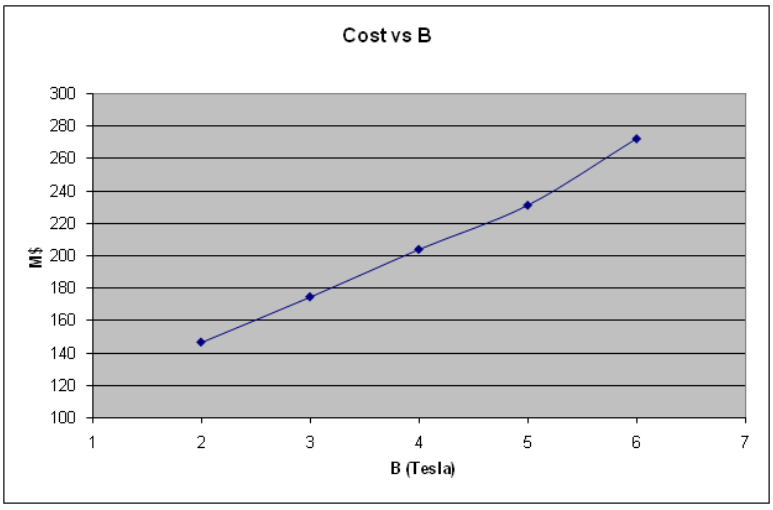

Figure 5.6: SiD Base Cost vs B.

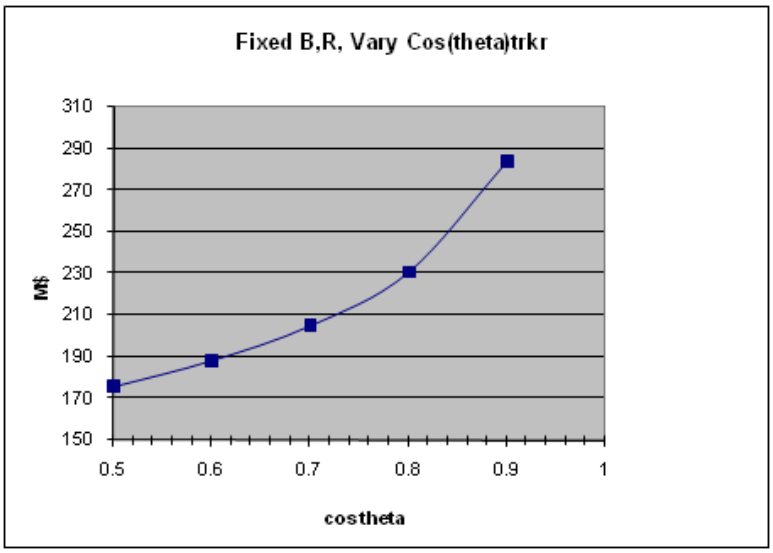

Figure 5.7: SiD Base Cost vs Tracker Aspect Ratio.

Figure 5.4 through Figure 5.7 show simple examples of the parametric costs of SiD. In all cases, the non-varied parameters are the SiD baseline: tracker radius = 1.25 m, tracker polar-angle coverage, $|\cos|\theta = 0.8$, B= 5 T, and HCAL thickness = 4.5 λ. Finally, physics performance versus PFA resolution is used to study physics performance versus SiD cost. This is discussed in more detail in chapter 1.

The cost estimate has several important "commodity" items whose costs have recently been fluctuating significantly. These include most metals and processed Si detectors. Table 5.2 illustrated the cost sensitivity to these prices by indicating the unit cost used in the estimate and the effect on the SiD cost of doubling the unit cost.

Item	Nominal Unit Cost	ΔSiD Base M&S Cost (M$)
Magnet Iron (finished and delivered)	\$7/Kg	56
Tungsten (powder alloy) plate	\$88/Kg	7
Si Detector	\$3/cm^2	39
HCAL Detector	\$2000/m^2	7

Table 5.2: Cost Sensitivity to selected unit costs.

The superconducting coil cost is difficult to estimate, because there is little data and experience with coils of this size and field. An attempt was made to extract the CMS coil cost, and it is believed to be ~\$48M for the cold mass and vacuum tank. An industrial estimate for the SiD coil was obtained, and it was approximately the same as CMS, but for a coil with roughly half the stored energy. Cost functions linear in the stored energy and with a 0.66 exponential dependence have been studied, and are shown in Figure 5.8. SiD has taken a conservative approach and for the parametric study has used a linear model fit to the Babar coil at the low end and the industrial estimate at the high end. The result for the

current SiD design is \$55M, higher than the CMS cost, but inflation and currency exchange variations have been ignored. SiD is doing R&D on advanced conductor design, and there is some reason to expect the coil cost estimate to decrease.

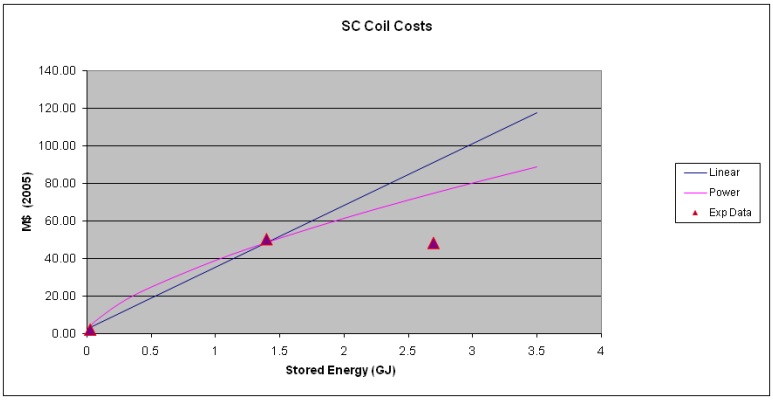

Figure 5.8: Superconducting coil costs. The triangles are, from the left, the estimated cost of the BaBar coil, an industrial estimate for an earlier version of SiD, and our understanding of the CMS coil cost.

The SiD cost in ILC value units is \$238M for M&S, 206 MY engineering, 613 MY technical, and 25 MY administrative labor. The estimated M&S contingency, reflecting uncertainty in unit costs and some estimate of the maturity of this study, is \$88M. The cost in US accounting, assuming a construction start in 2016 and 3.5% per year inflation and US National Laboratory labor rates, is \$700M. For the SiD Detector Outline Document in 2006, the base M&S cost estimate was \$203M, to be compared with the \$238M present value. About \$20M of the difference is in the approach used for estimating the superconducting solenoid.

Chapter 6

SiD R&D

The SiD R&D Plan is designed to provide a technical basis for an optimized SiD detector in 2012.

Critical R&D for the SiD Detector Concept

Members of the SiD detector concept have been engaged in R&D for detector components and software systems at the International Linear Collider (ILC) for a number of years. In this section we summarize the critical R&D tasks for each area of SiD.

1) General. For the overall performance of the SiD detector, we need to demonstrate that the detector can adequately address the full spectrum of the physics at a 500GeV ILC, with extension to 1 TeV, including studies of benchmark reactions. This requires a full and realistic simulation of the detector, track reconstruction code, and development of a fully functional Particle Flow Algorithm (PFA). While we have working versions of the simulation, reconstruction, and the PFA, we anticipate significant further developments, which will provide the critical tools to optimize and finalize the detector design.

2) Vertex Detector. No ILC ready vertex detector sensor yet exists. The main needs are to develop one or more solutions for the sensors, a demonstrably stable and low mass mechanical support, and pulsed power/cooling solutions. Sensor technologies are being developed, as well as mechanical support concepts, materials, pulsed power, and cooling.

3) Tracking Detector. The priorities for tracking are testing a multi-sensor prototype with readout in the absence of a magnetic field and at 5T, refining the track finding and fitting performance, understanding the optimal forward sensor configuration, developing more detailed understanding of the mechanical stability and power distribution, and designing the alignment system. Work is underway in all of these areas, some by members of the SiLC Collaboration.

4) Electromagnetic Calorimetry. For the baseline silicon-tungsten ECAL design, the operability of a fully integrated active layer inside the projected 1.25mm gap between absorber plates must be demonstrated. Sufficient S/N, successful signal extraction, power-

ing, and adequate cooling must be shown as well. Mechanical prototypes with steel rather than tungsten will first be built, followed by a full depth tower appropriate for beam tests. Sensor operation at 5T will be demonstrated. For the alternative MAPS technology, the physics advantage must be clarified, large sensors produced with sufficient yield, and power requirements understood.

5) Hadronic Calorimetry. The priority for hadronic calorimetry is to demonstrate the feasibility of assembling a fully integrated, full-size active layer within an 8 mm gap between absorber plates. Several technologies are being investigated, which need technical demonstration: RPC's, GEM's, Micromegas, and scintillating tiles/SiPM's. All of this work is being carried out in conjunction with the CALICE Collaboration, and the results will form a critical component of SiD's future technology selection. An alternative approach, using homogeneous crystal calorimetry with dual readout, is also being studied. This effort needs to demonstrate good hadronic energy linearity and resolution in a test beam, to develop suitable crystals, to produce a realistic conceptual design, and to simulate physics performance.

6) Electronics. One critical item in electronics is the demonstration of the operation of the 1024 channel version of the KPiX chip and full documentation of its performance. Another is to develop power distribution schemes with DC-DC conversion or serial powering. A third is development of a readout chip for the Beamcal that can handle unit occupancy and a high radiation environment.

7) Magnet. For the superconducting solenoid, it is required to demonstrate that a 5T field can be achieved with acceptable forces, reliability and cost. To address cost reduction, a new conductor is being studied. R&D for the Detector Integrated anti-Dipole coils is also required. The field uniformity required for pattern recognition in the tracker must be understood, and accommodated with refined designs for the flux return steel.

8) Engineering Issues. A credible scheme for push-pull operation is required that achieves acceptable repositioning of the detector, preserving internal alignment, in an acceptably short cycle time. Equally important is achieving the required mechanical stability of the quadrupole focusing lenses.

9) Forward Calorimetry. A sensor that can survive the radiation environment in the beamcal is required. Some of this work is collaborative with the FCAL Collaboration.

10) Muon system. Emphasis is placed on development of reliable, and robust RPCs. SiPMs for scintillator strips are an alternative technology of interest, also under development.

Prioritization of SiD R&D

The previous section enumerated the critical R&D areas for the SiD detector concept. Prioritization of R&D is a complicated undertaking, and we understand that not every aspect of the R&D can have the same emphasis. Many considerations need to be balanced in setting priorities: importance of the R&D to viability of the detector concept; expected return on investment; growth of the collaboration; and proper exploitation of developments world-wide.

Of critical importance for any high energy collider detector is achieving superb jet energy resolution. Although significant progress has been made establishing the viability of the Particle Flow concept, it has not been demonstrated experimentally. Proving that SiD's choice of hadron calorimeter can do the physics and is cost effective is our top priority. Calorimetry is thus seen as critical to the SiD detector concept. A very fine-grained Silicon-Tungsten electromagnetic calorimeter and an RPC based hadronic calorimeter form the baseline for the detector, with GEM, micromegas, and scintillator as interesting alternative technologies. It is proposed that both baseline technologies be readied for large scale prototype efforts as quickly as possible, together with the development of the associated particle flow based software. It is strategically important to also start R&D on a crystal based total absorption calorimeter, which is complementary to particle flow calorimetry. The SiD tracker employs a hybrid-less readout scheme. The sensors have been procured in previous funding cycles. To establish the hybrid-less concept, the development of an array of sensors mounted on a support structure, with full readout in actual detector configuration in a test beam is given high priority. Readout through the baseline architecture, employing the KPiX chip, is given priority. Because the deployment of two detectors will be achieved through the push-pull mechanism, it is deemed critical to engineer structures that will preserve the alignment of the tracker during this operation. The 3D vertical integrated silicon technology and the further development of the Chronopixel are given priority in the area of the vertex detector, since no viable technology for an ILC vertex detector exists yet.

R&D Efforts

Ongoing R&D efforts closely linked to SiD are described below along with the expected evolution of the R&D in 2010-12 (see Tables 6.1 and 6.2). Other efforts world-wide may also contribute to SiD's R&D goals.

Vertex Detector

High efficiency identification of heavy flavor quarks, with the ability to distinguish quarks from anti-quarks, will be of crucial importance for the anticipated spectrum of physics signals at the ILC. While it is foreseen that the needed performance can be developed, to date no vertex detector technology meets the ILC requirements. This is reflected in the fact that vertex detector technologies are an SiD priority. Many different technologies are being pursued, such as DEPFET detectors, monolithic active pixel sensors (MAPS), in-situ storage imaging sensors (ISIS), and charge-coupled detectors (CCD), such as fine pixel, column parallel and short column CCDs. Because it is not a priori clear which technology will give the best overall performance, SiD has not adopted a baseline technology for the vertex detector. But SiD is engaged in developing technologies which can time stamp individual bunch crossings, which it considers highly desirable.

Future year vertex detector developments

The technology for an ILC vertex detector has not been established. Efforts are proceeding globally on a number of different solutions (ISIS, DEPFET, CCDs, 3D Vertical Integrated Silicon, and MAPS, for example). On the other hand, there is time to find a solution. Once technologies are identified as holding promise for an ILC environment, the

R&D will move towards full-scale sensors with the associated readout. Given the expense of silicon technology, we expect this level of R&D to require funding levels beyond the current level. There should be a technology selection by the time of ILC construction approval. The selected technology will then be applied to the design and construction of a small prototype. R&D in parallel will include understanding the number of background pulses that can be integrated without destroying tracking capability, developing mechanics, powering schemes, and understanding the realistic limits on material reduction.

Tracker

The ILC experiments demand tracking systems unlike any previously envisioned. In addition to efficient and robust track-finding over the full solid angle, the momentum resolution required to enable precision physics at ILC energies must improve significantly beyond that of previous trackers. The design must minimize material in front of the calorimeter that might compromise particle-flow jet reconstruction. Establishing and maintaining the alignment for the tracker is critical. Even with the largest feasible magnetic field, the tracking volume is quite large, demanding optimized tracker components which facilitate mass production. Finally, the tracker must be robust against beam-related accidents and aging. All these requirements must be maintained within a "push-pull" scenario.

Future year tracking detector developments

The emphasis in the area of the tracking detector is currently on the development of the double-metal sensor with the associated readout. These sensors need to work in a 5 T magnetic field and remain stable and aligned during power pulsing. The forward tracker design must be optimized. A small scale system consisting of a few sensors with full readout will be tested in a test beam under these operating conditions. Only then can issues associated with the Lorentz forces and mechanical stability be tested. Tracking R&D will require an increased level of support to address these questions.

Calorimeters

To measure hadronic jets of particles produced in high-energy collisions of electrons and positrons, with sufficient precision, it is widely accepted that a new approach is necessary. The most promising method, utilizing Particle Flow Algorithms (PFAs), uses the tracker to measure the energy of charged particles and the calorimeter to measure the energy of neutrals. The baseline SiD detector concept accepts that a PFA is necessary, and is designed to optimize the PFA performance with the goal of obtaining jet energy resolutions of the order of 3-4% of the jet energy.

SiD has adopted initial baseline technologies for both the electromagnetic and hadron calorimeters, and is also pursuing alternative technologies, since it is not, a priori, clear which combination(s) of hardware and PFA software will produce the most cost-effective performance.

We have defined performance criteria for the calorimeter systems, both in terms of basic design requirements for use with a PFA, and detailed hardware performance for efficient and reliable operation. These criteria will be used in the final selection of electromagnetic and hadron calorimeter technologies once all the required R&D has been completed.

Project Descriptor	Institution(s)	Past Funding	Current Funding	Future Funding
ENGINEERING				
SC Solenoid	Fermilab, SLAC	DOEL	DOEL	DOEL
Flux Return	Fermilab, SLAC, Wisc.	DOEL	DOEL	DOEL
MDI/Push-pull	Fermilab, SLAC	DOEL	DOEL	DOEL
General	Fermilab, SLAC, etc.	DOEL	DOEL	DOEL
VERTEX				
Chronopix	Yale, Oregon, SLAC	LCDRD	sLCDRD, DOEL	ULCDP, DOEL
CAPS	Hawaii	LCDRD	sLCDRD	ULCDP
ISIS	Bristol, Oxford, RAL	UK, term. 2008	internal	new fund.
MAPS	Strasbourg	France	France	France
Sensor Powering	Fermilab	DOEL	DOEL	DOEL
Sensor Thinning	Fermilab, Cornell	DOEL	DOEL	DOEL
Vertex Mechanics	Washington, Fermilab	LCDRD, DOEL	DOEL	ULCDP, DOEL
3D Sensor	Fermilab	DOEL	DOEL	DOEL
3D Sensor Sim.	Cornell		DOEL	ULCDP
TRACKING				
Alignment	Michigan, Spain, Spain	LCDRD, Spain	Spain	ULCDP, Spain
DC-DC converters	Yale, SLAC	LCDRD, DOEL	DOEL	ULCDP, DOEL
DS/SS Si Det. & calor (eg. lum)	Kyungpook N Univ.	Korea	Korea	Korea
Forward Tracking	Spain	Spain	Spain	Spain
Sensor QA, cables	New Mexico			ULCDP
Sensor QA	UC Santa Cruz	LCDRD	sLCDRD	ULCDP
Tracking Sim.	Santa Cruz, Oregon, SLAC, Fermilab	DOEL	DOEL	DOEL ULCDP

Table 6.1: SiD R&D Projects, part 1. Definitions: LCDRD is 3 year US DOE/NSF Linear Collider Detector R&D grant beginning 2005; sLCDRD is 2008-9 LCDRD supplement; DOEL is US DOE laboratory funding; ULCDP is SiD US University LC Detector Proposal to DOE/NSF on February 18, 2009.

Project Descriptor	Institution(s)	Past Funding	Current Funding	Future Funding
CALORIMETRY				
Beamcal, Readout/Sim	Colorado, SLAC	LCDRD, DOEL	DOEL	ULCDP, DOEL
Dual Readout	Caltech, Fermilab	DOEL	DOEL	DOEL ULCDP
ECAL Mechanics	Annecy, SLAC	France, DOEL	France, DOEL	France, DOEL
GEM HCAL	UTA, MIT	LCDRD		ULCDP
Micromegas HCAL	Annecy	France	France	France
MAPS ECAL	B'ham, Bristol, Imperial, Oxford, RAL	UK	SPiDeR	SPiDeR
PFA	Iowa, MIT, ANL, SLAC	LCDRD, DOEL	DOEL	ULCDP, DOEL
Radhard Bmcal Sens.	UCSC, SLAC		DOEL	ULCDP, DOEL
RPC HCAL	BU, Iowa, ANL, FNAL	LCDRD, DOEL	sLCDRD, DOEL	ULCDP, DOEL
Scint HCAL	NIU	LCDRD		ULCDP
SiPM Readout	Fermilab, SLAC	DOEL	DOEL	DOEL
Si-W ECAL & Readout	Oregon, Davis, SLAC, BNL	LCDRD, DOEL	sLCDRD, DOEL	ULCDP, DOEL
MUON				
RPC Muon/HCAL	Princeton	LCDRD		ULCDP
RPC Muon System	Wisconsin	LCDRD		ULCDP
SiPM Muon System	WS, IU, ND, NIU, Fermilab	LCDRD, DOEL	sLCDRD, DOEL	ULCDP, DOEL
BEAMLINE MEAS.				
Energy Spectrometer	Notre Dame, Oregon	LCDRD	sLCDRD	ILC accel?
Polarimeter	Iowa	LCDRD		ILC accel?

Table 6.2: SiD R&D Projects, part 2. See table 6.1 for definitions.

Future year calorimeter developments

For the Si-W ECAL, we anticipate that the test-beam related data taking and analysis will continue beyond August 2010. First the module will be tested in an electron beam (possibly at SLAC), followed later by a beam test with hadrons. Completion of this R&D is expected by 2012. For the MAPS ECAL the goals are to assess the physics potential for the device with simulation studies and to make a second generation chip which is sufficiently large to make an ECAL stack to study digital eletromagnetic calorimetry in detail.

The RPC option for the HCAL will continue with testing the CALICE $1m^3$ stack beyond the first year. The calorimeter will be exposed to muons and pions and positrons of various energies. The response and energy resolution will be measured together with characteristics of hadronic showers, such as the lateral and longitudinal shower shapes, which are relevant for Particle Flow Algorithms. The GEM option will test its $1m^2$ layers as part of the CALICE hadron calorimeter prototype, and will design and build a complete, integrated layer with minimal thickness and full services. Thick GEM prototypes will also be assembled and tested as large sections of thick GEMs become available. Gas studies for thick GEMs will also continue. The micromegas option will see the continued testing and analysis of results from the $1m^3$ stack. Finally, the major activity for the scintillator/SiPM option will be the insertion of the integrated readout layer planes fabricated with the CALICE/EUDET electronics into the CALICE absorber stack. This installation will be followed by the commissioning and exposure of this prototype to a test beam.

The homogeneous dual-readout calorimetry will continue development of suitable crystals, photodetectors, and associated readout electronics, all in preparation for a demonstration of linearity and energy resolution for hadrons in a test beam, while developing a conceptual design for inclusion of this technology into SiD, and evaluating physics performance.

Continued effort will also be directed towards improving and refining the SiD Particle Flow algorithm and simulation of the dual-readout concept. This will involve several SiD groups and focus on improvements for higher jet energies.

Progress on all calorimetry options will be monitored closely, with a technology selection for SiD during 2011.

Muons

The SiD muon system is designed to identify muons from the interaction point with high efficiency and to reject almost all hadrons (primarily pions and kaons). The muon detectors will be installed in gaps between steel layers of the solenoid flux return. Since the central tracker will measure the muon candidate momentum with high precision, the muon system only needs sufficient position resolution to unambiguously match calorimeter tracks with muon tracks. Present studies indicate that a resolution of 1-2 cm is adequate. These position resolutions and the required rate capabilities can be met by more than one detector technology. The baseline design uses double layers of resistive plate chambers(RPC). Also under consideration are extruded scintillator strips read out by silicon photomultipliers (SiPMS). Cost, reliability and physics capabilities should determine the preferred choice between RPCs and scintillators.

Future Year Muon Developments

The muon detector effort will work toward a technology choice during 2011. RPC efforts include cost-effective readouts and aging studies. The scintillator SiPM work is expected to include evaluation of SiPM manufacturers, mounting, temperature control, and monitoring, as well as development or acquisition of an SiPM compatible ASIC, possibly a modified KPiX. Planning for construction of a larger-scale prototype of the selected technology would begin, with simulation studies of overall detector performance for muons. The simulation model of the muon system would be derived from measurements with prototypes.

Forward Calorimetry

Two photon processes present a major background to searches for certain supersymmetric particles. These processes can be identified by detecting a high energy electron or positron in the beamcal, above the beamstrahlung background. Developing highly efficient techniques for tagging electrons and suppressing background is being done with full GEANT simulation.

Through its participation in the CERN-based RD50 R&D collaboration, SiD collaborators are working on the development of Czochralski-process silicon diode sensors for application to high-radiation environments. Due to the relatively high oxygen content, it is expected that Czochralski sensors will be much more resistant to damage than standard sensors produced from float-zone process silicon. Studies are investigating the suitability of Czochralski sensors for forward calorimetry.

Future Year Forward Calorimeter Developments

The outcomes of these studies of two photon backgrounds will lead to refined designs of the beamcal. Radiation hard detectors and readout electronics for the beamcal must be developed.

Beamline Instrumentation

SiD is interested in beamline instrumentation, particularly work on energy spectrometry and polarimetry. This area of needed R&D can be followed jointly with other detector groups, as well as machine groups.

Schedule and Milestones

2009

- **Simulation/Reconstruction:** PFA improvements; tracking simulation and reconstruction improvements and background studies; simulation of dual readout concept; optimization of SiD design.
- **Electronics:** Full KPiX chip; develop beamcal readout.
- **Tracker:** Sensor test; sensor with readout test; develop alignment concept.
- **ECAL:** Sensor test; sensor with readout test.
- **Beamcal:** Evaluation of beamcal sensor technologies.
- **HCAL:** RPC and GEM with readout tests; GEM slice test; Micromegas slice test; RPC construct 1 m^3; engineering design of HCAL module; dual readout crystal candidate selection and photon detection studies.

- **Vertex:** Develop sensors; continue mechanical and power distribution designs.
- **Muon:** Test RPCs, scintillating fiber, and RPC longevity.

2010

- **Simulation/Reconstruction:** Update physics studies; dual readout full simulation and physics performance.
- **Electronics:** Test beamcal sensor readout; develop SiPM readout (if needed).
- **Tracker:** Test alignment concept; beam test sensors with readout and support system in B field; test Lorentz forces and mechanical stability with pulsed power.
- **ECAL:** Build and test ECAL tower; build mechanical prototype for ECAL module.
- **HCAL:** Produce engineering design of module with integrated readout; dual readout beam test of concept; continue beam tests and analysis; ready 1 m^2 modules of GEM and Micromegas; continue development of suitable crystals.
- **Vertex:** Develop sensors; continue mechanical and power distribution designs.
- **Muon:** Prototype muon chambers; longevity test; study costs.
- **MDI:** Develop push pull designs; vibration studies; study alignment issues.
- **Magnet:** Develop new conductor jointly with others.
- **Beamcal:** Design sensors.

2011

- **Technology Selections:** ECAL, HCAL, Muon.
- **Engineering:** Complete engineering designs for ECAL, HCAL and Muons for chosen technologies and forward systems; plan preproduction and detailed design phase.
- **Simulation/Reconstruction:** Complete detector optimization; realistic GEANT4 detector description based on technology choices; generate MC data.
- **Complete beam testing:** SiW ECAL, RPC, GEM, Micromegas, Scint & SiPM HCAL; proof of principle development of suitable crystals and photodetectors.
- **Tracker:** Test large scale system.
- **Vertex:** Test sensors; continue mechanical and power distribution designs.
- **Benchmarking:** Studies with final detector choices and optimized design.
- **Magnet:** Continue new conductor development.

2012

- Complete optimized SiD detector design.
- Begin tests of magnet material.
- Begin full scale prototyping.
- Write SiD proposal.

Conclusion

The SiD R&D Plan has been evolving for several years, and the definition of SiD's critical needs has sharpened through the LoI process. The SiD R&D Plan is designed to deliver the results needed to provide a solid technical basis of an optimized SiD detector design in 2012.